Geochemical and Fluid Dynamic Investigations Into the Nature of Chemical Heterogeneity in the Earth's Mantle

by

Erik Harold Hauri

B.S. University of Miami, Florida, 1988

SUBMITTED IN PARTIAL FULFILLMENT OF THE
REQUIREMENTS FOR THE DEGREE OF
DOCTOR OF PHILOSOPHY

at the

MASSACHUSETTS INSTITUTE OF TECHNOLOGY
and the
WOODS HOLE OCEANOGRAPHIC INSTITUTION

September, 1992

Signature of the author_____
Joint Program in Oceanography
Department of Geology and Geophysics,
Woods Hole Oceanographic Institution and
Department of Earth, Atmospheric, and Planetary Sciences,
Massachusetts Institute of Technology, July, 1991

Certified by_____
Stanley R. Hart, Thesis Supervisor

Accepted by_____
Chairman, Joint Committee for Marine Geology and Geophysics,
Massachusetts Institute of Technology-Woods Hole Oceanographic
Institution

Geochemical and Fluid Dynamic Investigations
Into the Nature of Chemical Variability
in the Earth's Mantle

by

Erik H. Hauri

Submitted to the Department of Earth, Atmospheric, and Planetary Sciences
Massachusetts Institute of Technology
and
Department of Geology and Geophysics
Woods Hole Oceanographic Institution
on July 21, 1992
in partial fulfillment of the requirements
for the degree of Doctor of Philosophy

Abstract

Variations in the abundances of elements and radiogenic isotopes in mantle derived peridotites and volcanic rocks are chemical integrals over time, space, and process, which ultimately contain information about the role of convection in the earth's mantle in creating, maintaining, and destroying geochemical heterogeneities. Successful inversion of these integrals requires extensive knowledge of the geochemical behavior of elements, the length scales of chemical variability, the evolution with time of geologic systems, the physical properties of mantle rocks, and the driving forces of phenomena which govern heat and mass transport in a dynamic earth. This dissertation attempts to add to this knowledge by examining the trace element and isotope geochemistry of mantle peridotites and oceanic island basalts, and by studying aspects of the flow of viscous fluids driven by thermal buoyancy.

The trace element and isotopic systematics of peridotites and associated mafic layers from the Ronda Ultramafic Complex, southern Spain (Chapter 2), provides information bearing on the geochemical behavior of the highly incompatible elements U, Th, and Pb in the mantle, and on the length scales of geochemical variability in a well exposed peridotite massif. Garnet is demonstrated to be a significant host for U in the mantle, and together with clinopyroxene, these two minerals control the abundances and partitioning relationships of U and Th during the melting of anhydrous peridotite. Clinopyroxene, plagioclase, and to a lesser extent garnet are hosts for Pb in mantle peridotite; however, the role of trace sulfide may exert some control over the abundance and partitioning of Pb in some samples. Due to the possibility that Pb is partitioned into sulfide, the U/Pb, Th/Pb, and Ce/Pb ratios measured in clinopyroxene are likely to be higher than the bulk rock. U-Pb age systematics of garnet-clinopyroxene pairs from Ronda peridotites and mafic layers indicate Pb isotopic equilibrium in these samples up to 20-50 Ma ago. The Pb-Pb systematics of garnet- and spinel-facies peridotites and mafic layers indicate a heterogeneity on the order of 3 Ga old. This Pb isotope signature may have been created within the massif 3 Ga ago, or may have been metasomatically imprinted on the massif 1.3 Ga ago by basaltic melts with island arc affinities. The isotopic evolution of Ronda is consistent with

an origin as ancient (3 Ga) MORB source mantle which experienced a partial melting event at 1.3 Ga ago, and was subsequently incorporated into the subcontinental lithosphere. The very low U, Th, and Pb concentrations in depleted peridotite indicate that recycled crustal materials, with U-Th-Pb concentrations 10^2-10^4 times higher than peridotite, will have a larger influence on the isotopic composition of Pb in the mantle than on the Sr and Nd isotopic composition.

An investigation of the trace element and isotopic compositions of clinopyroxenes in peridotite xenoliths from Savaii, Western Samoa and Tubuai, Austral Islands (Chapter 3) reveals geochemical signatures which are not present in basalts from these islands, due to the inherent averaging of melting processes. The data indicate similarities in the melting and melt segregation processes beneath these isotopically extreme islands. Samples with LREE depleted clinopyroxenes, with positive Zr and negative Ti anomalies, are the result of polybaric fractional melting of peridotite in the garnet- and spinel lherzolite stability fields, with the Savaii samples having experienced a larger mean degree of melting than the Tubuai samples. The extreme fractionation of HREE in the Savaii samples requires that they have melted to the clinopyroxene-out point (about 20%) while retaining residual garnet; the low concentrations of HREE in these same samples requires a further 10-20% melting in the spinel lherzolite stability field. The extremely high total degrees of melting experienced by the Savaii samples (33-42%), as well as the high degree of melting in the garnet lherzolite stability field, suggests a mantle plume origin for these xenoliths.

A large majority of the xenolith clinopyroxenes from both Savaii and Tubuai are LREE enriched to varying degrees, and many samples display significant intergrain trace element heterogeneity. This highly variable yet systematic heterogeneity was the result of metasomatism by percolating melts undergoing chromatographic trace element fractionation. The trace element compositions of some LREE enriched clinopyroxenes are consistent with the percolating melt being typical oceanic island basalt. The clinopyroxenes with the highest LREE concentrations from both islands, which also have very low Ti and Zr concentrations and large amounts of grain-boundary hosted Ba, require that the percolating melt in these cases had the trace element signature of carbonatite melt. The isotopic composition of one of these "carbonatitic" samples from Tubuai is similar to basalts from this island. The isotopic composition of clinopyroxene in a "carbonatitic" sample from Savaii records $^{87}Sr/^{86}Sr$ and $^{143}Nd/^{144}Nd$ values of .71284 and .512516 respectively, far in excess of the most extreme Samoa basalt values ($^{87}Sr/^{86}Sr=.70742$, $^{143}Nd/^{144}Nd=.51264$). These "carbonatitic" signatures indicate the presence of volatile-rich, isotopically extreme components in the mantle beneath Tubuai and Savaii, which likely have their origins in recycled crustal materials.

The Re-Os isotope systematics of oceanic island basalts from Rarotonga, Savaii, Tahaa, Rurutu, Tubuai, and Mangaia are examined (Chapter 4). Os concentration variations suggest that olivine, or a low Re/Os phase associated with olivine, controls the Os concentration in basaltic magmas. The Savaii and Tahaa samples, with high $^{87}Sr/^{86}Sr$ and $^{207}Pb/^{204}Pb$ ratios (EMII), as well as basalts from Rarotonga, have $^{187}Os/^{186}Os$ ratios of 1.026-1.086, within the range of estimates of bulk silicate earth and depleted upper mantle. The basalts from Rurutu, Tubuai, and Mangaia (Macdonald hotspot), characterized by high Pb isotope ratios (HIMU), have $^{187}Os/^{186}Os$ ratios of 1.117-1.248, higher than any estimates for bulk silicate earth, and higher than Os isotope ratios of metasomatized peridotites. The high $^{187}Os/^{186}Os$ ratios indicate the presence of recycled oceanic crust in the mantle sources of Rurutu, Tubuai, and Mangaia. Inversion of the isotopic data for Mangaia (endmember HIMU) indicate that the recycled crustal component has Rb/Sr, Sm/Nd, Lu/Hf, and Th/U ratios which are very similar to fresh MORB glasses, and U/Pb and Th/Pb ratios which are within the range of MORB values, but slightly higher than average N-MORB. These results indicate that the low-temperature alteration signature of

altered oceanic crust may be largely removed during subduction, and that oceanic crust was recycled into to the lower mantle source of the Macdonald hotspot plume. Furthermore, the high $^{187}Os/^{186}Os$ ratios of the Tubuai and Mangaia basalts indicates that percolation through depleted mantle peridotite ($^{187}Os/^{186}Os=1.00$-1.08), observed to occur in the Tubuai xenoliths, had little influence on the composition of the erupted basalts.

A fluid dynamic model for mantle plumes is developed (Chapter 5) by examining a vertical, axisymmetric boundary layer originating from a point source of heat, and incorporating experimentally constrained rheological and physical properties of the mantle. Comparison of linear (n=1) and non-Newtonian (olivine, n=3) rheologies reveals that non-Newtonian plumes have narrower radii and higher vertical velocities than corresponding Newtonian plumes. The non-Newtonian plumes also exhibit "plug flow" at the conduit axis, providing a mechanism for the transport of deep mantle material, through the full depth of the mantle, in an unmixed state. Plumes are demonstrated to entrain ambient mantle via the horizontal conduction of heat, which increases the buoyancy and lowers the viscosity of mantle at the plume boundary. Streamlines calculated from the fluid dynamic model demonstrate that most of the entrained mantle originates from below 1500 km depth. Parameterization of the entrainment mechanism indicates that the factional amount of entrained mantle is lower in stronger, hotter plumes due to their higher vertical velocities.

Examination of the global isotopic database for oceanic island basalts reveals the presence of a mantle component (FOZO), common to many hotspots worldwide, characterized by depleted $^{87}Sr/^{86}Sr$ and $^{143}Nd/^{144}Nd$, radiogenic $^{206,207,208}Pb/^{204}Pb$, and high $^{3}He/^{4}He$. This component is isotopically distinct from the source of MORB; thus, with the exception of ridge centered hotspots such as Iceland and the Galapagos, upper mantle does not appear to be a component in most hotspots, in agreement with entrainment theory. The combined fluid dynamic and isotopic results indicate that both FOZO and the enriched mantle components (EMI, EMII, and HIMU) are located in the lower mantle. Furthermore, high $^{3}He/^{4}He$ in FOZO precludes an origin for FOZO-bearing plumes in a thermal boundary layer at 670 km depth in the mantle. Since a 670 km thermal boundary layer would be replenished by the downward motion of the upper mantle, an origin for FOZO at 670 km would require either 1) a high $^{3}He/^{4}He$ signature in the MORB source, or 2) entrainment of MORB mantle into intraplate plumes, neither of which is observed in the OIB isotope data. This indicates that the 670 km discontinuity is not a barrier to mantle convection. The preservation of isotopically different upper and lower mantles does not require layered convection, but is probably the result of an increasing residence time with depth in the mantle, possibly caused by an increase in the mean viscosity of the mantle with depth.

Thesis Supervisor: Stanley R. Hart
                      Senior Scientist
                      Woods Hole Oceanographic Institution

Acknowledgements

First of all, warm thanks to my mentor and friend Stan Hart, an advisor without peer, a truly visionary scientist, and a first class person. Some of the most important aspects of an education cannot be taught in the classroom; Stan's confident "state-of-the-art" attitude toward all aspects of research has been nothing less than inspiring. His perspective and approach to the large scale problems in geochemistry has contributed greatly to the ways in which I view the earth. I am grateful to Stan for the freedom and the means to follow my instincts for the last four years, especially in the face of urgent requests for funds emanating from the South Pacific. It is no coincidence that my predecessors have established a lofty standard in Stan's lab; I consider myself fortunate to have the opportunity to "come of age" in an environment where anything was possible. It has been a fun run, and everything I hoped it would be.

A large measure of thanks goes to Nobu Shimizu, my initial liason to MIT and the Joint Program. His role as a geochemical "sounding board" during many morning conversations is sincerely appreciated. Nobu's readiness to call into question the most fundamental underpinnings of geochemistry is an admirable quality. I have benefitted tremendously from his knowledge of metamorphic petrology and attention to the micron-scale aspects of geochemistry, all of which fundamentally influenced my view of the world. The ability to gain knowledge about the workings of the planet through the analysis of nanograms provided the initial inspiration for me to pursue isotope geochemistry; Nobu's approach reinforced this view, and I am grateful for his impact on my development as a scientist.

Thanks to Ken Burrhus, curator of a truly blue-blood family of mass spectrometers. Ken's ability to take a perplexing problem and break it down into its most fundamental aspects is a trait which I hope has rubbed off on me. His patience with the litany of blown power supplies during the N-TIMS revolution was appreciated by this particular "wizard of Os". NIMA-B is a mass spec which eats new isotope systems for lunch, and the fact that this machine, now 16 years old, is still putting out state-of-the-art data is an enduring tribute to Ken's thoughtfullness. Thanks for all of it.

Jack Whitehead deserves special thanks for introducing me to the world of fluid mechanics. His ability to instinctively grasp the most important aspects of problems, in a field so rich in non-linearity, is truly amazing and inspiring. I will be forever in Jack's debt for instilling in me a desire to link geochemistry and fluid mechanics; it is a link that permeates my thinking, and one that I have really enjoyed working with.

Thanks also to the other members of my committee; to Marcia McNutt for her expertise as MC, to Fred Frey for instructing me in the ins and outs of trace element geochemistry, and to Tim Grove for a proper petrological education and for encouraging me to take JBT's course (I think). Thanks also to Jake Pierson, Abbie Jackson, and Ronnie Schwartz of the Education Office for their support.

An extra dose of appreciation goes to Hans Barsczus (Montpellier), without whose knowledge and experience (both geological and logistical) the trip to the South Pacific would have been less of a scientific success and more of a boondoggle.

A host of others have, in no small fashion, provided inspiration and contributed in thought, word, and deed toward my journey to becoming a scientist, which began some 20 years ago. While it is impossible to name them all, there are those whom I cannot fail to mention: Vincent Salters, for introducing me to the isotope lab, and for inspiration ("That's good-if you try to finish in four years, then you'll definitely finish in five"), Jurek Blustzajn for a good clean lab education and many enjoyable discussions on geochemistry and sports, Greg Ravizza for tutelage in the finer arts of fire assay and Os chemistry, Jon Snow, Larry McKenna, Graham "Galena Man" Layne, Dave Bercovici (want some gorp?), Tom "Young Embassador" Wagner, Dave Kammer (why, yes, I would love some gorp),

5

Mark Kurz, and Lynn Oschmann. Thanks also to Fred Nagle, Cesare Emiliani, Jerry Stipp, and David Price for supporting my fledgling isotope career at Miami. Thank you to Judy Boisen for getting me hooked on research in a big way; and thanks to J.R. Hoffman for showing me the power of the mind.

Last, but of the utmost importance, the biggest thank you goes to my parents, Karen and Larry. For convincing me that any goal was attainable, for that set of encyclopedias (!), and for your love, encouragement, and hard work, you planted the seeds and made it all possible. Though it is probably difficult to see, there is a lot of you in these pages. Finally, to Tracy, my dearest wife and best friend. I can think of few things more difficult than being married to a graduate student, except having to do it without your love and support. Thank you so much for helping me to do my best, and for keeping my feet on the ground. And thank you Kevin, for just being the sweetest boy, and making this the best year of my life.

EHH
August, 1992

To Tracy,
who had the hardest job of all,
and handled it with grace under pressure

And to my mother Karen,
for her unshakable optimism

TABLE OF CONTENTS

CHAPTER 1

Introduction

The geochemical variability expressed in the trace element and isotopic signatures of mantle derived peridotites and basalts is the end product of the processes of mantle mixing, melting, and melt segregation acting over various spatial and temporal scales. In addition to these processes, surficial weathering, mass transport, and alteration may contribute to the geochemical signatures of mantle derived materials if crustal components are recycled into the deep mantle. In attempting to relate specific geochemical signatures to specific mantle processes, one must have a firm understanding of the mechanisms by which these different processes influence the distribution of different elements over the spatial and temporal scales observable in mantle derived rocks. This dissertation attempts to place geochemical observations in mantle peridotites and basalts into the context of fluid dynamic processes in the earth's mantle, and thereby forge a better understanding of the ways in which physical process determine chemical signatures.

Chapter 2 applies a long-standing geochemical tool, the U-Th-Pb isotopic system, to an examination of the scales of chemical heterogeneity in peridotites and mafic rocks from the Ronda Ultramafic Complex, Southern Spain. Though the isotopic composition of Pb in the mantle was first shown to be demonstrably heterogeneous in 1964 (Gast et al., 1964), the application of the U-Th-Pb system has lagged far behind the pace of Sr and Nd isotopic studies of mantle peridotites. As a result, we know little about the geochemical behavior of these elements in the mantle, complicating the interpretations of the Pb isotopic signatures of basaltic rocks (Tatsumoto, 1966; Gast, 1969; Tatsumoto, 1978; Sun, 1980). The low concentrations (ppb) of U, Th, and Pb in the Ronda peridotites indicates that the Pb isotopic composition of the mantle will be strongly influence by any recycled crustal components. Compared with the more limited isotopic variability observed in other ultramafic massifs (Polvé and Allègre, 1980; Hamelin and Allegre, 1988), the large degree of isotopic heterogeneity at Ronda, present at both small and large scale lengths, suggests a residence in the subcontinental lithosphere for about 1.3 Ga. The isotopic evolution of Ronda is consistent with an origin as ancient (>1.3 Ga) MORB source mantle incorporated into the subcontinental lithosphere 1.3 Ga ago.

Chapter 3 examines the trace element characteristics of clinopyroxene in peridotite xenoliths from the islands of Savaii (Western Samoa, Samoa hotspot) and Tubuai (Austral Islands, Macdonald hotspot) which were collected by the author during the fall of 1990. Basaltic rocks from the Samoa and Macdonald hotspots are characterized by extreme isotopic compositions ($^{87}Sr/^{86}Sr$ to .7075, $^{207}Pb/^{204}Pb$ to 15.70 (EMII) at Tutuila,

American Samoa (Farley et al., 1992); $^{206}Pb/^{204}Pb$ to 21.80 (HIMU) at Mangaia, Cook Islands (Nakamura and Tatsumoto, 1988), Chapter 4), and so the geochemical signatures of these xenoliths were expected to place constraints on the origins of these endmember signatures and the melt generation/segregation processes operative in their plume sources. The trace element characteristics of LREE depleted xenoliths indicate an origin as residues of polybaric fractional melting in the stability fields of garnet and spinel lherzolite. Compared with abyssal peridotites (Johnson et al., 1990), the high degrees of melting in the garnet lherzolite stability field experienced by the Savaii samples (up to 22%), coupled with their high total degrees of melting (33-42%) suggest a mantle plume origin for these xenoliths. The extreme variability of LREE enrichment in most of the xenoliths is consistent with metasomatism by percolating basaltic and carbonatitic melts which were undergoing chromatographic trace element fractionation (Navon and Stolper, 1987). The isotopic compositions of clinopyroxenes with "carbonatitic" trace element patterns from both Savaii and Tubuai indicate the presence of volatile-rich, isotopically extreme components in the Samoa and Macdonald mantle plumes. These components likely have their origins in recycled crustal materials.

Chapter 4 applies a relatively new geochemical tool, the Re-Os isotopic system, to the analysis of oceanic island basalts with extreme isotopic signatures for $^{87}Sr/^{86}Sr$ (EMII, Savaii,Western Samoa and Tahaa, Society Islands) and $^{206,207,208}Pb/^{204}Pb$ (HIMU, Rurutu, Tubuai, and Mangaia, Cook-Austral Islands). Re and Os are both chalcophile (affinity for sulfide) and siderophile (affinity for metal) elements. Os is strongly depleted in basaltic melts compared with Re, and so basaltic melts have much higher Re/Os ratios than residual peridotites (Morgan, 1986). As a result of the different geochemcal properties of Re and Os compared with other parent-daughter systems, the analysis of Os isotopes in the South Pacific OIBs was expected to yield new constraints on the origins of these isotopically extreme mantle compositions. The $^{187}Os/^{186}Os$ ratios of the Savaii and Tahaa basalts lie within the range of estimates for primitive and depleted mantle, but the high $^{187}Os/^{186}Os$ ratios in the HIMU basalts indicate the presence of recycled oceanic crust in their mantle sources, in agreement with previous studies (Chase, 1981; Hofmann and White, 1982), and indicating that subducted oceanic lithosphere is recycled into the lower mantle. In addition, the homogeneity of the Os isotope ratios in the basalts from Tubuai and Mangaia require that melt migration through depleted mantle had an insignificant effect on the chemistry of these basalts. The identification of a low $^{87}Sr/^{86}Sr$-high $^{206,207,208}Pb/^{204}Pb$ signature with recycled oceanic crust suggests its presence in the mantle sources of other oceanic basalts, including some high $^{206}Pb/^{204}Pb$ mid-ocean ridge basalts.

Chapter 5 examines the mantle mixing consequences of fluid flow in mantle plumes, modelled as the axisymmetric boundary layer rising from a point source of heat. By incorporating experimentally and theoretically constrained mantle properties, the effects of these properties on the entrainment of ambient mantle into plumes is evaluated. The entrainment theory indicates that the entrained mantle originates almost entirely from below 1500 km depth. The Sr-Nd-Pb-He isotopic database on oceanic basalts indicates the presence of a mantle component (FOZO) which is present in many hotspots from around the world. The results from entrainment theory, and the isotopic signatures of OIB confirm, that the entrainment of MORB source mantle (upper mantle) in mantle plumes is minimal (except for ridge centered hotspots), and that both FOZO and the enriched mantle components (EMI-EMII-HIMU) are located in the lower mantle. The combined geochemical and fluid dynamic results suggest that mantle plumes may not originate from a thermal boundary layer at 670 km depth, evidence which probably rules out layered convection.

Finally, the most important results of this research are integrated in Chapter 6. The low concentrations of the most incompatible elements in mantle peridotite indicate that the signature of recycled crustal components should be most clear in the isotopic signatures of Th, Pb and Sr. The unique properties of the U-Pb system, due to the existence of two parent-daughter systems in a single element-element pair, make this system a powerful tool for studies of mantle peridotites. The U-Pb (and Th-Pb) isotopic systematics of peridotites are very sensitive to resetting by recent melting and metasomatic processes, due to the incompatibility of these elements. However, the age information contained in Pb-Pb isochrons is more difficult to reset, requiring perfect homogenization, and thus the Pb-Pb system is more likely to contain ancient age information than other isotopic systems. Similar to the situation at mid-ocean ridges (Johnson et al., 1990), fractional melting in mantle plumes requires that erupted melt products are integrated collections of small batches of melt generated throughout the plume. However, the abundance of LREE enriched xenoliths from oceanic islands indicates that melt extraction processes, and thus probably also melt mixing processes, are more efficient at mid-ocean ridges than at hotspots. As a result, the degree of chemical variability of the upper mantle cannot be evaluated from the equivalent variability in MORB, and thus the upper mantle may not be as "well mixed" as is often suggested (White and Schilling, 1978; Ito et al., 1987). Although mixing processes are likely to occur in mantle plumes, the expression of plume-ambient mantle mixing in the chemistry of hotspot basalts is complicated by the mixing processes of plume-lithosphere interaction (Yuen and Fleitout, 1985; Griffiths and Campbell, 1991) and melt segregation (McKenzie, 1984; Navon and Stolper, 1987; Kenyon, 1990). A more detailed inversion of

OIB geochemistry to examine the chemical structures of mantle plumes requires a better characterization of plume-lithosphere interactions, and knowledge of the mechanisms of melt extraction from the mantle beneath ridges and hotspots, both employing well constrained rheological and physical parameters for the upper mantle.

REFERENCES

Chase, C. G. (1981) Oceanic island lead: two-stage histories and mantle evolution. Earth Planet. Sci. Lett., **52**, 277-284.

Farley, K. A., J. Natland and H. Craig (1992) Binary mixing of enriched and undegassed mantle components in Samoan lavas. Earth Planet. Sci. Lett., **111**, 183-199..

Gast, P. W. (1969) The isotopic composition of lead from St. Helena and Ascension Islands. Earth Planet. Sci. Lett., **5**, 353-359.

Gast, P. W., G. R. Tilton and C. Hedge (1964) Isotopic composition of lead and strontium from Ascension and Gough Islands. Science, **145**, 1181-1185.

Griffiths, R. W. and I. H. Campbell (1991) Interaction of mantle plume heads with the earth's surface and onset of small scale convection. J. Geophys. Res., **96**, 18,295-18,310.

Hamelin, B. and C. J. Allegre (1988) Lead isotope study of orogenic lherzolite massifs. Earth Planet. Sci. Lett., **91**, 117-131.

Hofmann, A. W. and W. M. White (1982) Mantle plumes from ancient oceanic crust. Earth Planet. Sci. Lett., **57**, 421-436.

Ito, E., W. M. White and C. Goepel (1987) The O, Sr, Nd and Pb isotope geochemistry of MORB. Chem. Geol., **62**, 157-176.

Johnson, K. T. M., H. J. B. Dick and N. Shimizu (1990) Melting in the oceanic upper mantle: an ion microprobe study of diopsides in abyssal peridotites. J. Geophys. Res., **95**, 2661-2678.

Kenyon, P. (1990) Trace element and isotopic effects arising from magma migration beneath mid-ocean ridges. Earth Planet. Sci. Lett., **101**, 367-378.

McKenzie, D. P. (1984) The generation and compaction of partially molten rock. J. Petrol., **25**, 713-765.

Morgan, J.W. (1986) Ultramafic xenoliths: clues to Earth's late accretionary history. J. Geophys. Res., **91**, 12,375-12,387.

Nakamura, Y. and M. Tatsumoto (1988) Pb, Nd, and Sr isotopic evidence for a multicomponent source for rocks of Cook-Austral Islands and heterogeneities of mantle plumes. Geochim. Cosmochim. Acta, **52**, 2909-2924.

Navon, O. and E. Stolper (1987) Geochemical consequences of melt percolation: the upper mantle as a chromatographic column. J. Geol., **95**, 285-307.

Polvé, M. and C. J. Allègre (1980) Orogenic lherzolite complexes studied by 87Rb-87Sr: a clue to understand the mantle convection processes. Earth Planet. Sci. Lett., **51**, 71-93.

Sun, S. S. (1980) Lead isotopic study of young volcanic rocks from mid-ocean ridges, ocean islands, and island arcs. Philos. Trans. R. Soc. London, **A297**, 409-445.

Tatsumoto, M. (1966) Genetic relations of oceanic basalts as indicated by lead isotopes. Science, **153**, 1094-1101.

Tatsumoto, M. (1978) Isotopic composition of lead in oceanic basalts and its implication to mantle evolution. Earth Planet. Sci. Lett., **38**, 63-87.

White, W. M. and J. G. Schilling (1978) The nature and origin of geochemical variation in Mid-Atlantic Ridge basalts from central North Atlantic. Geochim. Cosmochim. Acta, **42**, 1501-1516.

Yuen, D. A. and L. Fleitout (1985) Thinning of the lithosphere by small-scale convective destabilization. Nature, **313**, 125-128.

Chapter 2

U-Th-Pb Isotope Systematics of Peridotites and Associated Mafic Rocks from the Ronda Ultramafic Complex

1. Introduction

Geochemical studies of mantle derived basalts and peridotites have established the unequivocal existence of chemical heterogeneities in the earth's mantle which require that various segments of the mantle have evolved independently over time scales of up to several billions of years (Tatsumoto, 1966; Gast, 1969; Brooks et al., 1976) The most direct approach for examining the origins of these heterogeneities is through the study of mantle peridotites, either xenoliths erupted to the surface by igneous processes, or tectonically emplaced orogenic peridotite massifs. Orogenic peridotites offer the advantage of examining mantle geochemistry within its geologic context, and their large size facilitates direct observation of the scale of mantle heterogeneity.

Orogenic peridotite massifs (alpine, or high temperature peridotites) are large bodies, up to several hundred square kilometers, typically composed of 90 - 95% lherzolite and harzburgite with up to 5-10% mafic rocks occurring as bands or layers within the peridotite. They are distinguished from ophiolite peridotites (low temperature peridotites) by the lack of an associated volcanic section. Major element studies of orogenic peridotites (Dick, 1977; Sinigoi et al., 1980; Quick, 1981; Sinigoi et al., 1983; Frey et al., 1985) have determined that they are residues from various degrees of partial melting at mantle pressures and temperatures (Kornprobst, 1969; Dickey, 1970; Obata, 1980). Their trace element characteristics are consistent with this interpretation, but also suggest histories more complicated than a single melt extraction (Frey, 1969; Loubet et al., 1975; Loubet and Allegre, 1979; Loubet and Allegre, 1982). With a few exceptions (Reisberg and Zindler, 1986), the peridotites are almost exclusively depleted in the light rare earth elements (LREE) relative to the heavy rare earths (HREE) (Bodinier et al., 1988), and in this way are quite different from mantle xenoliths, which are dominantly LREE enriched (Nixon, 1987).

The origins of mafic layers in alpine peridotites have proven enigmatic. In some cases, such as at the Lherz peridotite massif, some mafic rocks containing hydrous phases, which exhibit cross-cutting relationships with an earlier generation of anhydrous mafic layers, likely represent magma conduits associated with basaltic volcanism (Bodinier et al., 1987). The origins and age relationships of mafic layers at other peridotite massifs are not as clear, and they likely do not have a simple relationship to the peridotites (Loubet and Allegre, 1982; Suen and Frey, 1987). Unlike the dominantly LREE depleted peridotites in which they occur, the mafic layers often exhibit a variety of REE patterns. Theories pertaining to the mafic layers suggest their origins as crystal cumulates from basic magmas (Suen and Frey, 1987), melts of peridotite and/or an earlier generation of mafic layers

(Loubet and Allegre, 1982), and subducted oceanic crust deformed during mantle convection (Allegre and Turcotte, 1986).

Isotopic studies of orogenic peridotites have demonstrated that significant isotopic heterogeneities exist on a variety of scale lengths (Menzies and Murthy, 1976; Polvé and Allègre, 1980; Richard and Allegre, 1980; Reisberg and Zindler, 1986; Hamelin and Allegre, 1988; Reisberg et al., 1989; Reisberg et al., 1991). Isotopic compositions of peridotites display large ranges both within and between individual massifs. Isotopic results on mafic layers from some massifs have demonstrated heterogeneities of the same range as associated peridotites (Zabargad, Beni Bousera), while mafic rocks from other massifs (Lherz) display a limited heterogeneity (Polve, 1983; Hamelin and Allegre, 1988). Sm-Nd mineral isochrons from Ronda and Beni Bousera mafic rocks are believed to date the time of emplacement of the peridotite bodies into the crust (Polvé and Allègre, 1980; Zindler et al., 1983; Reisberg et al., 1989).

The long-term chemical variability of the mantle is reflected in the large range of the radiogenic isotope ratios of Sr, Nd and Pb measured in basaltic rocks from oceanic islands (ex. Zindler and Hart, 1986), as well as Sr and Nd isotopic studies of mantle peridotites (Menzies and Murthy, 1980a,b; Stosch and Seck, 1980; Stosch et al., 1980). However, investigations of the U-Th-Pb isotopic system in mantle peridotites have been hampered by the very low concentrations of these elements in peridotite. As a result, we know little about the geochemical behavior and residence sites of U, Th, and Pb in the mantle. Pb isotope analyses of whole rock peridotites are likely to be dominated by extraneous contaminants (basaltic veinlets, alteration products, groundwater precipitates, etc.), as has been demonstrated for the Rb-Sr and Sm-Nd systems (Zindler and Jagoutz, 1988). Thus the analysis of purified mineral separates is the only way in which reliable Pb isotope data can be obtained on mantle peridotite samples. This strategy presents a substantial analytical challenge in two ways. First, a mineral separate must be prepared which is free of crustal U, Th and Pb; this is even more crucial than for Sr and Nd analysis, because of the order of magnitude lower U-Th-Pb concentrations (ppb, 10^{-9} grams/g) in the constitutent minerals. Second, analytical blanks must be reduced to a very low level for the chemical separation procedure, in order to minimize their contribution to these small quantities of U, Th and Pb. This is particularly challenging for Pb because of the pervasive nature of anthropogenic Pb contamination. Once these potential sources of contamination are characterized and eliminated, reliable U-Th-Pb data can be obtained on peridotite mineral separates.

The Ronda peridotite, a 300 km^2 orogenic peridotite located in the Betic Cordillera of southern Spain, has been the focus of numerous investigations (Dickey, 1970; Obata

and Dickey, 1976; Dickey et al., 1977; Lundeen, 1978; Dickey et al., 1979; Obata, 1980; Obata, 1982; Zindler et al., 1983; Frey et al., 1985; Reisberg and Zindler, 1986; Suen and Frey, 1987; Reisberg et al., 1989; Reisberg et al., 1991), and is perhaps the most well studied of the orogenic peridotites. The massif is mineralogically zoned from garnet peridotite facies in the northwest, through spinel peridotite to plagioclase peridotite facies to the southeast and east (Fig. 1, from Obata, 1980), and it is likely that this zonation reflects the polybaric cooling history of the massif (Obata, 1980). Investigations by Frey et al. (1985), Zindler et al. (1983), Reisberg and Zindler (1986), Reisberg et al., (1989) and Reisberg et al. (1990) have demonstrated that the massif underwent a partial melting event at about 1.3 Ga. This melting event is reflected in the depletions of basaltic constituents (Ca, Al, Fe, Ti, Na) in the peridotites, as well as depletions in Nd/Sm and Re/Os which resulted in isochronous relationships between whole rock samples in the Sm-Nd and Re-Os systems. This event was contemporaneous with the formation of the mafic layers, as indicated by a whole rock Re-Os isochron for the mafic layers with an age of 1.3 Ga (Reisberg et al., 1990). A small portion of the eastern end of the massif was subject to a metasomatic infiltration at about 300 Ma (Reisberg and Zindler, 1986). The massif was subsequently emplaced into the crust, and cooled past the Sm-Nd closure temperature at about 22 Ma (Zindler et al., 1983).

The Ronda ultramafic complex thus represents a well studied location in which to investigate the geochemical behavior of U, Th and Pb in the mantle. In addition, the purposes of this study are: 1) to demonstrate the feasibility of obtaining accurate and reproducible U-Th-Pb data from mantle peridotite by analysis of mineral separates, avoiding the contamination problems known to disturb the incompatible element systematics of whole rocks; 2) to examine the scale of trace element and Pb isotopic heterogeneity; 3) to examine correlations among the isotopes of Sr, Nd, and Pb at a variety of scale lengths, 4) to document the isotopic character of the mafic layers, and 5) to further evaluate models proposed for the origins of heterogeneity in the mantle, and at Ronda in particular.

2. Sample Descriptions and Analytical Procedures

The locations of all the samples in this study are shown in Fig. 1. Samples R140-R148 and R163-R166 from the plagioclase facies were selected from mapped sections of interlayered peridotite and mafic layers (Fig. 3). The remaining samples with the designation Rxxx were selected to cover the geographic expanse of the massif; some of these samples have been studied by Obata (1980), Frey et al., (1985), and Suen and Frey (1987). A selection of samples from the spinel and garnet facies studied by Reisberg et al.

1 9

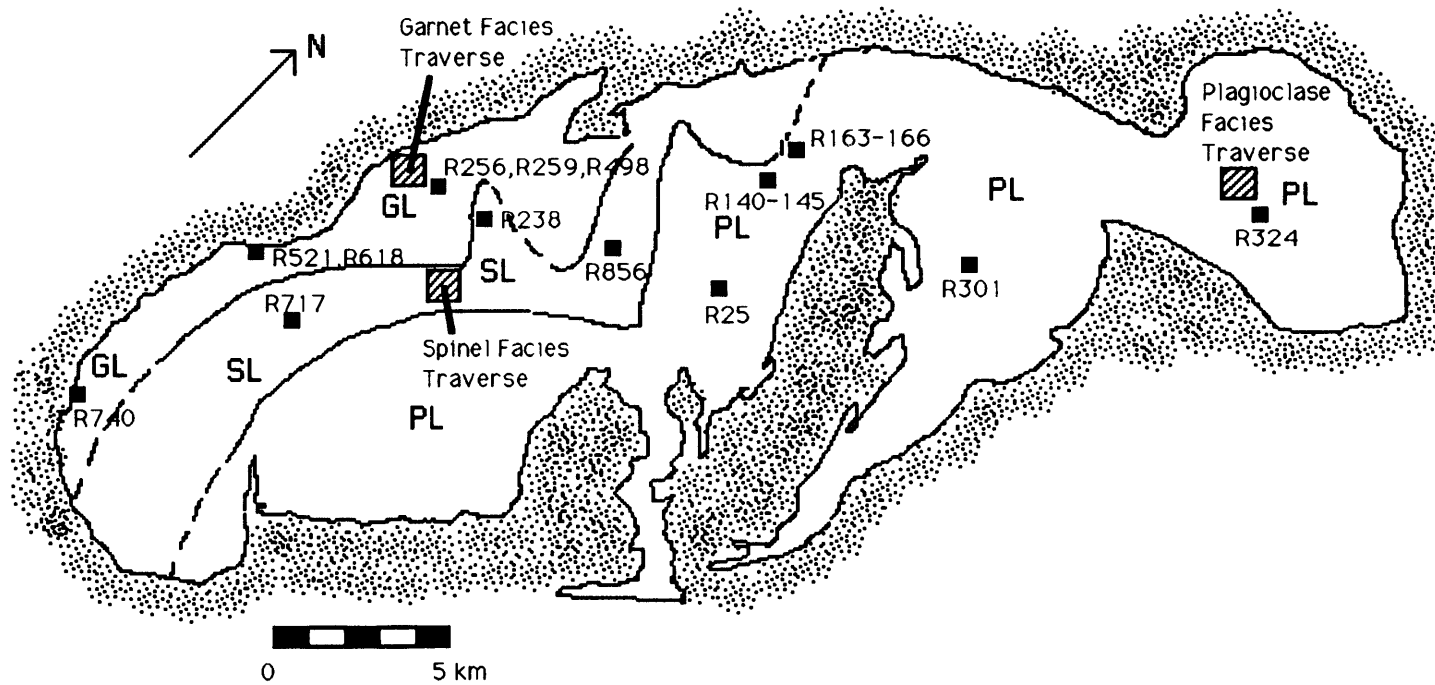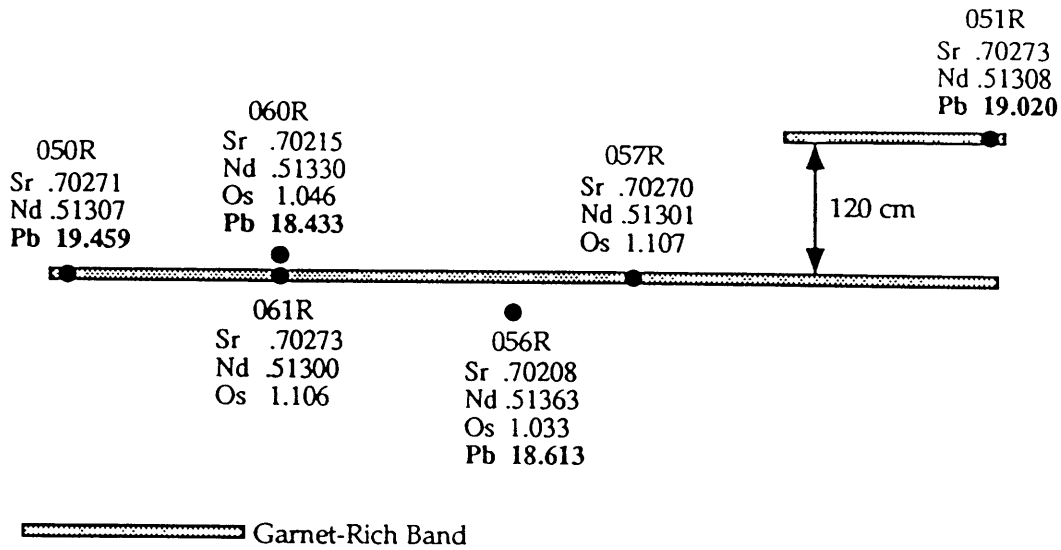Figure 1. Map of the Ronda Ultramafic Complex. Metamorphic facies boundaries are from Obata (1980). PL=plagioclase-lherzolite facies, SL=spinel-lherzolite facies, GL=garnet-lherzolite facies. Small squares mark the locations of samples from the MIT collection. Large squares (LDGO samples) mark the locations of fine-scale sampling traverses described in Reisberg and Zindler (1986), Reisberg (1988), and Reisberg et al. (1989).

A

050R
Sr .70271
Nd .51307
Pb 19.459

060R
Sr .70215
Nd .51330
Os 1.046
Pb 18.433

051R
Sr .70273
Nd .51308
Pb 19.020

057R
Sr .70270
Nd .51301
Os 1.107

120 cm

061R
Sr .70273
Nd .51300
Os 1.106

056R
Sr .70208
Nd .51363
Os 1.033
Pb 18.613

Garnet-Rich Band

B

013R   016R
          009R
008R   SAMPLES 412R, 414R, 416R, AND 418R
005R   COLLECTED AT 2m INTERVALS
003R   002R
001R

N

STREAM

50m

407R

404R   403R

400RG
STREAM
SEDIMENT

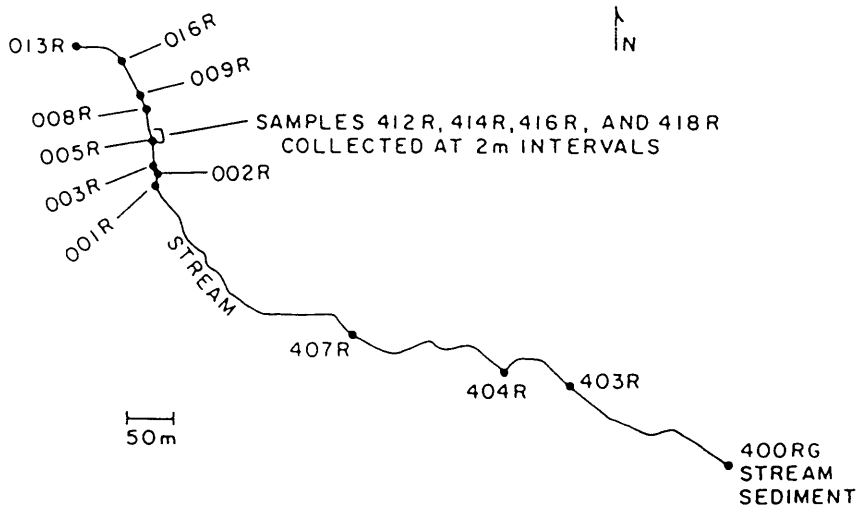Figure 2. Detailed maps of the fine-scale sampling areas in the garnet and plagioclase facies, after Reisberg (1988). A) Garnet facies sampling area. Shaded line marks the location of a garnet-rich band. Sample 060R is located 15 cm above the band, sample 056R is located 35 cm below the band. Isotopic data from Reisberg et al. (1989) (Sr-Nd) and Reisberg et al. (1990) (Os). B) Plagioclase facies sampling traverse.
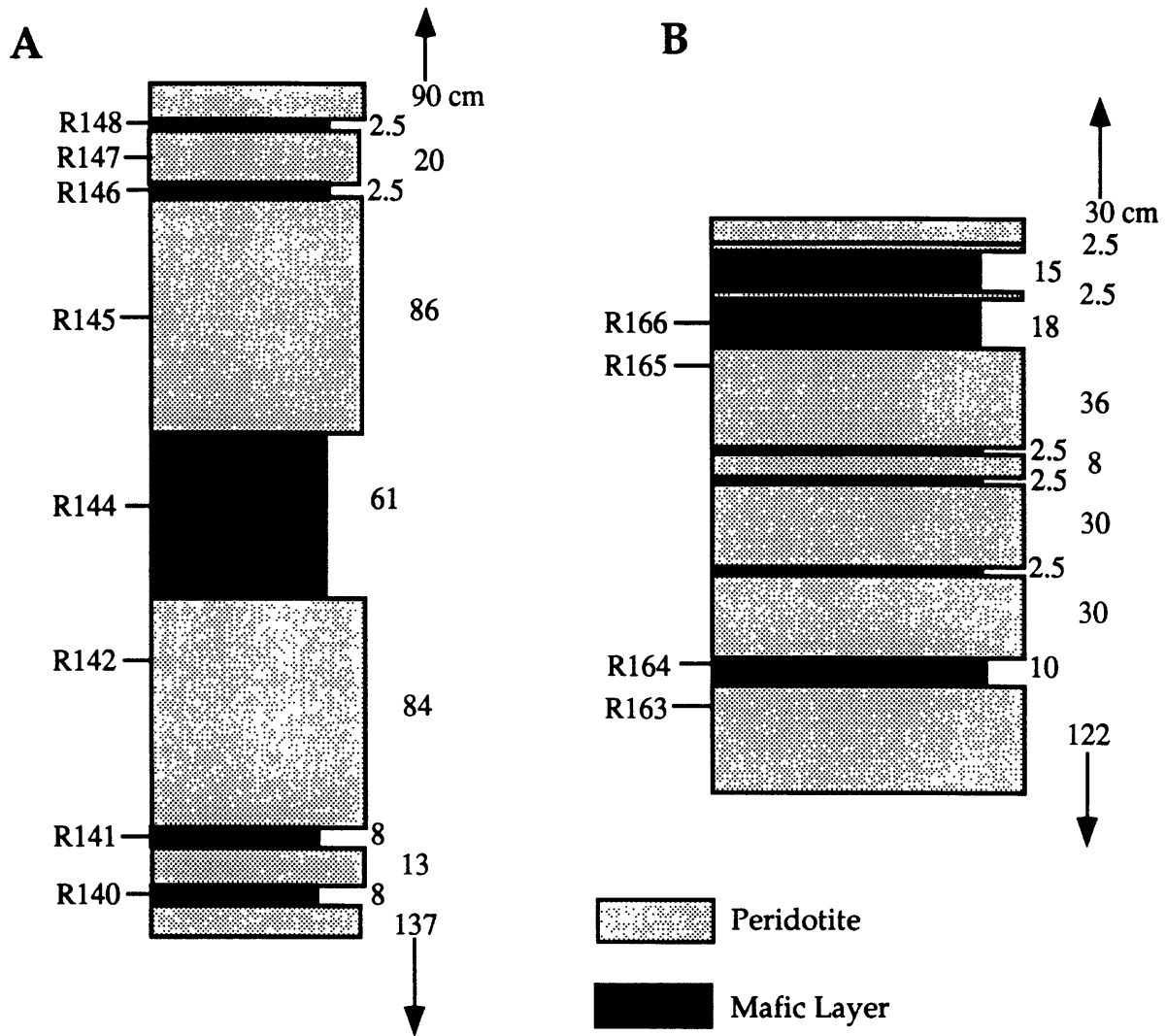
21

Figure 3. Stratigraphic columns for two regions of interlayered peridotites and mafic layers in the plagioclase facies (see Fig. 1 for locations). Light colored layers are peridotite, and dark layers are mafic layers. Layer thicknesses are given in cm, and sample numbers are given on the left side of the columns.

22

(1989) were also analyzed. Samples 050R, 051R, 056R, and 060R are from an area of closely spaced sampling around a garnet-rich band of lherzolitic composition (Fig. 2). In addition, U-Th-Pb isotope data obtained by Alan Zindler on plagioclase facies samples studied by Reisberg and Zindler (1986) are included in this chapter. Samples 002R, 008R, 009R, 013R, and 016R are from a small scale traverse in the plagioclase facies, and are all located within 150 meters of each other (Fig. 2). Sample descriptions, petrographic details, and additional data can be found in these references.

To avoid contamination during processing, samples were wrapped in plastic wrap and cotton towels and crushed to 50-100 mesh size with a plastic mallet on a wooden block. Plagioclase, clinopyroxene and garnet were concentrated magnetically and purified by repeated crushing (with an agate mortar and pestle) and handpicking following procedures similar to (Zindler and Jagoutz, 1988). Great care was taken to avoid inclusions, films and subgrain boundaries known to host incompatible elements. At this point, several representative grains of clinopyroxene and garnet were selected for analysis by ion microprobe. Clinopyroxene separates were leached using two different procedures: 1) 2.5 N HCl at 100°C for 1 hr, followed by 5% HF at room temperature for 20 minutes, followed by 2.5 N HCl at 100°C for 30 minutes; 2) 2.5 N HCl at 100°C for 1 hr, followed by a solution of 8N HNO_3-0.6N HCl-0.05N HF at 100°C for 2 hr. Garnets were leached using the first procedure. The second leaching procedure was later developed to ensure the solution of U and Th during the leaching procedure, though repeat analyses of R238 cpx indicate that the different leaching procedures did not fractionate U, Th, and Pb (see below). Grains were rinsed with water between acid leaching steps, and finally the grains were rinsed five times with water and dried at 75°C. Plagioclase was leached in 2.5 N HCl at room temperature for 30 minutes. All leaching steps used reagents cleaned by sub-boiling distillation in teflon stills, and took place in clean, filtered air. A detailed description of the procedures for the sample dissolution, separation of U, Th, and Pb, and mass spectrometry of these elements are given in the appendix.

REE and the trace elements Sc, Cr, Ti, Zr and Sr were analyzed *in situ* using a Cameca IMS 3f ion microprobe, employing energy filtering to exclude molecular ion interferences (Shimizu and Hart, 1982). Concentrations were determined through the use of working curves based on a set of well determined standards. Precision of the analyses is 5-15%, except for Ce and Nd in garnet, where precision is estimated at 40-50% and 20-40% respectively. All concentrations with errors greater than 50% are reported as maximum values.

23

	Sc	Ti	V	Cr	Sr	Zr	La	Ce	Nd	Sm	Eu	Dy	Er	Yb
MIT Samples														
R25 cpx	94	1510	319	6657	0.8	12.6		5.01	3.85	1.29	0.42	2.57	1.68	1.84
R142 cpx	78	7278	377	8308	6.1	75		7.00	11.08	4.80	1.68	5.97	3.19	3.35
R145 cpx	67.7	5817	250	9600	14.3	80.9		9.53	13.30	4.38	1.37	3.13	1.51	1.69
R163 cpx	47	3659	228	5345	21.1	35.3		5.13	5.47	2.09	0.86	2.77	1.70	1.90
R165 cpx	27	2606	159	3786	9.9	36		5.25	7.65	2.93	1.03	3.32	1.86	2.02
R324 cpx	46	220	216	6722	5.4	1.1		1.21	0.50	0.13	0.05	0.32	0.38	0.37
R238 cpx	35.8	2333	264	6618	70.6	22.7		4.22	4.39	2.00	0.86	3.54	2.08	2.36
R238 opx														
R717 cpx	60	3473	277	3824	59	48		5.91	5.84	2.49	1.07	4.05	2.30	2.58
R856 cpx	53	854	212	5607	13	13.9		1.09	1.13	0.62	0.25	1.43	0.99	1.02
R498 cpx	35	4957	335	5628	99.6	43.3		6.45	7.37	3.21	1.09	1.94	0.79	0.91
R498 garnet	128	1042	145	7908		38.6		0.61	0.46	0.68	0.59	5.51	4.42	5.64
R521 cpx	51	2193	244	7499	58	24.5		5.91	5.43	1.97	0.71	0.97	0.37	0.41
R521 garnet	153	1241	194	9258		31.1		0.29	0.40	0.63	0.55	5.99	5.07	6.16
R618 cpx	15	4580	301	4446	90.9	34.1		6.45	7.28	2.24	0.92	1.58	0.51	0.54
R618 garnet	141	726	145	6893		23.8		0.04	0.25	0.56	0.41	6.43	6.67	9.60
R740 cpx	28	3545	294	6343	61	29.9		5.55	5.84	2.16	0.90	1.65	0.67	0.62
R740 garnet	90	2037	179	5345		43.6		0.10	1.00	1.19	0.78	5.78	4.47	5.67
LDGO Samples														
002R cpx	43	250	221	5907	15.5	0.63	0.52	1.17	0.48	0.06	0.06	0.62	0.54	0.73
008R cpx	33	209	188	5938	17.3	2.8	0.69	1.40	0.74	0.17	0.03	0.59	0.47	0.62
009R cpx	37	232	191	5713	18.7	2.3	0.97	1.66	0.54	0.17	0.10	1.00	0.75	0.87
013R cpx	47	218	218	6163	15.5	2.1	0.70	1.32	0.45	0.08	0.05	0.95	0.78	0.93
016R cpx	42	181	204	5195	24.5	1.6	0.65	1.00	0.40	0.11	0.05	0.46	0.34	0.37
403R cpx	27	370	238	9944	88.5	11.3	2.48	6.73	3.63	0.81	0.25	0.50	0.35	0.34
404R cpx	33	119	190	7096	26.9	2.6	5.33	9.30	1.58	0.21	0.09	0.36	0.35	0.36
414R cpx	32	160	210	6788	10.4	1.7	1.03	1.01	0.41	0.09	0.06	0.40	0.38	0.59
R85-32 cpx	60.1	1327	236	4910	40.5	19.1	0.69	2.27	2.59	1.27	0.51	2.45	1.40	1.47
R85-35 cpx	58.2	3064	255	4435	42.9	39.1	0.99	2.93	2.91	1.61	0.74	2.89	1.90	1.80
R85-41 cpx	51.3	2644	247	5735	40.6	37.6	0.99	2.79	2.90	1.13	0.50	1.93	1.19	1.26
R85-43 cpx	50.3	3377	251	3928	58	41.3	1.50	5.72	4.94	1.48	0.74	2.68	1.71	1.60
R85-47 cpx	47.6	2559	238	4238	49.2	34.7	0.74	2.83	2.72	1.46	0.55	2.52	1.47	1.30
040R cpx	50.5	1740	236	5158	47.9	23	0.48	1.51	2.35	1.27	0.60	2.42	1.70	1.95
050R cpx	9	3759	305	3742	70.2	32	2.01	6.37	4.78	1.43	0.55	0.74	0.36	0.15
051R cpx	57.9	4254	262	4579	70.9	49.5	2.03	5.84	4.80	1.83	0.64	2.83	1.67	1.59
056R cpx	46.2	1939	226	6648	35.8	23.5	0.59	2.21	2.95	1.34	0.72	2.58	1.75	1.82
060R cpx	44.4	3682	258	4572	65.3	48.3	1.12	3.79	4.37	1.91	0.86	2.99	1.73	1.86
Mafic Layers														
R140 cpx	65	7212	464	6367	3	71.1		6.21	12.17	5.83	2.04	8.69	4.94	5.74
R141 cpx	83	7397	543	7207	3.8	70.7		5.85	11.94	5.74	1.84	8.98	5.15	5.66
R301 cpx	39	354	138	8198	15	0.5		0.72	0.81	0.32	0.12	0.32	0.16	0.17
R256 cpx	26	3471	311	1163	225.7	10.3		3.50	3.30	1.46	0.55	0.95	0.35	0.33
R256 garnet	142	783	231	833		4.5		0.19	0.25	0.53	0.44	2.38	1.67	1.93

Table 1. Ion microprobe data for clinopyroxenes and garnets from Ronda peridotites and mafic layers.

	Mineral Facies	Sr (ppm)	Sm (ppm)	Nd (ppm)	U (ppb)	Th (ppb)	Pb (ppb)
MIT Samples							
R25 cpx	PL	1.6	0.872	2.613	1.462	3.149	8.21
R142 cpx	PL	4.7	3.712	8.899		2.346	33
R145 cpx	PL	23.7	4.013	13.680	1.737	1.225	26.1
R163 cpx	PL	17.3	2.618		1.064	0.244	39.4
R165 cpx	PL	14.8	2.827	7.764	6.572	17	54.2
R324 cpx	PL	11.3	0.084	0.364	21.4	22.3	123
R324 opx	PL						1.9
R324 olivine	PL						0.978
R238 cpx #1	SL	71.3	1.720	4.218	11.6	24.6	42.9
R238 cpx #2	SL				9.86	24.4	41.2
R238 opx	SL						0.792
R717 cpx	SL				7.11	17.0	31.5
R856 cpx #1	SL	19.0	0.562	1.276			38.6
R856 cpx #2	SL				8.37	3.80	41.5
R498 cpx	GL	85.9	2.055	6.034	8.53	25.6	149
R498 garnet	GL				2.83	1.55	1.46
R521 cpx	GL	69.5	1.618	4.345	8.89	26.1	173
R521 garnet	GL		0.650	0.342	2.70	1.87	2.83
R618 cpx	GL	103.0	2.196	7.280	18.6	45.1	276
R618 garnet #1	GL	0.2	0.749	0.445		1.71	2.35
R618 garnet #2	GL				3.06	1.44	2.18
R740 cpx	GL	74.2	2.007	5.460	43.8	100	357
R740 garnet	GL				4.27	5.17	9.65
LDGO Samples							
002R cpx	PL	18.1	0.082	0.471		25.6	23.5
008R cpx	PL	21.8	0.173	0.738	6.56	30.9	22.1
009R cpx	PL	20.6	0.142	0.498		39.1	19.9
013R cpx	PL	18.5	0.091	0.407	4.55	31.6	25.5
016R cpx	PL	28.7	0.098	0.426	5.13	32.9	28.6
403R cpx	PL	106.1	0.891	4.490	11.4	59.2	56.5
404R cpx	PL	24.4	0.204	1.651	78.2	287	63.1
414R cpx	PL	11.8	0.072	0.321	4.68	30.7	38.8
R85-32 cpx #1	SL	42.5	1.137	2.540	7.30	13.2	122
R85-32 cpx #2	SL				4.71	13.9	89.8
R85-34 cpx	SL	46.8	0.996	2.444	17.6	93.4	27.0
R85-35 cpx	SL	46.4	1.400	2.940	15.0	58.6	105
R85-41 cpx	SL	45.4	1.370	2.820	5.99	14.1	38.5
R85-43 cpx	SL	72.0	1.860	5.460	3.82	14.3	163
R85-47 cpx	SL	53.3	1.420	3.290	7.12	10.9	
040R cpx	GL	53.4	1.089	2.335	2.38	8.33	54.9
050R cpx	GL	71.3		5.320	10.4	22.9	172
051R cpx #1	GL	73.7	1.410	4.895	26.9	138.3	138
051R cpx #2	GL				24.8	146.4	128
056R cpx	GL	37.4	1.181	2.502	8.06	14.3	122
060R cpx	GL	64.8		4.490	7.98	8.40	173
Mafic Layers							
R140 cpx	PL	3.9	6.974	14.43			36.8
R141 cpx #1	PL						38.2
R141 cpx #2	PL	4.1	5.310	11.02			
R148 plag	PL	126.3	0.816	2.356	3.41	1.22	78.3
R166 cpx	PL	10.1	1.475	3.631	5.66	1.40	149
R301 cpx #1	SL	18.9	0.224	0.578	3.78	9.38	73.2
R301 cpx #2	SL				3.93	9.30	76.7
R256 cpx	GL	197.6	0.861	2.604	7.85	24.2	227
R256 garnet	GL	0.3	0.400	0.212	1.95	1.68	2.79
R259 cpx	GL	113.8	0.615	2.604	4.97	8.53	60.1

Table 2a. Isotope dilution trace element data for mineral separates from Ronda peridotites and mafic layers. Mineral facies describes location of the sample (Fig. 1) in the plagioclase-lherzolite (PL), spinel-lherzolite (SL), and garnet-lherzolite (GL) facies as defined by Obata (1980). Sr and Nd data for all LDGO samples are from Reisberg and Zindler (1986) and Reisberg et al. (1989). U-Th-Pb data for LDGO plagioclase-facies samples are from Zindler (unpublished data).

	Mineral Facies	$^{87}Sr/^{86}Sr$	$^{143}Nd/^{144}Nd$	$^{206}Pb/^{204}Pb$	$^{207}Pb/^{204}Pb$	$^{208}Pb/^{204}Pb$	$^{147}Sm/^{144}Nd$	$^{238}U/^{204}Pb$	$^{232}Th/^{204}Pb$	Th/U
MIT Samples										
R25 cpx	PL	.703207	.512859	20.168	15.650	39.741	0.202	13.37	29.02	2.15
R142 cpx	PL	.703480	.512577	18.834	15.580	38.676	0.252	0.00	5.27	
R145 cpx	PL	.702902	.512729	19.519	15.463	39.141	0.177	4.96	3.53	0.71
R163 cpx	PL	.703357	.512659	19.036	15.602	38.963		2.00	0.46	0.23
R165 cpx	PL	.703175	.513069	18.751	15.514	38.627	0.220	8.90	23.18	2.59
R324 cpx	PL	.703518	.512968	18.984	15.649	38.981	0.140	12.89	13.53	1.04
R324 opx	PL			18.784	15.655	38.512				
R324 olivine	PL			18.544	15.406	38.128				
R238 cpx #1	SL	.701936	.513383	17.047	15.203	36.277	0.247	18.66	39.87	2.12
R238 cpx #2	SL			17.077	15.206	36.292		16.53	41.21	2.47
R238 opx	SL			18.259	15.693	38.188				
R717 cpx	SL			18.924	15.585	38.386		16.56	39.88	2.39
R856 cpx #1	SL			18.564	15.610	38.451	0.266			
R856 cpx #2	SL	.703486	.512691	18.583	15.576	38.488		14.75	6.74	0.45
R498 cpx	GL	.702274	.513141	17.715	15.344	37.021	0.206	4.04	12.21	3.00
R521 cpx	GL	.702705	.513185	18.292	15.454	37.988	0.225	3.71	10.97	2.94
R521 garnet	GL		.513299	18.740	—	38.252	1.145	70.35	49.08	0.69
R618 cpx	GL	.702588	.513236	18.289	15.524	37.866	0.182	4.86	11.88	2.42
R618 garnet #1	GL	.702448	.513362	18.531	—	37.952	1.017		53.60	
R618 garnet #2	GL							89.05	43.46	0.47
R740 cpx	GL	.702892	.513088	18.500	15.627	38.813	0.222	9.01	20.71	2.28
R740 garnet	GL			18.659	—	38.582		32.23	39.30	1.21
LDGO Samples										
002R cpx	PL	.703410	.512703	20.336	15.658	40.245	0.105		84.16	
008R cpx	PL	.703260	.512510	20.658	15.613	40.506	0.142	22.92	108.68	4.71
009R cpx	PL	.703310	.512690	20.092	15.665	40.001	0.172		150.74	
013R cpx	PL	.703270	.512731	20.808	15.642	40.594	0.135	13.80	96.43	6.94
016R cpx	PL	.703160	.512821	20.156	15.709	39.662	0.140	13.64	88.24	6.42
403R cpx	PL	.703490	.512482	20.216	15.710	40.296	0.120	15.45	80.96	5.20
404R cpx	PL	.703440	.512277	21.688	15.799	41.930	0.075	98.96	365.19	3.66
414R cpx	PL	.703960	.512848	21.387	15.809	41.534	0.136	9.55	63.09	6.56
R85-32 cpx #1	SL	.702110	.513512	19.314	15.686	39.093	0.271	4.47	8.13	1.81
R85-32 cpx #2	SL			19.347	15.642	38.953	0.271	3.90	11.57	2.94
R85-34 cpx	SL	.703330	.512967	18.860	15.595	39.195	0.246	48.22	258.10	5.31
R85-35 cpx	SL	.703380	.512986	18.711	15.611	38.859	0.288	10.53	41.51	3.91
R85-41 cpx	SL	.702170	.513506	17.701	15.421	37.119	0.294	10.99	26.14	2.36
R85-43 cpx	SL	.703120	.512773	17.989	15.570	38.515	0.206	1.70	6.43	3.75
R85-47 cpx	SL	.702050	.513412				0.261			1.53
040R cpx	GL	.703270	.513523	17.659	15.583	37.371	0.282	3.09	10.85	3.49
050R cpx	GL	.702710	.513071	19.459	15.754	39.204		4.53	10.05	2.20
051R cpx #1	GL	.702730	.513082	19.024	15.672	39.064	0.174	14.42	74.65	5.14
051R cpx #2	GL			19.020	15.696	38.968	0.174	14.35	85.42	5.91
056R cpx	GL	.702080	.513631	18.613	15.633	38.354	0.285	4.83	8.64	1.78
060R cpx	GL	.702150	.513302	18.433	15.548	38.336		3.35	3.55	1.05
Mafic Layers										
R140 cpx	PL	.703411	.512692	18.797	15.453	38.425	0.292			
R141 cpx #1	PL	.703269	.512694	18.996	15.506	38.698				
R141 cpx #2	PL	.703264	.512681	18.947	15.496	38.541	0.290			
R148 plag	PL	.702952	.512671	18.198	15.511	37.868	0.209	3.13	1.13	0.36
R166 cpx	PL	.703859		18.823	15.644	38.790	0.246	2.80	0.70	0.25
R301 cpx #1	SL			18.614	15.698	39.336	0.234	3.82	9.56	2.48
R301 cpx #2	SL			18.622	15.723	39.341		3.80	9.05	2.37
R256 cpx	GL	.703242	.512691	18.797	15.648	38.612	0.200	2.54	7.90	3.09
R256 garnet	GL	.705660	.513333	18.927	—	38.595	1.142	50.86	44.18	0.86
R259 cpx	GL	.703093	.513066	18.908	15.491	38.344	0.143	6.05	10.46	1.72

Table 2b. Isotopic composition data for mineral separates from Ronda peridotites and mafic layers. Mineral facies describes location of the sample (Fig. 1) in the plagioclase-lherzolite (PL), spinel-lherzolite (SL), and garnet-lherzolite (GL) facies as defined by Obata (1980). Pb isotope data for garnets was normalized relative to the 207Pb/204Pb ratio of cpx from the same sample (see text). Sr and Nd data for all LDGO samples are from Reisberg and Zindler (1986) and Reisberg et al. (1989). U-Th-Pb data for LDGO plagioclase-facies samples are from Zindler (unpublished data).
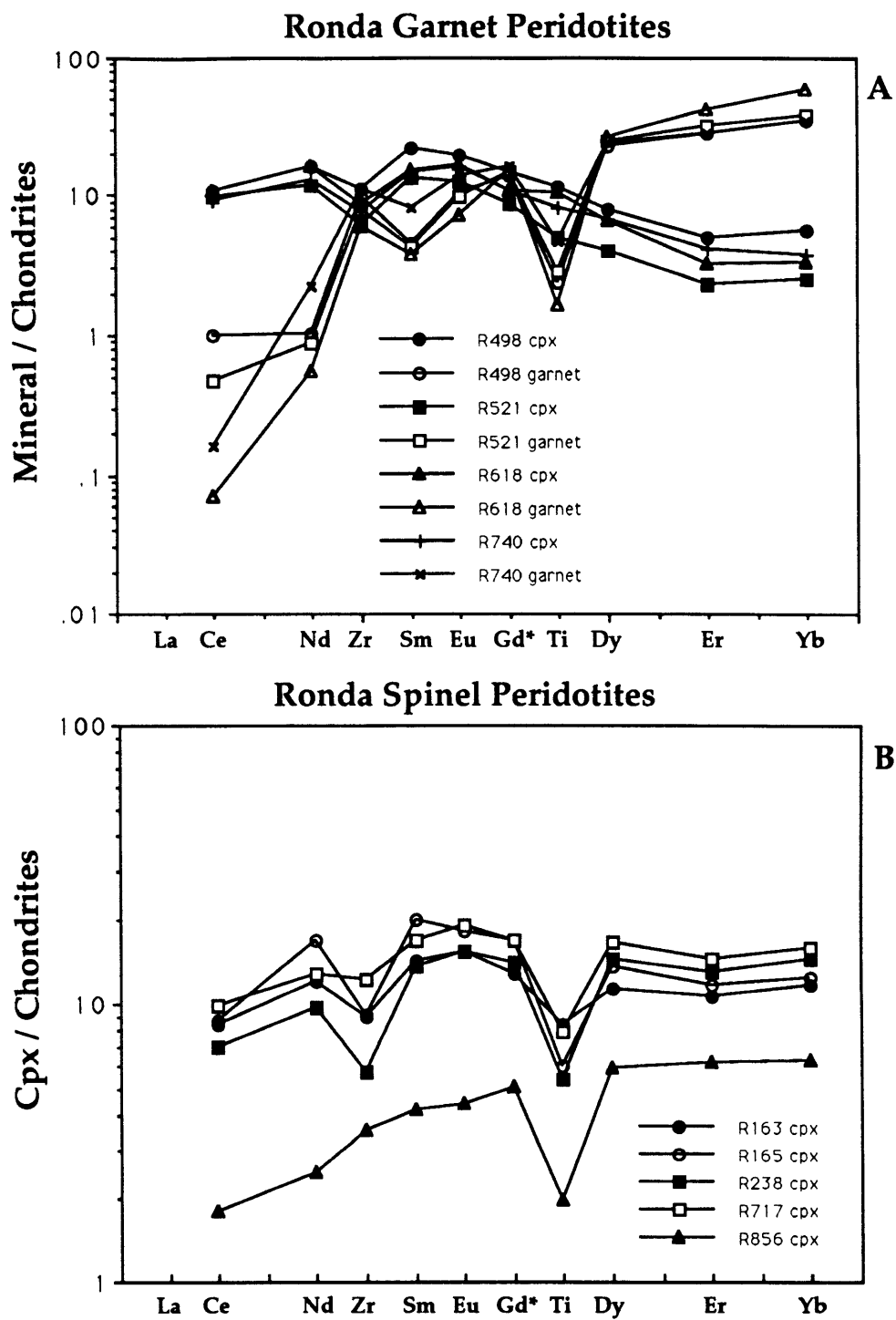
Figure 4. Chondrite-normalized trace element patterns for Ronda garnets and clinopyroxenes. A) Ronda garnet-facies peridotites (MIT samples). B) Ronda spinel-facies peridotites (MIT samples).
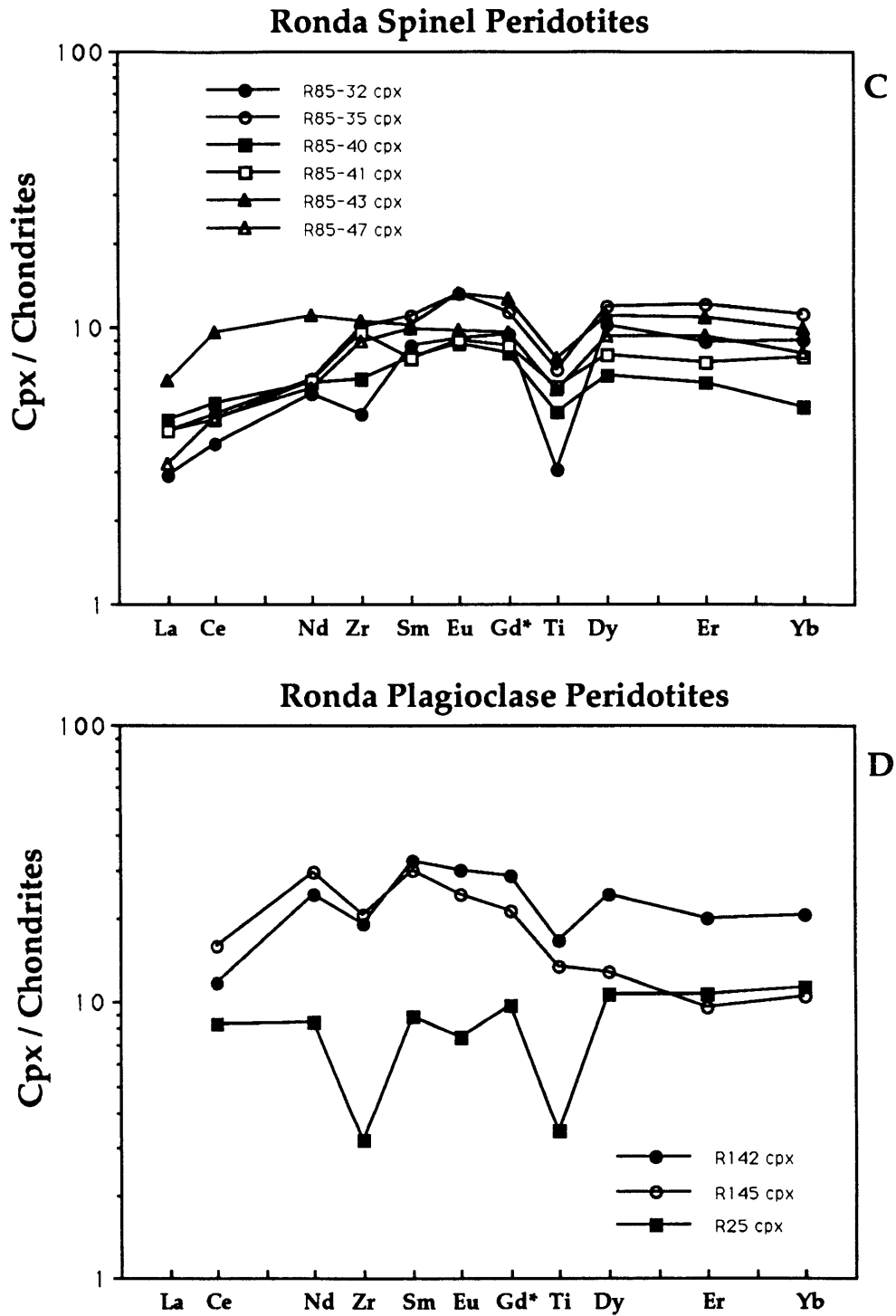
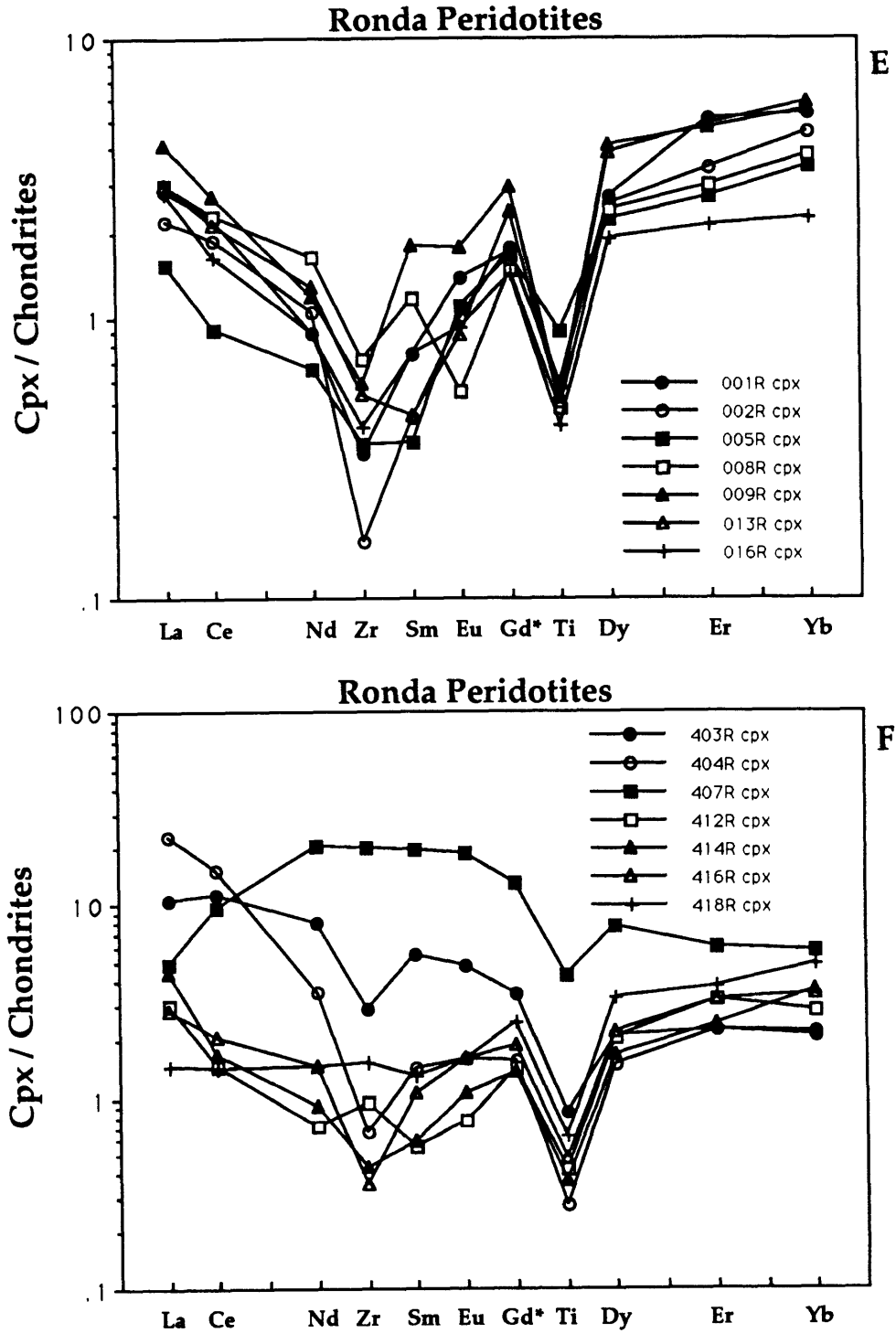27

Ronda Spinel Peridotites

Ronda Plagioclase Peridotites

Figure 4. Chondrite-normalized trace element patterns for clinopyroxenes from Ronda peridotites. C)Ronda spinel-facies peridotites (LDGO samples). D) Ronda plagioclase-facies peridotites (MIT samples). Cpx from R25 shows a negative Eu anomaly, indicating equilibrium with plagioclase. Though samples R142 and R145 contain plagioclase, cpx from these samples do not have Eu anomalies. Concave downward patterns fo R142 and R145 are probably inherited from adjacent mafic layers.

28

Figure 4. Chondrite-normalized trace element patterns for clinopyroxenes from
Ronda peridotites. E) and F) Rondaplagioclase-facies peridotites (LDGO samples).
Most samples show varying degrees of LREE enrichment, except 407R with a concave
downward pattern similar to peridotites near mafic layers (R142, R145, Fig. 4d).

29

Ronda Mafic Layers

G
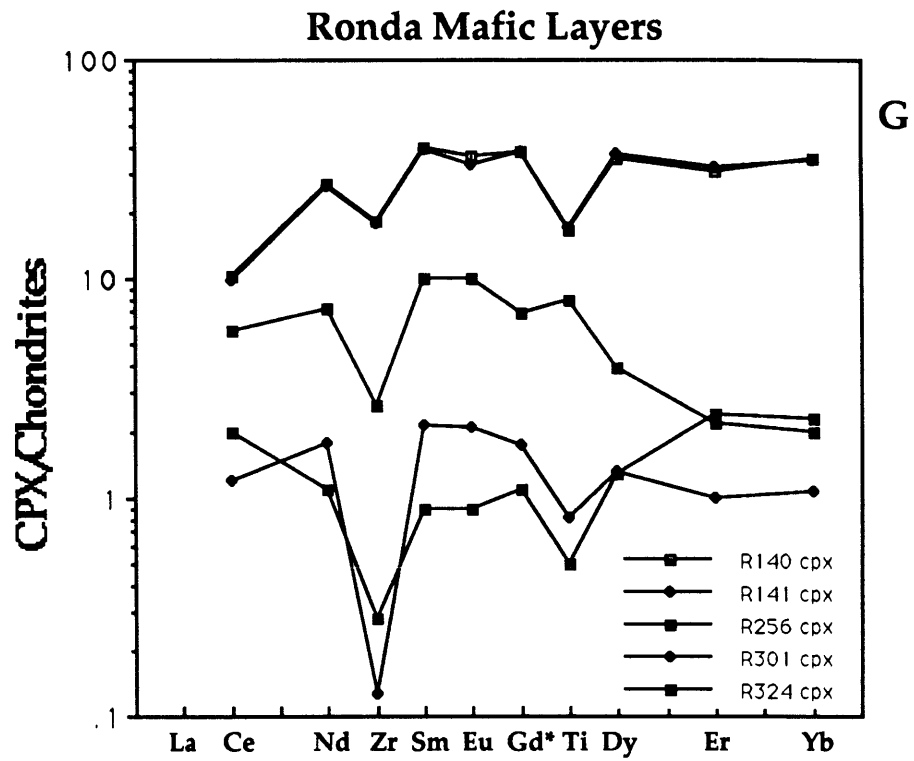
Figure 4. G) Chondrite-normalized trace element patterns for clinopyroxenes from Ronda mafic layers. R256 is from the garnet facies, the rest are from the plagioclase facies.

3. Results

3.1 Trace element concentrations

Ion microprobe results are given in Table 1. Compared to peridotite cpx, mafic layer cpx have on the average higher Ti, Zr, and REE concentrations, though there is a large overlap in REE abundances. Mafic layer and peridotite cpx have similar abundances of Sc and V, whereas peridotite cpx have higher Cr abundances. All elements from the peridotite cpx show significant variations: factor of 2 for V and a factor of 3 for Cr, while Ti and Zr vary by almost two orders of magnitude. For mafic layer cpx, the range in Ti and Zr is only about a factor of 3, but Cr varies by a factor of 7. There is a large variation in Sr in cpx from both peridotites and mafic layers, but this is related to the partitioning of Sr into plagioclase in some of the samples (peridotites R25, R142, R145, R163; mafic layers R140, R141), though in most of the samples from the plagioclase facies studied by Reisberg and Zindler (1986) (002R, 013R, 016R, 403R, 404R, 414R), plagioclase has not been observed in thin section. The two plagioclase facies peridotite samples from the section interlayered with mafic layers (R142, R145) have cpx with higher Ti and Zr than the rest of the peridotite cpx. For both mafic layers and peridotites, Ti/Zr in cpx is generally near the chondritic ratio of 111 (Anders and Grevesse, 1989). Most of the samples are LREE depleted (Fig. 4a-d), with $(Ce/Sm)_N$ ranging from 0.1 to 0.95, with no systematic differences between peridotites and mafic layers. The plagioclase facies peridotite samples 002R, 008R, 009R, 013R, 016R, 403R, 404R, 414R, and R324 (mafic layer) from the far eastern end of the massif (Fig. 1) contain clinopyroxenes which are LREE enriched (Fig. 4e,f). Some cpx from the plagioclase facies samples display small negative Eu anomalies (R25, R140, R141), and the low Sr concentrations in these cpx indicates equilibration with plagioclase. With the exception of Sr, Ti and Zr in cpx from R142 and R145, and the LREE enriched samples from the plagioclase facies traverse, no systematic variation of trace elements or REE pattern with mineral facies is evident.

3.2 U-Th-Pb Isotopic Data

In order to assess the accuracy of the U-Th-Pb concentrations, clinopyroxene separates from peridotite R238 and mafic layer R301 from the spinel facies were each split into two fractions and leached by different techniques:

CPX#1) 2.5 N HCl-100°C-60 min.; 5% HF-25°C-20 min.; 2.5 N HCl-100°C-30 min.

CPX#2) 8N HNO$_3$-0.6N HCl-0.05N HF mixture at 100°C for 2 hours

In both cases, CPX#1 was leached so that about 10% of the sample was dissolved away, while CPX#2 experienced 30% partial dissolution. As shown in Table 2, the U, Th and Pb concentrations are reproduced to better than 5%, except for the U concentrations of R238 cpx which are different by 17% (the higher value may be the result of a high loading blank for U). In both cases, the Pb isotopic compositions are reproduced within the quoted precision of 0.07%/amu. This indicates that the leaching procedure did not fractionate U, Th and Pb from each other, yet removed any extraneous components which may have resided on grain surfaces, as indicated by the reproducible isotopic compositions. As a result, the precision of the U-Th-Pb concentrations is estimated at 5%, and the uncertainty in the Pb isotopic composition is estimated at 0.07%/amu.

Two other samples for which replicate analyses were performed show poorer agreement for both concentrations and isotopic compositions (R85-32, 051R, Table 2). In this case, the two analyses for each sample correspond to different magnetic fractions of clinopyroxene, with the first analyses (cpx 1) corresponding to the more magnetic fractions. All of these aliquots were of very high quality, and leached using leaching method #2. However, during leaching, the more magnetic fractions experienced about 5-10% partial dissolution, whereas the less magnetic fractions were partially dissolved to 15-30% using exactly the same procedure. The reason for this is unclear. However, based on the difference in the Pb isotopic compositions of the pairs for each sample, it would seem that the different magnetic fractions may be slightly heterogeneous. This explanation is contrary to the work of Reisberg et al. (1989), who demonstrated that different magnetic fractions of clinopyroxene from sample 407R were in Sr and Nd isotopic equilibrium.

Data for the U-Th-Pb system is given in Table 2 and plotted in Fig. 5. Large variations in the abundances of these elements are evident: Pb varies from 8 to 357 ppb, U varies from <1 to 78 ppb, and Th varies from <1 to 286 ppb. For the plagioclase and spinel peridotite cpx, the U and Pb concentrations are similar to cpx from other orogenic peridotite massifs studied by Hamelin and Allegre (1988), as well as cpx in xenoliths from San Carlos (Galer and O'Nions, 1989) and Dish Hill (Meijer et al., 1990). The garnet peridotite cpx have Pb concentrations similar to some samples reported by (Kramers et al., 1983) and (Cohen et al., 1984), but are generally lower than cpx concentrations reported in other studies (Zartman and Tera, 1973; Kramers, 1977; Kramers, 1979). The Th analyses of Kramers (1977) are much higher than concentrations for Ronda cpx, but this may be due to the autolithic nature of those cpx from kimberlite. U concentrations are distinctly lower than cpx analyses reported by Kramers (1979) and fission track results (Kleeman et al., 1969; Haines and Zartman, 1973). Some of these differences could be due to contamination of the fission track analyses by glass inclusions and kimberlite alteration
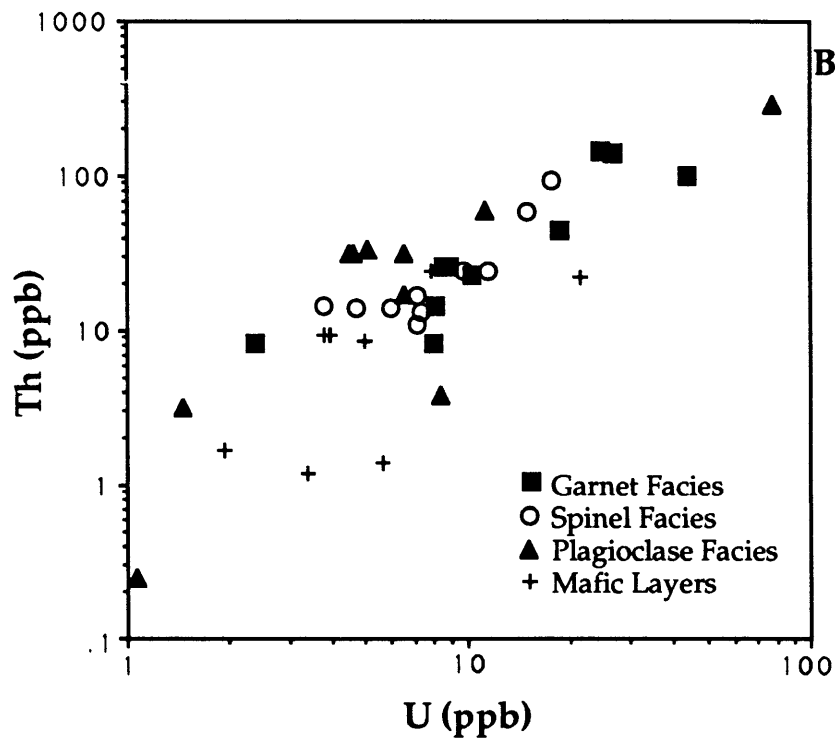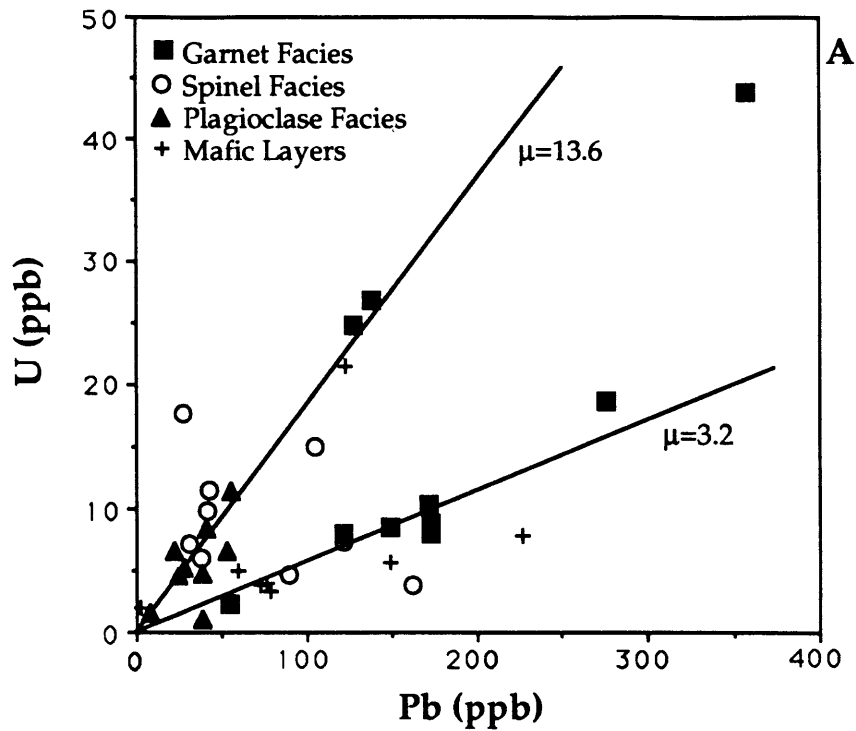
Figure 5. A) U versus Pb concentrations (ppb) in clinopyroxenes from Ronda peridotites and mafic layers. The clinopyroxene data fall into two groups based on U/Pb ratios with average μ (μ=238U/204Pb) of 13.6 and 3.2. Most of the garnet-facies cpx fall in the low-μ group, while most of the plagioclase-facies data fall into the high-μ group. B) Th versus U data for clinopyroxenes. The positive trend indicates an average Th/U of 3.96; however, the low-μ group has an average Th/U of 2.5, and the high-μ group an average Th/U of 4.20.

33
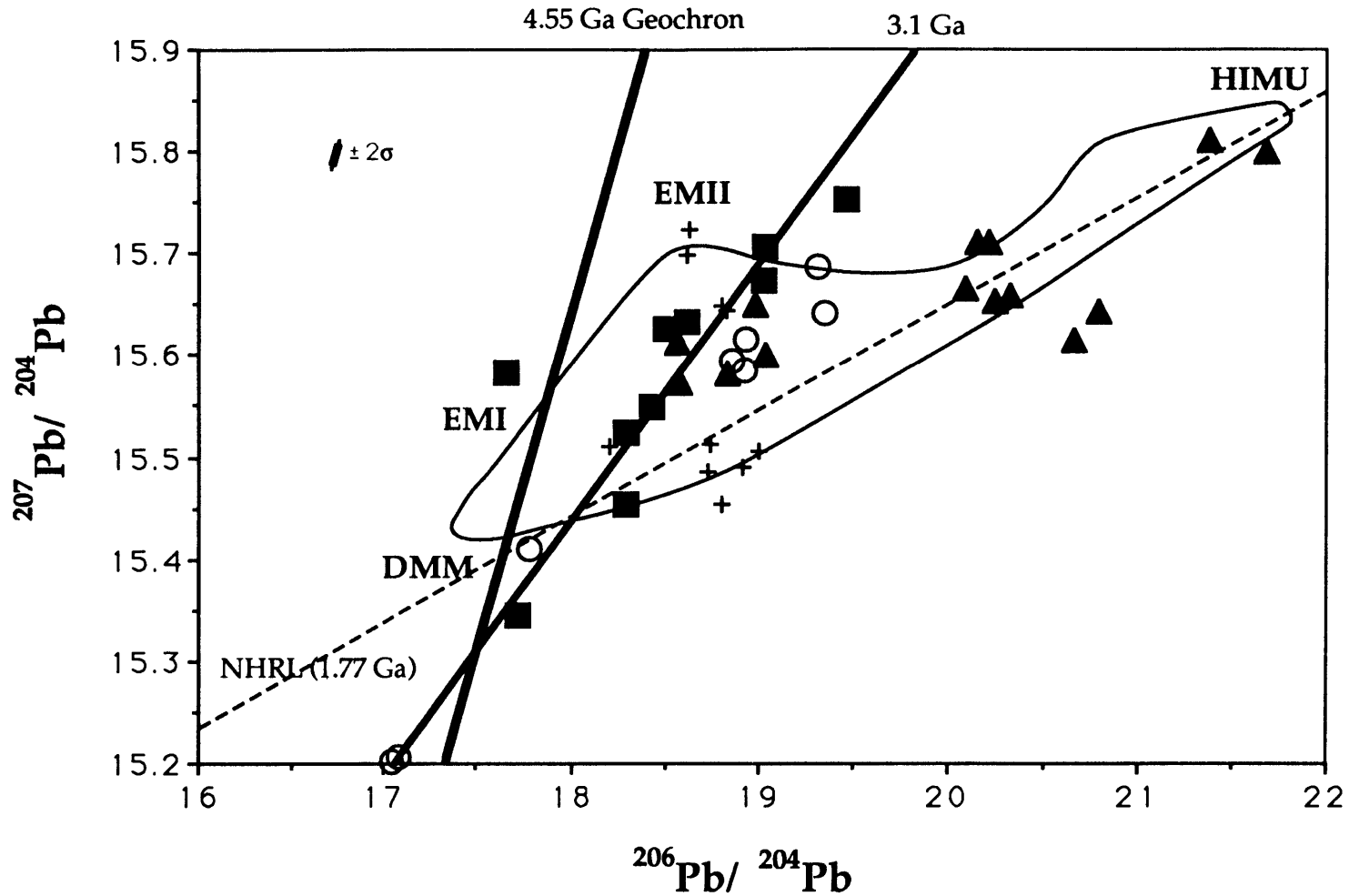
Figure 6a. 206Pb/204Pb diagram for clinopyroxene separated from Ronda peridotites and mafic layers, relative to the field of oceanic basalts (Hart, 1988 and references therin). Samples are from garnet facies (squares), spinel facies (circles), plagioclase facies (triangles), and mafic layers (plusses). Most data, except for east-end plagioclase facies samples, scatter about a 3.1 Ga isochron.
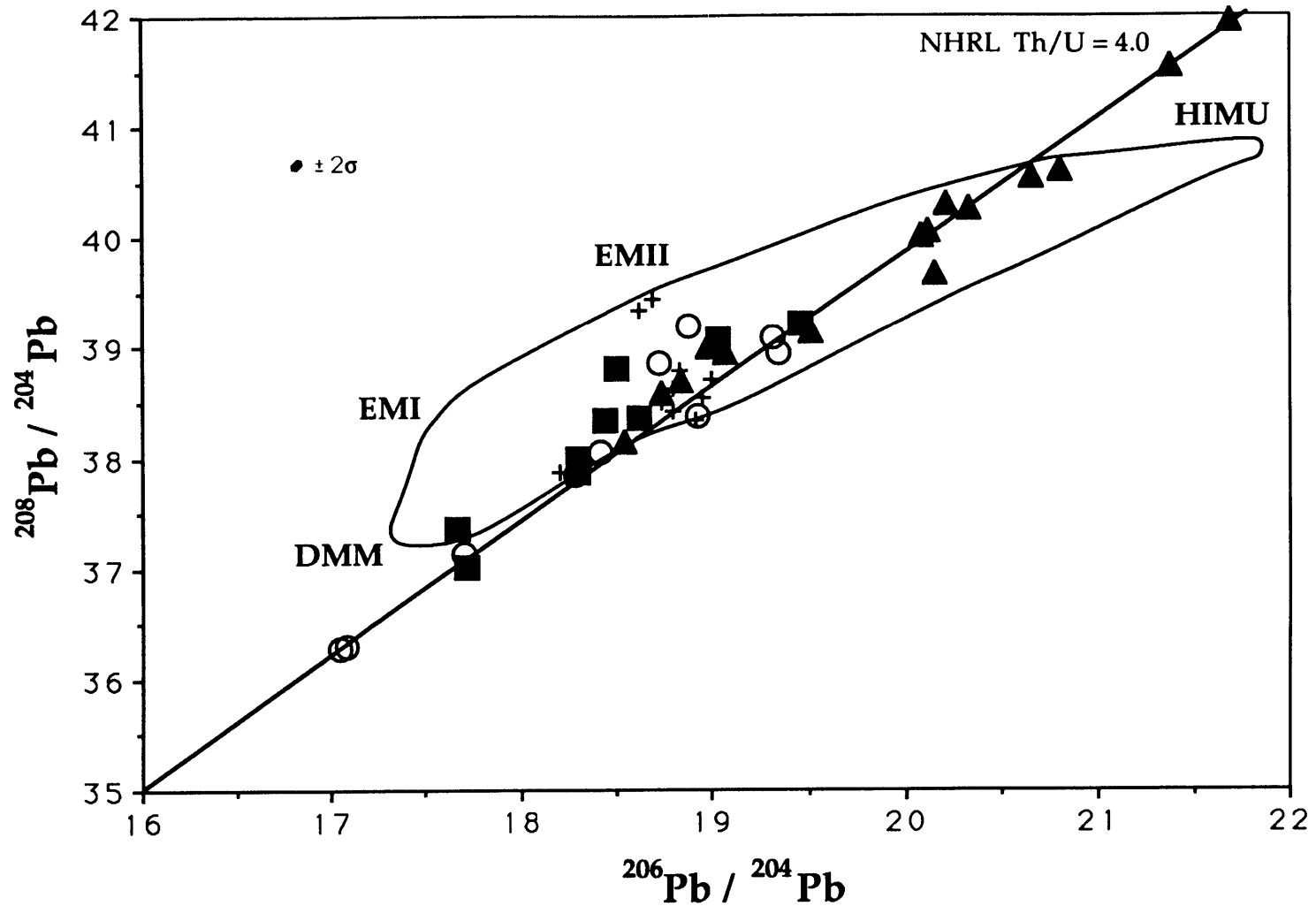
Figure 6b. 208Pb/204Pb-206Pb/204Pb diagram for clinopyroxenes separated from Ronda peridotites and mafic layers, relative to the field of oceanic basalts (Hart, 1988 and references therein). Samples are from garnet facies (squares), spinel facies (circles), plagioclase facies (triangles), and mafic layers (plusses). The data fall on a line indicating a Th/U ratio of 4.00.
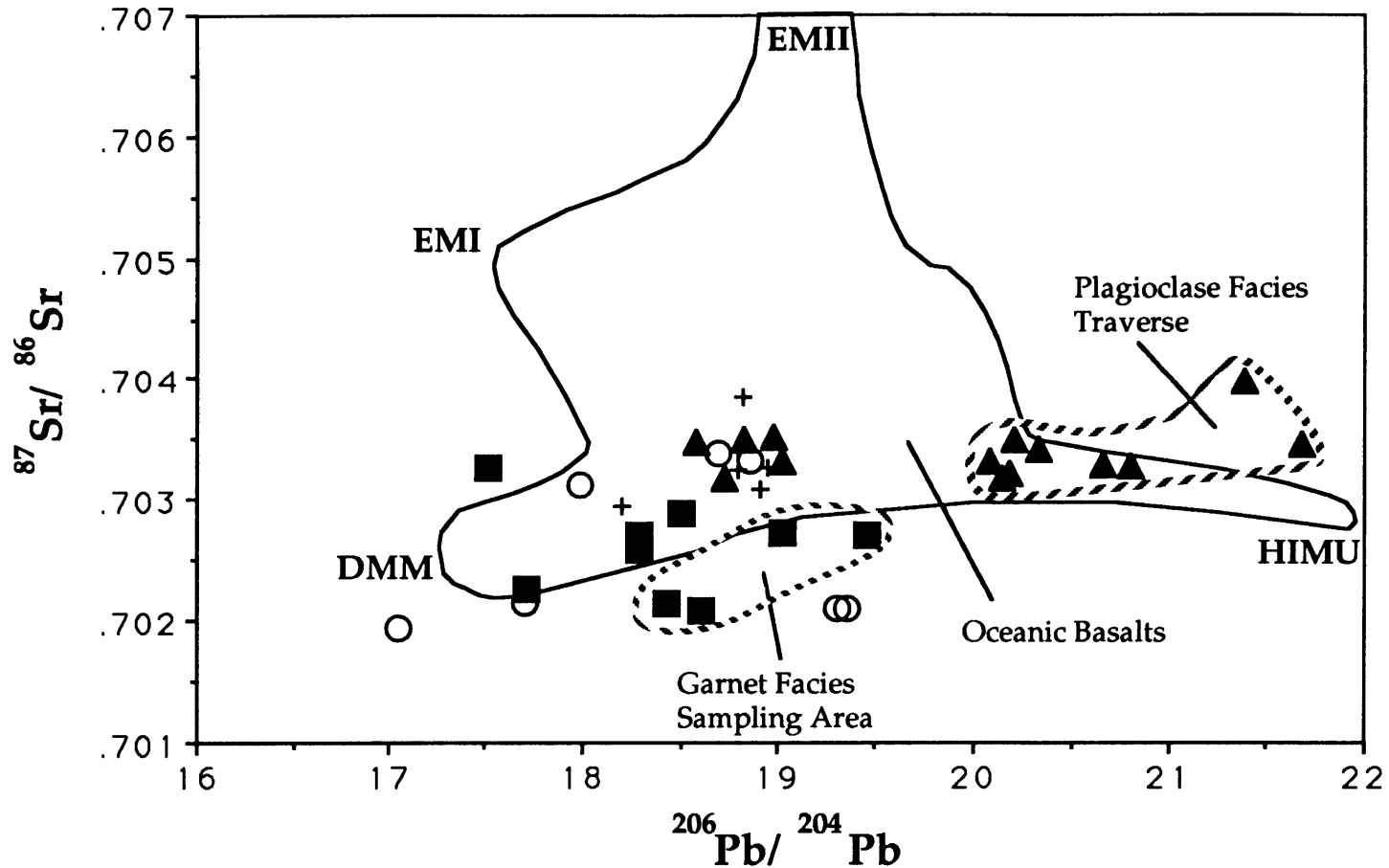
Figure 6c. Sr-Pb diagram for clinopyroxenes separated from Ronda peridotites and mafic layers, relative to the field of oceanic basalts (Hart, 1988 and references therein). Samples are from garnet facies (squares), spinel facies (circles), plagioclase facies (triangles), and mafic layers (plusses). Though much of the data has high 207Pb/204Pb ratios approaching EMII values, these data do not show high the 87Sr/86Sr characteristic of EMII. The samples with highest 206Pb/204Pb have 87Sr/86Sr higher than the HIMU basalts from Mangaia. Hatched lines enclose data for samples from the small scale sampling areas in the garnet and plagioclase facies. Analytical errors are smaller than the size of the symbol.
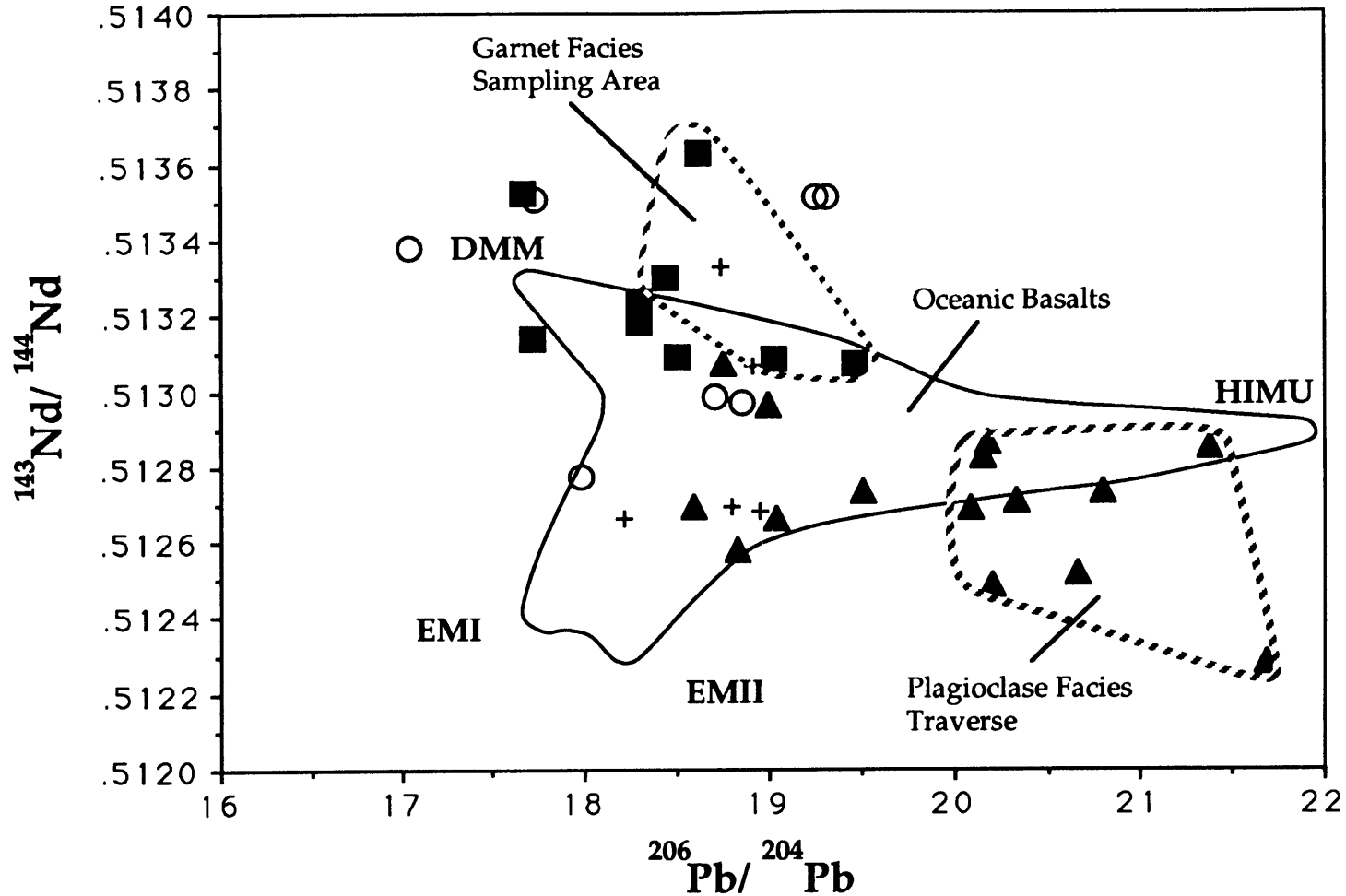
Figure 6d. Nd-Pb isotope diagram for clinopyroxenes separated from Ronda peridotites and mafic layers, relative to the field of oceanic basalts (Hart, 1988 and references therein). Samples are from garnet facies (squares), spinel facies (circles), plagioclase facies (triangles), and mafic layers (plusses). Several sample from Ronda lie outside the field of oceanic basalts; some spinel and garnet facies have higher 143Nd/144Nd than MORB, and several plagioclase facies samples have lower 143Nd/144Nd than HIMU basalts from Mangaia. Hatched lines enclose data for samples from the small scale sampling areas in the garnet and plagioclase facies. Analytical errors are smaller than the size of the symbols.

products. The low concentration of Pb in some plagioclase facies samples (peridotites R25, R142, R145, R163, 404R; mafic layers R140, R141) may be attributed to partitioning of Pb into plagioclase. Unfortunately, plagioclase in the peridotite samples is badly altered, and cannot be trusted to give reliable Pb isotopic information. In general, the range in concentration follows the relative incompatibility of the elements in cpx; the most highly incompatible elements display the greatest range. As a consequence, $^{238}U/^{204}Pb$ (μ) ranges from 1.17 to 78.8, and Th/U ranges from 0.45 to 6.94 for cpx. Garnets are characterized by very low abundances of U (2.7-4.3 ppb), Th (1.4-5.2 ppb) and Pb (1.5-9.7 ppb), but have high μ (28-122). The single plagioclase analyzed is characterized by high Pb and low U and Th abundances. Clinopyroxenes from garnet facies peridotites show high abundances of U, Th and Pb relative to other peridotite cpx, with the exception of R85-32 from the spinel facies.

The cpx data fall into two groups based on their U/Pb ratios (Fig. 5a). One group has generally high concentrations of Pb (>70 ppb) and low U/Pb ratios (average μ=3.2, low-μ group); the other group has generally lower Pb concentrations (<70 ppb) and higher U/Pb ratios (average μ=13.6, high-μ group). These two groups also have different Th/U ratios; the average Th/U of the low-μ group is 2.5 whereas the high-μ group has an average Th/U of 4.2.

Lead isotope ratios are given in Table 2 and plotted in Figure 6. For the Pb isotopic analyses of the garnet separates, the amount of Pb analyzed was exceedingly small (150-500 pg), and suffered from a hydrocarbon interference on ^{204}Pb during mass spectrometry. In order to correct for this effect, the garnet Pb isotope data was corrected by normalizing the measured $^{207}Pb/^{204}Pb$ relative to $^{207}Pb/^{204}Pb$ measured for clinopyroxene from the same sample. The $^{207}Pb/^{204}Pb$ ratio of cpx from sample R145 also likely suffers from this effect, and so the Pb isotope data for this sample is not plotted in Fig. 6. The amounts of Pb analyzed for R238 opx, R324 opx and R324 olivine were also quite small, but did not suffer from this hydrocarbon interference. Analytical uncertainties for these Pb isotopic compositions are on the order of 0.25%/amu.

For the peridotites, large ranges in $^{206}Pb/^{204}Pb$ (17.047-21.688), $^{207}Pb/^{204}Pb$ (15.203-15.799) and $^{208}Pb/^{204}Pb$ (36.277-41.930) are evident, exceeding the range of Pb isotopic compositions reported for oceanic basalts. The large spread in $^{207}Pb/^{204}Pb$ is clearly well outside analytical uncertainty. The garnet and spinel facies samples largely overlap in Pb isotopic composition, and the $^{207}Pb/^{204}Pb$-$^{206}Pb/^{204}Pb$ data for these samples scatter about a Pb-Pb isochron with an age of 3.1 Ga (Fig. 6a); the garnet-facies samples are particularly well have particularly well correlated $^{207}Pb/^{204}Pb$ and $^{206}Pb/^{204}Pb$ (with one exception). The samples from the plagioclase facies traverse are shifted to higher

^{206}Pb/^{204}Pb than the spinel and garnet facies samples (Fig. 6a). The whole-rock Pb isotope data from the Beni Bousera orogenic peridotite massif exhibits a similar range for all the Pb isotope ratios, while Pb isotope data for whole rocks from the Lherz and Zabargad orogenic peridotites are more restricted and have lower ^{207}Pb/^{204}Pb ratios (Hamelin and Allegre, 1988). Pb isotope results for cpx separates from xenoliths from the southwestern United States reported by Galer and O'Nions (1989) and Meijer et al. (1990) are distinctly less radiogenic and have lower ^{207}Pb/^{204}Pb. Peridotite xenoliths from Africa (Kramers, 1977, 1979; Cohen et al., 1984) also show large ranges in Pb isotopes in their constitutent clinopyroxene. The normalized ^{206}Pb/^{204}Pb and ^{208}Pb/^{204}Pb ratios in garnets from samples R498, R521, R618, R740, and R256 are more radiogenic than the values for their corresponding cpx (Table 2). Many of the garnet and spinel facies samples have high ^{207}Pb/^{204}Pb relative to ^{206}Pb/^{204}Pb, suggesting the possibility of crustal contamination. However, these same samples do not have high ^{87}Sr/^{86}Sr and low ^{143}Nd/^{144}Nd signature of continental crust (Fig. 4c-d). New Sr and Nd isotope data for the MIT samples largely fall within the range of values measured by Reisberg and Zindler (1986) and Reisberg et al. (1989). Sample R238 is notable for its very low ^{87}Sr/^{86}Sr and Pb isotopic compositions. Sample 040R from the garnet facies has high ^{207}Pb/^{204}Pb, and lies to the left of the 3.1 Ga isochron and the 4.55 Ga geochron. This sample has high ^{143}Nd/^{144}Nd, but also has fairly high ^{87}Sr/^{86}Sr as noted by Reisberg et al. (1989); these characteristics are quite different from the other garnet-facies samples in which ^{87}Sr/^{86}Sr and the Pb isotopes are well correlated.

Mafic layers from Ronda display a much smaller range in ^{206}Pb/^{204}Pb (18.20-18.95) and ^{208}Pb/^{204}Pb (37.88-39.34) than the peridotites, but display a significant range in ^{207}Pb/^{204}Pb (15.45-15.74). The mafic layers do not exhibit any systematic differences in isotopic compositions with mineral facies.

4. Discussion

4.1 Partitioning of U, Th, and Pb in Peridotite Minerals

In order to determine the host phases for U, Th, and Pb in mantle peridotites, analyses of olivine, orthopyroxene, and garnet were made on several samples, and the relevant mineral/mineral partition coefficients are given in Table 3. Olivine and orthopyroxene contain essentially no U and Th (measured amounts were essentially indistinguishable from blank levels), but were found to host a small amount of Pb. Though the absence of U and Th in these minerals suggests minimal contamination, the olivine and orthopyroxene analyses are not in Pb isotopic equilibrium with their corresponding clinopyroxenes (Table 2). This suggests that the olivine and opx mineral

Sample	U Dgt/cpx	Th Dgt/cpx	Pb Dgt/cpx	Pb D ol/cpx	Pb D opx/cpx
R238					<0.0184
R324				<0.0080	<0.0155
R498	0.331	0.0607	0.0098		
R521	0.304	0.0717	0.0164		
R618		0.0379	0.0085		
R740	0.164	0.0320	0.0079		
R256	0.248	0.0694	0.0123		
Average	0.262	0.0543	0.0110	<0.0080	<0.0170

	D_U	D_{Th}	D_{Pb}	D_U/D_{Pb}	D_{Th}/D_U
cpx/melt	0.006	0.013	0.01	0.6	2.2
garnet/melt	0.0016	0.00065	0.00011	14.5	0.41

Table 3. Partition cofficients for U, Th, and Pb. Average cpx/melt partition coefficients are from: (Pb) Watson et al. (1987) and (U,Th) LaTourrette and Burnett (1992). Garnet/melt values are calculated from the garnet/cpx and cpx/melt data.
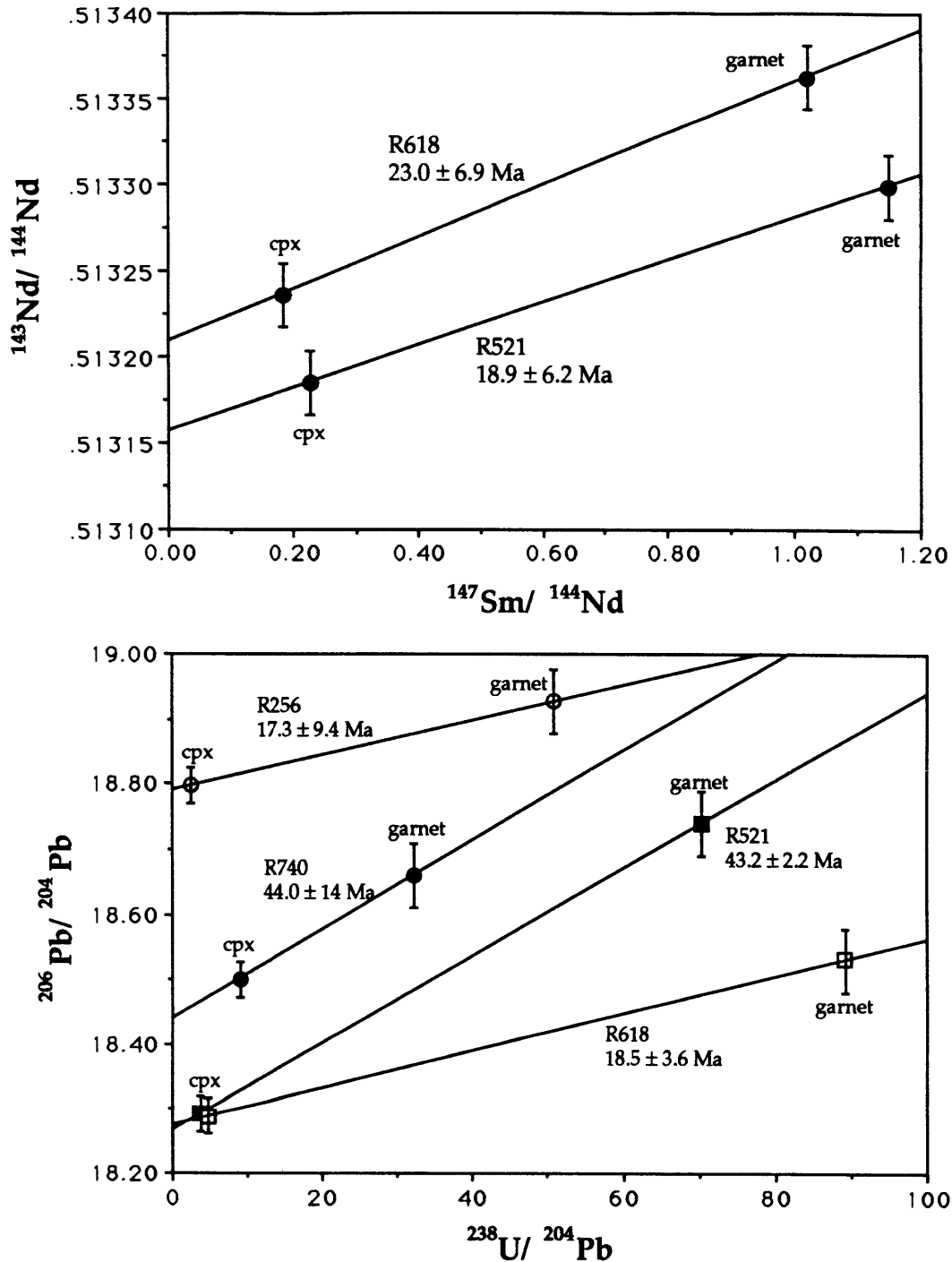
Figure 7. A) Sm-Nd and B) U-Pb isochron plots for garnet-cpx pairs from Ronda garnet peridotites (R521,R618,R740) and a garnet-bearing mafic layer (R256). Uncertainties (2σ) are estimated at ±0.0035% and 0.5% on 143Nd/144Nd and 147Sm/144Nd, respectively, and ±0.14% and ±0.5% on 206Pb/204Pb for cpx and garnet, respectively, and 20% on 238U/204Pb. The U-Pb ages of R618 and R256 are within error of Sm-Nd garnet-cpx ages from Ronda garnet peridotites (Reisberg et al., 1989) and Rb-Sr dates of anatectic country rocks (Priem et al., 1979). Isochron ages of R521 and R740 are within error of each other, but outside the range of previously reported garnet-cpx Sm/Nd ages. The Sm-Nd and U-Pb ages of R618 are concordant, but those of R521 are not, suggesting the possibility of a very slight U or Pb contamination of R521 garnet, and probably R740 garnet.

41

separates may have contained a small amount of a contaminant with low U/Pb and Th/Pb ratios. Thus the olivine/cpx and opx/cpx partition coefficients given in Table 3 are considered to be upper limits.

Figure 7 shows the Sm-Nd and U-Pb systematics of garnet-cpx pairs from Ronda garnet peridotites (R 521, R618, R740) and a garnet bearing mafic layer (R256). The Sm-Nd ages are within error of a Sm-Nd isochron age on a garnet-bearing mafic layer analyzed by Zindler et al. (1983), and garnet-cpx Sm-Nd ages measured by Reisberg et al. (1989) on Ronda garnet peridotites. The U/Pb ratios and Pb isotopic compositions of garnet from the garnet-bearing samples listed in Table 2 are distinctly higher than their corresponding clinopyroxenes. On a $^{238}U/^{204}Pb$-$^{206}Pb/^{204}Pb$ isochron diagram, these garnet-cpx pairs display a range of ages from 17.3 Ma to 44.0 Ma, with large errors (Fig. 7b). The mineral isochron ages for R256 and R618 are within error of the Sm-Nd garnet-cpx ages determined by Zindler et al. (1983) for a Ronda garnet-clinopyroxenite (21.5 ± 1.8 Ma), and by Reisberg et al. (1989) for Ronda garnet peridotites (21.0 ± 7.0 Ma to 24.5 ± 7.3 Ma). In addition, these ages are in agreement with Rb-Sr ages of about 22 Ma for anatectic granites associated with the peridotite massif (Loomis, 1975; Priem et al., 1979). However, the garnet-cpx pairs for R521 and R740 are different from the above ages, though they are within error of each other. The Sm-Nd and U-Pb ages for R618 are concordant, but those for R521 are not. The most likely explanation for this discordance is a slight Pb contamination of the R521 garnet separate. For the $^{232}Th/^{204}Pb$-$^{208}Pb/^{204}Pb$ system, two of the garnet-cpx pairs are essentially in equilibrium, while R618 gives a garnet-cpx age of 41.6 Ma, and R521 gives a garnet-cpx age of 140 Ma (not shown). The larger amount of noise in the Th-Pb system is probably the result of a smaller Th/Pb fractionation between garnet and cpx, compared with the large fractionation in U/Pb (Table 2). The U-Pb ages are barely resolvable, and probably represent the lower limit obtainable for mantle derived garnet peridotites.

These age relationships indicate that the minerals of the Ronda peridotites were in Pb isotopic equilibrium 20 Ma ago. As a result, the partitioning relationships for U, Th, and Pb between garnet and cpx are more well constrained than for olivine and orthopyroxene, and the garnet/cpx partition coefficients given in Table 3 are considered to represent a close approach to equilibrium. These results indicate that garnet is a significant host for U in the mantle, and to a lesser degree also for Th and Pb. This is reflected in the high U/Pb ratios and low Th/U ratios of these garnets compared with their corresponding clinopyroxenes. These mineral/mineral partitioning results indicate that, of the major anhydrous silicate phases present in mantle peridotite, clinopyroxene and garnet are effectively the dominant host phases for U, Th, and Pb. Even though opx and especially

42

olivine are modally abundant in peridotites and contain measurable amounts of Pb, they contribute little Pb to the whole rock budget.

The garnet/cpx partition coefficients indicate that the relative solid/melt partitioning behavior of U and Pb depends on the garnet/cpx ratio in the bulk rock. Assuming that garnet and clinopyroxene are the only phases which influence U and Pb partitioning in a garnet lherzolite, the ratio D_U/D_{Pb} for the bulk rock is:

$$\frac{D_U}{D_{Pb}} = \frac{X_{cpx}\, D_U^{cpx/l} + X_{gt}\, D_U^{gt/l}}{X_{cpx}\, D_{Pb}^{cpx/l} + X_{gt}\, D_{Pb}^{gt/l}} \qquad (1)$$

where Xmineral=weight fraction of the mineral in the bulk rock, and $D_i^{j/l}$ is the solid/melt partition coefficient for element i in phase j. Substituting in the expressions:

$$R = X_{gt}/X_{cpx} \qquad (2)$$

$$D^{gt/cpx}\, D^{cpx/l} = D^{gt/l} \qquad (3)$$

and the average garnet/cpx values from Table 3, equation (1) reduces to:

$$\frac{D_U}{D_{Pb}} = \frac{D_U^{cpx/l}(1 + 0.26R)}{D_{Pb}^{cpx/l}(1 + 0.011R)} \qquad (4)$$

Watson et al., (1987) determined values of .009-.0125 for $D_{Pb}^{cpx/l}$. Given the probability of Pb loss to Pt loops used in these experiments, this value likely represents an upper limit. LaTourrette and Burnett (1992) have measured values for $D_U^{cpx/l}$ of 0.0034-0.015 and $D_{Th}^{cpx/l}$ of 0.008-0.036, and demonstrated that $D_U^{cpx/l}$ is highly dependent on oxygen fugacity due to multiple valence states of U, with the values of $D_U^{cpx/l}$ decreasing with increasing fO_2 and increasingly oxidized U valence states. These values are higher than the value of $D_U^{cpx/l} = 0.0003$ determined by Watson et al. (1987); these experiments were performed in air at 1 atm, and so U^{+6} is likely to be present in their charges (Watson et al., 1987). By consideration of equation (4), it is clear that the ratio D_U/D_{Pb} for the bulk rock increases with increasing garnet/cpx ratio. This is due not to an increasing compatibility of U, but a decreasing compatibility of Pb with increasing garnet/cpx ratios. Within the uncertainty in the relevant partition coefficients of U and Pb, it is apparent that the ratios D_U/D_{Pb} and D_{Th}/D_{Pb} may exceed unity. During melting of a garnet-bearing

assemblage, the result of this effect would be to leave a residue with a higher U/Pb and Th/Pb ratios than before melting. In addition, the ratio D_{Th}/D_U will be lower in a garnet-bearing peridotite than in a garnet-free peridotite. Thus, the Th/U ratio in a partial melt of garnet peridotite should have higher Th/U than a melt of spinel peridotite; this is consistent with the generally higher Th/U ratios of OIB compared to MORB (ex. Tatsumoto, 1978). Though a large degree of uncertainty still remains about the precise mineral/melt partition coefficients for U, Th, and Pb, it is clear that the retention of garnet in a residue of melting will leave that residue with higher U/Pb, Th/Pb, and lower Th/U than a garnet-free residue of melting. As a result, it is possible that a peridotite which is residual after partial melting in the garnet stability field may develop radiogenic Pb isotope ratios, even though it is a residue of melting.

4.2 U-Th-Pb Budget of Mantle Peridotite

Figure 8 shows the $^{238}U/^{204}Pb-^{206}Pb/^{204}Pb$ data for the Ronda clinopyroxenes. The data are not well correlated, but nonetheless show a broad positive trend. The cpx data scatter on both sides of a 3.1 Ga reference isochron, which corresponds to the 3.1 Ga Pb-Pb isochron in Fig. 6a. If the whole rock Ronda peridotites lie on the 3.1 Ga reference isochron, the cpx data indicate the possible presence of U and Pb (and Th) in the whole rock budget which is not contained in clinopyroxene; thus the clinopyroxene U/Pb ratio would not be representative of the whole rock U/Pb ratio. The cpx data from the garnet facies lie largely to the left of the isochron. This is consistent with the presence of garnet in these samples, and thus the bulk rock U/Pb ratios of the garnet-bearing samples would be shifted toward the isochron once the U-Pb budget of garnet is accounted for. However, a number of clinopyroxenes from spinel- and plagioclase-facies samples, as well as cpx from mafic layers, also lie to the left of the isochron, suggesting that some of the U (and Th) budget of these whole rocks may not reside in clinopyroxene.

The studies of Zindler et al. (1983) and Zindler and Jagoutz (1988) have demonstrated that most of the budget of the highly incompatible elements in whole rock ultramafic samples resides as a labile component along grain boundaries, though the extent to which this material is indigenous to the sample is difficult to determine. Thus it cannot be excluded that U, Th, and Pb may have resided on grain boundaries, and may have been lost during leaching of the mineral separates. However, the agreement of the U-Pb garnet-cpx isochron ages with the Sm-Nd garnet-cpx ages could be used to argue that the U, Th, and Pb which may have resided at grain boundaries was not a component which was indigenous to these samples. Rutile has been observed as inclusions in garnet in some garnet-bearing mafic layers (Obata, 1980), and since this mineral has high U and Th concentrations and high U/Pb and Th/Pb ratios, small amounts of this mineral in the bulk
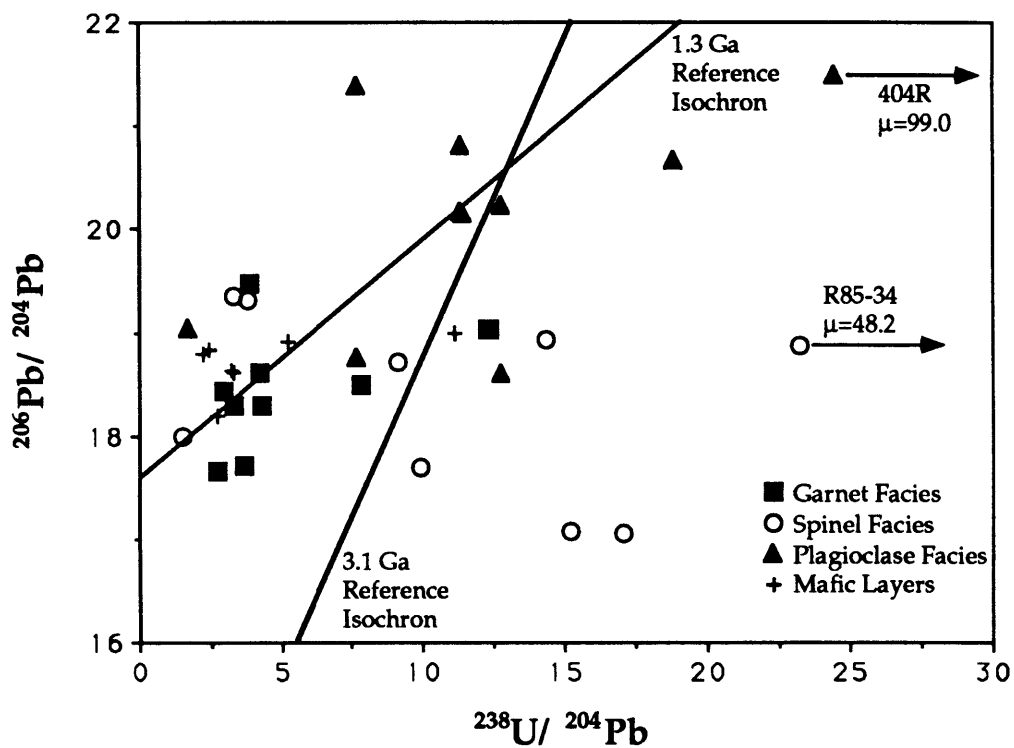
44

Figure 8. U-Pb isochron diagram for clinopyroxenes from Ronda peridotites and mafic layers. The 3.1 Ga reference isochron corresponds to the 3.1 Ga isochron shown in Figure 6a. The data show a broad positive correlation, but do not define an isochron. Clinopyroxene data lie on both sides of the 3.1 Ga reference isochron; if the Ronda whole rock peridotites lie on a 3.1 Ga isochron, the cpx data indicate the possible presence of trace U (and Th) and Pb bearing phases in the peridotites.

rock could conceivably result in low U/Pb and Th/Pb ratios in constitutent cpx of garnet-free samples. Though this mineral was not observed in the samples studied here, small amounts of this phase may have escaped detection. Alternatively, if these samples represent residues of melting, or the products of crystallization from a maic melt, the low U/Pb and Th/Pb ratios may be the result of lower solid/melt partition coefficients for U and Th than for Pb.

Nearly all the plagioclase facies samples, as well as samples R238, R717, and R85-34 from the spinel facies, seem to have U/Pb, Th/Pb, and Ce/Pb ratios in clinopyroxene which are in excess of these ratios for the remaining samples (Figs. 5,8). This suggests that Pb may be partitioning into phases other than clinopyroxene in these samples. In the case of samples R25, R142, R145, R140, and R141, the low Sr/Nd ratios of the cpx indicates that Pb has been partitioned into plagioclase, leaving the constituent cpx with high U/Pb, Th/Pb, and Ce/Pb ratios. The remaining plagioclase facies samples (002R-404R) have normal Ce/Sr ratios and high Sr/Nd ratios, and plagioclase has not been observed in these rocks. These samples are LREE enriched, and thus U, Th, and the LREE may have been enriched relative to Pb in these samples. This could also account for the high Pb isotope ratios of these samples, which are from the east end plagioclase facies traverse (Fig. 1). However, clinopyroxenes in peridotite xenoliths from San Carlos (Galer and O'Nions, 1989), which are plagioclase-free and dominantly LREE depleted, also have high Ce/Pb and U/Pb ratios (Figs. 8-10). (Ce concentrations for San Carlos cpx were estimated by extrapolation of the REE slope between Nd and Sm).

Figure 9b shows a plot of Sr/Pb versus Pb concentration for the Ronda and San Carlos clinopyroxenes; this plot tends to "normalize" the effect of cpx equilibration with plagioclase, since both Pb and Sr partition into plagioclase. The data for the plagioclase facies samples lie systematically below the trend defined by the Ronda spinel- and garnet-facies samples and the San Carlos data; this suggests that the plagioclase/cpx partition coefficient for Sr may be higher than for Pb. Figure 10a shows that the U/Pb ratio in cpx is also a strong function of the Pb concentration in cpx. Figure 10b shows that those samples with high Ce/Pb also tend to have high U/Pb; this is also indicated by the San Carlos cpx data. In addition, though there is a good correlation between Sm/Nd and $^{143}Nd/^{144}Nd$ in the Ronda cpx data (Reisberg and Zindler, 1986; Reisberg et al., 1989), the measured U/Pb ratios of the Ronda cpx are not correlated with high $^{206}Pb/^{204}Pb$. Taken together, these features of the cpx data suggest the possible influence of an additional Pb bearing phase in the Ronda peridotites (and also the San Carlos xenoliths).

Pb in the Ronda peridotites may have partitioned into a trace phase such as sulfide. For example, assuming that all the U and Ce in a peridotite is contained in cpx, and
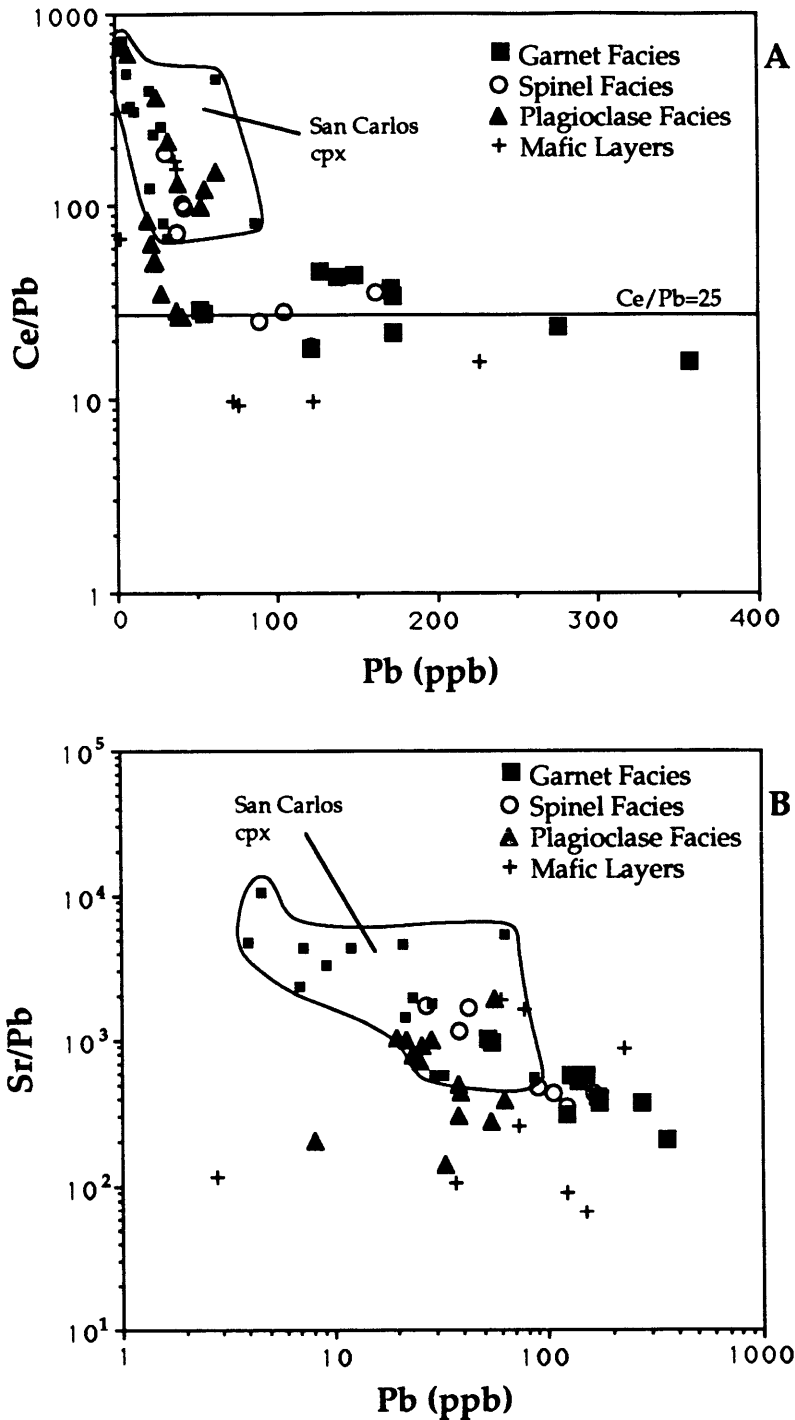
Figure 9. A) Ce/Pb versus Pb for clinopyroxenes from Ronda peridotites and mafic layers. Cpx with Pb concentrations greater than about 70 ppb have Ce/Pb ratios near the oceanic basalt average of 25 (Hofmann et al., 1988). However, most of the data define a negative trend. Ce data for cpx from San Carlos xenoliths (Galer and O'Nions, 1989) were estimated by extrapolation of the REE pattern between Nd and Sm. B) Sr/Pb versus Pb in Ronda clinopyroxenes. The data, including data for cpx from San Carlos xenoliths, define a negative trend, suggesting that the bulk solid/melt partition coefficient of Pb is less than that of Sr.

47
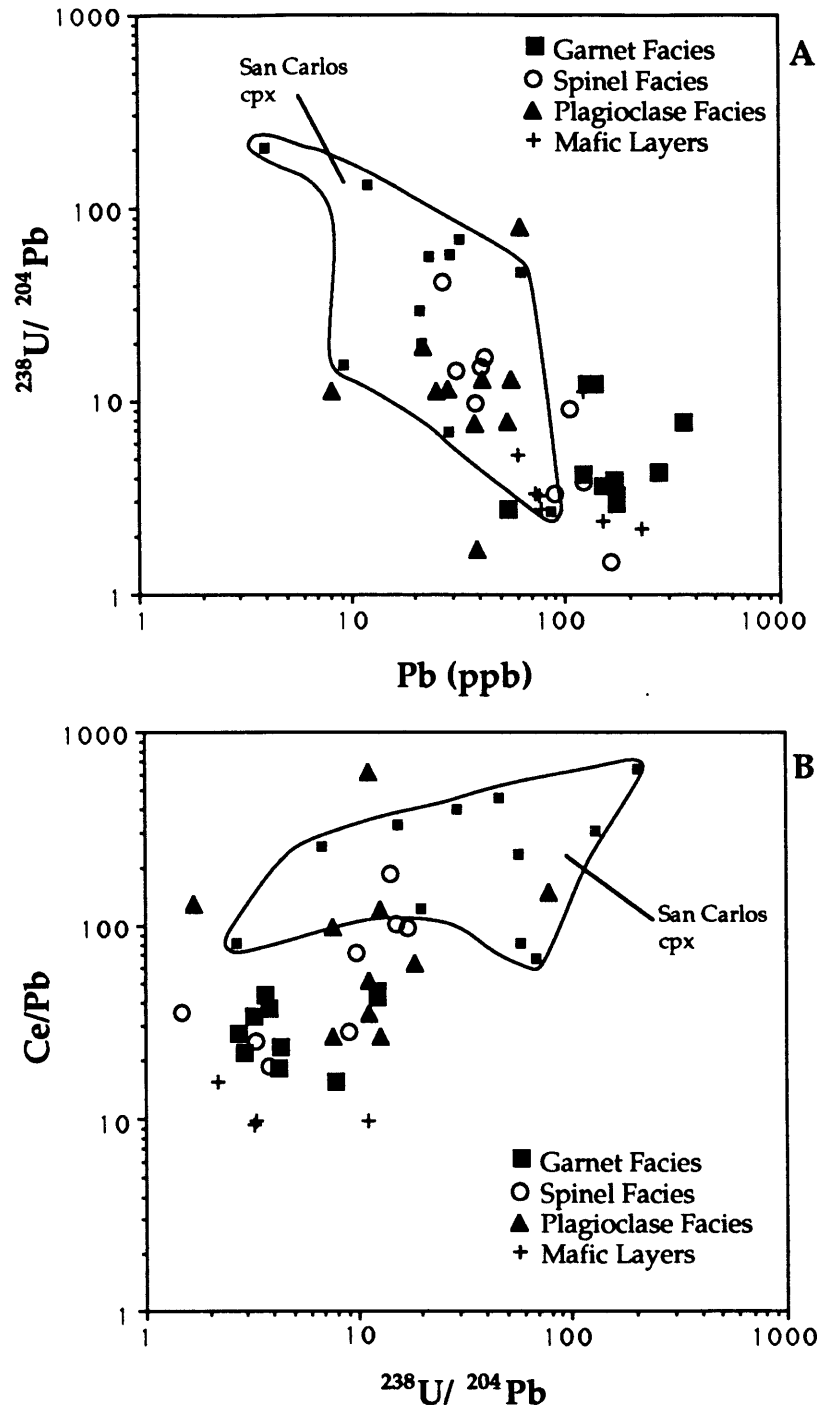
Figure 10. A) 238U/204Pb versus Pb for Ronda clinopyroxenes. Small squares are cpx data from San Carlos xenoliths (Galer and O'Nions, 1989). The group of Ronda cpx with high μ have systematically lower Pb concentrations than the low-μ cpx. B) Ce/Pb versus 238U/204Pb for Ronda clinopyroxenes. The data display a broad positive trend, indicating that variations in Pb concentration determine the μ and Ce/Pb ratios of clinopyroxene. The high-μ group of cpx scatter to higher Ce/Pb ratios.

assuming 5% modal cpx, 0.4% of a sulfide phase with a Pb concentration of 10 ppm (Meijer and Rogers, 1990) in sample R238 would drop the whole rock Ce/Pb ratio to 51, which is well within the range of other cpx Ce/Pb ratios, and μ would decrease to 7.75 (the single stage value indicated by the position of R238 near the geochron). Though it has not been firmly established that sulfide is a major host for Pb in the mantle, its role cannot be excluded. If sulfide is an important host for Pb in mantle peridotite, then the U/Pb, Th/Pb, and Ce/Pb ratios measured in clinopyroxene would not be representative of the whole rock. This is supported by the lack of a correlation between U/Pb and $^{206}Pb/^{204}Pb$ for the cpx data. However, based on the fact that the $^{238}U/^{204}Pb$ and Ce/Pb ratios measured in the Ronda cpx are reasonably close to values estimated for the mantle. (Hofmann et al, 1988), the fraction of the whole rock Pb budget which is "missing" from clinopyroxene probably amounts to no more than about 50% in the most extreme case.

4.3 Ce/Pb Ratios of the Ronda Peridotites

The Ce/Pb ratio of MORB and OIB appears to show relatively little variation around a value of 25 over a wide range of concentrations (Newsom et al., 1986), suggesting that this value is representative of the present day upper mantle (Hofmann et al., 1986). Based on this observation, Hofmann et al. (1986) have proposed that the apparent peridotite/melt partition coefficients for Ce and Pb are very similar. If true, this implies that the Ce/Pb ratio in residual mantle peridotites should also be around a value of 25. The above arguments suggest that the Ce/Pb ratios measured in cpx are not representative of the whole rock peridotite. If sulfide is an important Pb-bearing phase in mantle peridotite, then the Ce/Pb ratios of the Ronda clinopyroxenes will be systematically higher than the bulk rock peridotites. This will probably be most important for the samples which show low Pb concentrations in clinopyroxene. Figure 9a shows a plot of Ce/Pb versus Pb for the Ronda clinopyroxenes, as well as Ce/Pb estimates for cpx from San Carlos xenoliths studied by Galer and O'Nions (1989). The data at high Pb concentrations scatter about the oceanic basalt average. The negative correlation at low Pb concentrations may be the result of cpx equilibration with either plagioclase or sulfide, as mentioned above. If true, the bulk rock Ce/Pb ratios would be lower than the cpx Ce/Pb ratios. We cannot correct for this effect without knowledge of the relevant partitioning relationships for plagioclase and sulfide. However, from Fig. 10b is is clear that such a correction could lower both Ce/Pb and U/Pb from the high values measured in cpx to lower values thought to be more representative of the mantle. Given these uncertainties, the relative incompatibilities of Ce and Pb cannot strictly be determined by comparing the Ronda cpx Ce/Pb data to the Ce/Pb ratios of oceanic basalts.

However, if Ce and Pb are not fractionated at the degrees of melting represented by MORB and OIB, and thus have closely similar bulk solid/liquid partition coefficients (Hofmann et al, 1986), the Ronda data suggest that Ce and Pb concentrations in a partial melt are determined by two different phases (cpx for Ce, cpx and sulfide for Pb). The existing experimental partitioning data for Ce indicate a clinopyroxene/melt partition coefficient of about 0.15 (ex. Irving, 1978). However, Watson et al., (1987) measure a cpx/melt partition coefficient of 0.009-0.012 for Pb. This would seem to require an additional phase to buffer the Pb concentration in both residual peridotite and cumulate rocks in the mantle, possibly the aforementioned sulfide.

Based on the observations that both Nd and Pb isotope ratios in MORB are generally higher than bulk silicate earth estimates (Tatsumoto, 1966), some process must be acting on the upper mantle to decouple U/Pb and Sm/Nd fractionations. Newsom et al., (1986) and Hofmann et al., (1986) have pointed out that the continental crust has a lower Ce/Pb ratio than the mantle (Ce/Pb=9), and it has been suggested that the mechanisms which create the continental crust are responsible for this fractionation (e.g. (Hofmann, 1988)). This would seem to implicate the continental crust as a major reservoir of Pb, including unradiogenic Pb which may balance the radiogenic character of mantle Pb (Doe and Zartman, 1979; Hart, 1988; Reid et al., 1989). A strong transfer of Pb from the mantle to the crust would suggest that the Pb isotope evolution of the mantle may be more highly influenced by the processes of crustal growth and recycling than Sr and Nd isotope evolution.

4.4 Peridotite Sr-Nd-Pb Isotope Systematics

In general, among the samples from the spinel and garnet facies, $^{206}Pb/^{204}Pb$ is positively correlated with $^{87}Sr/^{86}Sr$ (Fig. 6c). This feature is also present within the small scale sampling area in the garnet facies. The samples from the plagioclase facies traverse show little variation in $^{87}Sr/^{86}Sr$, despite a large variation in $^{206}Pb/^{204}Pb$. The Sr-Pb isotope data are suggestive of mixing between a MORB-like component and HIMU (Fig. 6a). For $^{143}Nd/^{144}Nd$, the overall data, as well as the data from the garnet facies sampling area, show a broad negative correlation with $^{206}Pb/^{204}Pb$, but this correlation breaks down in the small scale sampling area within the plagioclase facies (Fig. 6d). In particular, many samples plot outside the range of oceanic basalts, with both high and low $^{143}Nd/^{144}Nd$ for a given $^{206}Pb/^{204}Pb$. The samples from the plagioclase traverse, with radiogenic $^{206}Pb/^{204}Pb$, have lower $^{143}Nd/^{144}Nd$ than HIMU; in addition, these peridotites have low $^{187}Os/^{186}Os$ (Reisberg et al., 1990), unlike the high $^{187}Os/^{186}Os$ signature of HIMU (Chapter 4). Given our present knowledge of U, Th, and Pb partitioning between mantle minerals and basaltic melts, the Nd-Pb systematics of the garnet facies data are consistent

50

with these samples being residues of melting. In particular, samples with high $^{143}Nd/^{144}Nd$ have very depleted REE patterns, but these samples have both high and low $^{206}Pb/^{204}Pb$; this is consistent with the similarity of the mineral/melt partition coefficients of U and Pb (Table 3), since the residue may have U/Pb higher or lower than before melting. The lack of a correlation between $^{143}Nd/^{144}Nd$ and $^{206}Pb/^{204}Pb$ within the plagioclase facies traverse is probably related to the metasomatic event suggested by Reisberg and Zindler (1986). In particular, the varying degrees of LREE enrichment of these samples (Fig. 4e-f) is consistent with metasomatism by percolating melts (e.g. Navon and Stolper, 1987). However, given the limited variability of these REE patterns, it is not possible to constrain the composition of this metasomatizing agent.

Taken as a group, the samples from the garnet and spinel facies define a linear trend from low Pb isotope ratios near the geochron (R238) to very high $^{207}Pb/^{204}Pb$ ratios for a given $^{206}Pb/^{204}Pb$, and scatter about a Pb-Pb isochron with an apparent age of 3.1 Ga (Fig. 6a). Even if the $^{207}Pb/^{204}Pb$-$^{206}Pb/^{204}Pb$ trend represents a mixing array, this age is indicative of the time needed to generate this degree of heterogeneity in $^{207}Pb/^{204}Pb$. If this trend were due to contamination of the peridotite by a crustal component, then the samples with high $^{207}Pb/^{204}Pb$ ratios would be expected to have the slightly high $^{208}Pb/^{204}Pb$, high $^{87}Sr/^{86}Sr$ and low $^{143}Nd/^{144}Nd$ signature of continental crust, which is evidently not the case (Figs. 6c,d).

The apparent 3.1 Ga Pb-Pb age is in excess of the whole-rock isochron ages of 1.3 Ga (Sm-Nd, Reisberg and Zindler, 1986) and 1.2 Ga (Re-Os, Reisberg et al, 1990) previously determined for Ronda peridotites. The evidence is strong that the Sm-Nd and Re-Os ages date a melting event (Reisberg and Zindler, 1986; Reisberg et al., 1989; Reisberg et al., 1990). The garnet and spinel facies peridotites, as a group, do not define a U-Pb or Th-Pb isochron, but it is difficult to determine the extent to which the clinopyroxene U/Pb and Th/Pb ratios are representative of the whole rock. This is certainly not the case for the garnet-bearing samples. Garnet contains significant amounts of U and Th, and the whole rock U/Pb and Th/Pb ratios depend strongly on the garnet/cpx ratio of these samples, which is difficult to determine given the heterogeneous distribution of garnet in hand specimen. Due to the uncertainty in the relationship between the bulk rock U/Pb and Th/Pb ratios to those ratios in cpx, no parent-daughter isochron relationships can be established on a massif wide basis, as was possible for the Sm-Nd and Re-Os systems. However, the broad positive trend in Figure 8, defined largely by the different positions of the garnet-spinel facies data and the plagioclase facies data, is consistent with a 1.3 Ga age.

In addition, Reisberg and Zindler (1986) have documented evidence for a metasomatic event about 200-300 Ma ago which was reflected in the Sr and Nd isotopic

51

compositions of samples from the eastern plagioclase-facies traverse (Fig. 1). This event probably was not responsible for creating the high $^{206,207,208}Pb/^{204}Pb$ and low $^{143}Nd/^{144}Nd$ signatures of the plagioclase traverse samples, because (1) the high $^{206,207,208}Pb/^{204}Pb$ signature was likely already present 200-300 Ma ago (Fig. 8), and (2) the Sm-Nd isotopic systematics of sediment clinopyroxenes from the area of this traverse, as well as the weighted average of the Nd isotopic compositions of the traverse samples themselves, have $^{143}Nd/^{144}Nd$ and $^{147}Sm/^{144}Nd$ ratios less than bulk earth (LREE enriched), and also plot on the 1.3 Ga Sm-Nd isochron defined by samples from the rest of Ronda (Reisberg and Zindler, 1986). This evidence indicates that the partial melting event at 1.3 Ga ago also created a low Sm/Nd, high U,Th/Pb section in the eastern end of the massif, and that the metasomatic event at 200-300 Ma ago resulted in the mixing event documented in the plagioclase facies traverse (Reisberg and Zindler, 1986), as well as changes in Sm/Nd and U,Th/Pb ratios.

4.5 Peridotite-Mafic Layer Relationships

The isotopic compositions of the samples from the interlayered peridotite-mafic layer sections in Fig. 3 are all broadly similar, though signficant differences are present (Table 2). In particular, the similarity of the REE patterns of cpx from samples R140 (ML), R141 (ML), R142 (PD), and R145 (PD) indicate that some trace element exchange and equilibration has taken place. However, the 8 cm thick mafic layers R140 and R141 preserve distinct isotopic compositions, both of which are different from the thick peridotite layer R142 (Fig. 3). This indicates that isotopic heterogeneity at Ronda is present down to the centimeter scale, in agreement with Pb isotope results from Beni Bousera (Hamelin and Allegre, 1988).

Relative to the peridotites, the mafic layers are more restricted in their isotopic compositions, especially in $^{206}Pb/^{204}Pb$ (Fig. 6). This is in contrast to the data of Hamelin and Allegre (1988) for mafic layers from Beni Bousera, which show isotopic variability comparable to that of the peridotites. Since Beni Bousera and Ronda are thought to be parts of the same peridotite body, this is a somewhat surprising result. The number of mafic layers analyzed is small (7), and this may only be a fortuitous result. However, the Ronda garnet-bearing peridotites are very likely mixtures of garnet-bearing mafic layers and depleted wallrock peridotite, as suggested by Reisberg et al. (1989) and Reisberg et al. (1990). This suggestion is supported by the generally high U, Th, and Pb concentrations in the garnet-facies peridotites. In detail, many of the Ronda clinopyroxenes, from all mineral facies, have Pb concentrations which are higher than cpx from San Carlos xenoliths (Fig. 9); there also seems to be a bimodal distribution of Pb concentrations in cpx on either side of about 70 ppb (Fig. 5), which also corresponds to two different groups

based on Ce/Pb ratios (Fig. 9). Given the evidence for physical mixing of mafic layers into the host peridotite (Reisberg et al., 1989), it is suggested that the samples with cpx Pb concentrations in excess of about 70 ppb may have been derived from mixing of mafic layers into peridotite. If this is indeed the case, then the isotopic heterogeneity of the garnet facies samples reflects that of the pre-existing mafic layers, which argues for substantial mafic layer isotopic heterogeneity, in agreement with Pb isotope results from Beni Bousera (Hamelin and Allegre, 1988). Indeed, the high concentrations of U, Th and Pb in the garnet facies cpx, compared to other analyses for residual peridotites (Hamelin and Allegre, 1988; Galer and O'Nions, 1989) indicates that these peridotites have derived a large fraction of their trace elements from mafic layers.

The higher trace element concentrations of the mafic layers represent an important source of components which may effect the isotopic and trace element systematics of the peridotites. Mafic layer clinopyroxenes have higher Ti and Zr and lower Cr compared those from peridotites (Table 1). It should also be noted that some mafic layer cpx have higher Cr than others. These high Ti peridotites (R142, R145) and high Cr mafic layers (R140, R141) are from the interlayered section of the plagioclase facies (Fig. 2b), suggesting some exchange of trace elements between the peridotites and mafic layers. However, these interlayered samples display significant isotopic variability, indicating the preservation of isotopic heterogeneity on the scale of tens of centimeters (Fig. 2). The mechanism responsible for this interaction is difficult to pinpoint. Simple mixing can be ruled out, as this would create straight lines on element-element plots (not shown), with the affected samples lying directly between the compositions of the mafic layers and the peridotites. Diffusive interaction between peridotites and mafic layers may also be important (Hamelin and Allegre, 1988; Reisberg et al., 1989), but a more detailed study is required to definitively answer this question. It is also possible that the peridotites may have interacted with a melt of some kind, either during crystallization of the layers, or from a partial melt of the layers.

5. Isotopic Evolution of Ronda

Two features of the U-Th-Pb data remain puzzling: the origin of the 3.1 Ga trend in Fig. 6a, and the lack of a strong 1.3 Ga signal in the Pb isotope data. The lack of a correlation between $^{143}Nd/^{144}Nd$ and $^{206}Pb/^{204}Pb$ for the garnet and spinel facies samples (Fig. 6d) indicates that the Pb isotope characteristics of Ronda were probably not determined, to a large extent, by depletion of U and Th relative to Pb (or vice versa) in a melting event at 1.3 Ga. In this context, two explanations exist to account for the 3.1 Ga

Pb-Pb age and the 1.2-1.3 Ga Sm-Nd and Re-Os ages for Ronda, both of which are consistent with the data.

5.1 Ronda as Ancient MORB Source

An event at 3.1 Ga ago (partial melting?) created the present Pb isotope heterogeneity at Ronda, and the subsequent partial melting event at 1.3 Ga ago reset the Sm-Nd and Re-Os isochrons, but left the Pb-Pb isochron relationship intact. Thus the presently observable Pb isotopic heterogeneity at Ronda is an intrinsic feature of the peridotite. This evolution is shown in Fig. 8; extrapolation of the 3.1 Ga Ronda Pb-Pb isochron back to the geochron at 3.1 Ga ago indicates a first stage μ=7.87, possibly slightly less than the proposed bulk silicate earth =8.0 (Tatsumoto, 1978; Hart and Zindler, 1989). To generate the present $^{207}Pb/^{204}Pb$ isotope heterogeneity at Ronda requires a range of second-stage μ=7.3-11.2, suggesting a slightly high U/Pb reservoir for the second stage.

This scenario would appear to require that the event at 1.3 Ga ago resulted in an isotopic homogenization which was less efficient for Pb than for Nd and Os. However, the effect of isotopic homogenization on a Pb-Pb isochron is to move the points toward some average Pb isotopic composition on the isochron. Thus, if Pb isotopic homogenization is not perfectly efficient, the resulting Pb-Pb array will still retain a slope which indicates the initial age of the Pb isotope heterogeneity. In addition, this slope would be maintained through time if the U/Pb ratios of the points on the isochron were not drastically changed during the homogenization event. Under this scenario, there should also be a certain amount of $^{143}Nd/^{144}Nd$ and $^{187}Os/^{186}Os$ heterogeneity at 1.3 Ga ago, which almost certainly can be accommodated within the errors on the initial ratios.

The initial $^{143}Nd/^{144}Nd$ derived from the Reisberg and Zindler (1986) Sm-Nd isochron indicates an ε_{Nd} of +6.0 for Ronda at 1.3 Ga ago. The initial $^{187}Os/^{186}Os$ calculated from the Reisberg et al. (1990) Re-Os isochron is 0.996±0.005 at 1.3 Ga ago, which would be depleted relative to bulk silicate earth (BSE) if BSE had a present-day $^{187}Os/^{186}Os$ of >1.08 (Martin et al., 1992). Together with the low $^{87}Sr/^{86}Sr$ of many of the Ronda samples, and the depleted Pb isotopic composition of R238, this evidence suggests that at least some parts of Ronda were already depleted at 1.3 Ga ago, and that the evolution from 1.3 Ga ago to the present represents a "third stage" in the isotopic evolution of Ronda since the formation of the earth.

If the time period of the "second stage" is taken to be 3.1 Ga-1.3 Ga ago, this would indicate that Ronda evolved from ε_{Nd}=0 at 3.1 Ga ago to ε_{Nd}=+4.3 at 1.3 Ga ago, and also developed a depleted $^{87}Sr/^{86}Sr$ signature during this time. However, for the U-Pb
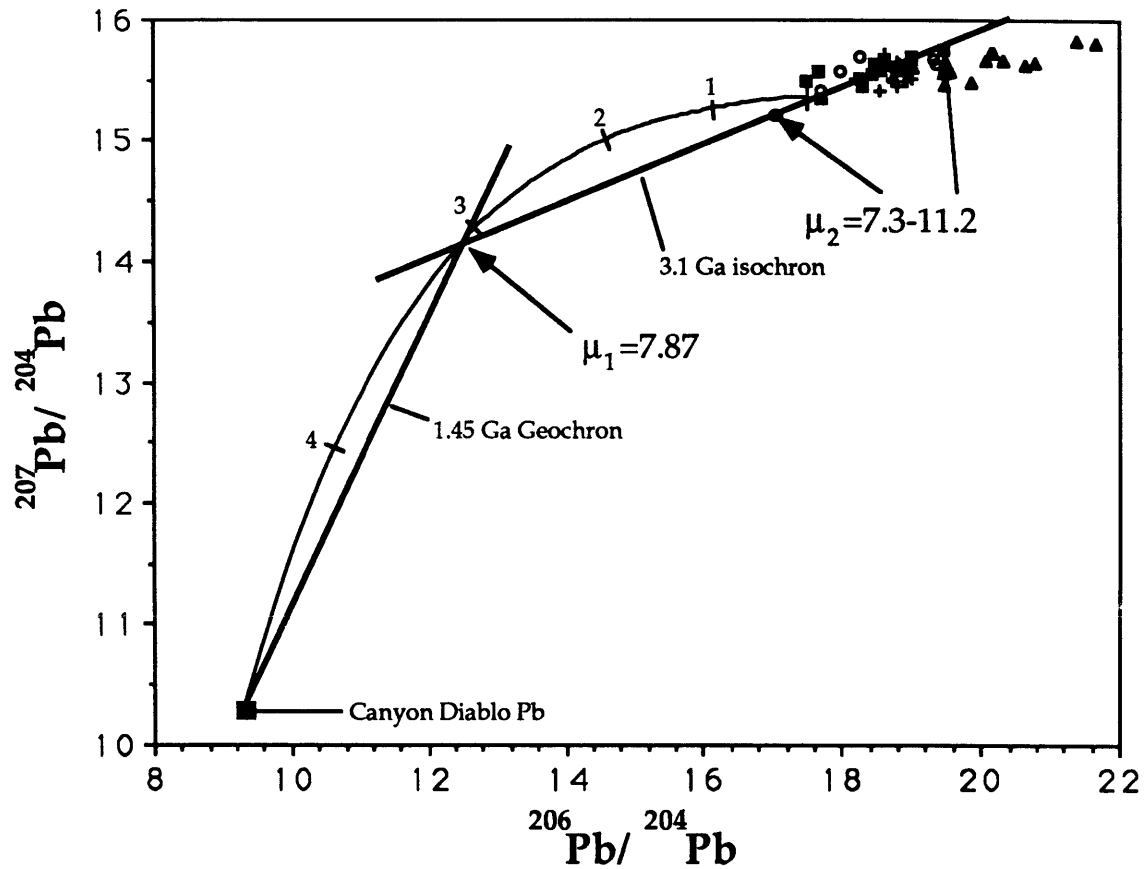
54

Figure 11. Pb isotope evolution of the Ronda peridotite. Single stage growth curve from Canyon Diablo is for μ=8.0 with tickmarks every 1 Ga. The Ronda 3.1 Ga isochron intersects the 1.45 Ga geochron (geochron 3.1 Ga ago) at a first stage μ=7.87. Calculated second stage μ ranges from 7.3-11.2 for the Ronda garnet and spinel peridotites. Additional events at 1.3 Ga ago (partial melting) and 300 Ma ago (metasomatism) potentially result in scatter about the 3.1 Ga isochron.

system, a range of μ ($^{238}U/^{204}Pb$) from 7.3-11.2 is needed to create the observed heterogeneity in $^{207}Pb/^{204}Pb$ (Fig. 8). Essentially, this would mean that, in the time period 3.1-1.3 Ga ago, Ronda would have had depleted $^{143}Nd/^{144}Nd$ and $^{87}Sr/^{86}Sr$, and enriched Pb isotopic compositions relative to bulk silicate earth. This is exactly the signature exhibited by present-day MORB. In support of this model, $^{208}Pb/^{206}Pb$ is broadly correlated with Th/U in most of the Ronda cpx (Fig. 12a), recent metasomatism notwithstanding.

5.2 Ronda as Metasomatized Mantle

The partial melting event at 1.3 Ga ago, which created isochronous relationships in the Sm-Nd and Re-Os systems, was contemporaneous with an event which introduced a component with $^{143}Nd/^{144}Nd$ and $^{187}Os/^{186}Os$ similar to Ronda at 1.3 Ga ago, but with a Pb isotopic composition characterized by high $^{207}Pb/^{204}Pb$. In this model, the Pb isotopic heterogeneity of the garnet and spinel facies samples could be the result of mixing with a high $^{207}Pb/^{204}Pb$ component, or this $^{207}Pb/^{204}Pb$ heterogeneity could be characteristic of the metasomatizing agent itself. In this case, the 3.1 Ga age would simply represent the length of time needed to create the difference in $^{207}Pb/^{204}Pb$ between Ronda and the metasomatic component.

This scenario requires that the introduced component has no relationship to the Ronda peridotite, and that the presently observable Pb isotopic heterogeneity is a metasomatic feature. The isotopic characteristics of this metasomatic component at 1.3 Ga ago would be depleted $^{143}Nd/^{144}Nd$ and $^{87}Sr/^{86}Sr$, and high $^{207}Pb/^{204}Pb$ relative to $^{206}Pb/^{204}Pb$. These are essentially the isotopic characteristics of many present-day island arc volcanics (e.g. Morris and Hart, 1983). In support of this model, $^{87}Sr/^{86}Sr$ is positively correlated with $\Delta7/4$ within the garnet and spinel facies, and among the samples from the plagioclase facies and mafic layers. The isotopic characteristics of the Ronda garnet-bearing peridotites essentially reflect the isotopic characteristics of disaggregated garnet-bearing mafic layers, as discussed in Section 4. Thus the Ronda mafic layers could represent cumulates from magmas with isotopic characteristics similar to island arc volcanics. In this model, the Pb isotopic heterogeneity observed in the Ronda spinel and garnet peridotites would be an inherent property of the throughgoing magmas, because the high Pb concentrations of magmas relative to peridotite would cause the metasomatic Pb signature to completely dominate the peridotite. However, this would also be expected to be the case for the Sr and Nd isotope signatures of the garnet-bearing samples. In this case, the Sm-Nd isochron of Reisberg and Zindler (1986) would not necessarily represent the melt depletion event recorded by the Re-Os isochron (Reisberg et al., 1990).
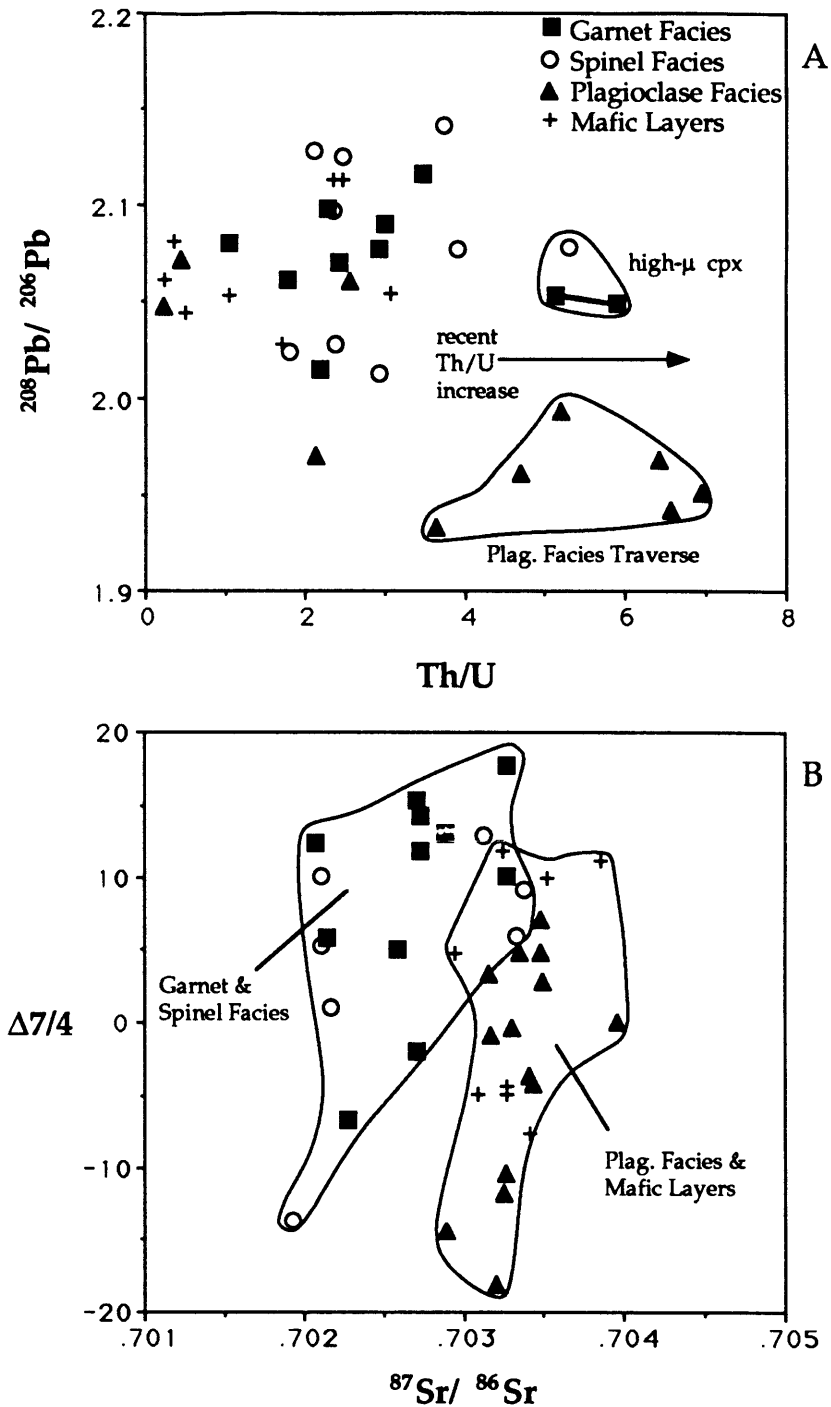
Figure 12. A) 208Pb/206Pb versus Th/U for Ronda cinopyroxenes. LREE-enriched samples from the plagioclase facies traverse, as well as the spinel- and garnet-facies samples with the highest μ (R85-34, 051R) are shifted to high Th/U ratios. The remaining samples form a broad positive trend, suggesting that the heterogeneity in 208Pb/206Pb is old, and broadly reflected in the measured TH/U of the clinopyroxenes. B) $\Delta 7/4$ versus 87Sr/86Sr. The two groups of data, spinel+garnet-facies samples and plagioclase-facies samples+mafic layers, show positive correlations, suggesting possible mixing toward a component with high 207Pb/204Pb and moderately high 87Sr/86Sr (about .7040).

6. Conclusions

The picture of the U-Th-Pb system which emerges from this study is one of a complexity befitting highly incompatible elements. Large variations in the abundances of U, Th, and Pb are evident, and are consistent with varying degrees of mixing of incompatible element-rich mafic layers with variably depleted peridotite. Olivine and opx contain no U and Th, but may contain a small amount of Pb. Thus olivine may contribute a significant amount of Pb to the whole rock budget in clinopyroxene-poor peridotites. Garnets are characterized by low abundances of U (2.7-4.3 ppb), Th (1.4-5.2 ppb) and Pb (1.5-9.7 ppb), but have high μ (28-122). These mineral/mineral partitioning results indicate that, of the major anhydrous silicate phases present in mantle peridotite, clinopyroxene and garnet are the dominant host phases for U, Th, and Pb. However, trace amounts of sulfide, not detected in this study, may exert an influence over the whole rock budget and partitioning relationships for Pb in mantle peridotites.

Garnet-cpx pairs from garnet-bearing samples display a range of ages from 17.3 Ma to 44.0 Ma, and are consistent with the Sm-Nd garnet-cpx ages determined by Zindler et al. (REF) for a Ronda garnet-clinopyroxenite (21.5$\pm$1.8 Ma), and by Reisberg et al. (1989) for Ronda garnet peridotites (21.0$\pm$7.0 Ma to 24.5$\pm$7.3 Ma). These results indicate that mineral phases in the Ronda peridotites were in isotopic equilibrium 22 Ma ago. For the peridotites, large ranges in $^{206}Pb/^{204}Pb$ (17.047-21.688), $^{207}Pb/^{204}Pb$ (15.203-15.799) and $^{208}Pb/^{204}Pb$ (36.277-41.930) are evident, exceeding the range of Pb isotopic compositions reported for oceanic basalts. The garnet and spinel facies samples largely overlap in Pb isotopic composition, and the $^{207}Pb/^{204}Pb$-$^{206}Pb/^{204}Pb$ data for these samples scatter about a Pb-Pb isochron with an age of 3.1 Ga. The high Pb isotope ratios of samples from the plagioclase facies traverse were probably created at about 1.3 Ga ago, when the massif was subject to a partial melting event. A subsequent event at about 200 Ma, which may have involved a small amount of local partial melting and melt percolation, resulted in metasomatism and further LREE enrichment in the eastern end of the plagioclase facies.

Based on the integrated isotopic data, the Ronda peridotite may represent either 1) a segment of MORB source mantle which was formed about 3 Ga ago, and incorporated into the subcontinental lithosphere at about 1.3 Ga; or 2) a segment of depleted mantle which was subject to metasomatism by a component similar in isotopic composition to island arc volcanics. In the first model, the Ronda mafic layers may have been formed during a melting event 1.3 Ga ago, or were formed around 3 Ga ago and partially re-equilibrated at 1.3 Ga ago. In the second model, the mafic layers probably represent crystal cumulates of

58

melts derived both from the melting Ronda peridotites, and also from melts with island arc affinities.

Appendix-Analysis of U, Th, and Pb in Mineral Separates

Mineral separates of 17 to 200 mg were dissolved on a hotplate at 125°C for 5-10 days in 3 ml Savillex screw cap beakers in either 1) a 3:2 mixture of HF:HBr or 2) a mixed acid solution consisting of equal parts concentrated HNO_3-6.2 N HCl-concentrated HF. A mixed spike containing ^{235}U, ^{230}Th and ^{205}Pb was added before dissolution. Pb was separated in 0.5 N HBr on 20 µl of Dowex 1 using a scaled down version of the technique of (Manhes et al., 1978), reserving the liquid for subsequent separation steps. It was found necessary to repeat the column separation for Pb using a separate, clean column in order to entirely eliminate Ca from the Pb fraction. The Pb fraction was evaporated to a small volume with 1-2 drops of 0.03 N H_3PO_4. After evaporation into H_3PO_4, the Pb fraction was evaporated repeatedly with concentrated HNO_3 in order to eliminate organics, which can interfere with $^{204}Pb^+$ measurement during mass spectrometry.

At this point in the procedure, it was necessary to extract as much U and Th as possible from the fluorides which invariably form during dissolution in HF. Radiotracer studies have shown that U and especially Th partition strongly into Ca fluoride formed during the dissolution step (A. Zindler, pers. comm.). During dissolution, flourides form rapidly on the surfaces of mineral grains, and continuously replace the components which go into solution, resulting in fluoride pseudomorphs after the original mineral grains. The potential for sample-spike disequilibrium for U and Th may thus exist during dissolution, and it is important to make every effort to achieve dissolution of the fluoride residue. The fluoride residue was attacked with aqua regia at 150°C for several days, evaporated to dryness, and redissolved in 8 N HNO_3. Roughly half the time, the residue went completely into solution (especially for smaller samples). The sample was centrifuged, and U and Th were separated together on AG1X8 anion exchange resin in 8 N HNO_3 (saving the eluant for Sr and Nd separation), and eluted with 6.2 N HCl and 0.5 N HBr. 1-2 drops of 0.015 N H_2SO_4 was added to the U+Th fraction, and the solution was evaporated down to a tiny drop for loading. The solution left from the U+Th step was dried down, redissolved in 6.2 N HCl several times, and finally dissolved in 2.5 N HCl. Subsequent procedures for the separation of Sr and Nd follow the procedures of (Richard et al., 1976; Hart and Brooks, 1977; Zindler, 1980). Blanks for the total procedure ranged from 9-45 pg Pb, <1-3 pg Th, <1-10 pg U, <200 pg Sr, and <30pg Nd and Sm. Reagents used during the separation procedures typically accounted for 75-100% of the measured Pb blank. The isotopic composition of the Pb blank was consistently MORB-like ($^{206}Pb/^{204}Pb$=18.5-19.5, $^{207}Pb/^{204}Pb$=15.4-15.6, $^{208}Pb/^{204}Pb$=37-39), which resulted in minimal blank corrections for most analyses.

Pb was run on single Re filaments (0.001" x 0.030") using the silica gel-phosphoric acid activation technique (Akishin et al., 1957; Cameron et al., 1969). The Pb fraction was heated on a hotplate, and 1-2 mg of silica gel was added. The solution was allowed to evaporate by about 20%, and then the entire solution was picked up and loaded. Picking up the solution out of a hot beaker minimizes the amount of Pb left in the bottom of the beaker. The Pb solution was then loaded in as small an area as possible in the center of the filament, and dried at 1.0 amps. The filament current was then raised slowly to fume off the excess phosphoric acid (about 2.5-2.8 amps), then taken to dull red for 3 seconds. The filament current was then decreased to about 2.2 amps, and the load was allowed to cook in air for 2-5 minutes. The filament must be closely watched during this period, as heating the Re filament in air at 2.2 amps can cause the filament to recrystallize and crack, and this step should be stopped if the filament appears to be recrystallizing. This heating step in air reduces the amount of "low temperature Pb" observed during mass spectrometry, and results in a more stable, more intense signal compared with runs for which this was not done. Due to the very small amounts of Pb analyzed (150 pg to 20 ng), data were collected using an electron multiplier operated in analog mode at a gain of 2×10^4. Early in the Pb runs, a "low temperature" fraction of Pb was always observed at filament currents <2.0 amps, which was characterized by rapidly growing or dying signals and a persistent interference on $^{204}Pb^+$, resulting in very low $^{207}Pb/^{204}Pb$ and $^{206}Pb/^{204}Pb$ ratios. In addition, interferences were typically found at masses 205 and 203, which probably correspond to $^{203,205}Tl^+$. These interferences were always found at filament currents of <2.0 amps (1x30 mil Re), which corresponds to approximately 1000°C filament temperature, and sometimes as high as 2.2 amps for nanogram amounts of Pb. As a result, isotopic composition data was only taken above 2.1-2.2 amps. Data for $^{205}Pb^+$ for isotope dilution measurements was always taken after the data for Pb isotopic composition, in order to allow Tl^+ to burn off, which was always the case (as determined by measuring the 203/204 ratio). Typical ion currents for $^{208}Pb^+$ were $0.5\text{-}3 \times 10^{-12}$ A for 1 ng of Pb. A correction factor of 0.375 %/amu was employed based on repeated analysis of NBS 981 common Pb, using the values of Todt et al., (1984). Precision for most runs is less then 0.1% on all ratios, and the reproducibility of NBS981 runs (300-2000 pg) is 0.07%/amu (Table A1). Reproducibility of duplicate samples is also generally on the order of 0.07%/amu.

For the loading of U and Th, a small amount of water was added to the sample in the beaker, and warmed on a hotplate. The reason for evaporating U and Th in H_2SO_4 is that Ca sulfates are quite insoluble, while U and Th sulfates are soluble in water. Thus, by evaporating the U+Th fraction down into H_2SO_4, potential contaminants are made

insoluble, and are not loaded if U and Th are picked up in water. U and Th were loaded together on single Re filaments with colloidal graphite, and also run using the electron multiplier. Colloidal graphite should be chosen with care, as nearly all brands have substantial U blanks (alternatively, U could be run as an oxide with silica gel and phosphoric acid). In addition, the zone refined Re filament sometimes had a small Th blank, which was generally eliminated by outgassing the Re filaments at 5.5-6.0 amps (about 20 minutes), and checking each filament for Th before loading. A small amount of Ca was typically observed during the U-Th runs, which usually burned off after 10-20 minutes at 3.0 amps. U^+ was typically run at 3.4-4.0 amps, and Th^+ run at 4.0-5.0 amps. A correction factor of 0.4%/amu was applied to the U and Th data based on repeated analysis of SRM 960 U. Isotope dilution measurements of U, Th and Pb are believed to be accurate to about 5%, and this error is reported except for concentration data for olivine, opx, and garnet, where uncertainties approach 10%.

References

Akishin, P. A., O. T. Nikitin and G. M. Panchenkov (1957) A new effective ion emitter for the isotopic analysis of lead. Geokhimiya, **5**, 429-434.

Allegre, C. J. and D. L. Turcotte (1986) Implications of a two component marble-cake mantle. Nature, **323**, 123-127.

Anders, E. and N. Grevesse (1989) Abundances of the elements: Meteoritic and solar. Geochim. Cosmochim. Acta, **53**, 197-214.

Bodinier, J. L., C. Dupuy and J. Dostal (1988) Geochemistry and petrogenesis of Eastern Pyrenean peridotites. Geochim. Cosmochim. Acta, **52**, 2893-2907.

Bodinier, J. L., M. Guirard, J. Fabries, J. Dostal and C. Dupuy (1987) Petrogenesis of layered pyroxenites from the Lherz, Freychinede and Padres ultramafic bodies (Arieges, French Pyrenees). Geochim. Cosmochim. Acta, **51**, 279-290.

Brooks, C., S. R. Hart, A. Hofmann and D. E. James (1976) Rb-Sr mantle isochrons from oceanic regions. Earth Planet. Sci. Lett., **32**, 51-61.

Cameron, A. E., D. H. Smith and R. L. Walker (1969) Mass spectrometry of nanogram size samples of lead. Anal. Chem., **41**, 525-526.

Cohen, R. S., R. K. O'Nions and J. B. Dawson (1984) Isotope geochemistry of xenoliths from East Africa: implications for development of mantle reservoirs and their interaction. Earth Planet. Sci. Lett., **68**, 209-220.

Dick, H. J. B. (1977) Partial melting in the Josephine Peridotite I. The effect on mineral composition and its consequence for geobarometry and geothermometry. Am. J. Sci., **277**, 801-832.

Dickey, J. S. (1970) Partial fusion products in alpine-type peridotites: Serrania de la Ronda and other examples. Min. Soc. Am. Special Paper, **3**, 33-49.

Dickey, J. S., M. Obata and C. J. Suen (1977). Partial fusion *versus* fractional crystallization: hypotheses for the differentiation of the Ronda ultramafic massif of southern Spain. in *Magma Genesis*. Bull. Oregon Dept. Geol. Min. Indust.

Dickey, J. S., M. Obata and C. J. Suen, Ed. (1979). Chemical differentiation of the lower lithosphere as represented by the ronda ultramafic massif, southern Spain,. in *Origin and Distribution of the Elements*. New York, Pergamon Press.

Doe, B. R. and R. E. Zartman (1979). Plumbotectonics: the Phanerozoic. in *Geochemistry of hydrothermal ore deposits*. New York, John Wiley and Sons. 22-70.

Frey, F. A. (1969) Rare earth abundances in a high-temperature peridotite intrusion. Geochim. Cosmochim. Acta, **33**, 1429-1447.

Frey, F. A., J. Suen and H. W. Stockman (1985) The Ronda high temperature peridotite: Geochemistry and petrogenesis. Geochim. Cosmochim. Acta, **49**, 2469-2491.

Galer, S. J. G. and R. K. O'Nions (1989) Chemical and isotopic studies of ultramafic inclusions from the San Carlos volcanic field, Arizona: a bearing on their petrogenesis. J. Petrol., 30, 1033-1064.

Gast, P. W. (1969) The isotopic composition of lead from St. Helena and Ascension Islands. Earth Planet. Sci. Lett., 5, 353-359.

Haines, E. L. and R. E. Zartman (1973) Uranium concentration and distribution in six peridotite inclusions of probable mantle origin. Earth Planet. Sci. Lett., 20, 45-53.

Hamelin, B. and C. J. Allegre (1988) Lead isotope study of orogenic lherzolite massifs. Earth Planet. Sci. Lett., 91, 117-131.

Hart, S. R. (1988) Heterogeneous mantle domains: signatures, genesis and mixing chronologies. Earth Planet. Sci. Lett., 90, 273-296.

Hart, S. R. and C. Brooks (1977) The geochemistry and evolution of the early precambrian mantle. Contrib. Mineral. Petrol., 61, 109-128.

Hart, S.R. and Zindler, A. (1989) Constraints on the nature and development of chemical heterogeneities in the mantle, in: Mantle Convection, W.R. Peltier, ed., Gordon and Breach Science Publishers, New York, p. 261-387.

Hofmann, A. W. (1988) Chemical differentiation of the Earth: the relationship between mantle, continental crust, and oceanic crust. Earth Planet. Sci. Lett., 90, 297-314.

Hofmann, A. W., K. P. Jochum, M. Seufert and W. M. White (1986) Nb and Pb in oceanic basalts: new constraints on mantle evolution. Earth Planet. Sci. Lett., 79, 33-45.

Irving, A. J. (1978) A review of experimental studies of crystal/liquid trace element partitioning. Geochim. Cosmochim. Acta, 42, 743-770.

Kleeman, J. D., D. H. Green and J. F. Lovering (1969) Uranium distribution in ultramafic inclusions from Victorian basalts. Earth Planet. Sci. Lett., 5, 449-458.

Komprobst, J. (1969) Le massif ultrasique des Beni Bouchera (Rif Interne, Maroc); etude des peridotites de haute temperature st de haute pression et des pyroxenolites, a grenat ou sans grenat, qui leur sont associees. Contrib. Mineral. Petrol., 23, 283-322.

Kramers, J. D. (1977) Lead and strontium isotopes in Cretaceous kimberlites and mantle-derived xenoliths from Southern Africa. Earth Planet. Sci. Lett., 34, 419-431.

Kramers, J. D. (1979) Lead, uranium, strontium, potassium and rubidium in inclusion-bearing diamonds and mantle-derived xenoliths from southern Africa. Earth Planet. Sci. Lett., 42, 58-70.

Kramers, J. D., J. C. M. Roddick and J. B. Dawson (1983) Trace element and isotope studies on veined, metasomatic and "MARID" xenoliths from Bultfontein, South Africa. Earth Planet. Sci. Lett., 65, 90-106.

LaTourrette, T. Z., and D. S. Burnett (1992) Actinide element fractionation in solar system processes: the role of oxygen fugacity. Earth Planet. Sci. Lett., 110, 227-244.

Loomis, T. P. (1975) Tertiary mantle diapirism, orogeny, and plate tectonics east of the Strait of Gibralter. Am. J. Sci., **275**, 1-30.

Loubet, M. and C. J. Allegre (1979) Trace element studies in the Alpine type peridotite of Beni Bousera (Morocco). Geochem. J., **13**, 69-75.

Loubet, M. and C. J. Allegre (1982) Trace elements in orogenic lherzolites reveal the complex history of the upper mantle. Nature, **298**, 809-814.

Loubet, M., N. Shimizu and C. J. Allegre (1975) Rare earth elements in alpine peridotites. Contrib. Mineral. Petrol., **53**, 1-12.

Lundeen, M. T. (1978) Emplacement of the Ronda peridotite, Sierra Bermeja, Spain. Geol. Soc. Am. Bull., **89**, 72-180.

Manhes, G., J.-P. Minster and C. J. Allegre (1978) Comparative uranium-thorium-lead and rubidium-strontium of St. Severin amphoterite: Concequences for early solar system chronology. Earth Planet. Sci. Lett., **39**, 14-24.

Martin, C. E., B. K. Esser and K. K. Turekian (1992) Re-Os isotopic constraints on the formation of mantle and crustal reservoirs. Austral. J. Earth Sci., **38**,

Meijer, A., T.-T. Kwon and G. R. Tilton (1990) U-Th-Pb partitioning behavior during partial melting in the upper mantle: implications for the origin of high-mu components and the "Pb paradox". J. Geophys. Res., **95**, 433-448.

Meijer, A. and P. S. Z. Rogers (1990) Pb distribution in ultramafic nodules from the upper mantle beneath the western United States (abst.). Geol. Soc. Austr. Abstr., **27**, 66.

Menzies, M. A. and V. R. Murthy (1976) Sr isotopic composition of clinopyroxenes from some medeterranean alpine lherzolites. Geochim. Cosmochim. Acta, **40**, 1577-1581.

Menzies, M. A. and V. R. Murthy (1980a) Nd and Sr isotope geochemistry of hydrous mantle nodules and their host alkali basalts; implications for lacal heterogeneities in metasomatically veined mantle. Earth Planet. Sci. Lett., **46**, 323-334.

Menzies, M. A. and V. R. Murthy (1980b) Enriched mantle: Nd and Sr isotopes in diopsides from kimberlite nodules, Nature, **283**, 634-636.

Morris, J. D. and S. R. Hart (1983) Isotopic and incompatible element constraints on the genesis of island arc volcanics: Cold Bay and Amak Islands, Aleutians. Geochim Cosmochim Acta, **47**, 2015-2030.

Newsom, H. E., W. M. White, K. P. Jochum and A. W. Hofmann (1986) Siderophile and chalcophile element abundances in oceanic basalts, Pb isotope evolution and growth of the Earth's core. Earth Planet. Sci. Lett., **80**, 299-313.

Navon, O. and E. Stolper (1987) Geochemical consequences of melt percolation: the upper mantle as a chromatographic column. J. Geol., **95**, 285-307.

Nixon, P. H. (1987). *Mantle Xenoliths*. New York, John Wiley and Sons.

Obata, M. (1980) The Ronda peridotite: garnet-, spinel-, and plagioclase-lherzolite facies and the P-T trajectories of a high-temperature mantle intrusion. J. Petrol., **21**, 533-572.

Obata, M. (1982) Reply to W. Schubert's Comments on 'The Ronda Peridotite: garnet-, spinel-, and plagioclase-lherzolite facies and the P-T trajectories of a high-temperature mantle intrusion'. J. Petrol., 23, 296-298.

Obata, M. and J. S. Dickey (1976) Phase relations of mafic layers in the Ronda peridotite. Carnegie Inst. Wash. Yearb., 75, 562-566.

Polve, M. (1983) Les isotopes du Nd et du Sr dans les lherzolites orogeniques: contribution a la determination de la structure et de la dunamique du manteau suprieur. These de doctorat d'etat, Universite Paris VII.

Polvé, M. and C. J. Allègre (1980) Orogenic lherzolite complexes studied by 87Rb-87Sr: a clue to understand the mantle convection processes. Earth Planet. Sci. Lett., 51, 71-93.

Priem, H. N. A., N. A. I. M. Boelrijk, E. H. Hebeda, I. S. Oen, E. A. T. Verdurmen, et al. (1979) Isotopic dating of the emplacement of ultramafic masses in the Serrania de Ronda, southern Spain. Contrib. Mineral. Petrol., 70, 103-109.

Quick, J. E. (1981) Petrology and petrogenesis of the Trinity Peridotite, and upper mantle diapir in the eastern Klamath Mountains, northern California. J. Geophys. Res., 86, 11,837-11,863.

Reid, M. R., S. R. Hart, E. R. Padovani and G. A. Wandless (1989) Contribution of metapelitic sediments to the composition, heat production, and seismic velocity of the lower crust of southern New Mexico, U.S.A. Earth Planet. Sci. Lett., 95, 367-381.

Reisberg, L. and A. Zindler (1986) Extreme isotopic variations in the upper mantle: evidence from Ronda. Earth Planet. Sci. Lett., 81, 29-45.

Reisberg, L., A. Zindler and E. Jagoutz (1989) Further Sr and Nd isotopic results from peridotites of the Ronda Ultramafic Complex. Earth Planet. Sci. Lett., 96, 161-180.

Reisberg, L. C., C. J. Allegre and J. M. Luck (1991) The Re-Os systematics of the Ronda Ultramafic Complex of southern Spain. Earth Planet. Sci. Lett., 105, 196-213.

Richard, P. and C. J. Allegre (1980) Neodymium and strontium isotope study of ophiolite and orogenic lherzolite petrogenesis. Earth Planet. Sci. Lett., 47, 65-74.

Richard, P. N., N. Shimizu and C. J. Allegre (1976) $^{143}Nd/^{146}Nd$, a natural tracer: An application to oceanic basalts. Earth Planet. Sci. Lett., 31, 269-278.

Shimizu, N. and S. R. Hart (1982) Applications of the ion microprobe to geochemistry and cosmochemistry. Ann. Rev. Earth Planet. Sci., 10, 483-526.

Sinigoi, S., P. Comin-Chiramonti and A. A. Alberti (1980) Phase relations in the partial melting of the Baldissero spinel-lherzolite (Ivrea-Verbano zone, western Alps, Italy). Contrib. Mineral. Petrol., 75, 111-121.

Sinigoi, S., P. Comin-Chiramonti, G. Demarchi and F. Siena (1983) Differentiation of partial melts in the mantle: evidence from the Balmuccia peridotite, Italy. Contrib. Mineral. Petrol., 82, 351-359.

Stosch, H.-G. and S. A. Seck (1980) Geochemistry and mineralogy of two spinel peridotite suites from Dreiser Weiher, West Germany. Geochim. Cosmochim. Acta, **44**, 457-470.

Stosch, H. G., R. W. Carlson and G. W. Lugmair (1980) Episodic mantle differentiation: Nd and Sr isotopic evidence. Earth Planet. Sci. Lett., **47**, 263-271.

Suen, C. J. and F. A. Frey (1987) Origins of the mafic and ultramafic rocks in the Ronda peridotite. Earth Planet. Sci. Lett., **85**, 183-202.

Tatsumoto, M. (1966) Genetic relations of oceanic basalts as indicated by lead isotopes. Science, **153**, 1094-1101.

Tatsumoto, M. (1978) Isotopic composition of lead in oceanic basalts and its implication to mantle evolution, Earth Planet. Sci. Lett., **38**, 63-87.

Todt, W., R. A. Cliff, A. Hanser and A. W. Hofmann (1984) $^{202}Pb + ^{205}Pb$ double spike for lead isotopic analyses. Terra Cognita, **4**, 209.

Watson, E. B., D. Ben Othman, J. M. Luck and A. W. Hofmann (1987) Partitioning of U, Pb, Hf, Yb, Cs, Re, Os between chromian diopsidic pyroxene and haplobasaltic liquid. Chem. Geol., **62**, 191-208.

Zartman, R. E. and F. Tera (1973) Lead concentration and isotopic composition in five peridotite inclusions of probable mantle origin. Earth Planet. Sci. Lett., **20**, 54-66.

Zindler, A. (1980) Geochemical processes in the earth's mantle and the nature of crust-mantle interactions: Evidence from studies of Nd and Sr isotope ratios in mantle derived igneous rocks and lherzolite nodules. PhD, Massachusetts Institute of Technololy, Cambridge, Massachusetts.

Zindler, A. and S. R. Hart (1986) Chemical Geodynamics. Ann. Rev. Earth Planet. Sci., **14**, 493-571.

Zindler, A. and E. Jagoutz (1988) Mantle cryptology. Geochim. Cosmochim. Acta, **52**, 319-333.

Zindler, A., H. Staudigel, S. R. Hart, R. Endres and S. Goldstein (1983) Nd and Sr isotopic study of a mafic layer from Ronda ultramafic complex. Nature, **304**, 226-230.

Chapter 3

Constraints on the Nature of Melting and Melt Migration in Mantle
Plumes: A Trace Element Study of Mantle Xenoliths from the Islands
of Savaii and Tubuai

1. Introduction

The study of peridotites derived from the mantle is the most direct way to investigate the geochemical processes at work in the deep interior of the earth. Samples of mantle peridotite occur as tectonically emplaced bodies ("orogenic peridotites") and also as xenoliths carried to the surface by volcanic eruptions. Compared with orogenic peridotites, mantle xenoliths are generally less modified by retrograde metamorphism and crustal contamination; however, their small size and discrete nature eliminate any spatial relationships between xenoliths which may have existed before entrainment and eruption. Modification by the volcanic host rock can also effect the texture, mineralogy, and chemistry of the xenolith.

The origins of mantle xenolith samples from oceanic islands are generally more well constrained than their more common counterparts found in continental volcanics. Xenoliths in continental alkali basalts and kimberlites are typically samples which have been part of the subcontinental lithosphere for long periods of time, in excess of 3 Ga in some cases (Richardson et al., 1985). These samples have often been subject to many episodes of metamorphism and metasomatism during their residence in the subcontinental lithosphere. Xenoliths from oceanic islands will be either 1) igneous inclusions which have crystallized from mantle melts (either MORB or OIB magmas), 2) pieces of the mantle which have been accreted to the oceanic lithosphere, either at a mid-ocean ridge or by conductive cooling of the plate, or 3) entrained samples of the convecting mantle. The geochemical characteristics observed in OIB-hosted xenoliths are thus 1) results of events, usually associated with volcanic activity, which have taken place in a period of time which is limited by the age of the oceanic lithosphere beneath the individual island, or 2) characteristics present in the mantle source of the volcanics, or both. In these respects, OIB-hosted xenoliths represent the subset of mantle samples which are most likely to contain geochemical information about the convecting mantle.

Mantle derived xenoliths are often texturally and chemically heterogeneous on the scale of a single specimen (e.g. Cox et al., 1987). These samples often show evidence of processes which are largely averaged together during magma genesis, and are thus either unobservable or have only subtle effects on the chemistry of magmas. An example of such a process is melt migration and percolation, the chemical effects of which have been observed in peridotite samples (Navon and Stolper, 1987; Bodinier et al., 1990; Kelemen et al., 1990) but are not obvious in the geochemistry of mantle derived magmas (Hofmann, 1984).

The isotopic heterogeneity of oceanic island basalts requires the existence in the convecting mantle of geochemically distinct reservoirs, with quasi-independent chemical

histories over time periods up to several billion years (e.g. Chase, 1981). Isotopic and trace element studies of OIBs have provided much information on the chemistry of the source regions of these volcanics (e.g. Hofmann et al., 1986; Dupuy et al., 1989), but often our knowledge of the mantle source geochemistry is limited by the extent of our knowledge (or ignorance) of the melting process. In this context, the study of xenoliths from oceanic islands holds great potential for placing constraints on the origins of chemically distinct parts of the mantle, with the additional ability to target those islands with unique isotopic signatures (provided the xenoliths exist).

With this strategy, an investigation of mantle derived xenoliths from the islands of Savaii (Western Samoa) and Tubuai (Austral Islands) is presented. Basalts from Savaii are characterized by high $^{87}Sr/^{87}Sr$ and high $^{207}Pb/^{204}Pb$ (White and Hofmann, 1982; Wright and White, 1987; Farley et al., 1992), and lie close to the EMII isotopic endmember (Zindler and Hart, 1986). Tubuai volcanics are characterized by very high Pb and Os isotope ratios (Vidal et al., 1984; Palacz and Saunders, 1986; Nakamura and Tatsumoto, 1988; Chapter 4), and lie close to the HIMU endmember (Zindler and Hart, 1986). The petrographic and geochemical data reveal similarities and differences in the mantle beneath these two islands with very different isotopic signatures. This data provides information on the nature of melting and the efficiency of melt extraction in the hotspot mantle sources of these islands.

2. Sample Descriptions

2.1 Sample Locations

The island of Savaii is located on the western end of the Samoa Islands chain, in the western Pacific Ocean (Fig. 1). The ages of Samoan shield lavas display an age progressive trend toward the southeast end of the chain (Duncan, 1985; Natland and Turner, 1985), consistent with a hotspot origin (Wilson, 1963). However, the exposed volcanics on Savaii are largely post-shield alkali basalts (≤ 2 Ma), with only a small exposure of shield lavas (4-6 Ma) on the northeast side of the island. Ultramafic xenoliths were sampled from several sites on the island, with the largest number of samples coming from a tuff cone which serves as a mine for road mettle (SAV 1 locality).

The island of Tubuai is located in the Austral Island chain in the south Pacific Ocean (Fig. 2). The ages of the Cook-Austral Islands follow a hotspot trend of decreasing age toward the southeast from Mangaia (20 Ma) to historic eruptions of Macdonald seamount (Duncan and McDougall, 1976; Turner and Jarrard, 1982; Diraison, 1991), with Tubuai volcanics falling in the range of 6-10 Ma. Exposed on Tubuai are the remains of two volcanoes. The eastern volcano (6-10 Ma) consists of interlayered alkali basalt, ankaramite
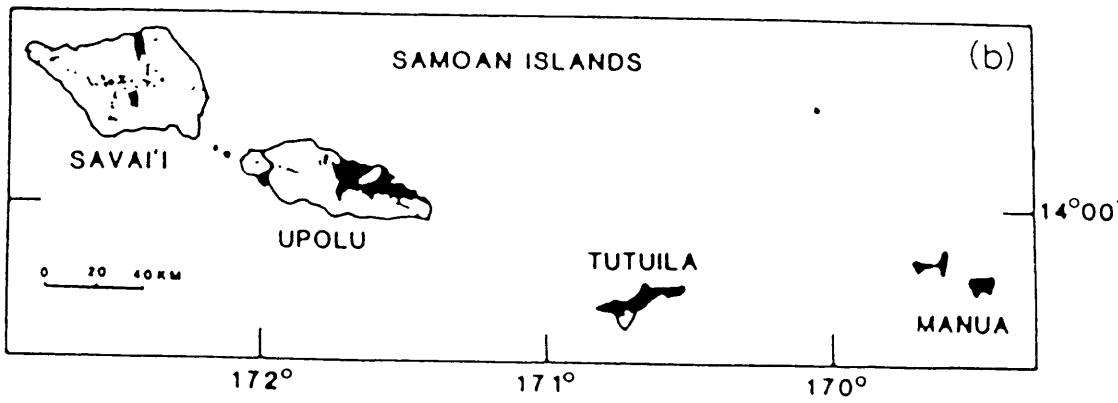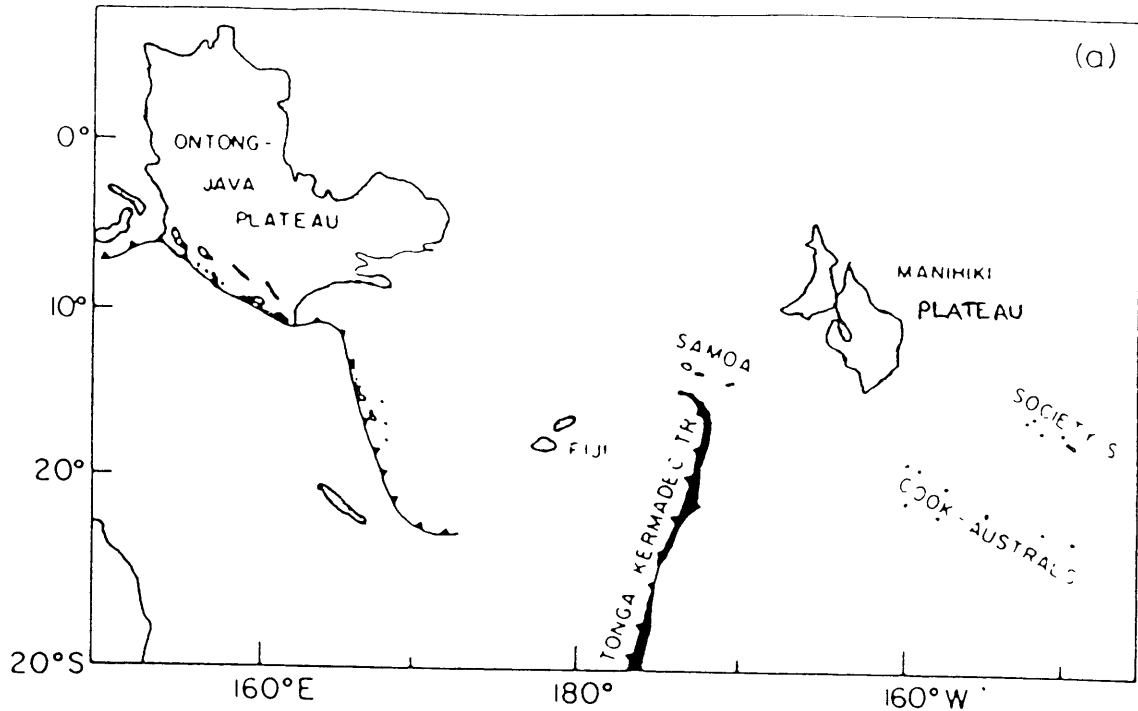
Figure 1. A) Map of the southwest Pacific Ocean showing the location of the Samoa Islands in relation to other hotspot chains (Society, Cook-Australs) and other geologic features. B) Map of the Samoa Islands. Black areas mark exposures of shield basalts, and dots mark the locations of post-shield eruptive centers. Xenoliths were collected from the island of Savaii. After Wright and White (1987).
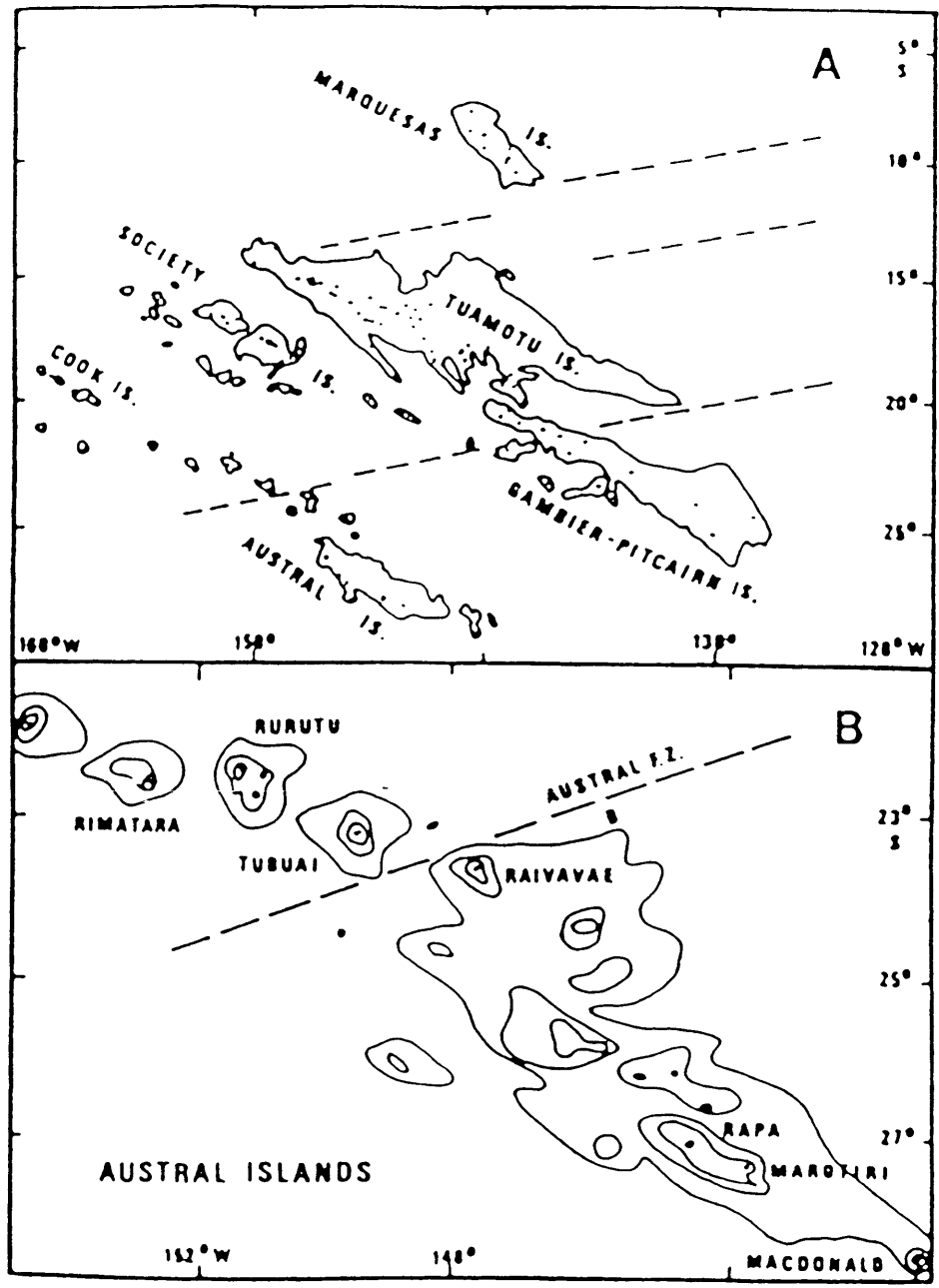
71

Figure 2. A) Map of the south-central Pacific Ocean showing the location of the Austral Islands in relation to other hotspot chains (Marqesas, Tuamotu, Gambier, Society) and other geologic features. B) Map of the Austral Islands. Xenoliths were collected from the island of Tubuai. After Dupuy et al. (1988).

72

and picrite with occasional exposures of phonolitic plugs. The exposure of the western volcano consists of a chain of small hills forming an arcuate structure which may be the remains of a small caldera (Brousse et al., 1980). The exposed rocks are dominantly of a silica-undersaturated basalt (SiO_2=41.35%, Ne_{norm}=29%), which has very high alkali contents (Na_2O=6.22%, K_2O=1.62%) and MgO=7.65% (Mg#=.52), and is referred to as a "mafic phonolite" (Liotard and Barsczus, 1989). Locally, this rock contains abundant olivine xenocrysts and peridotite microxenoliths (up to 1 cm). Larger xenoliths (1-6 cm) were collected from various exposures.

2.2 Textures and Petrography

To this point, a systematic petrographic study of the Savaii and Tubuai xenoliths has not been pursued. As a result, the extent to which the trace element characteristics of individual samples relates to their petrographic identities cannot be ascertained. However, some very broad generalizations are possible based on examination of hand specimens and a limited number of thin sections.

Most of the samples from Savaii were erupted in a tuffaceous flow, and have experienced limited interaction with the host basalt. The xenoliths from Tubuai were collected from massive boulders of basalt; the xenoliths show varying degrees of interaction with the host basalt. Some samples (ex. SAV 1-1, SA 3-11) have small veinlets running through the sample, either as well crystallized basalt or glass, which can be traced to the host basalt. Other samples show incongruent dissolution of pyroxene at the xenolith margins. The xenoliths have also experienced varying degrees of chemical weathering in the tropical environment; however, serpentinization of the xenoliths is minimal (typically less than 1%), and fresh olivine is preserved in all of the samples analyzed here.

The xenoliths from both islands show a range of textures. Several xenoliths with protogranular textures are present (SAV 1-27, SA 3-9, SA 3-11), with large olivine grains up to 5 mm. Most samples display porphyroclastic textures, with orthopyroxenes displaying a range of sizes up to 2-3 mm. In general, the Tubuai samples seem to have a smaller average olivine grain size than the Savaii samples. No consistent correlation of texture with trace element character is apparent, though most samples with depleted REE patterns have protogranular textures.

The xenoliths from Savaii and Tubuai are both characterized by low modal abundance of clinopyroxene, in most cases less than 5%, classifying these samples as harzburgites. One notable exception is TBA 1-9, which is a wehrlite (roughly 40% cpx, 60% olivine). In no case is the distribution of clinopyroxene uniform in these peridotites. Instead, the clinopyroxene is concentrated as small grains into patches or "stringers", often in conjunction with small orthopyroxene crystals. Clinopyroxene color is also slightly

73

variable; LREE-depleted clinopyroxenes are generally a dark green, whereas clinopyroxenes very strongly enriched in the LREE (ex. SAV 1-1, TBA 4-11) are often a light "apple green" color. Often these LREE enriched samples contain olivine which is characterized by extensive systems of annealed cracks, making the olivines appear cloudy-white in hand specimen. These olivines contain inclusions of glass and/or fluid along these annealed cracks. In general, from the examination of hand specimens, the Savaii xenoliths commonly contain substantial modal abundances of orthopyroxene, up to 40% in some clinopyroxene-free samples which have not been examined here. In those samples without clinopyroxene, the orthopyroxenes are commonly of a grey-green color. Some xenoliths from Savaii (SAV 1-3, SAV 1-19, SA 3-11) also contain symplectite intergrowths of spinel+opx±cpx. Symplectites of spinel+opx are also commonly found in the cpx-free xenoliths from Savaii. No symplectites have been found thus far in the Tubuai xenoliths.

3. Analytical Procedures

For some samples, fragments of polished thin sections were gold coated for ion microprobe analysis. For samples without corresponding thin sections, mineral grains were handpicked and mounted in epoxy, polished, and gold coated. This was necessary in those cases where clinopyroxenes or symplectites were not present in the thin sections. Handpicked separates of olivine (SAV 1-1) and clinopyroxene (SAV 1-1, TBA 4-11) were also prepared for isotopic analysis, the methods for which are summarized in Chapter 2.

Trace elements (Sc, Ti, V, Cr, Sr, Zr) and rare earth elements (La, Ce, Nd, Sm, Eu, Dy, Er, Yb) in individual phases were analyzed *in situ* by secondary ionization mass spectrometry (SIMS) using the Cameca IMS 3f ion microprobe at the Woods Hole Oceanographic Institution. For most trace element analyses, a primary beam of O^- ions with a current of approximately 0.2 na was focussed to a spot size of 8-15 mm. For REE analyses, and for Sr and Zr analyses below 1 ppm, a 1-2 na primary beam was used, focussed to a spot size of approximately 20-30 mm. Positive secondary ions were collected and counted by an electron multiplier, and molecular interferences were excluded by energy filtering ($\pm$10V energy window, -90V offset for trace elements, -35V to -60V offset for REE elements, Shimizu and Hart, 1982). Concentrations for clinopyroxenes were determined from empirical working curves using a set of well determined standards. Reproducibility of the trace element concentrations is generally on the order of 10%-30% for the data reported here, with the exception of some low level REE measurements approaching the detection limit, where uncertainties may be as high as 50%. Analyses with estimated errors in excess of 50% are not reported. Each reported analysis in Tables 1 and 2 corresponds to a single grain.

	Sc	Ti	V	Cr	Sr	Zr	La	Ce	Nd	Sm	Eu	Dy	Er	Yb	Group
SAV 1-1 cpx1	126	27.7	234	5510	541	71.6	101.80	190.80	58.10	8.38	1.44	2.63	1.26	0.55	3a
SAV 1-1 cpx2							60.60	134.00	63.80	12.40	2.00	3.23	1 29	0 55	3a
SAV 1-3 cpx2	34.4	28.1	170	5722	1	1	0.29	0.31	0.22	0 13	0.06	0.79	0.88	1.55	2
SAV1-3 cpx1	32.2	33.8	185	7322	2 2	2.3	1.06	1 49	0 45	0.07		0.06	0.04	0 03	2
SAV1-3 cpx (opx-sp1)							0.10	0.11	0.27			0.18	0.23	0.34	2
SAV1-3 cpx (opx-sp2)							0.25	0.14	0 30			0 36	0.50	0 54	1
SAV 1-12 cpx 1	19	4390	219	5181	59.3	27.9	3.57	9.28	6 86			1.84	1.06	0 88	3b
SAV 1-12 cpx2	24	4276	236	5242	35.8	22.7	3.16	7.15	4 64			2.10	1.18	0.92	3b
SAV 1-12 cpx3	29	6104	378	7769	64.1	39.8									3b
SAV 1-13 cpx1	35.6	379	132	4982	86.7	32.2	8.70	20 30	8 86	1.53	0 53	0 94	0.53	0 35	3b
SAV 1-13 cpx2	38.7	281	137	4745	84.4	26.2	9.04	21.80	12.60	3 06	1.04	2.01		0 96	3b
SAV 1-13 cpx4	43 3	59	187	5588	78.5	19.6	7.50	16.40	5 57	0 80	0 21	0.50	0 24	0 22	3b
SAV 1-13 cpx6	27.5	1278	178	5910	61.4	19.9	2.84	7.70	5 16	1 61	0.60	1.71	0.89	0 89	3b
SAV 1-13 cpx7	33.5	48.7	193	7613	72.2	19.2									3b
SAV 1-18 cpx1	36.7	79.8	207	8429	123	3.6	9.36	11.50	1 77	0 17	0 05	0.26		0 33	2
SAV 1-18 cpx2	42.2	76	175	6256	143	2.2	10.80	14.90	2 99	3 76	0 09	0 20		0 30	2
SAV 1-18 cpx3	40.5	135	193	7493	51.9	4	2.41	2.76	0 46	0 09	0 03	0.18	0 18	0 22	2
SAV 1-19 cpx1	48	1557	186	6699	96.5	83.9	3.89	13.30	11 00	2.65	0.76	1.93	1.07	0 84	3b
SAV 1-19 cpx-sp1	30	389.2	154	5474	84.2	35.3	10.80	33.60	21 90	5.69	1.69	3.27	1.83	1.45	3b
SAV 1-19 cpx-sp2	56	2645	226	7703	125.5	104	7.91	26.80	20.50	6.02	1.91	4.03	2.04	1 46	3b
SAV 1-19 cpx2	24.7	435	144	6493	64.1	22.2	8.02	22.30	11.60	2.82	0.79	1 26		0.62	3b
SAV 1-19 cpx3	34.8	738	144	6016	74.3	49	9.49	28.20	20.70	5.33	1.80	3.06		1.49	3b
SAV 1-19 cpx4	25.1	1106	121	5468	96.1	51.1	11.70	35.60	27 00	7.47	2.41	4.61		2.38	3b
SAV 1-19 cpx5	51.6	662	194	6851	116.5	60.7									3b
SA 3-3 cpx2	60	13.8	169	2838	24.5	0.1	8.95	17.60	13.00	3.80	1.37	2.86	1.63	1 19	3a
SA 3-9 cpx1	29.2	25.2	171	7158	0.1	1.8	0.01	0.02	0.01	0.00	0.00	0.01	0.03	0 02	1
SA 3-9 cpx3	30.8	25.9	185	7561	0.1	2.5	0.12	0.09	0.02	0.01	0.00	0.05	0 14	0.33	1
SA 3-9 cpx4	37.3	28.2	157	5889	0.3	2.9	0.64	0.50	0.06	0.02	0.01	0.02	0.03	0.04	1
SA 3-11 cpx1	30	10.9	158	4547	0.1	1.9	0.71	0.77	0.08	0.01	0.00	0.01	0.02	0.03	2
SA 3-11 cpx2	21.6	10.1	136	4207	0.1	2	0.56	0.68	0.13	0.02	0.01	0.01	0.02	0.04	1
SA 3-11 cpx3	31.3	9.3	132	3908		0.7	0.00	0.01	0.01			0.01	0.02	0.05	1
SA 3-11 cpx4	29.8	8.4	136	3864	0.1	1.1									2
SA 3-11 cpx-sp1	37.2	16.3	131	3354	0.7	22.4	1.61	2.03	0 21	0.03		0.01	0.04	0 08	2
SA 3-11 cpx-sp2	21.1	26.2	119	2679	0.5	15.2									2
SAV 3-1 cpx1	31.5	20.7	151	6012	18.8	3.4	1 59	2 18	0 47	0 08	0 02	0 06	0 06	0 07	2
SAV 3-1 cpx2	22.6	18.7	137	5330	2.9	3.3	3.06	3.57	0 64	0.09		0.06	0 12	0 14	2
SAV 3-1 cpx3	25.6	104	140	5201	39.4	8 9	6.48	15 90	6 84	1.09	0 28	0 61	0 26	0 20	3b
SAV 3-1 cpx4	31.7	17.5	146	5679	14 5	5	3.71	5.54	1 28	0.20	0.08	0 16		0 14	3b
SAV 3-2 cpx1	33.2	95.5	163	5447	0 1	4 2	0.02	0 04	0 02			0 10	0 24	0 38	1
SAV 3-2 cpx4	34.5	106	185	6361	0 1	3.8	0.36	0 18	0 10		0 02	0.12	0.19	0 30	2
SAV 3-3 cpx1	28	5243	238	8649	37.7	36.6	1.59	5.84	6 37	2.69	0.95	2.46	1.38	1.23	3b
SAV 3-3 cpx4	22.5	3565	209	9644	29.7	21.8	1.11	3.83	4.19	1.81	0.63	1.51	0.76	0 79	3b
SAV 3-3 cpx5	23.4	3696	197	8103	40	29.2	3.22	8.91	6.89	2.67		2.37	1.33	1.27	3b

	Sc	Ti	V	Cr	Sr	Zr	La	Ce	Nd	Sm	Eu	Dy	Er	Yb	Group
SAV 1-27 cpx1	42.9	66.8	191	7183	0 1	5.1	0.00		0 03			0.11	0.22	0 47	1
SAV 1-27 cpx2	48.6	66.4	158	5468	0 2	1 6			0 05	0.15		0 68	0 94	2 07	1
SAV 1-27 cpx2									0 02			0 07	0 11	0 22	1
SAV 1-27 cpx3	40.7	66.8	164	5812	0 1	1 8			0 01			0 08	0.15	0 24	1
SAV 1-28 cpx1	45.4	687	181	6012	331 4	75 4	64 30	201 00	111 00	23 00	5 73	9 97		3 99	3b
SAV 1-28 cpx2							75.20	232.00	125 00	25.10	5 93	9.93		3 78	3b
SAV 1-28 cpx3	28.3	44 6	165	5688	66 3	4.1	22.00	37 80	7.51	0 80	0.18	0.29		0 23	2
SAV 1-28 cpx4	27.3	39.2	161	6009	78.7	2.8	31.70	64 90	15 10	1 73	0.48	0 64		0 31	2
SAV 1-30 cpx1	35.3	61.2	165	5972	119	16.7	5 72	9.48	1 64	0.19	0.05	0.05	0 10	0.10	2
SAV 1-30 cpx2	24.9	48.8	156	5948	79.9	22 3	6.59	11.70	2 49	0 25	0 08	0 19	0 15	0 16	2
SAV 1-30 cpx3	33	48.1	163	5931	133 8	4	9 34	24 30	9 03	1 29	0 41	0 52		0 37	2
SAV 1-36 cpx1	32 9	623	152	6665	56 2	22 7	3 18	10 50	7 56	1 74	0 60	1 30		0 69	3b
SAV 1-36 cpx4	37.3	2340	193	7625	88 1	64 4	4 50	15 80	14 10	4 58	1 44	3 25	1 53	1 43	3b
SAV 1-36 cpx5	34.4	5355	212	6479	83 7	86 1	3.60	13 70	12 10	3 59	-1 02	2 36	1 46	1 07	3b
SAV 1-41 cpx1	33.3	207.4	154	5844	35 7	4 8	7 49	16 70	8 38	2 08	0 07	1 20	0 91	0 57	2
SAV 1-41 cpx2	47.4	739.9	222	9139	83 2	34.5	7 05	14 30	6 55	1 40	0 46	0 68		0 42	2
SAV 1-41 cpx6	54 6	121.5	182	5801	60 5	9 2									2
SAV 1-41 cpx7	44.5	365	168	4912	62 9	19 4	6 92	14 10	6 06	1 23	0 41	0 56		0 31	2
SAV 1-42 cpx1	46	36.6	180	3079	321	3 4	26.50	32.60	4 56	0 35	0.10	0 18		0 23	2
SAV 1-42 cpx2	29.1	39.3	130	2276	255	4	10 80	11.20	1 18	0 09	0 04	0 05	0 13	0 14	2
SAV 1-42 cpx3	34.3	33 5	144	5726	17 1	2 7	2 70	1 90	0 14	0 04		0 04	0 08	0 18	2
SAV 1-42 cpx4	31 1	27.4	133	2795	123 1	1.5	1 54	0 82	0 06			0 03	0 07	0 15	2
SAV 1-42 cpx5	32.8	33.4	149	6642	14 2	2 8									2
SAV 1-46 cpx1	24 3	51.1	134	5309	1 6	1 2	0.11	0 05	0 01			0 09	0 18	0 53	1
SAV 1-46 cpx2	35.9	54.4	166	6434	38 2	4.6	22 50	30 30	6 29	0 86	0 28	0 36		0 32	2
SAV 1-46 cpx3	23	35.4	131	5217	0.9	0 6	10 50	10 10	1 81	0 20	0 06	0 11	0 21	0 21	2
SAV 1-46 cpx4	42.5	245.5	156	5381	77 4	15.9	78 10	118 00	24 00	3 45	1.24	1 91		1 09	2
SAV 1-46 cpx5	26 4	38.4	135	5383	5	0 9	8.08	7 40	0 90	0 13	0 02	0 09	0 14	0 18	2
SAV 1-46 cpx6	30 3	171 5	148	5945	31 3	3 5	18 80	33 10	7 99	1 01	0 33	0 45		0 36	2
SAV 1-47 cpx1							40.30	120 00	72 20	16 70	4 34	8 53		3 16	3b
SAV 1-47 cpx3	60	3842	239	7717	175	301	18.50	60 20	39 80	10 70	2.91	5.78	3 10	1 98	3b
SAV 1-47 cpx4	58 5	5544	258	7555	184	305									3b
SAV 1-47 cpx6							37 81	110.10	65 90	14 90	4.24	7 50	4 63	2 57	3b
SAV 1-50 cpx1	36.5	1978	192	6457	87	78	11 60	23 80	11 50	2 95	0.91	2 05		1 14	2
SAV 1-50 cpx2	46.3	3004	220	6585	61 1	54.8	2.58	7 75	5 55	1 65	0.34	1 36	0 64	0 55	2
SAV 1-50 cpx3	44	4253	253	7563	62 8	55 9	5 24	10 20	3 45	0 66	0 18	0 40		0 28	2
SAV 1-50 cpx4	29 8	4269	205	4403	152	113	8 91	19 70	8 09	1.73	0.46	0 89		0 31	2
SAV 1-50 cpx5	30 7	1052	183	6218	88 4	77 5	6 82	15 50	6 74	1 66	0 45	0.94		0 48	2
SAV 1-50 cpx6	33 3	2056	197	6253	75 3	39 6	5 15	9 65	3 09	0 59	0 14	0.23		0 17	2

Table 1. Trace element data (ppm) for clinopyroxenes from Savaii xenoliths. Column labelled "Group" refers to the classification described in the text
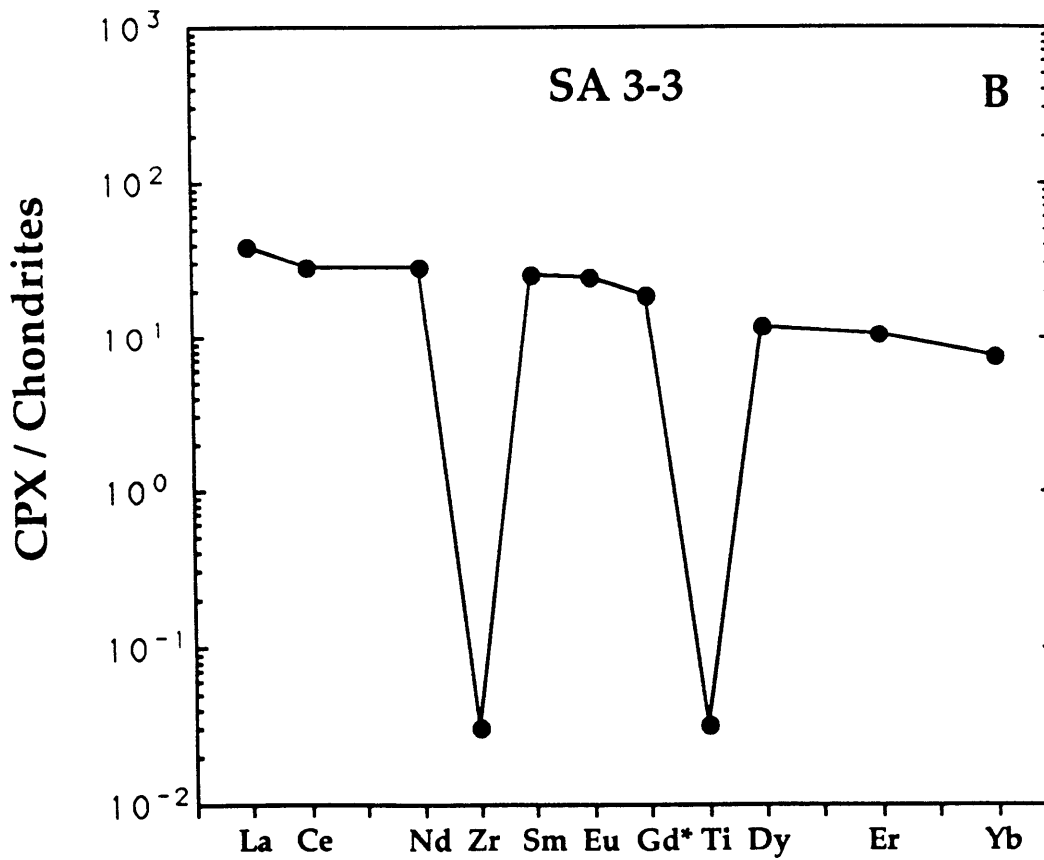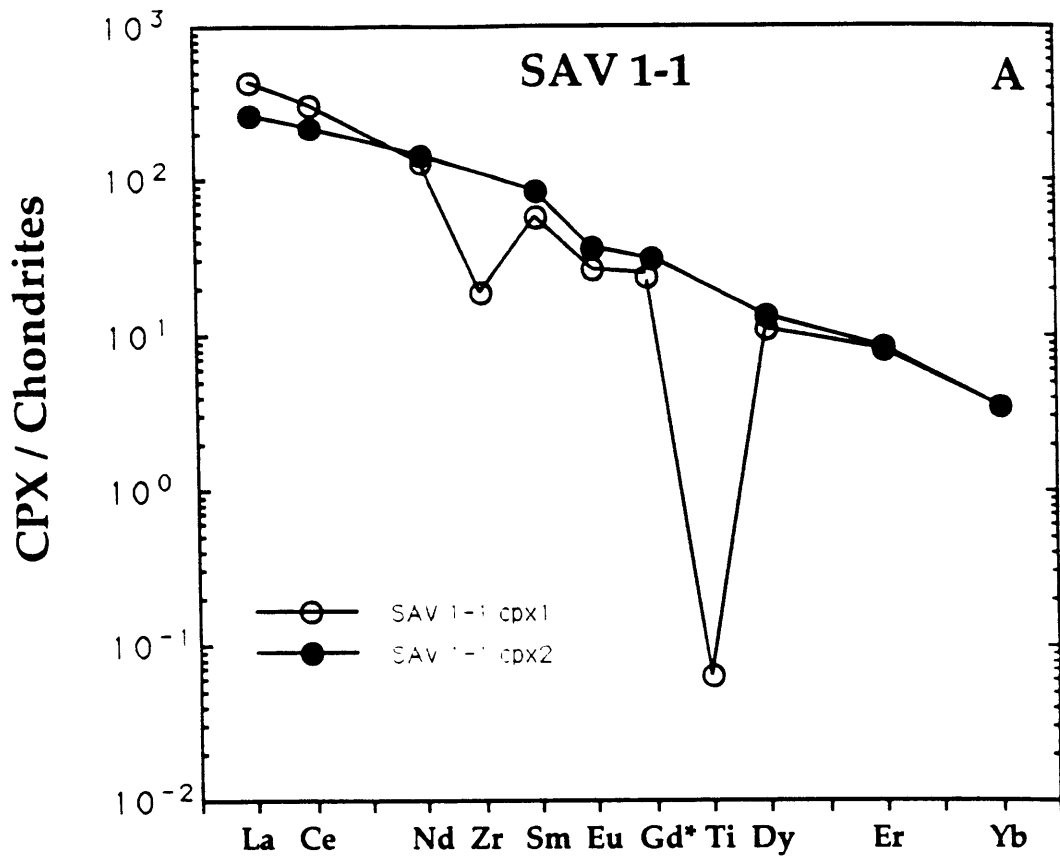
	Sc	Ti	V	Cr	Sr	Zr	La	Ce	Nd	Sm	Eu	Dy	Er	Yb	Group
TBA 1-7 cpx	90	247	255	7183	1 11	0 897	0 01	0 02	0 02	0 03	0.02	0 46	0 49	0 64	1
TBA 1-9 cpx	105	593	402	22814	980	42 5	56.39	121.80	54.10	11.65	3 79	6 66	4 81	2 99	3a
TBA 2-1 cpx1	49	146	250	7586	1 51	1 89	0.11	0 10	0 10	0 02	0.02	0 18	0 23	0 30	2
TBA 2-1 cpx2	40	136	235	7027	2 02	0 588	1.13	2 34	0 91	0 27	0 09	0.22	0 17	0 17	2
TBA 4-4 cpx1	45	576	228	6175	39	1.53	16.80	17.80	1 95	0.20	0.12	1.07	0 81	0 88	2
TBA 4-4 cpx2	74	225	242	5436	158	15.5	21.04	33 00	6 40	0 86	0.28	0.67	0.48	0 57	2
TBA 4-4 cpx3	73	404	190	6731	1 11	1.32	0 03	0 07	0 08	0 08	0 07	0 56	0.56	0 65	1
TBA 4-5 cpx1	18	876	178	4228	220	7 1	14.30	19.70	5 55	0 73		0 77		0 42	2
TBA 4-5 cpx2	40	431	237	7509	218	3 36	6.36	14.70	5 99	0 88		0 75		0 54	2
TBA 4-5 cpx3	64	430	243	7848	3 75	1 68	2 17	2 07	0 29	0 13	0 08	1 08	0 82	0 87	1
TBA 4-6 cpx1	58	719	213	3058	13 7	4 84	0 32	0 83	0 79	0 35	0 18	1 21	1.00	0 96	1
TBA 4-6 cpx2	51	766	210	3081	13 8	6 21	0.14	0 50	0 54	0 15	0 12	0 94	0 78	0 74	1
TBA 4-6 cpx4	53	850	228	5077	14 9	10.7	0 25	0 86	0 78	0 26	0.17	1.36	1.11	1 13	1
TBA 4-7 cpx1	46	186	218	5335	10 2	0 546	0.89	1.83	0 76	0 12	0 05	0 25	0 24	0 25	2
TBA 4-7 cpx2	49	169	223	5199	1 86	0 757									2
TBA 4-8 cpx1	29	418	167	2614	1 45	0 869	0 09	0 08	0 01	0 08	0 04	0 50	0 43	0 45	1
TBA 4-8 cpx2	40	521	183	2975	2 12	0.462	0.08	0.04	0.03	0 07	0.05	0.64	0.48	0 64	1
TBA 4-11 cpx1	63	251	211	6226	504	150	28.06	89.30	50 00	13 30	3 97	9 84	5 29	4.52	3b
TBA 4-11 cpx1	69	384	175	6292	347	130	25.60	83.10	60 80	16 40	5.45	10 20	5 02	4 16	3b
TBA 4-11 cpx2	74	303	232	5848	571	129	43.40	137 00	88 20	21 40	6.94	13 60	6.66	5 63	3a
TBA 4-11 cpx3	74	193	261	6530	638	144	80.13	238 00	127 00	29 30	9.35	18.30	10.00	8 40	3b
TBA 4-11 cpx4	60	377	195	7070	383	148	121.40	299 00	136 00	28 20	9.04	17.30	9.86	8 14	3b
TBA 5-1 cpx1	40	173	210	6073	0 761	1.22	0 00	0 01	0 01	0 03	0 01	0 22	0 25	0 35	1
TBA 5-1 cpx2	40	178	196	5506	4 64	1.09	0 01	0.01	0 01	0 04	0 03	0.34	0 46	0 57	1
TBA 5-1 cpx4	51	195	226	6416	0 697	2.91									1
TBA 5-2 cpx1	13	257	605	7485	2 4	7	0 35	0 82	0 25	0 13	0 10	1 06	1.10	1 33	1
TBA 5-2 cpx2	56	972	242	6375	6 68	27	0 51	1 99	1 70	0 59	0 25	1.22	0 79	0 83	1
TBA 5-2 cpx3	41	247	215	5639	0 56	1 84	0.19	0 44	0 26	0 14	0.07	0.74	0 83	0 92	1
TBA 5-4 cpx1	67	829	340	12474	13 9	58 9	125.00	324.00	153 00	32 20	10.18	18.50	9.85	8 02	3b
TBA 5-4 cpx2	91	93	335	11714	14 30	41 2	184.00	287.00	70 60	12 00	3.75	7.98	4.69	4 19	3a
TBA 5-4 cpx3	21	4595	307	3684	906	243 2	115 00	281.00	132 00	28 60	9.52	16.70	12.60	7 85	3b
TBA 5-5 cpx1	33	477	205	6997	18 5	5 5	0 02	0 07	0 03	0 04	0.03	0 05	0 12	0 19	1
TBA 5-5 cpx2	26	319	250	1578	300	5 9	18 50	25.50	5 38	0 87	0.29	0 65	0 38	0 37	2
TBA 5-5 cpx3	48	345	268	12494	318	2 4	16 00	29.10	8 99	1 50		0 92		0 50	2

Table 2. Trace element data for clinopyroxenes from Tubuai peridotite xenoliths. Column "Group" refers to classification described in the text.

	$^{87}Sr/^{86}Sr$	$^{143}Nd/^{144}Nd$	$^{206}Pb/^{204}Pb$	$^{207}Pb/^{204}Pb$	$^{208}Pb/^{204}Pb$	$^{187}Os/^{186}Os$	U (ppb)	Th(PPb)	Pb(ppb)
SAV 1-1 olivine	.712344	.512422	18.849	15.669	39.845	1.0717	228	782	629
SAV 1-1 cpx	.712838	.512516	18.845	15.660	39.806		788	2790	2444
SAV 1-27 WR						1.0179			
TBA 4-11 cpx	.702755	.512942	20.971	15.748	40.228	1.0725			358
TBA 1-7 WR						1.0884			

Table 3. Isotopic Data for Savaii and Tubuai xenoliths. Uncertainties are $\pm$ 0.004% on $^{87}Sr/^{86}Sr$ and $^{143}Nd/^{144}Nd$, 0.3% on $^{187}Os/^{186}Os$, and 0.1%/amu on Pb isotope ratios. Uncertainties for U-Th-Pb concentrations is estimated at 1-3%.
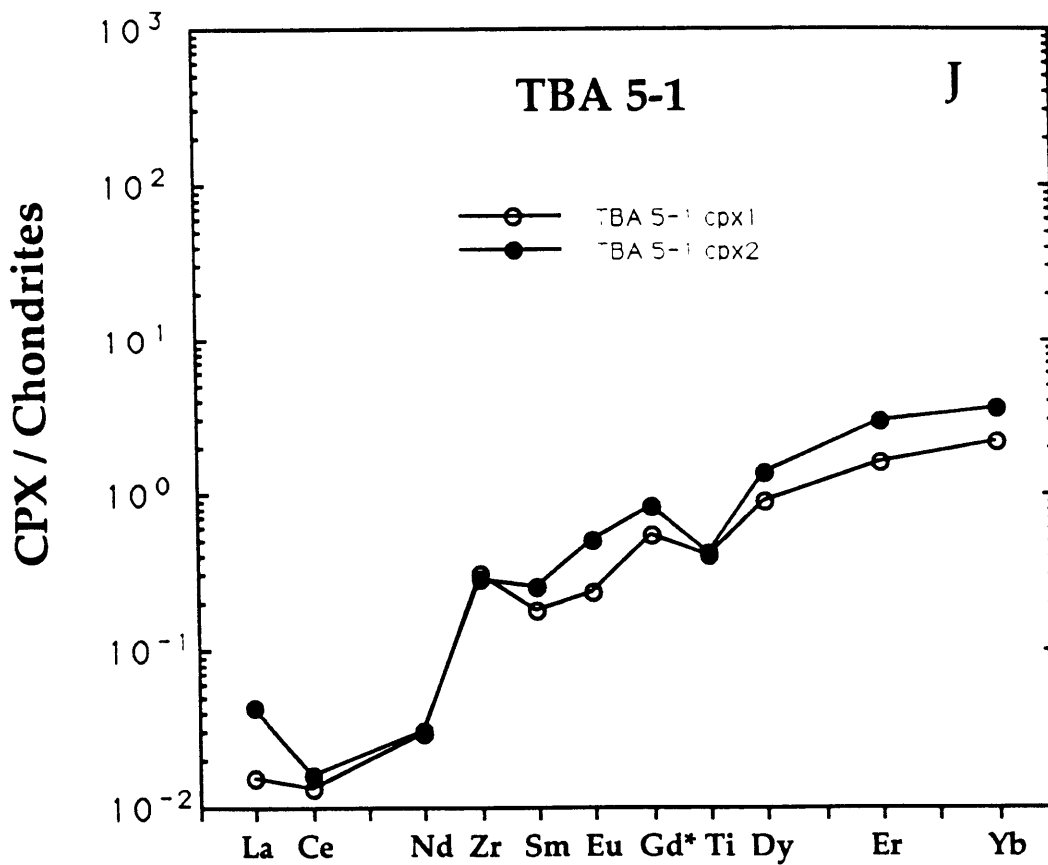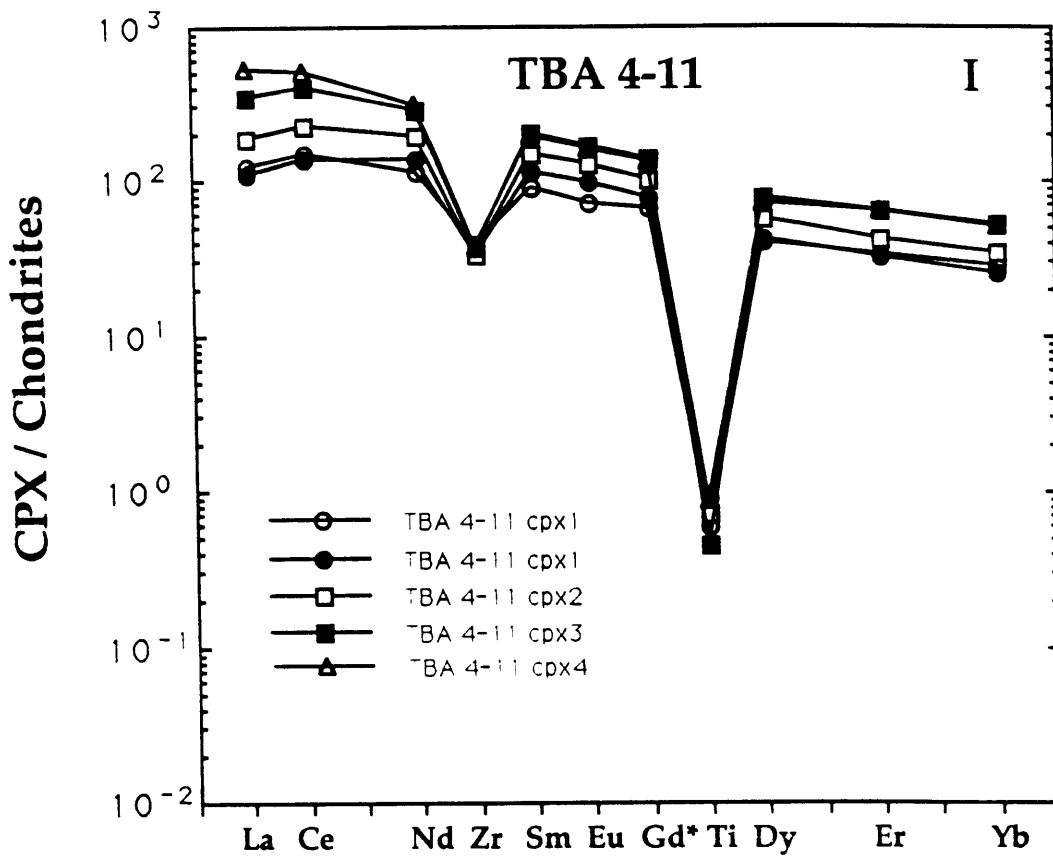
Figure 3 (a-s). Chondrite normalized trace element data for clinopyroxenes in peridotite xenoliths from the island of Savaii, Western Samoa. Each trace element pattern represents the analysis of a single grain. Data are normalized using the chondrite data of Anders and Grevesse (1989).

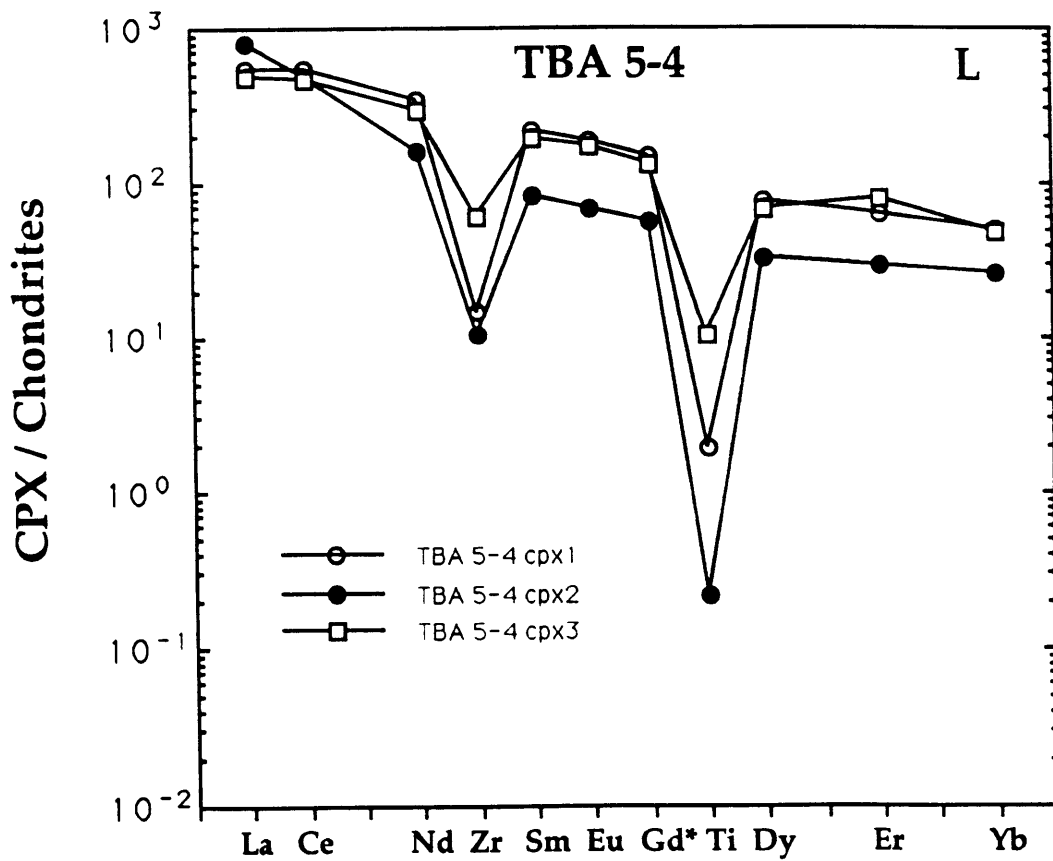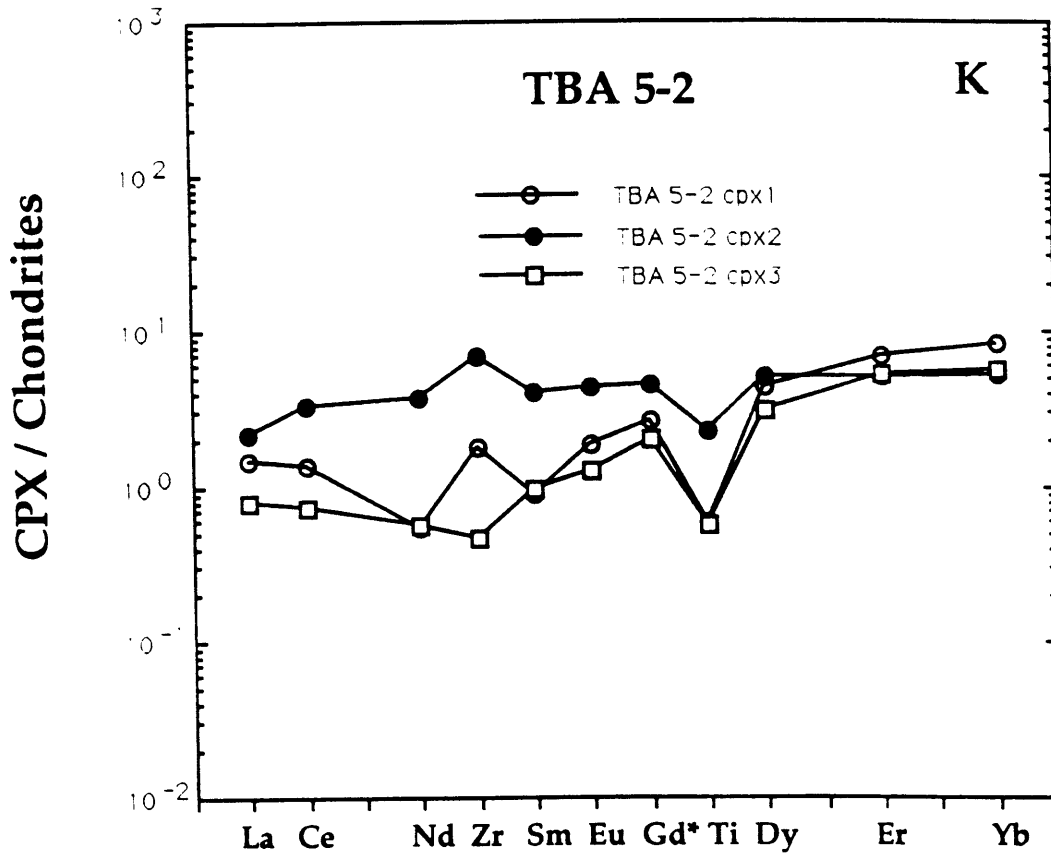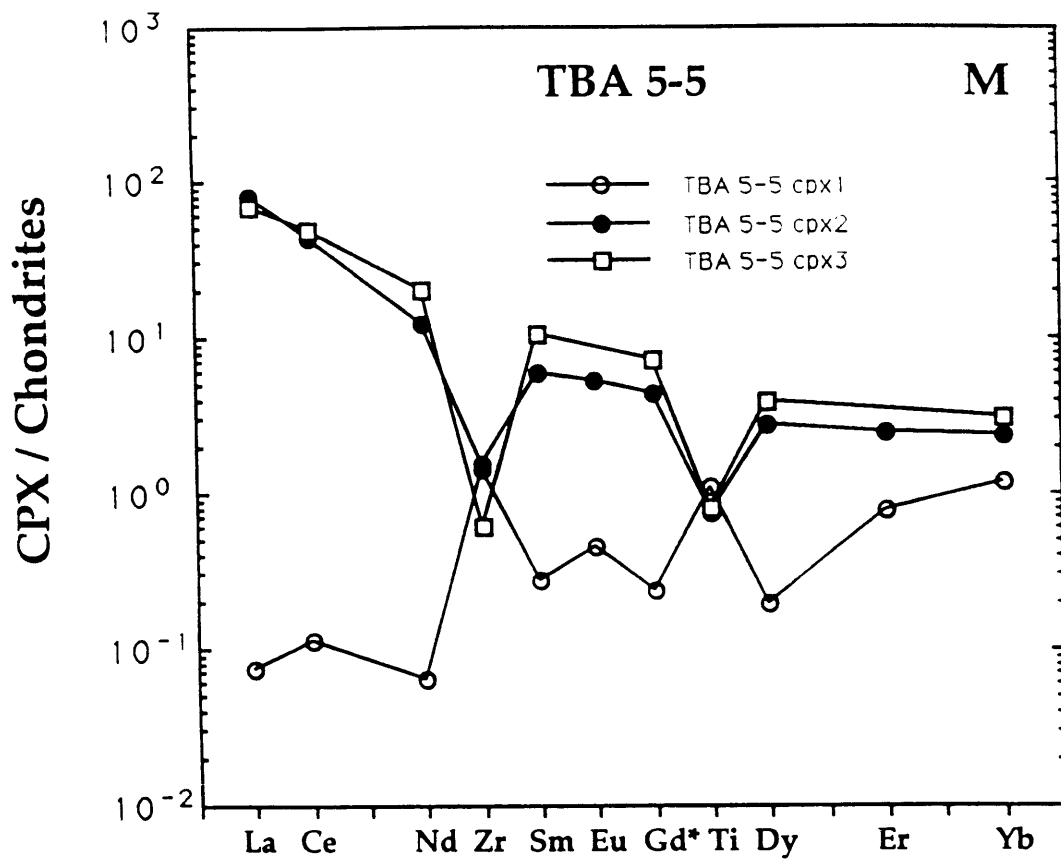SAV 1-13   E

CPX / Chondrites

SAV 1-13 cpx1
SAV 1-13 cpx2
SAV 1-13 cpx4
SAV 1-13 cpx6

La Ce   Nd Zr Sm Eu Gd* Ti Dy   Er   Yb

SAV 1-18   F

CPX / Chondrites

SAV 1-18 cpx1
SAV 1-18 cpx2
SAV 1-18 cpx3

La Ce   Nd Zr Sm Eu Gd* Ti Dy   Er   Yb

SAV 1-19

G

SAV 1-19 cpx-sp1
SAV 1-19 cpx-sp2
SAV 1-19 cpx1
SAV 1-19 cpx2
SAV 1-19 cpx3
SAV 1-19 cpx4

SAV 1-27

H

SAV 1-27 cpx1
SAV 1-27 cpx2
SAV 1-27 cpx3

8 3

SAV 1-28

I

SAV 1-28 cpx1
SAV 1-28 cpx2
SAV 1-28 cpx3
SAV 1-28 cpx4

SAV 1-30

J

SAV 1-30 cpx1
SAV 1-30 cpx2
SAV 1-30 cpx3

SAV 1-36

CPX / Chondrites

K

SAV 1-36 cpx1
SAV 1-36 cpx4
SAV 1-36 cpx5

La Ce Nd Zr Sm Eu Gd* Ti Dy Er Yb

SAV 1-41

CPX / Chondrites

L

SAV 1-41 cpx1
SAV 1-41 cpx2
SAV 1-41 cpx6
SAV 1-41 cpx7

La Ce Nd Zr Sm Eu Gd* Ti Dy Er Yb

SAV 1-47 O

SAV 1-47 cpx1
SAV 1-47 cpx3
SAV 1-47 cpx4
SAV 1-47 cpx6

La Ce Nd Zr Sm Eu Gd* Ti Dy Er Yb

SAV 1-50 P

SAV 1-50 cpx1
SAV 1-50 cpx2
SAV 1-50 cpx3
SAV 1-50 cpx4
SAV 1-50 cpx5
SAV 1-50 cpx6

La Ce Nd Zr Sm Eu Gd* Ti Dy Er Yb

SAV 3-1 Q

SAV 3-1 cpx1
SAV 3-1 cpx2
SAV 3-1 cpx3
SAV 3-1 cpx4

SAV 3-2 R

SAV 3-2 cpx1
SAV 3-2 cpx4

Figure 4 (a-m). Chondrite normalized trace element data for clinopyroxenes in peridotite xenoliths from the island of Tubuai, Austral Islands chain. Each trace element pattern represents the analysis of a single grain. Data are normalized using the chondrite data of Anders and Grevesse (1989).

TBA 2-1 C

TBA 2-1 cpx1
TBA 2-1 cpx2

CPX / Chondrites

La Ce Nd Zr Sm Eu Gd* Ti Dy Er Yb

TBA 4-4 D

TBA 4-4 cpx1
TBA 4-4 cpx2
TBA 4-4 cpx3

CPX / Chondrites

La Ce Nd Zr Sm Eu Gd* Ti Dy Er Yb

TBA 4-5 E

- ○—— TBA 4-5 cpx1
- ●—— TBA 4-5 cpx2
- □—— TBA 4-5 cpx3

CPX / Chondrites

La Ce Nd Zr Sm Eu Gd* Ti Dy Er Yb

TBA 4-6 F

- ○—— TBA 4-6 cpx1
- ●—— TBA 4-6 cpx2
- □—— TBA 4-6 cpx4

CPX / Chondrites

La Ce Nd Zr Sm Eu Gd* Ti Dy Er Yb

TBA 4-7 G

TBA 4-8 H

○ TBA 4-8 cpx1
● TBA 4-8 cpx2

94

TBA 5-2   K

TBA 5-4   L

TBA 5-5   M

- ○ TBA 5-5 cpx1
- ● TBA 5-5 cpx2
- □ TBA 5-5 cpx3

CPX / Chondrites

La Ce Nd Zr Sm Eu Gd* Ti Dy Er Yb
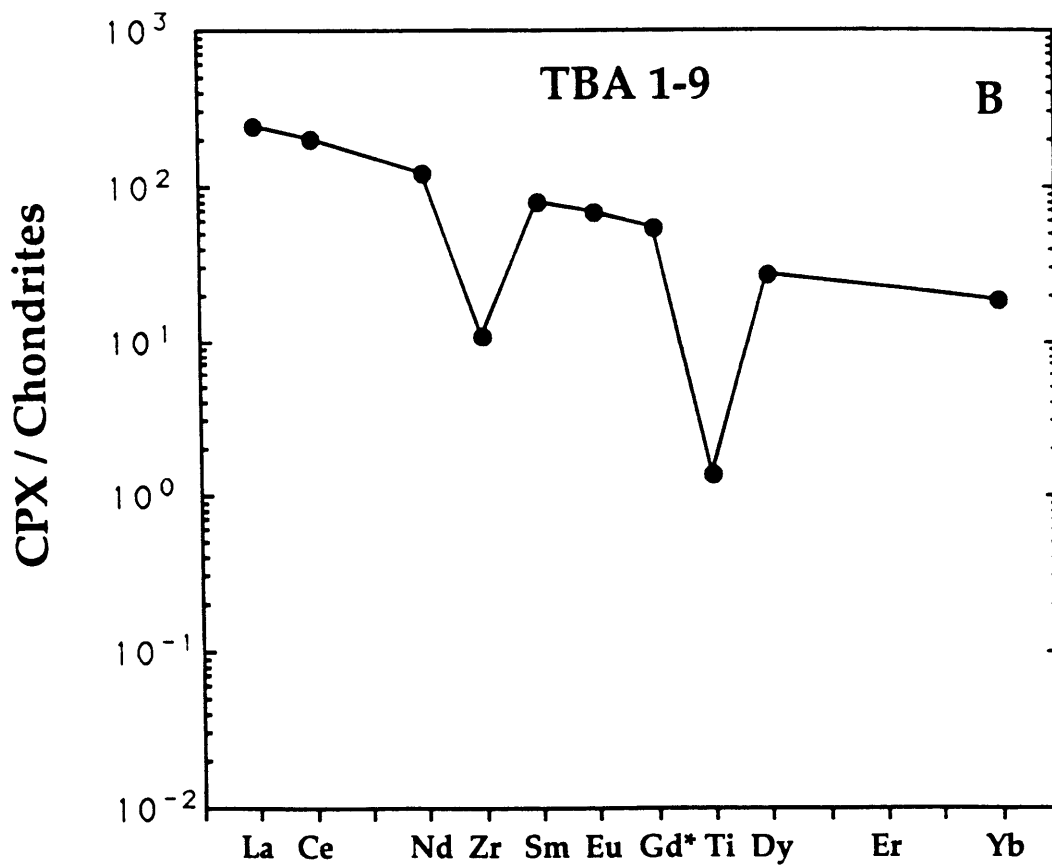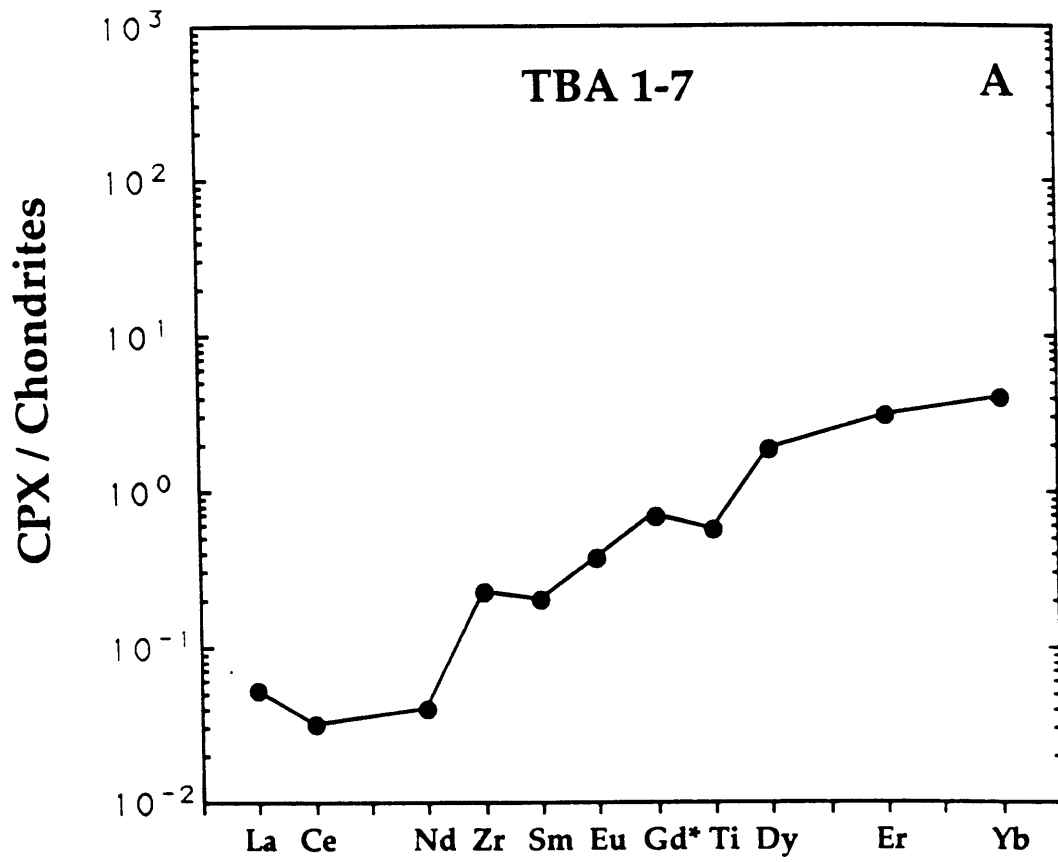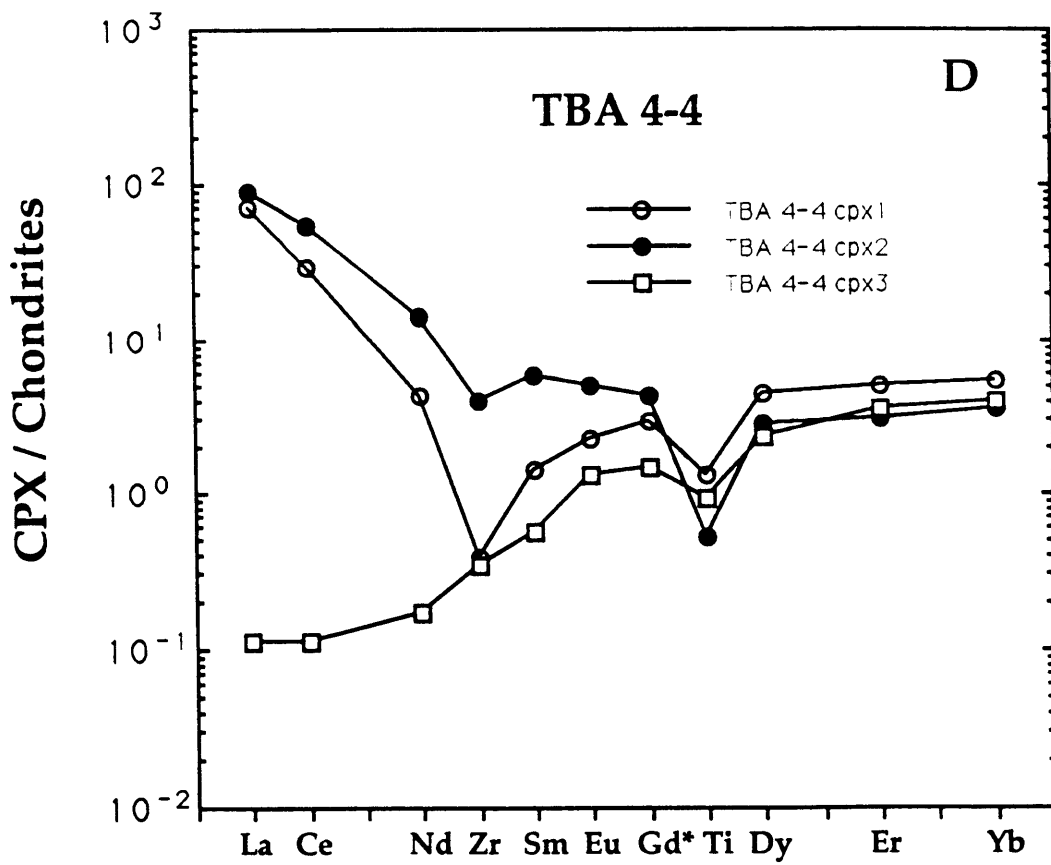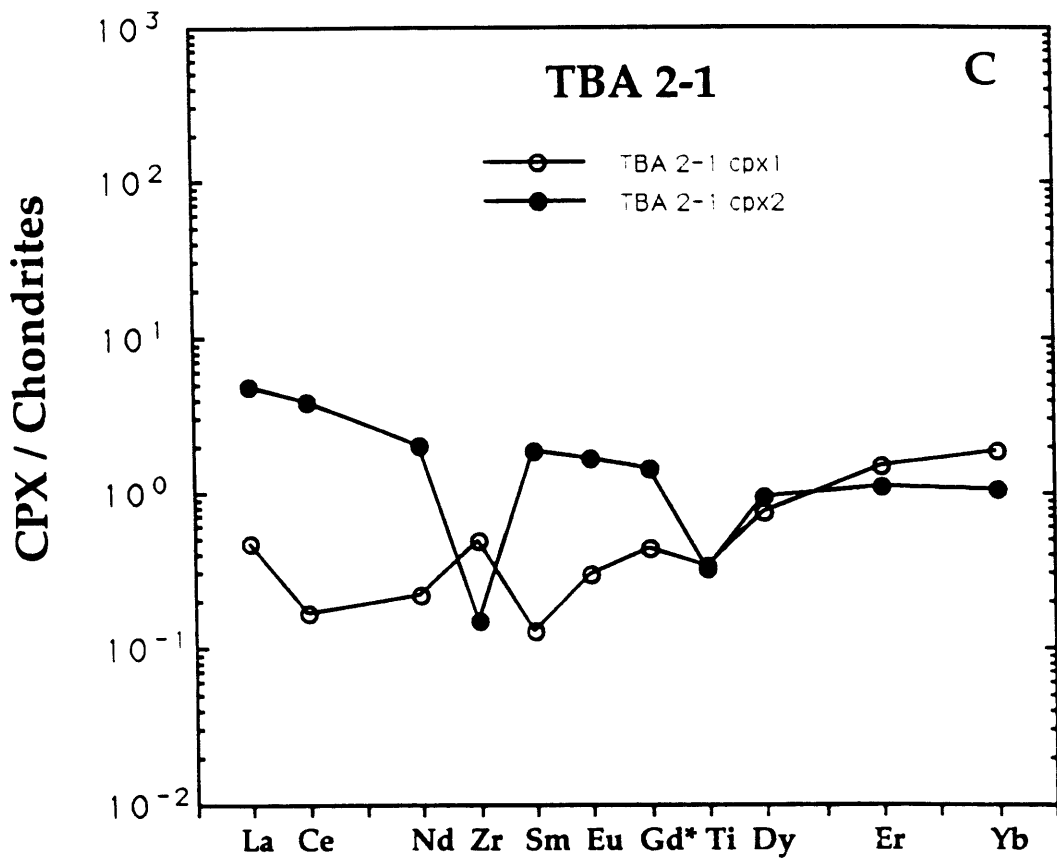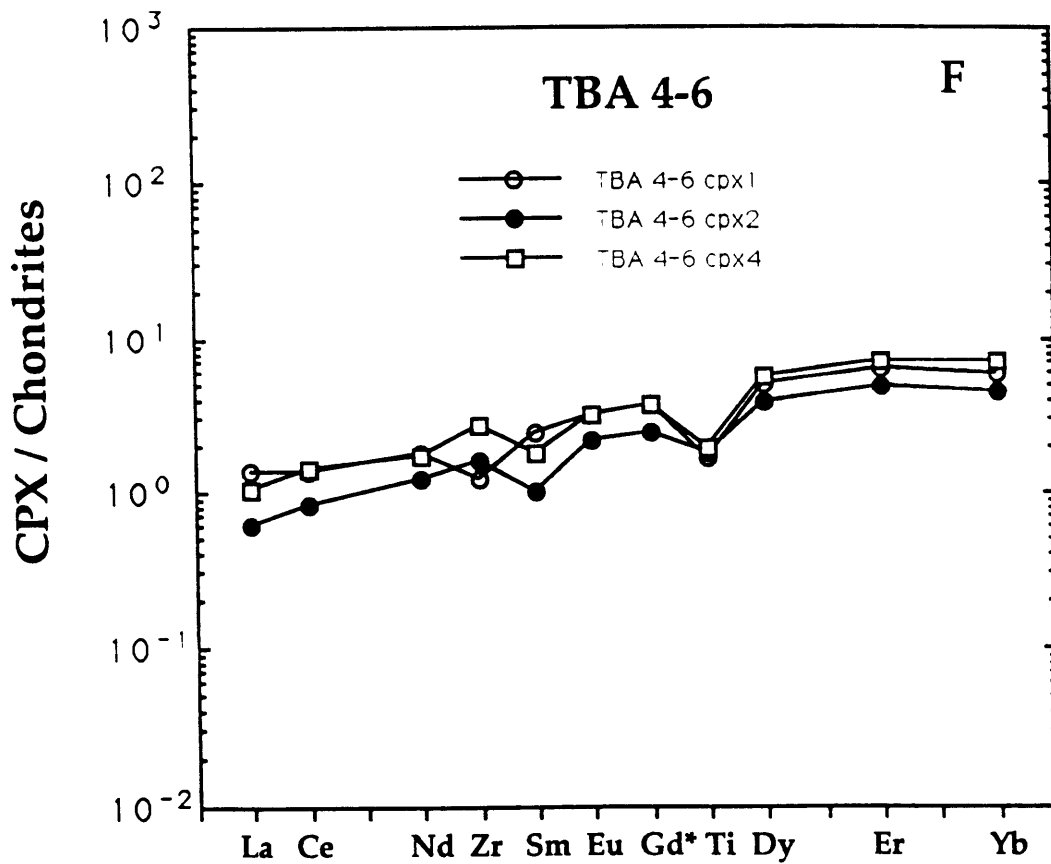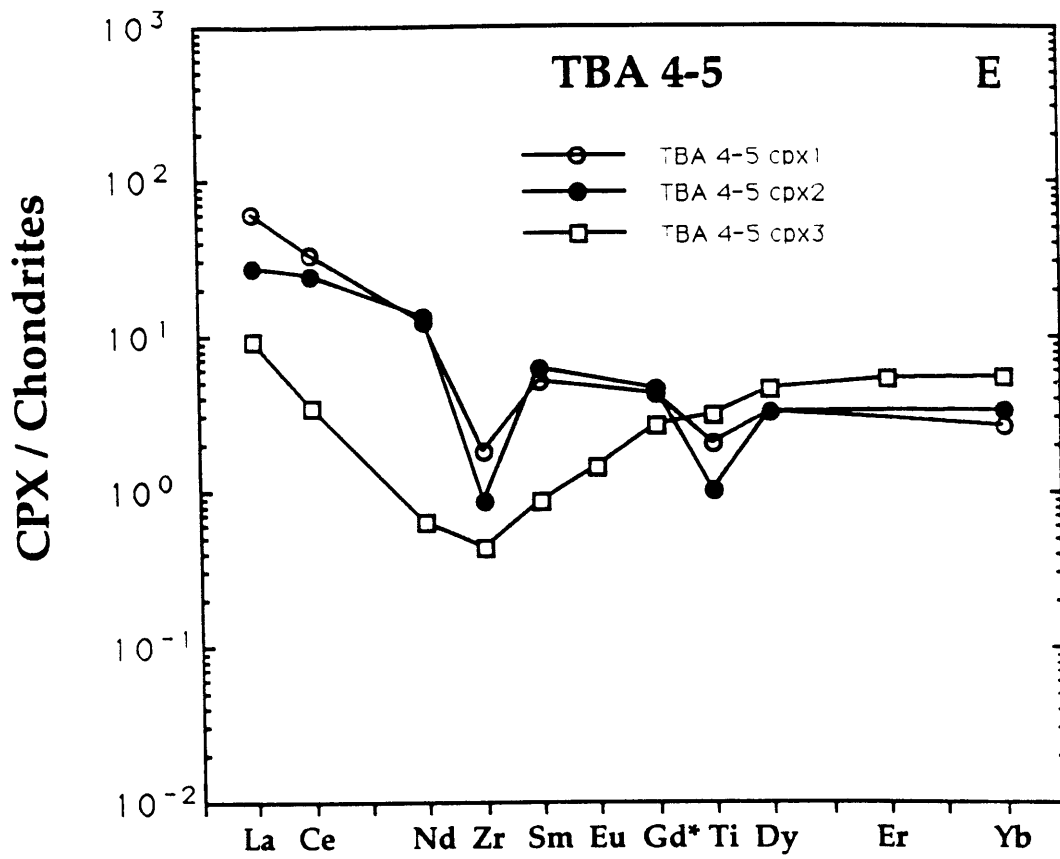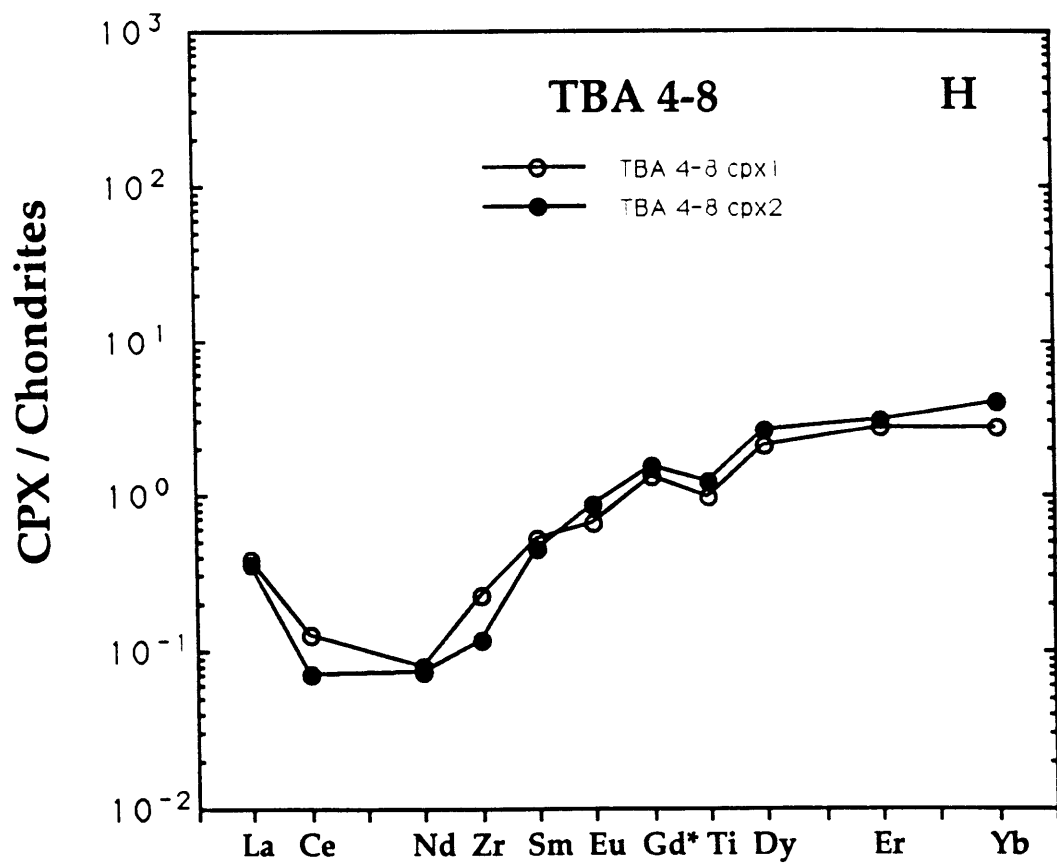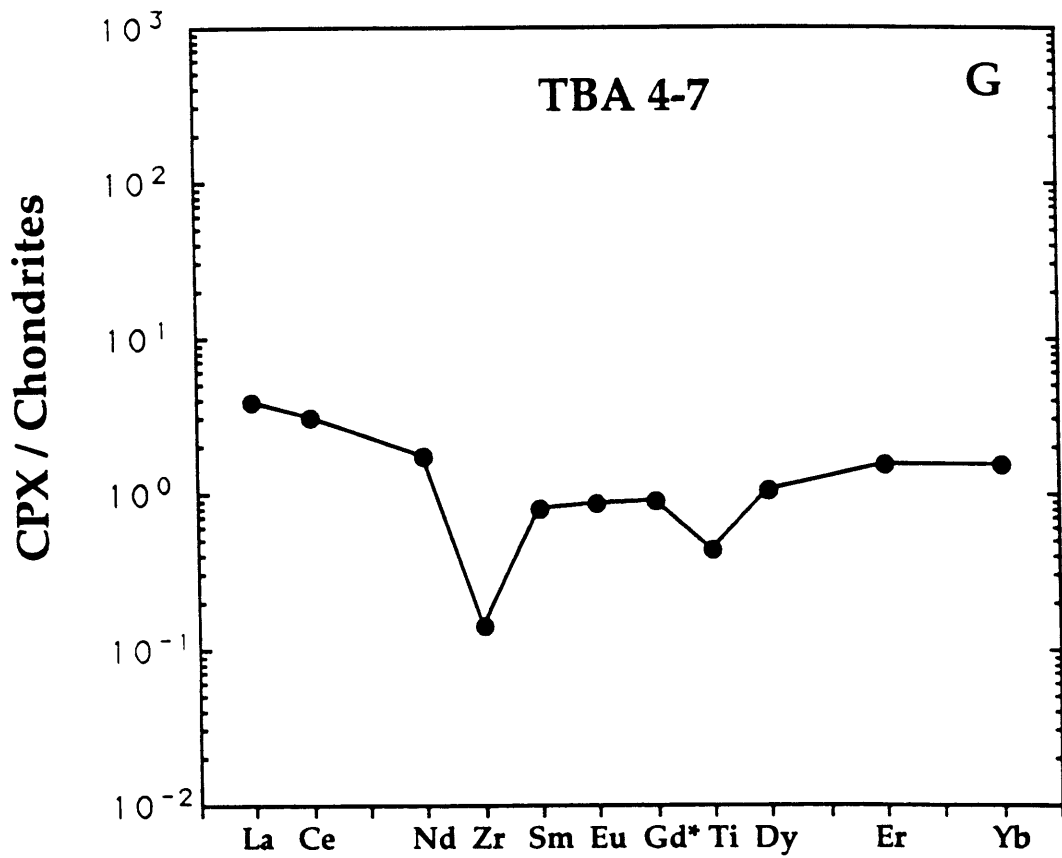
During REE analyses, it was common to measure large positive anomalies in Eu and smaller positive anomalies in Er. This is caused by the interference of barium oxides on the masses of interest ($^{135}Ba^{16}O$ on ^{151}Eu; $^{135}Ba^{16}O_2$ on ^{167}Er), which cannot be eliminated by energy filtering at -60V offset. The presence of Ba during the REE analysis of clinopyroxenes is correlated with cracks and cloudy areas in the mineral grains, and is not present (above about 1 ppm Ba) in clear, inclusion free areas. The Ba oxide interferences were eliminated by either moving to a different spot on the grain or employing the REE program with Ba oxide correction (on Eu only) during analysis. As a result, for some analyses, Eu and/or Er may have larger errors, or may be eliminated from the reported data.

4. Results

Trace element data for the Savaii xenoliths is given in Table 1 and plotted in Figure 1a-s; data for Tubuai xenolith clinopyroxenes is given in Table 2 and plotted in Figure 2a-m. The value for Gd* is interpolated between Sm and Dy to produce a smooth pattern, and is included to clarify possible anomalies in Eu and Ti concentrations. There is a large degree of heterogeneity present within the sample suite, as well as within individual samples (ex. SAV 1-41, SAV 1-46). The trace element patterns are characterized by varying degrees of LREE enrichment, with very few LREE depleted patterns. Sr seems to vary coherently with the LREE La, Ce, and Nd (Table 1); however, Ti and Zr show varying degrees of depletion with respect to the REE (Fig. 1). In general, the patterns appear to show varying amounts of LREE enrichment starting from LREE depleted patterns. The clinopyroxene analyses are classified into three groups based on REE pattern (Table 1):

Group 1: (examples SAV 1-27, TBA 1-7) clinopyroxenes with depleted REE patterns, or with only slight enrichment in La, Ce and Nd. These patterns are characterized by Yb(N) typically 1-3 (suffix (N) means chondrite normalized concentration), <1 ppm Sr, <4 ppm Zr, <100 ppm Ti, and low Ti/Zr ratios. This group of samples is also characterized by positive Zr and negative Ti anomalies relative to the REE on chondrite normalized trace element diagrams (FIG); this trace element pattern is parallel to that of mantle derived garnets, but shifted to lower absolute concentrations. REE and Ti concentrations are systematically lower than in abyssal peridotites (REF), however Zr and some LREE concentrations are similar.

Group 2: (examples SAV 1-18, TBA 4-4) clinopyroxenes with varying degrees of light rare earth element enrichment, typically with U-shaped REE patterns, and variable

concentrations of Sr, Ti, and Zr, and with generally negative anomalies (of variable magnitude) of Ti and Zr relative to the REE.

Group 3: clinopyroxenes with LREE enriched patterns which can be further subdivided into two subgroups;

> Group 3a: (examples SAV 1-1, TBA 5-4) LREE enriched clinopyroxenes with generally straight patterns, characterized by very large negative Ti and Zr anomalies (< 100 ppm Ti);
>
> Group 3b: (example SAV 1-19, TBA 4-11) clinopyroxenes which are enriched in the LREE (i.e. $La(N)/Yb(N) > 1$), but with a characteristic concave downward shape in the LREEs (i.e. $La(N)/Ce(N) \leq 1$). This "hump" in the LREE is typical of clinopyroxenes which have crystallized from a melt. Some of these patterns also have large negative Ti and Zr anomalies; other have only modest negative Ti and Zr anomalies relative to the REE.

The concentrations of the elements Sc, V, and Cr in clinopyroxene show considerable overlap among the three groups, except that Sc tends to be high in those samples with high heavy rare earth (HREE) concentrations.

Isotopic data for olivine and clinopyroxene separates from SAV 1-1, and a clinopyroxene separate from TBA 4-11 are given in Table 3. The clinopyroxenes from these two xenoliths have Group 3 trace element patterns, with very high LREE and very low Ti concentrations. The TBA 4-11 cpx is characterized by $^{87}Sr/^{86}Sr$ and Pb isotope ratios which fall within the range of basaltic lavas from Tubuai (REFS, Chapter 4). However, the cpx separate from SAV 1-1 is characterized by very high $^{87}Sr/^{86}Sr$, which is well outside the range of $^{87}Sr/^{86}Sr$ measured for Samoa basalts (highest $^{87}Sr/^{86}Sr$ is .7075, Farley et al., 1992). The $^{206}Pb/^{204}Pb$ and $^{208}Pb/^{204}Pb$ ratios for this sample is typical of lavas from Savaii, and the $^{207}Pb/^{204}Pb$ is near the highest values measured for Savaii lavas (see Chapter 4). An olivine separate was analysed from this sample in order to determine the isotopic composition of enclosed fluid and melt inclusions. The Pb isotope ratios are identical to the clinopyroxene within error (Table 3), and the $^{87}Sr/^{86}Sr$ is similar to, but slightly lower than, the extreme value for the SAV 1-1 cpx.

5. Origin of the Depleted (Group 1) Signatures

The Group 1 depleted clinopyroxenes are shown in Fig. 5 compared with the field for abyssal peridotite clinopyroxenes (REF). The Tubuai samples have lower REE concentrations on average than the abyssal peridotite samples. The Tubuai samples also have more fractionated HREE concentrations (higher Yb/Dy ratios) than abyssal peridotite cpx, and some samples show positive Zr anomalies relative to adjacent REE. All samples
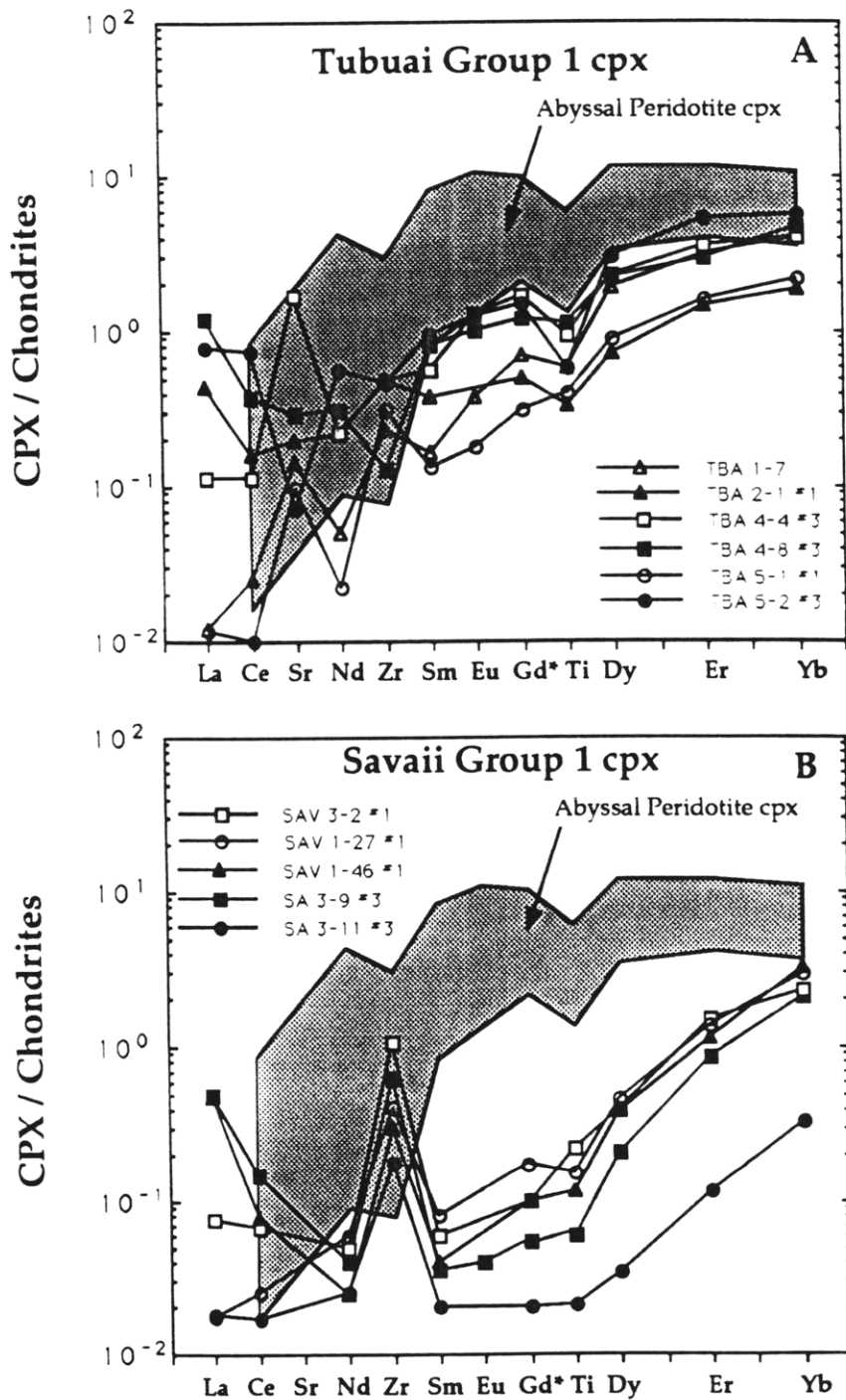
99

Figure 5. A) Tubuai Group 1 cpx patterns overlap the low end of the range of concentrations from abyssal peridotite cpx. B) Savaii Group 1 cpx patterns are much lower in REE and Ti concentrations than abyssal peridotite cpx, but have similar Zr concentrations. Abyssal peridotite data from Johnson et al. (1990).

have negative Ti anomalies. The strongly depleted patterns with positive Zr and negative Ti anomalies are signatures which are characteristic of garnet, though the REE concentrations in these cpx are lower than typical mantle-derived garnets. Some Tubuai Group 1 patterns have negative anomalies in both Ti and Zr, and bear some similarities to cpx from abyssal peridotites dredges from fracture zones near hotspots (Bouvet, Discovery II) (Johnson et al., 1990). LREE concentrations are variable, and suggest the earliest stages of a metasomatic enrichment process. However, in some cases (ex. SAV 1-27) the concentrations of the LREE (but not Zr) approach the detection limit of the ion probe analysis, in which case these concentrations would be upper limits.

The Savaii Group1 cpx patterns are distinctly different from both the abyssal peridotite and Tubuai Group 1 patterns. The Savaii Group 1 cpx are characterized by low Yb concentrations and very fractionated HREE, with $(Yb/Dy)n$ up to 10. These samples also display large positive Zr anomalies, with slightly negative or non-existent Ti anomalies. Though the Savaii cpx have Nd and Sm concentrations an order of magnitude lower than abyssal peridotites, the Zr concentrations are similar. These patterns are also suggestive of residual garnet, though the HREE concentrations in the Savaii cpx are somewhat lower than in the Tubuai cpx.

Most of these trace element signatures are suggestive of origins as residues of melting with variable amounts of garnet. Due to the extreme fractionations of some trace elements with very similar solid/melt partition coefficients (i.e. Yb and Dy), the Savaii and Tubuai cpx patterns are modelled as residues of fractional melting. This has been successfully done for abyssal peridotite cpx by Johnson et al. (1990). The equations of Shaw (1970) for non-modal fractional melting are used, and are cast into a form which describes the trace element concentrations in both the bulk solid and clinopyroxene as a function of the degree of melting:

$$\frac{C_i^s}{C_i^o} = \left[\frac{1}{1-F}\right]\left[1 - \frac{PF}{D_i^o}\right]^{\frac{1}{P}} \tag{1}$$

$$\frac{C_i^{cpx}}{C_i^o} = \left[\frac{D_i^{cpx/1}}{D_i^o - PF}\right]\left[1 - \frac{PF}{D_i^o}\right]^{\frac{1}{P}} \tag{2}$$

$$D_i^o = \sum D_i^{s/1} x_j^o \tag{3}$$

$$P = \sum D_i^{s/1} p_j \tag{4}$$

101

where:

C_i^s = concentration of element i in the bulk solid

C_i^0 = initial concentration of element i in the bulk solid

C_i^{cpx} = concentration of element i in cpx

$D_i^{s/l}$ = solid/liquid partition coefficient of element i

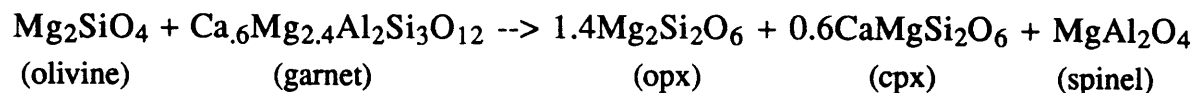X_j = weight fraction of phase j in the bulk rock (mineral mode)

P_j = proportion of phase j entering the melt (melt mode)

F = degree of melting

The initial concentrations in the bulk solid are assumed to be 2.5 times C1 chondrite for all trace elements. For the Savaii xenoliths, this assumption is justified by near-chondritic $^{143}Nd/^{144}Nd$ (.51264) measured for some Samoan lavas (e.g. Wright and White, 1987; Chapter 4). However, some lavas from Samoa, and all basalts from Tubuai are characterized by depleted $^{143}Nd/^{144}Nd$ signatures, and so an assumption of a depleted REE signature for the initial solid composition would be more appropriate in these cases. The most depleted $^{143}Nd/^{144}Nd$ signatures in the Samoa and Tubuai lavas could be created in a 1-3 Ga old source which had experienced 1-5% melting, and so the absolute degrees of melting calculated from the present model may be overestimates by about 1-5%; however, this has no bearing on the conclusions since the emphasis here is on the amount of melting in the garnet lherzolite stability field relative to the spinel lherzolite stability field.

The initial phase proportions in the solid are given in Table 4, and are appropriate for pyrolite (Ringwood, 1979) in the garnet lherzolite (GL) and spinel lherzolite (SL) stability fields. Also given in Table 4 are the melt modes for various peridotite mineralogies. These coefficients describe the proportions of phases which enter the melt. The term "garnet harzburgite" (GHz) is used here to refer to the 3-phase assemblage olivine+opx+garnet. When a mineral phase is exhausted, or when the mineralogy is changed (i.e. gt --> cpx+opx+sp) during the melting calculation, the bulk partition coefficients are recalculated according to the calculated phase proportions, and the calculation continued.
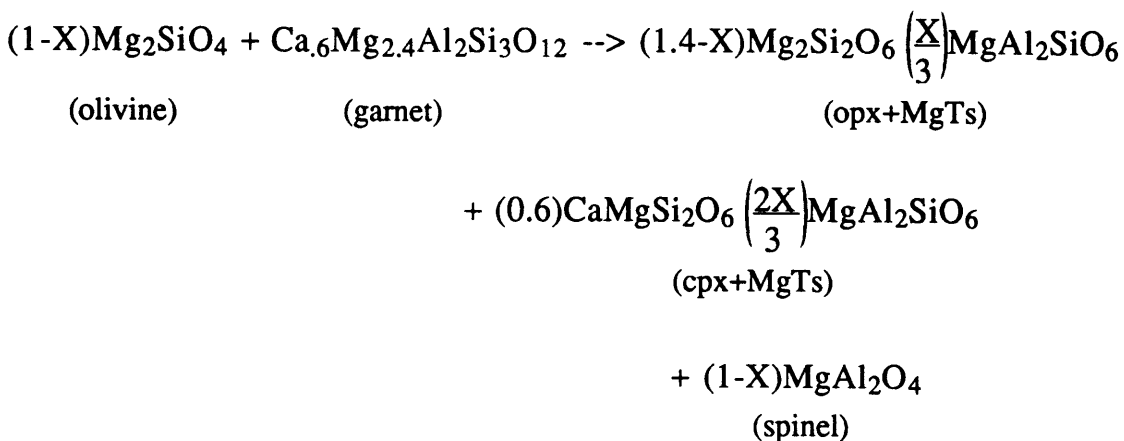
All of the trace element patterns are modelled by starting melting in the GL field, with subsequent further melting in the SL field. This requires the breakdown of garnet to cpx+opx+spinel by the following reaction:

$$Mg_2SiO_4 + Ca_{.6}Mg_{2.4}Al_2Si_3O_{12} \longrightarrow 1.4Mg_2Si_2O_6 + 0.6CaMgSi_2O_6 + MgAl_2O_4$$

(olivine)　　　　(garnet)　　　　　　　(opx)　　　　　(cpx)　　　　(spinel)

However, this reaction assumes no Al components in pyroxenes. I have modelled Al incorporation into pyroxenes as Mg-Tschermaks molecule (MgTs) by the reaction:

$$MgAl_2O_4 + Mg_2Si_2O_6 \longrightarrow MgAl_2SiO_6 + Mg_2SiO_4$$

(spinel)　　　　　(opx)　　　　　　(MgTs)　　　　(olivine)
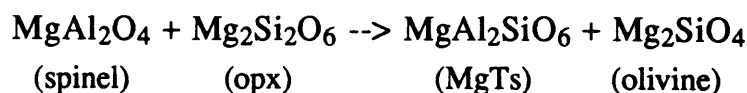
Assuming that MgTs is partitioned into cpx and opx in the ratio 2:1, the above two mineral reactions may be combined to give:

$$(1-X)Mg_2SiO_4 + Ca_{.6}Mg_{2.4}Al_2Si_3O_{12} \longrightarrow (1.4-X)Mg_2Si_2O_6 \left(\frac{X}{3}\right)MgAl_2SiO_6$$

(olivine)　　　　　　　(garnet)　　　　　　　　　　　　(opx+MgTs)

$$+ (0.6)CaMgSi_2O_6 \left(\frac{2X}{3}\right)MgAl_2SiO_6$$

(cpx+MgTs)

$$+ (1-X)MgAl_2O_4$$

(spinel)

The variable X determines the amount of spinel which is used to make MgTs, and could be chosen to have any value between zero (no Al in pyroxenes) and unity (all spinel as MgTs). A value of 0.5 results in a clinopyroxene with about 40% wollastonite, which is typical of many mantle derived clinopyroxenes. With X=0.5, the above reaction in terms of weight fractions is:

$$0.17 \text{ olivine} + \text{garnet} \longrightarrow 0.53 \text{ opx} + 0.47 \text{ cpx} + 0.17 \text{ spinel}$$
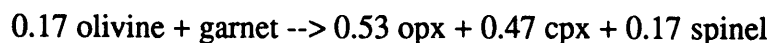
In addition, solid solution exists between clinopyroxene and orthopyroxene. In peridotitic bulk compositions, the effect of this solid solution with increasing temperature and pressure is to increase the modal abundance of cpx at the expense of opx:

opx --> cpx

Since the extent of opx-cpx solid solution is almost entirely a function of temperature, this reaction cannot be accurately modelled without a detailed temperature history for a parcel of melting peridotite. In modelling the Tubuai trace element patterns, it was not necessary to take pyroxene solid solution into account. For the Savaii modelling, a constant value of 8 wt% opx solution into cpx is assumed so that cpx is not exhausted during melting in the spinel lherzolite field. The "reaction modes" for these reactions are given in Table 4.

The mineral/melt partition coefficients used in the modelling are given in Table 5, and the partitioning patterns are shown in Figure 6. Clinopyroxene/liquid values are chosen from the experimental literature (e.g. Irving, 1978), and are similar to values reported by Johnson et al. (1990) and Hart and Dunn (1992). The Cpx/liquid pattern is characterized by a pronounced decrease in values for the LREE relative to the HREE, and a significantly lower value for $D(Zr)$ compared with $D(Nd)$ and $D(Sm)$. The value of $D(Ti)$ is slightly less than for the adjacent REE.

Garnet/liquid values are an average of experimental literature data (ex. Nicholls and Harris, 1980) and values calculated from garnet/cpx partition coefficients measured from Ronda (Chapter 2) and from garnet peridotite xenoliths from Patagonia (Salters, 1989). The garnet/melt partitioning pattern is characterized by a positive anomaly for $D(Zr)$ and a negative anomaly for $D(Ti)$.

Mineral/melt partition coefficients for olivine, orthopyroxene, and spinel are taken from mineral/mineral partition coefficients reported by Stosch (1982) and McDonough et al. (1992) combined with the above cpx/melt Ds, and from the data of McKay (1986), Irving (1978), Fujimaki et al. (1984), and Dunn (1987); the values are the same as those used by Kelemen et al. (1990). Olivine, opx, and spinel are all characterized by $D(Ti)$ and $D(Zr)$ values much higher than for adjacent REE. The olivine and opx REE partition coefficient patterns are characterized by a strong fractionation of LREE from HREE, and the HREE (Dy, Er, Yb) from each other.

These partition coefficients are assumed to be constant throughout melting. In fact, mineral/melt partition coefficients for the various phases are functions of pressure (P), temperature (T), and the composition of individual phases. For example, at P-T conditions above the pyroxene solvus, a single pigeonitic pyroxene is the stable pyroxene phase (Lindsley and Andersen, 1983). Since this phase has a different crystal structure than typical ortho- and clinopyroxenes, it will likely have different mineral/melt partition coefficients than either opx or cpx. The same effect may also apply to garnet, as pyroxene solid solution into garnet increases with increasing P and T (Takahashi, 1986). Since the

	Pyrolite GL Facies	Pyrolite SL Facies	GL Melt Mode	SL Melt Mode	GtHz Melt Mode	Gt RXN Mode	Pyroxene Solvus
olivine	.553	.552	.12	-.44	.10	-.17	---
opx	.193	.247	---	.55	.278	.53	-1.0
cpx	.095	.178	.46	.67	---	.47	1.0
garnet	.159	---	.42	---	.622	-1.0	---
spinel	---	.023	---	.22	---	.17	---

Table 4. Peridotite Mineral Modes, Melt Modes, and Mineral Reaction Modes

	olivine/melt	opx/melt	spinel/melt	cpx/melt	garnet/melt
La	.000007	.0025	.0006	.06	.0035
Ce	.00001	.005	.0006	.10	.008
Nd	.00007	.01	.0006	.20	.05
Zr	.007	.07	.07	.17	.40
Sm	.0007	.02	.0006	.30	.22
Eu	.00095	.03	.0006	.38	.45
Gd	.0012	.04	.0006	.40	.75
Ti	.015	.15	.15	.35	.16
Dy	.004	.05	.0015	.44	2.0
Er	.009	.07	.003	.45	3.5
Yb	.023	.11	.0045	.45	5.0

Table 5. Mineral/Melt Partition Coefficients
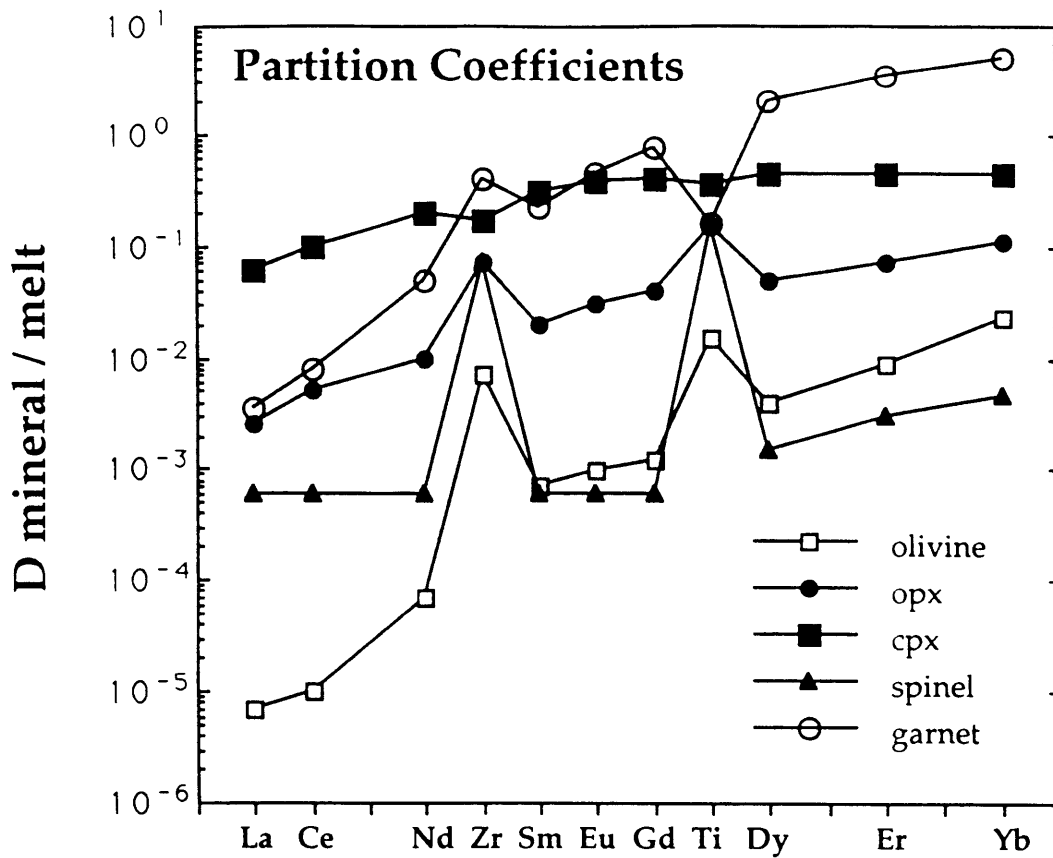
Figure 6. Mineral/melt partition coefficient patterns for olivine, orthopyroxene (opx), clinopyroxene (cpx), spinel, and garnet. The partitioning patterns for garnet, opx, and olivine all have steep negative slopes for the HREE (Dy, Er, Yb) and large anomalies for Zr (relative to Sm) and Ti (relative to Dy). The partitioning pattern for cpx has small negative anomalies for Zr and Ti. The changing proportions of these minerals during melting results in variable fractionation of Zr and Ti from the REE.

relevant mineral/melt partition coefficients are presently unknown, no attempt is made to account for these effects.

The solid/melt partition coefficient pattern for a given bulk rock will depend on the proportions of the various minerals. For example, the bulk rock partition coefficient pattern of pyrolite will be different in the GL facies than in the SL facies. Melting in the GL field, followed by garnet breakdown, will yield a clinopyroxene with a trace element pattern quite different from a cpx from a residue of melting in the SL field. Depending on how much melting takes place in the GL and SL stability fields, a variety of trace element patterns can be produced, with variable absolute concentrations, degrees of LREE depletions, and either positive or negative Zr anomalies.

5.1 Tubuai Xenoliths (Group 1)

The modelled trace element patterns for the Tubuai Group 1 pyroxenes (heavy lines) are shown in Fig. 7a-h along with the measured patterns. Since most of the measured clinopyroxenes show clear evidence of incipient LREE enrichment, the main goal was to try and fit the absolute and relative concentrations of Zr, Ti, and the HREE Dy, Er, and Yb. Critical melting, in which some fraction of liquid remains in the residue throughout melting (Maaloe, 1982), would conceivably result in a more efficient retention of the LREE in the residue; however, this phenomena would be largely indistinguishable from incipient LREE enrichment through metasomatism, which clearly effects most of these xenoliths. All of the trace element patterns are modelled by starting melting in the GL field, breaking down garnet, and continuing melting in the SL field. The total degree of melting modelled for the Tubuai samples ranges from 16.8% (TBA 4-6) to 27.5% (TBA 5-1). In the above melting model, the degree of HREE fractionation (i.e. Yb/Dy ratio), the Ti/Dy ratio, and the Zr/Sm ratio are sensitive to the amount of melting in the GL field. For example, sample TBA 4-8, with a negative Zr anomaly, is modelled by 9% melting in the GL field followed by 13% melting in the SL field (Fig. 7d). Sample TBA 1-7 is modelled with a larger relative amount of melting in the GL field (15% GL melting, 11.5% SL melting) due to the positive Zr anomaly and high Yb/Dy ratio (Fig. 7f). The absolute concentrations of the HREE and, to a lesser degree Ti, are sensitive to the amount of melting in the SL field. Since the cpx/melt partitioning pattern is relatively smooth for the elements Eu-Yb, melting in the SL field (under about 10%) has only minor effects on the trace element pattern for Eu-Yb, but has a significant effect on the absolute trace element concentrations. For example, samples TBA 4-6 (Fig. 7a) and TBA 4-8 (FIG. 7d), with pseudo-parallel patterns, are both modelled by 9% melting in the GL field, but different amounts of melting in the SL field, due to their different HREE concentrations. In all cases, the models result in a poor fit to the LREE concentrations, but Zr concentrations are

usually accurately modelled. A notable exception is the trace element pattern for TBA 5-1 (Fig. 7g), which has a garnet-like pattern, but a very high Zr/Sm ratio which cannot be modelled with any combination of melting in the two stability fields.

5.2 Savaii Xenoliths (Group 1)

The modelled trace element patterns for the Savaii Group 1 clinopyroxenes are plotted with the measured data in Fig. 8a-e. In general, the higher Yb/Dy ratios of the Savaii samples require a higher degree of melting in the GL field than the Tubuai samples. In fact, the only way that the melting model can fit many of the Savaii Group 1 patterns is to melt in the GL stability field to, and in some cases beyond, the point at which clinopyroxene is exhausted from the residue (cpx-out), in this case 20.6% melting, leaving a residue of olivine+opx+garnet. The exact degree of melting at which the cpx-out point is reached is dependent upon the initial GL modes and the GL melt mode (Table 4). However, the degree of Yb/Dy fractionation requires melting to the cpx-out point, no matter the absolute degree. Because the clinopyroxene/melt partition coefficients for Dy, Er and Yb are essentially the same (Table 5), melting to the cpx-out point in the GL stability field is required in order for the garnet/melt partitioning pattern to exert sufficient influence on the trace element pattern of the residue. The high Yb/Dy ratios and negative Ti anomalies of the Savaii Group 1 clinopyroxenes requires residual garnet to dominate the solid/melt partitioning during melting.

The low HREE concentrations in the Savaii clinopyroxenes also require substantial degrees of melting in the SL field, after melting in the GL field and garnet breakdown to opx+cpx+spinel (Fig. 8a-e). In order to match the observed HREE concentrations in the Savaii cpx, it was required to assume 8 wt% solution of opx into cpx, so that melting did not proceed to the cpx-out point in the SL field before the HREE concentrations were matched. The modelling was generally successful, with the exception of cpx from sample SA 3-11, which is characterized by a very high Yb/Dy ratio, very low HREE concentrations, and less than 9 ppm of Ti measured in the cpx. In order to fit these characteristics with the assumed partition coefficients, a very high degree of melting is needed (42.2%), accommodated by assuming 13% solution of opx into cpx (which may be excessive). In all of these cases, the mineral modes which are calculated from the model are characterized by very low modal abundances of cpx, in most all cases less than 2%. This is consistent with the general paucity of clinopyroxene observed in the Savaii Group 1 xenoliths. For the Savaii clinopyroxenes, the estimated total degree of melting for individual patterns ranges from 33% to 42.2% (Fig. 8a-e).

The polybaric melting model fails to fit the observed Zr concentrations in the Savaii Group 1 cpx, and the sample TBA 5-1 from Tubuai. In these samples, the concentration of

Zr varies with the HREE, whereas the concentrations of the LREE correlate neither with the HREE nor with Zr. This suggests that the observed Zr concentrations were determined by the melt depletion event which resulted in the HREE and Ti characteristics of these samples, and not the incipient LREE enrichment which is evident in the trace element patterns. This also suggests that the apparent solid/melt partition coefficient for Zr should be higher than that used in the model. For example, by setting D(Zr)=[D(Dy) + D(Er)]/2 in all the mineral phases, a much more satisfactory fit to the observed Zr concentrations is obtained. However, this would require values of D(Zr) of .45 and 2.8 for cpx/melt and garnet/melt, respectively. These values are much higher than the experimental values used in the modelling. There is no experimental evidence to support such high values in the diopsidic clinopyroxenes and pyrope-rich garnets typical of peridotites derived from the upper mantle.

The high Zr concentrations of the Savaii cpx cannot be the result of trapping of a residual melt. The Savaii cpx are characterized by $(Zr/Sm)_N$ of about 10. An instantaneous fractional melt formed in equilibrium with a very depleted garnet harzburgite will have a high Zr/Sm ratio, but such a melt will also have very low Zr and Sm concentrations, which would require trapping several tens of percent of melt in order to account for the Zr concentration. Not only would this increase the modal abundance of cpx in the peridotite, but would also increase the concentration of the HREE and Ti in cpx above that observed for the Savaii pyroxenes.

Another possible explanation for the high Zr/Sm ratios of the Savaii clinopyroxenes is the possible influence of a residual phase with a high value for D(Zr), and which has subsequently reacted out at lower pressure to form clinopyroxene. One possible candidate phase is pigeonitic pyroxene, which is the result of mutual solubilities of clino- and orthopyroxene as a function of temperature and pressure (Lindsley and Andersen, 1983). To date there have been no studies of trace element partitioning between high-pressure pigeonite and basaltic melts. Only the data of Takahashi (1986) allow some estimation of partitioning of Ti between high-P pigeonite and melt. Keeping in mind the complexities of deriving "near equilibrium" partitioning data from very high T and P experimental charges (Walker and Agee, 1989), the mineral and melt compositions from run #53 of Takahashi (1986) suggest a value of 0.1 for D(Ti) between pyroxene and melt. This value is between the opx/melt and cpx/melt values in Table 5. This may be the result of either the composition/crystal structure of high-P pigeonite, or possibly a lower value for D(Ti) at higher temperature (e.g. Nicholls and Harris, 1980). In either case, this may suggest lower values for tetravalent cations (i.e. Ti^{4+} and Zr^{4+}) in high-pressure pigeonite, which
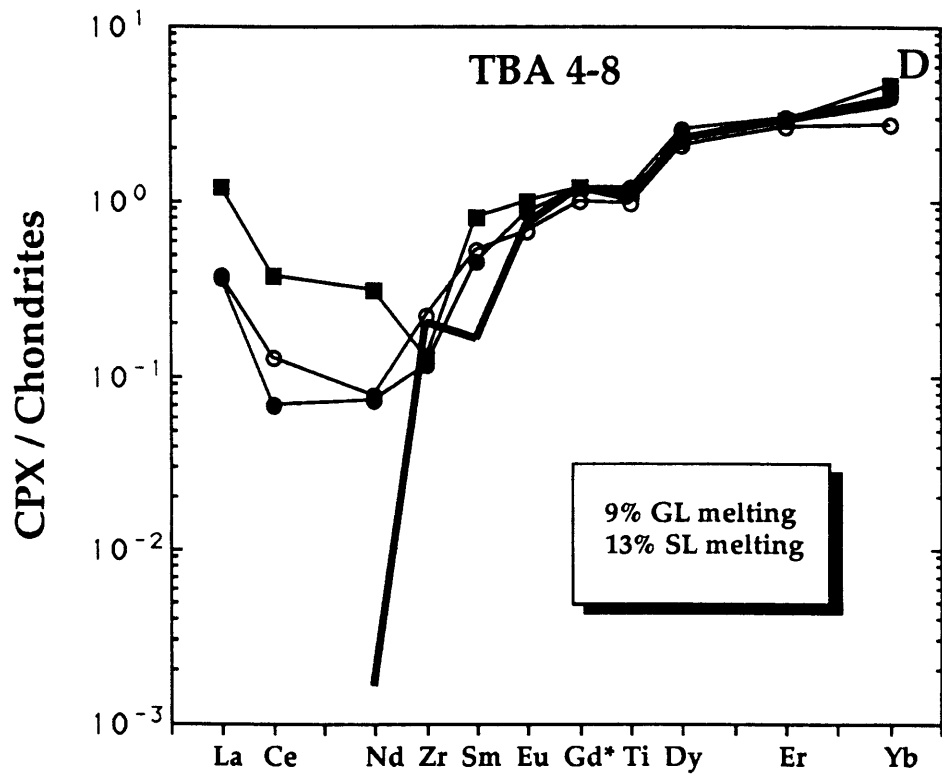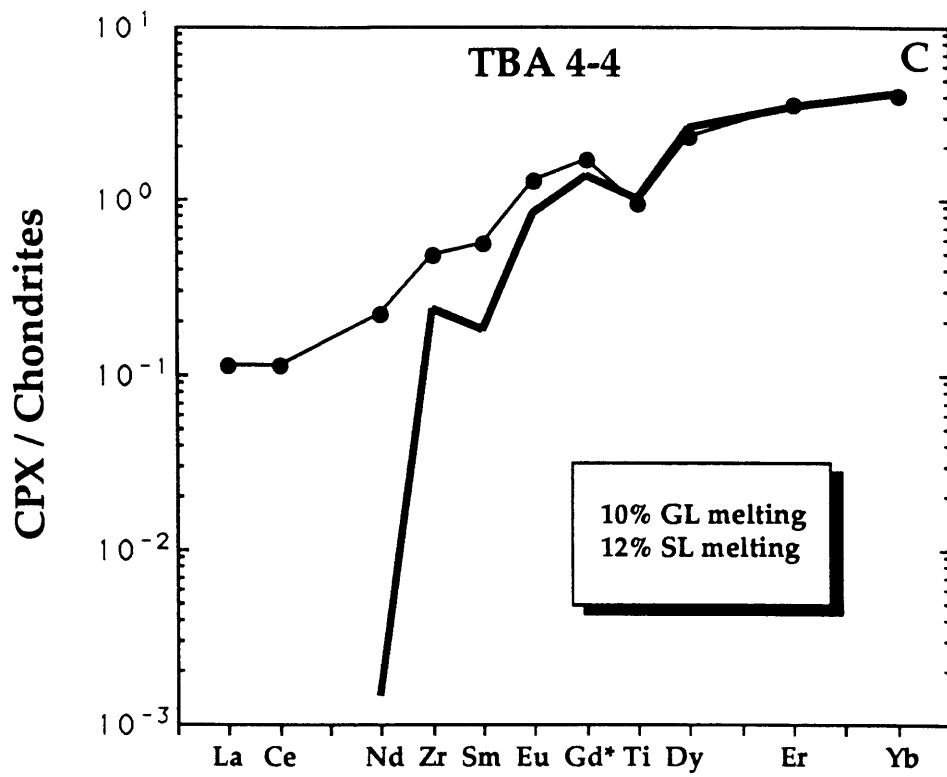
is in the opposite direction required to model the Zr concentrations in the Savaii clinopyroxenes.
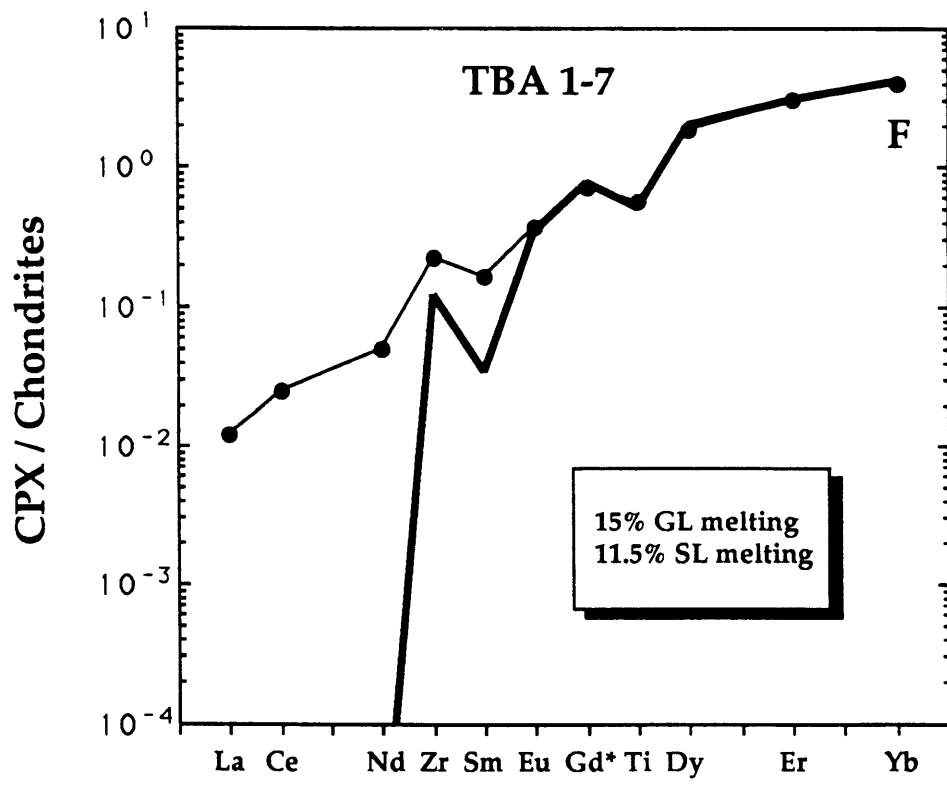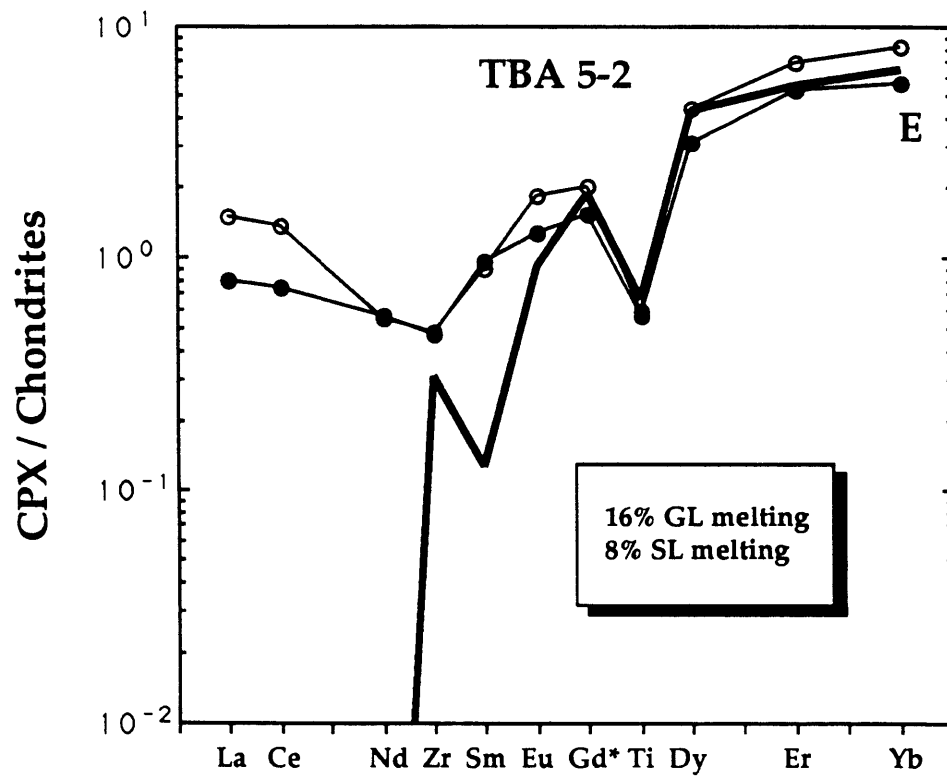
Another possible candidate phase is majorite garnet, which is the result of the increasing solubility of pyroxene into garnet (Takahashi, 1986). The trace element partitioning data of Kato et al. (1988) suggest values of 0.6 for D(Zr) and 0.2 for D(Sm) between majorite and ultrabasic liquid in a pyrolite starting composition at 16 GPa. The resulting ratio D(Zr)/D(Sm) for majorite/melt (3.0) is higher than the same ratio for garnet/melt in Table 5 (1.3-1.8), but the value of D(Zr) for majorite/melt might still be too low to account for the absolute concentration of Zr in the Savaii cpx. The Zr concentrations in the Savaii cpx appear to require a higher solid/melt partition coefficient for this element. However, the uncertainty in the measurements of the partition coefficients in high pressure phases is considerable, and no firm conclusions can be drawn on the possible influence of these phases on the trace element patterns of the Savaii clinopyroxenes without higher quality partitioning data.

Although the misfit of the LREE (and Zr for the Savaii cpx) in the melting model cannot be accounted for by retention of an instantaneous melt in the peridotite, it may be possible to account for the observed LREE concentrations by mixing of the highly depleted model peridotites with LREE depleted, but higher concentration instantaneous melts derived from the melting of less depleted peridotite at deeper levels in the melting column. The misfit of the LREE to the model trace element patterns likely cannot be matched by assuming a LREE enriched initial starting composition; because the model La concentrations are several orders of magnitude lower than those observed, this would require an enrichment of this magnitude in the starting composition. For example, the LREE enriched starting composition needed to fit the TBA 4-6 pattern (Fig. 7a) would require an approximate composition of $Yb_N=2.5$, $Sm_N=6$, $Zr_N=5$, $Nd_N=72$, and $La_N=>10^4$!   Such a steeply LREE enriched starting composition is clearly unjustified given the range of $^{143}Nd/^{144}Nd$ observed in the basalts from Samoa and Tubuai. To account for the high Zr concentrations of the Savaii cpx in a similar fashion would require a Zr enrichment of 100-500xC1. Instead, it is probable that the observed LREE concentrations in the Samoa and Tubuai xenoliths results from trapping of deeper level melts during melt generation and/or incipient metasomatic LREE enrichment.

Figure 7 (a-h).   Results of the polybaric fractional melting model for the
Tubuai xenolith clinopyroxenes. Heavy line (no points) represents the
clinopyroxene concentration calculated from the model, compared with the
actual measured concentrations in the clinopyroxene (line with points).
Legend indicates the degree of melting in the garnet lherzolite stability field
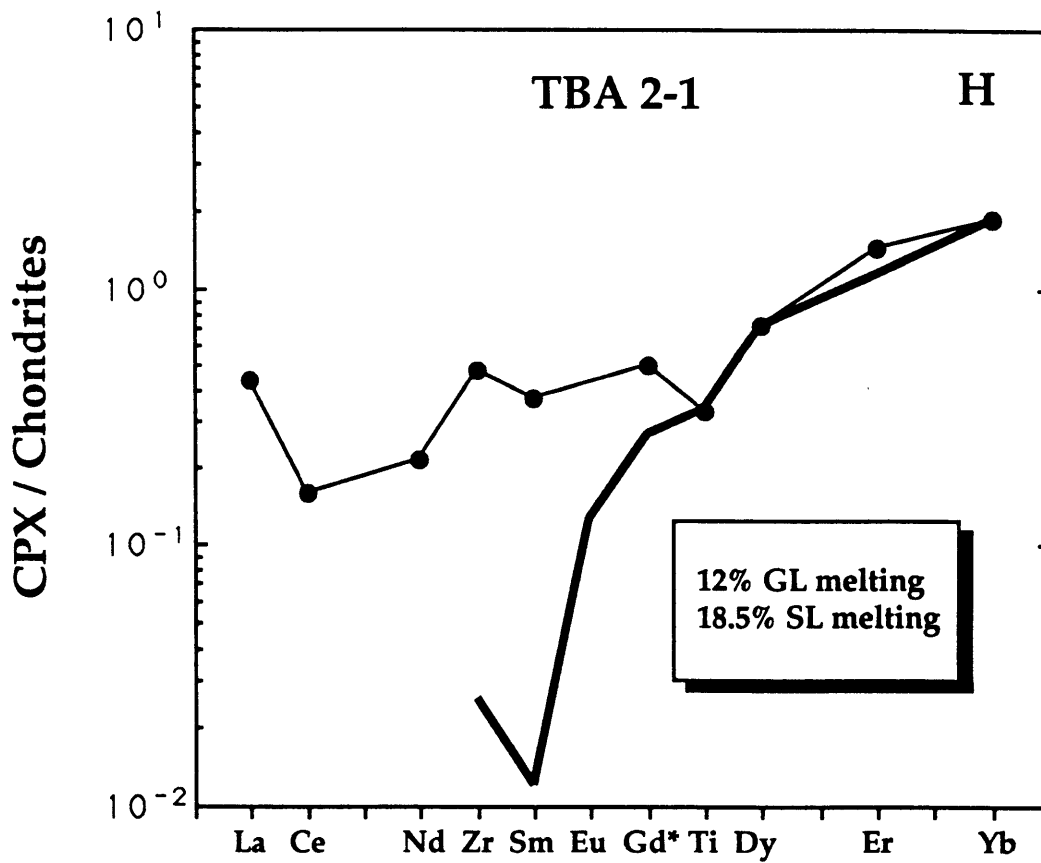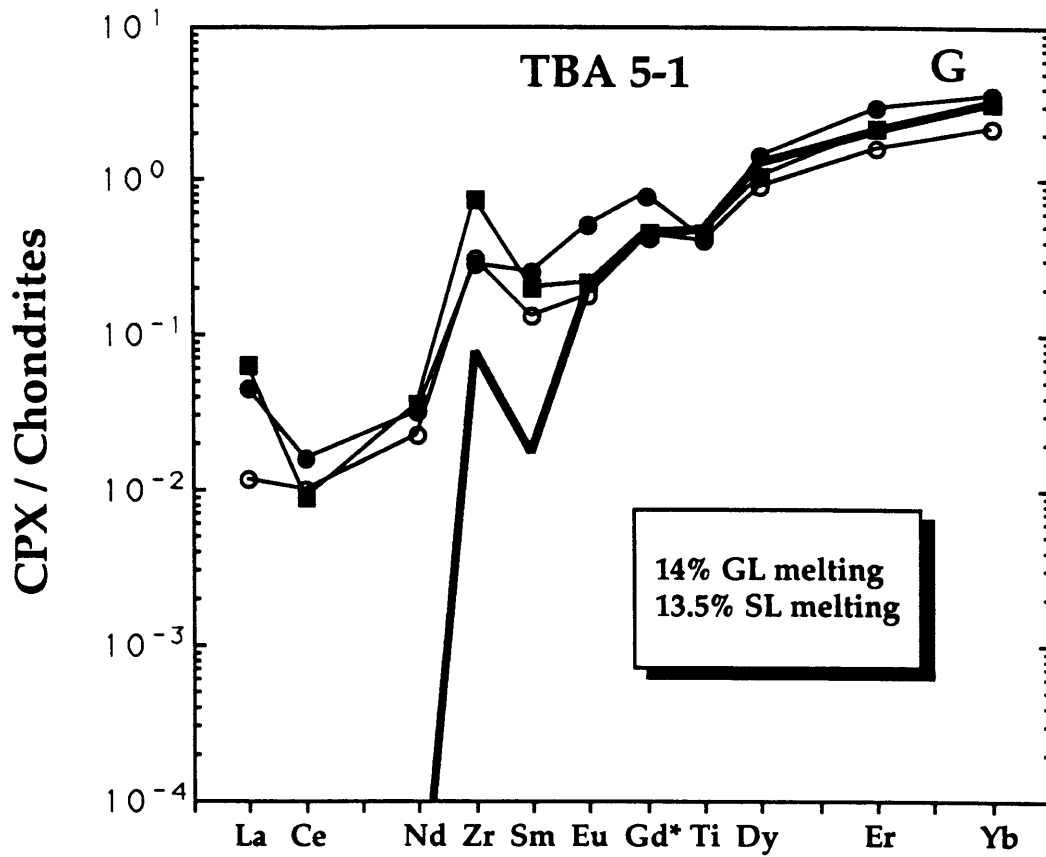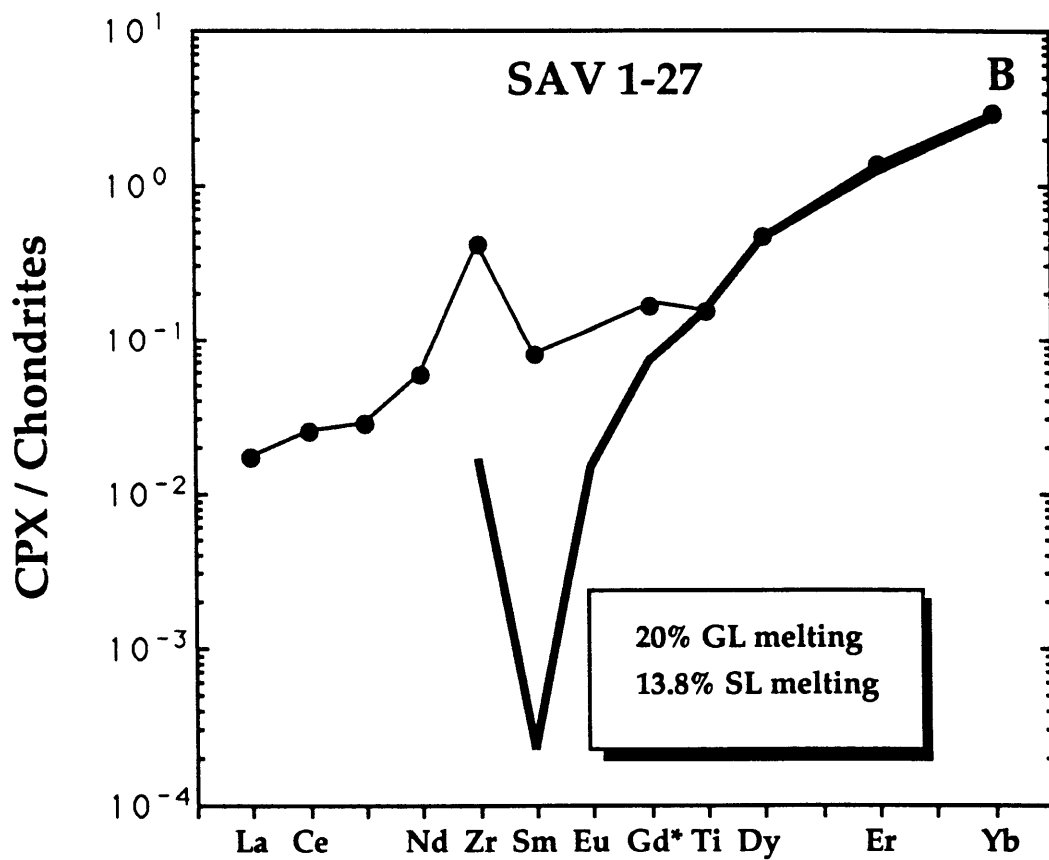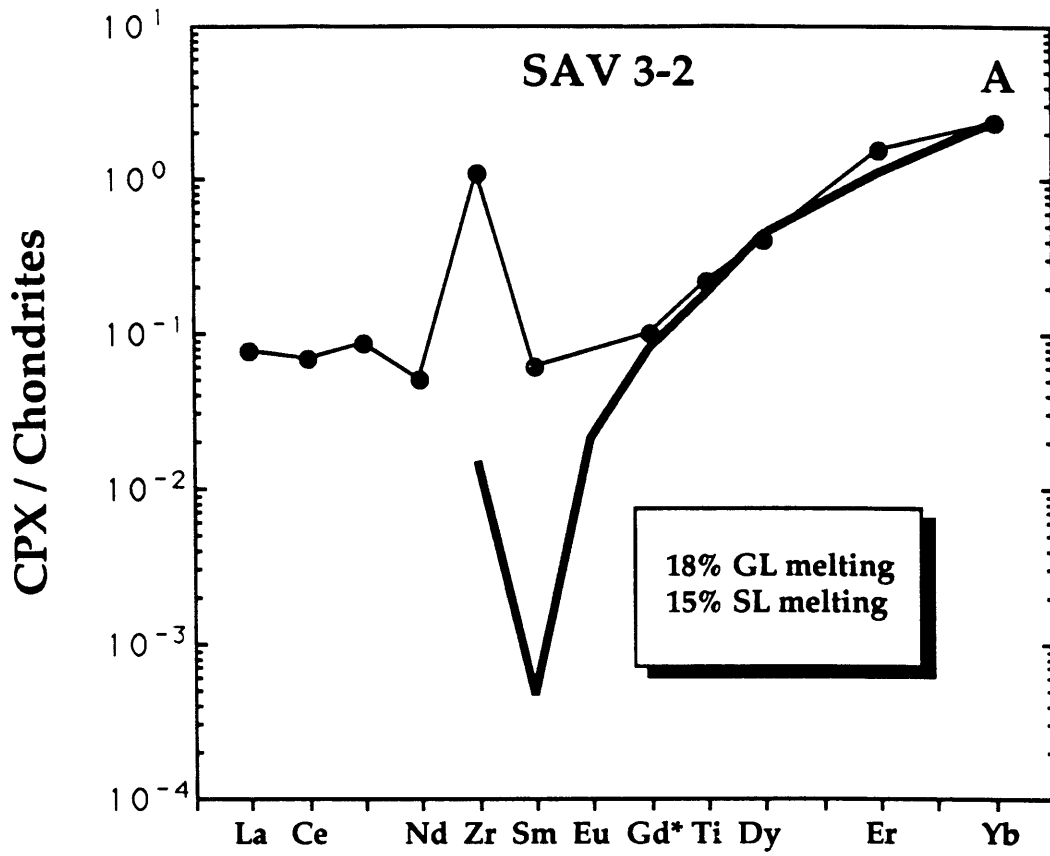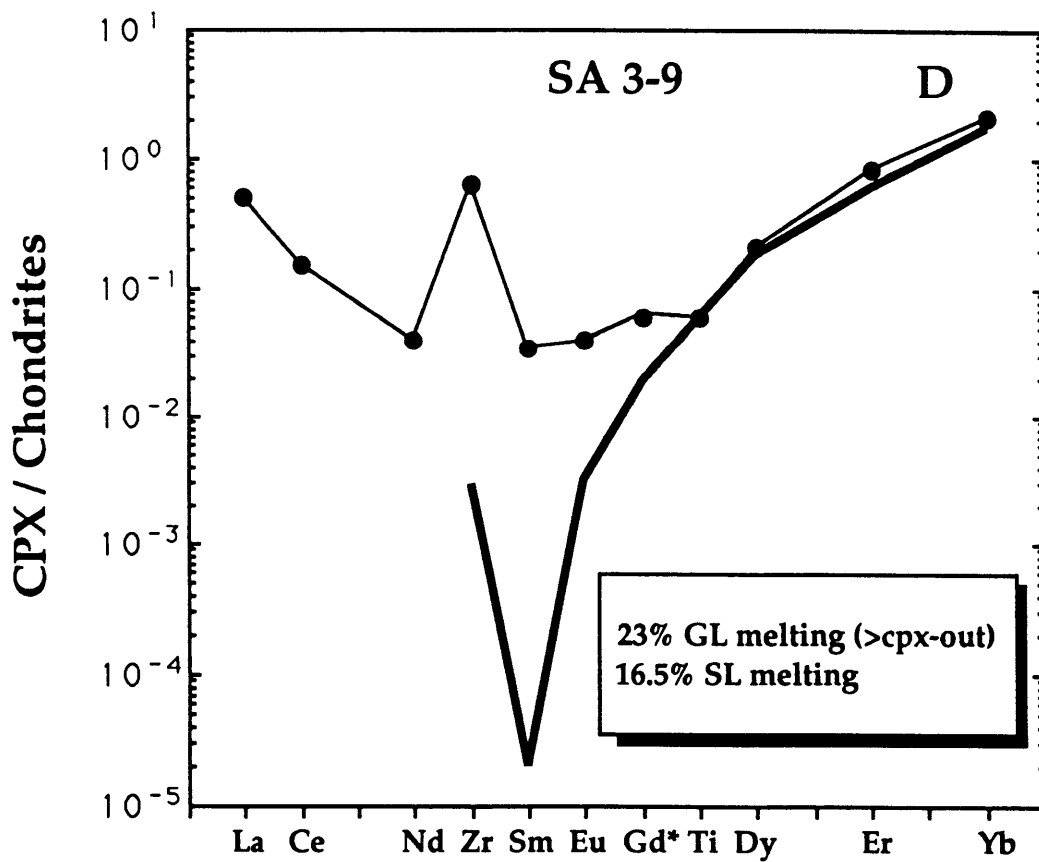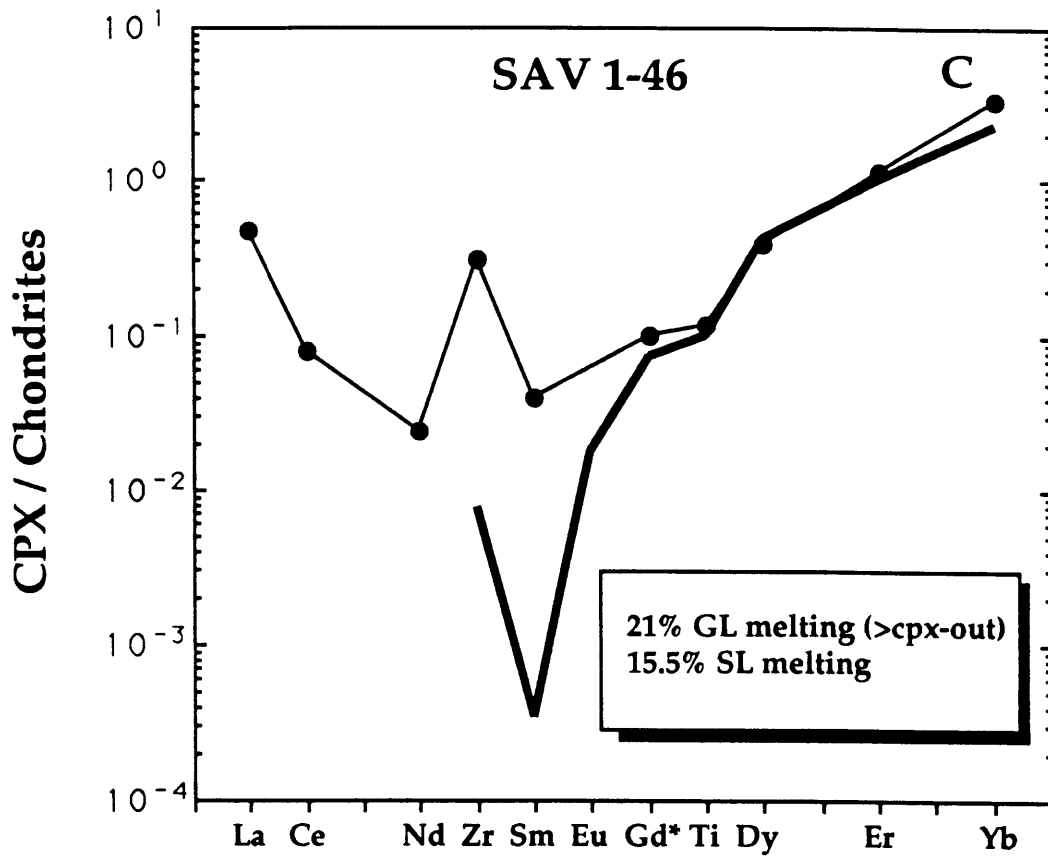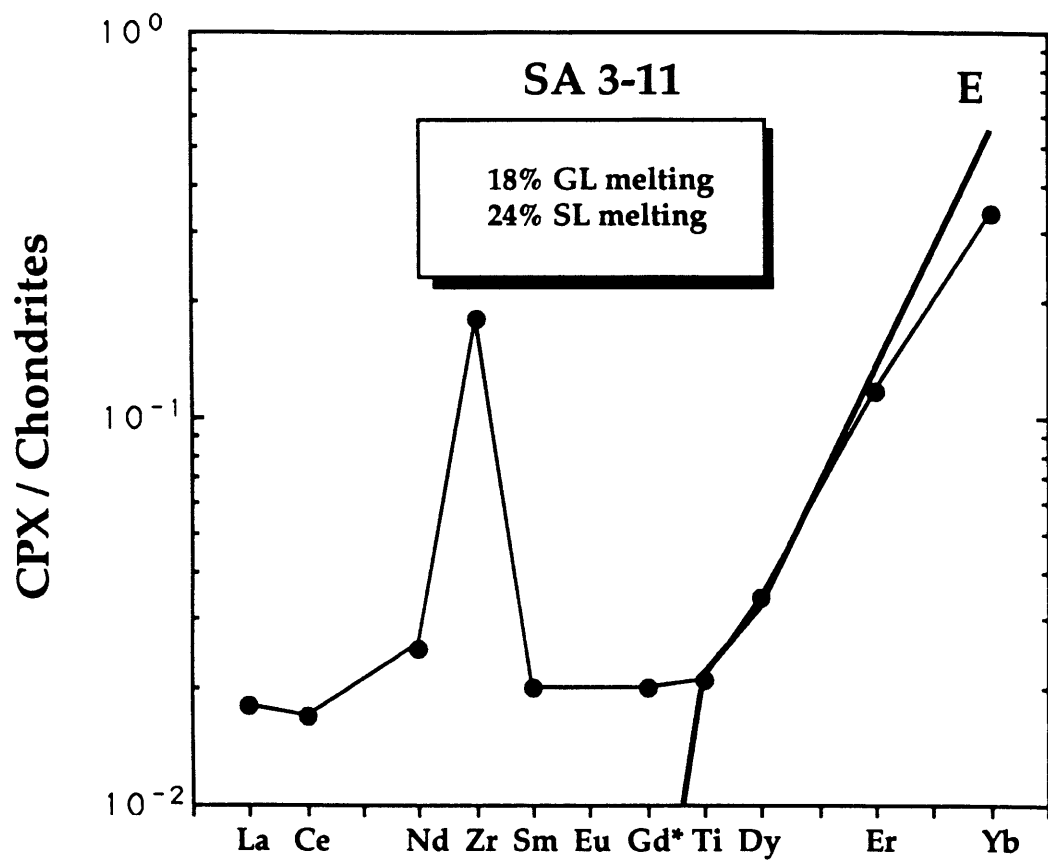(GL melting) and spinel lherzolite stability field (SL melting).

TBA 4-6

10¹

10⁰

10⁻¹

9% GL melting
7.8% SL melting

10⁻²

La Ce   Nd Zr Sm Eu Gd* Ti Dy   Er   Yb

A

CPX / Chondrites

TBA 4-5

10¹

10⁰

10⁻¹

10⁻²

12% GL melting
8.5% SL melting

10⁻³

La Ce   Nd Zr Sm Eu Gd* Ti Dy   Er   Yb

B

CPX / Chondrites

113

TBA 4-4

10% GL melting
12% SL melting

TBA 4-8

9% GL melting
13% SL melting

114

TBA 5-2

E

16% GL melting
8% SL melting

TBA 1-7

F

15% GL melting
11.5% SL melting

TBA 5-1 G

14% GL melting
13.5% SL melting

La Ce Nd Zr Sm Eu Gd* Ti Dy Er Yb

TBA 2-1 H

12% GL melting
18.5% SL melting

La Ce Nd Zr Sm Eu Gd* Ti Dy Er Yb

116
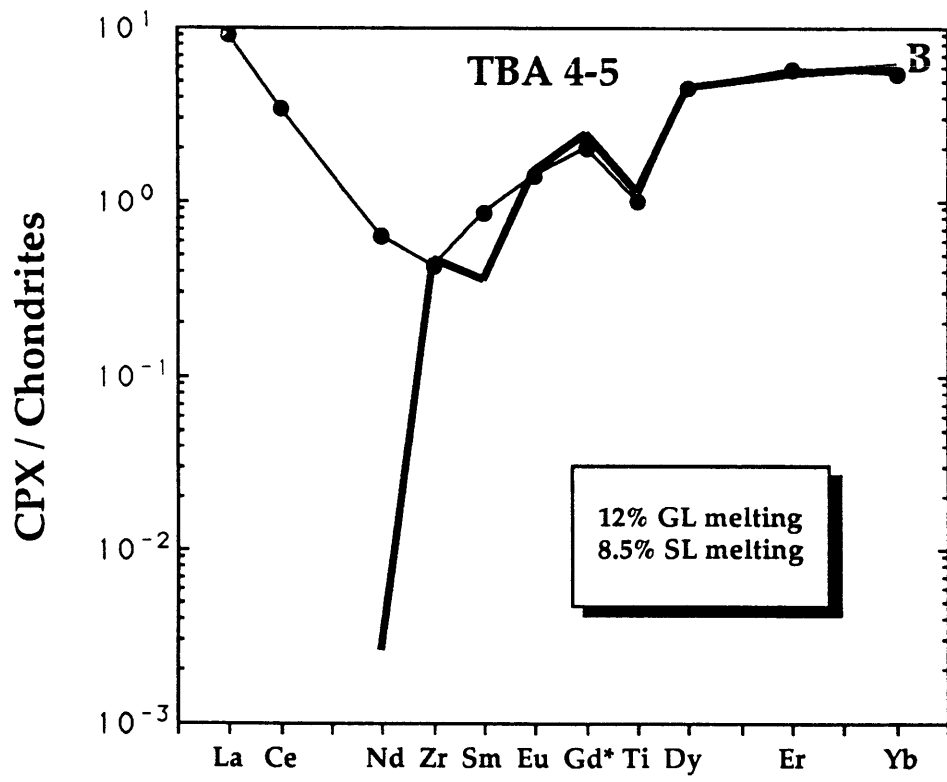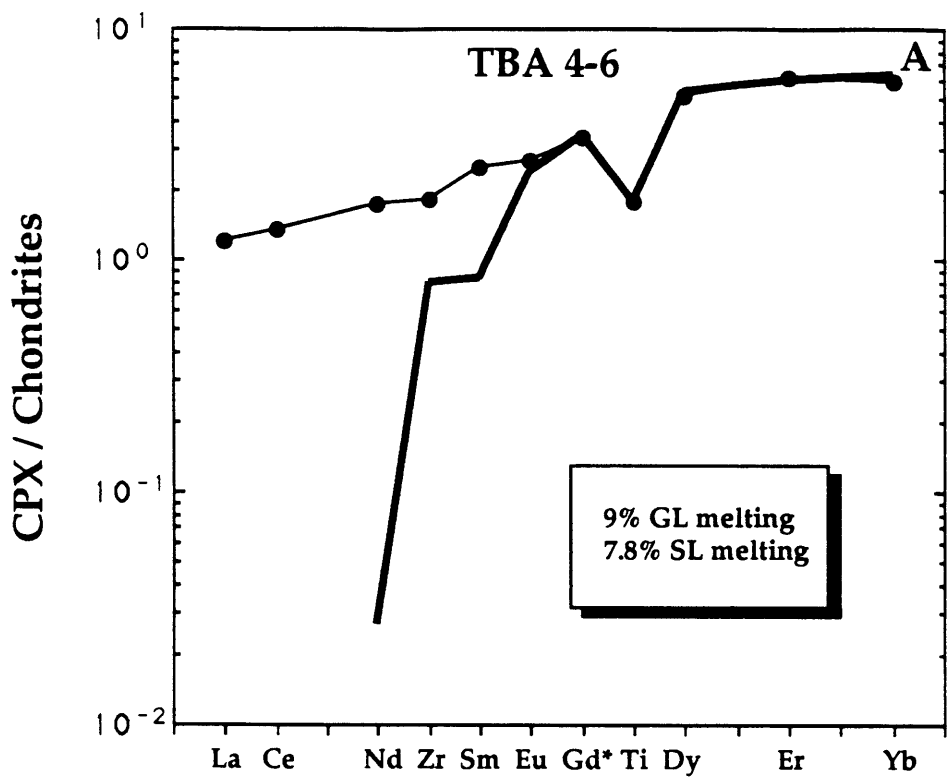
Figure 8 (a-e).   Results of the polybaric fractional melting model for the Savaii xenolith clinopyroxenes. Heavy line (no points) represents the clinopyroxene concentration calculated from the model, compared with the actual measured concentrations in the clinopyroxene (line with points). Legend indicates the degree of melting in the garnet lherzolite stability field (GL melting) and spinel lherzolite stability field (SL melting).

A

SAV 3-2

18% GL melting
15% SL melting

La Ce   Nd Zr Sm Eu Gd* Ti Dy   Er   Yb

B

SAV 1-27

20% GL melting

13.8% SL melting

La Ce   Nd Zr Sm Eu Gd* Ti Dy   Er   Yb

SA 3-11

18% GL melting
24% SL melting

E

6. Origin of the LREE Enriched (Group 2 and 3) Samples

The variable nature of the LREE enrichment in the Group 2 clinopyroxenes from both Tubuai and Savaii strongly resemble REE patterns which result from chromatographic-type melt migration processes acting on a LREE depleted mantle composition (Navon and Stolper, 1987). This process is typically modelled by porous flow of a melt with a constant trace element composition through a matrix with a different trace element composition. A well known feature of this process is that trace elements in the melt travel through the column at some fraction of the melt velocity, which is a function of the bulk solid/melt partition coefficients of the individual elements. Elements with very low solid/melt partition coefficients move through the matrix at velocities very close to the melt velocity, whereas those elements with high solid/melt partition coefficients move at smaller fractions of the melt velocity. With increasing distance into the column, trace elements with different solid/melt partition coefficients are increasingly fractionated in the melt, and this trace element signature is imprinted on the matrix material. This process is quite effective at creating U-shaped REE patterns like those in Figures 1 and 2.

The trace element patterns which are imprinted on the matrix during this process are largely determined by 1) the trace element composition of the input fluid, and 2) the bulk solid/melt partitioning pattern of the matrix material. For a given section of the column, the trace element composition of the matrix approaches the composition in equilibrium with the melt as more melt is percolated through. Clinopyroxene in such a matrix will have a trace element pattern identical to clinopyroxene in equilibrium with the percolating melt. The Group 3B clinopyroxenes (Figs. 1 and 2), with their concave-downward REE patterns, resemble "igneous" REE patterns suggestive of equilibrium with a melt. This group of clinopyroxenes very likely represents the closest approach to equilibrium with the migrating melts, and can be used to infer the trace element compositions of such melts.

The hypothetical melts in equilibrium with the Savaii and Tubuai Group 3B clinopyroxenes were calculated using the cpx/melt partition coefficients in Table 5, and are plotted in Fig 9. In Fig. 9a, some of these hypothetical melts show good agreement with the trace element patterns in alkali basalts from Tubuai and Samoa (Palacz and Saunders, 1986; Dupuy et al., 1989), which indicates the suitability of alkali basalt as the percolating melt in some cases. However, the REE concentrations, LREE enrichments, and Ti and Zr depletions of some of the hypothetical melts are distinctly different from the Tubuai and Samoa basalts. In particular, the model melts in equilibrium with the Group 3B clinopyroxenes from samples listed in Fig. 9b have higher REE concentrations, higher LREE/HREE ratios, and much larger negative Ti and Zr anomalies than typical oceanic island basalts. From Fig. 9b, it is obvious that these hypothetical melts have trace element
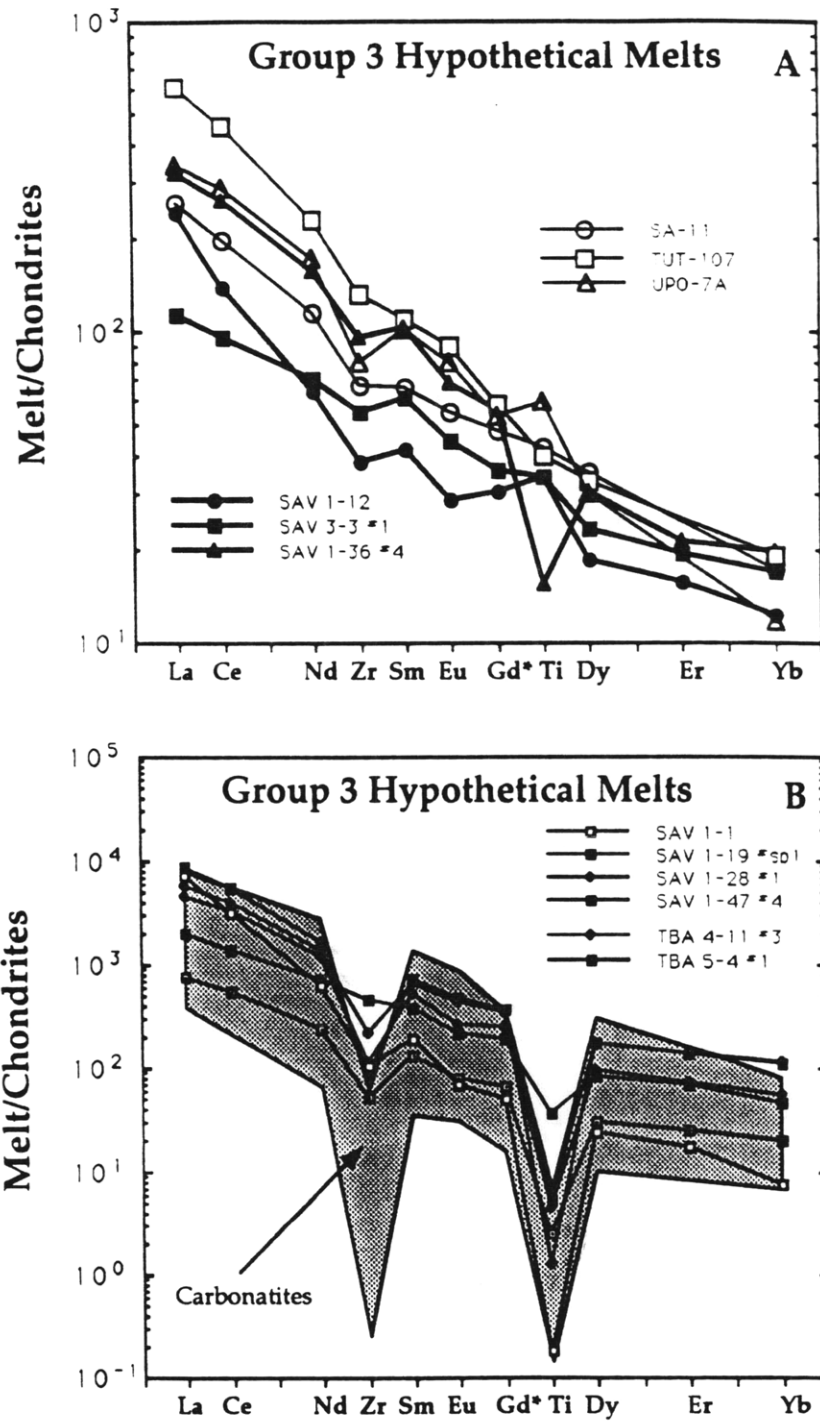
121

Figure 9. A) Hypothetical melts in equilibrium with some Savaii Group 3b clinoproxenes. The trace element patterns of these hypothetical melts are very similar to alkali basalts from Samoa. B) Hypothetical melts in equilibrium with Savaii and Tubuai Group 3b clinopyroxenes characterized by very high LREE concentrations and very large Zr and Ti depletions. The hypothetical melts for these cpx are very similar in their trace element signature to carbonatite melts. Carbonatite data from Nelson et al. (1988).

characteristics in common with carbonatites, typified by very high LREE concentrations and very large negative Ti and Zr anomalies.

With some observational constraints on the compositions of the migrating melts, we now turn to the matrix composition. A progressive enrichment of the LREE, Zr, and Ti with "reaction progress" is evident from the Group 2 trace element patterns, typified by the sequence of patterns measured in the clinopyroxenes from sample SAV 1-46 (Fig. 1n). Starting from the "depleted" Group 1 pattern (cpx 1), progressive enrichment in the LREE are observed with the concentrations of Zr, Ti, Dy, Er, and Yb remaining constant (cpx 3,5). As the LREE enrichment progresses, an increase in the concentrations of Zr and Dy is observed, with Ti and Yb remaining at the starting concentrations (cpx 2). With even further LREE enrichment, increases in the concentrations of Ti and Yb are finally observed (cpx 4). Assuming a constant composition in the input melt, this sequence of trace element enrichments strongly suggests that the solid/melt partition coefficients for Zr and Dy, and for Ti and Yb, are essentially the same; i.e. these pairs of elements are travelling through the matrix peridotite at essentially the same velocities. This indicates that the solid/melt partitioning pattern for the matrix should have high values for $D(Zr)$ and $D(Ti)$ relative to adjacent REE (Fig. 10), such as would be the case if the matrix consisted dominantly of olivine+opx (see Table 5). This is also consistent with the generally small amount of clinopyroxene in the observed modes for the Savaii and Tubaui xenoliths. Any melt percolating through a matrix with this partitioning pattern will develop negative anomalies in Zr and Ti, the magnitudes of which will increase with distance from the melt source as Zr and Ti are further fractionated from the REE.

In order to demonstrate the ability of the porous flow melt percolation process to reproduce the characteristics of the Group 2 clinopyroxene patterns, melt percolation was modelled according to the numerical method outlined by Navon and Stolper (1987) (see their Appendix A). In this version of the model, a melt of constant composition is percolated through a matrix of peridotite. The melt is assumed to percolate through the matrix with no reactions taking place, only trace element exchange between the melt and matrix. In reality, some reaction between melt and matrix might be expected to occur, such as the pyroxene dissolution reaction modelled by Kelemen et al. (1990). However, the considerable uncertainty in the phase equilibria of the above hypothetical melts, and the pressure and temperature at which the percolation takes place, make predicting such a reaction rather speculative. Simple percolation with trace element exchange is likely to model the most important features of the melt migration process in the present case. Trace element diffusion in the melt and matrix phases is taken into account by assuming a single diffusion coefficient for all elements in the matrix (10^{-13} cm^2/s) and in the melt (10^{-7}

cm^2/s). The effect of modelling diffusion in the solid matrix is to disperse the "fronts" of trace elements in the melt, thereby smoothing the concentration variations in the melt (Navon and Stolper, 1987). Two melt trace element compositions are used in the modelling, given in Table 6: 1) SA 3-11 glass veins, which are similar in composition to typical alkali basalt, and 2) the melt calculated to be in equilibrium with SAV 1-28 cpx, similar in its trace element composition to carbonatites (Nelson et al., 1988). In all cases, the matrix mineralogy is that calculated from the polybaric melting model for SAV 1-27 cpx (Fig. 10), and the matrix trace element composition is that in equilibrium with SAV 1-27 cpx (Fig. 1h). The results of this modelling are presented in Figs. 11 and 12.

By examining the behavior of the rare earth elements, it is apparent that some features of the melt percolation process are common to the alkali basalt and carbonatite cases, in particular the evolution of the matrix REE patterns with time (Figs. 11 and 12). Early in the percolation process, the LREE concentrations are elevated, with little change in the concentrations of the HREE (ex. SAV 1-46 cpx 3&5, Fig. 1n). Later in the process, the concentrations of all the REE are increasing (ex. SAV 1-46 cpx 2&4, Fig. 1n). Late in the percolation process, as the concentrations of the LREE approach equilibrium values, the REE patterns are characterized by large variations in the HREE, with little LREE variation (e.g. SAV 1-41 Fig. 1L). By varying such parameters as the matrix porosity, melt velocity, and percolation distance in the matrix, an infinite degree of variations of these three characteristics can be created. In addition, variable degrees of Zr and Ti depletion are possible, provided the matrix has positive anomalies for Zr and Ti in its solid/melt partitioning pattern (Fig. 10). Despite the ease with which the REE can be fractionated from Zr and Ti in this process (Fig. 11), the combination of extremely high LREE concentrations and extremely low Ti concentrations in some samples (SAV 1-1, SAV 1-28, TBA 4-11, TBA 5-4) require that the very high LREE and very low Zr and Ti concentrations be characteristics of the input melt (ex. Fig. 9b). Figure 12 shows the obvious fact that extreme LREE enrichment with concomitant Zr and Ti depletion can be accomplished by percolation of a carbonatitic melt (e.g. see Fig. 4i). In addition, these samples very commonly contain substantial amounts of Ba concentrated in inclusions, cracks, and grain boundaries. Although this Ba is not present in the cpx crystal structure, the measured intensity of Ba during ion microprobe analysis would be equivalent to 5-40 ppm (compared with <1 ppm in typical LREE enriched cpx, Zindler and Jagoutz, 1988). Combined with the presence of fluid inclusions (likely CO_2) present in those samples with very high LREE concentrations, this provides evidence for a volatile-rich melt at depth which is probably very similar in its trace element characteristics to carbonatite melt.

124

	SA 3-11 glass veins	SAV 1-28 "melt"
La	165	1650
Ce	314	2009
Nd	136	556
Zr	532	441
Sm	25	76
Eu	7.3	14.6
Ti	29200	1960
Dy	17.2	22.9
Er	11.8	8.5
Yb	6.8	8.9

Table 6. Trace element concentrations (ppm) of melts used in the percolation model. SA 3-11 veins column is the measured composition of glass veins and patches in SA 3-11 xenolith. SAV 1-28 "melt" is the hypothetical melt in equilibrium with SAV 1-28 cpx, calculated from the cpx/melt partition coefficients given in Table 5.
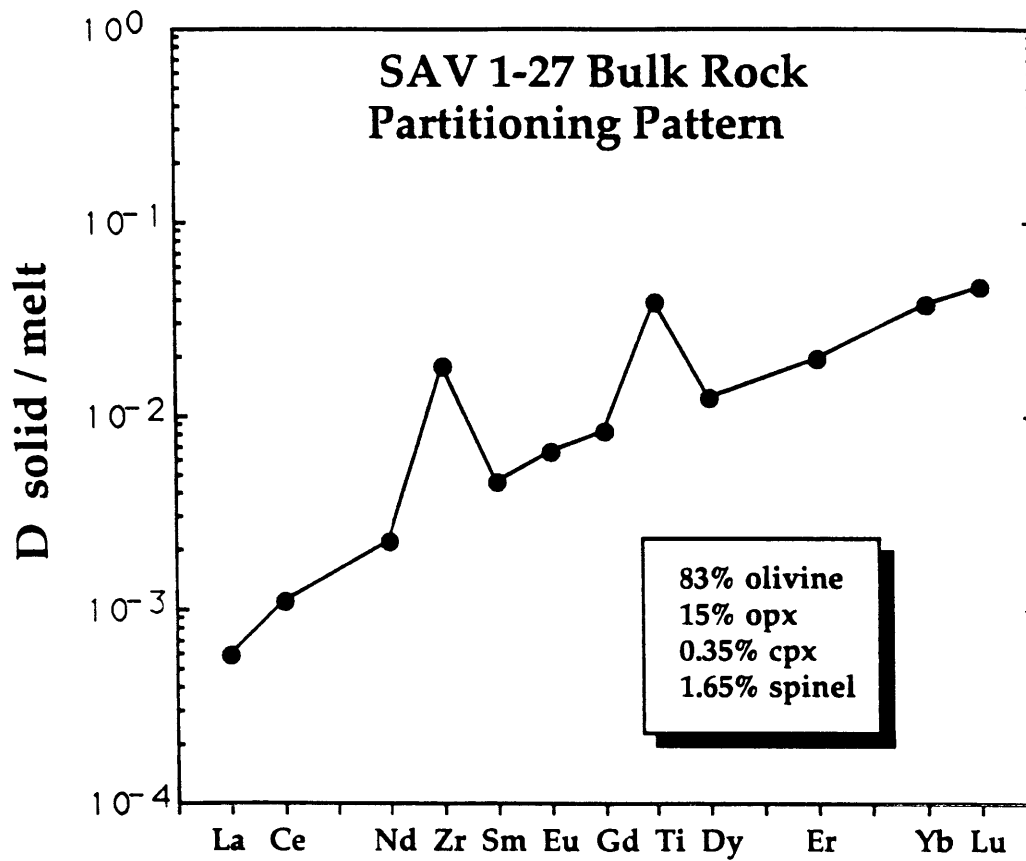
Figure 10. Bulk solid/melt partition coefficient pattern for the model bulk
rock in equilibrium with SAV 1-27 clinopyroxene. The mineralogy is that
calculated from the polybaric melting model, and the mineral/melt partition
coefficients are from Table 4. This partitioning pattern is characteristic of
harzburgite (olivine+opx mineral assemblage), with high values of $D(Zr)$ and
$D(Ti)$ relative to $D(Sm)$ and $D(Dy)$, respectively.
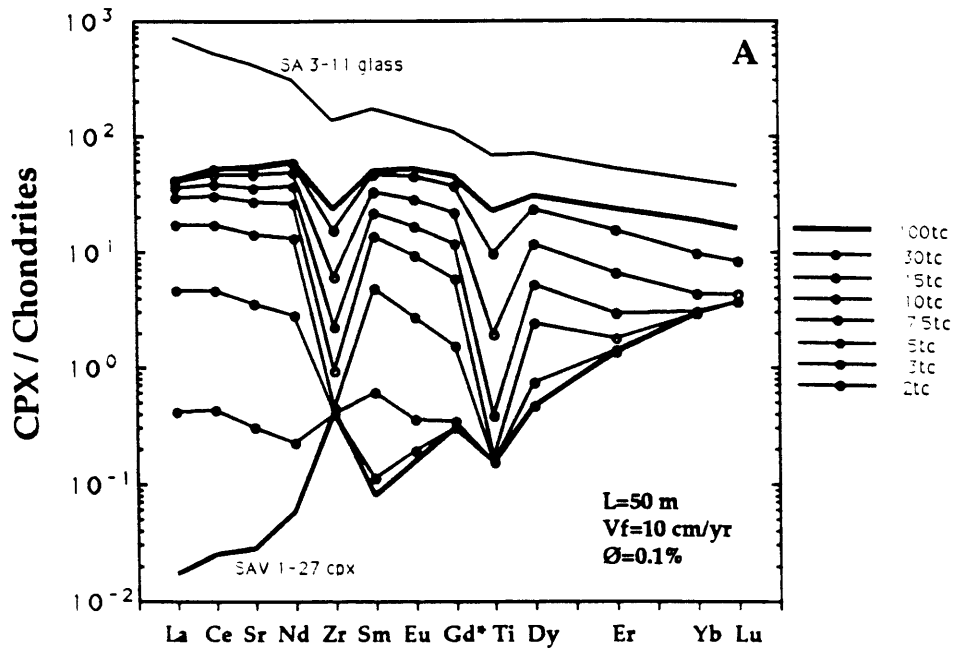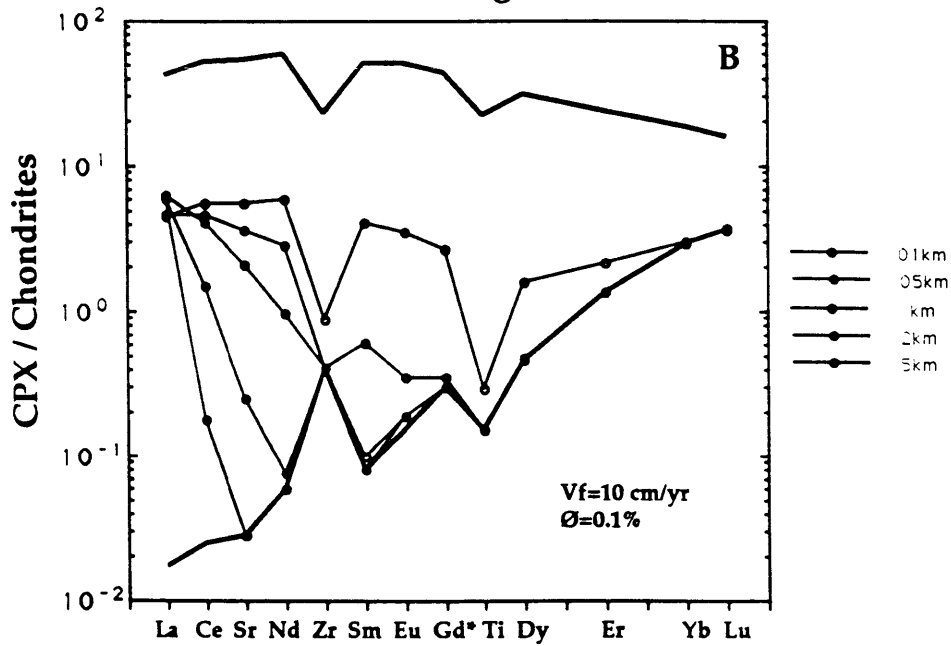
Figure 11. Progressive trace element enrichment in clinopyroxene due to the percolation of alkali basalt (trace element composition of SA 3-11 glass veins) through the model SAV 1-27 depleted harzburgite, calculated according to the model of Navon and Stolper (1987). Heavy lines represent SAV 1-27 cpx (lower line) and cpx in equilibrium with the melt (upper line). A) Trace element evolution with time of cpx in the matrix at a distance of 50 meters from the point of melt input. Melt velocity is 10 cm/yr, porosity (melt fraction) is 0.1%, and tc=50 years. Because the matrix has high values for D(Zr) and D(Ti) between harzburgite and basalt, depletions in Zr and Ti are easily created in the matrix. B) Trace element patterns of cpx in the matrix at various distances from the point of melt input, all with similar La concentrations. This demonstrates that the LREE are increasingly fractionated with increasing distance from the melt input point, resulting in very steep LREE patterns. Melt velocity is 10 cm/yr and porosity is 0.1%.
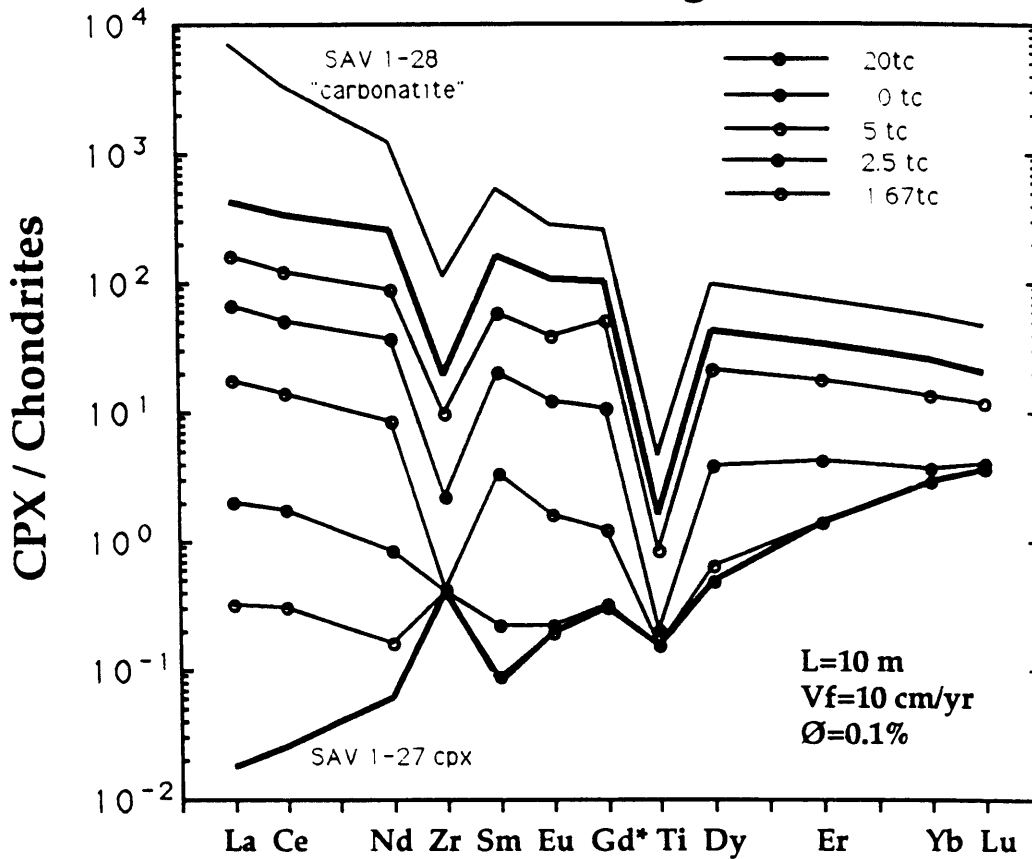
Figure 12. Trace element evolution with time of clinopyroxene in harzburgite due to percolation of a melt with trace element characteristics of carbonatite, calculated using the model of Navon and Stolper (1987). Model "carbonatite" is the hypothetical melt in equilibrium with SAV 1-28 clinopyroxene, and the matrix is the same as in Fig. 11. Trace element patterns in clinopyroxene calculated at a distance of 10 meters from point of melt input. Melt velocity is 10 cm/yr, porosity is 0.1%, and tc=10 years.

7. Implications for Melting and Melt Segregation in the Samoa and Tubaui Mantle Plumes

In the trace element modelling from the previous section, non-modal ploybaric fractional melting was successfully used to model the trace element characteristics of the Savaii and Tubuai Group 1 xenolith clinopyroxenes. The issue of a lithospheric versus asthenospheric origin for these xenoliths must now be addressed. Based on the trace element modelling presented in the previous section, several features of the melting histories experienced by the Group 1 xenoliths favor an asthenospheric origin.

A notable feature of the Group 1 hotspot xenoliths is the large degrees of melting calculated from the modelling. The Tubuai Group 1 cpx patterns are modelled by 17-28% total melting (Fig. 7a-h), and the Savaii Group 1 cpx signatures require 33-42% total melting (Fig. 8a-e). These degrees of melting are higher than the estimates of Johnson et al. (1990), who calculated a range of 5-20% total melting for abyssal peridotites far from hotspots, and about 20% total melting for abyssal peridotite samples from the near-hotspot Bouvet and DiscoveryII fracture zones. Thus, the Tubuai and Savaii xenoliths have experienced 8-22% more melting than the abyssal peridotite samples of Johnson et al. (1990). As pointed out by Dick et al. (1984), abyssal peridotites represent the end-points of melting, in that these samples originate from the top of the mid-ocean ridge melting column, and thus represent the mantle which has experienced the most melting. Thus far, no abyssal peridotite samples have been found with trace element patterns indicative of the degrees of melting required by the Tubuai and Savaii xenoliths. However, it should be noted that the abyssal peridotite samples studied by Johnson et al. (1990) were dredged from fracture zones, where the extent of melting of the mantle may be less than at the ridge axis between fracture zones. Thus far, no abyssal peridotites dredged from the ridge axis have been analyzed for trace elements, and so we cannot definitively say whether the Johnson et al. samples represent the most depleted abyssal peridotites. In addition, abyssal peridotites from the fast-spreading East Pacific Rise have not been analyzed for their trace element compositions. Given the faster spreading rate of the EPR compared with the spreading rates of the ridge systems from which the Johnson et al. peridotites were dredged, it is possible that the Pacific lithospheric mantle may have started melting deeper (i.e. within the garnet lherzolite stability field) and melted to a larger degree than the peridotite samples of Johnson et al. (1990).

A lithospheric origin for the Tubuai xenoliths is supported by the $^{187}Os/^{186}Os$ ratios of two xenoliths from this island (Table 3). As shown in Fig. 13, TBA 1-7, with a depleted garnet-like trace element pattern, and TBA 4-11, with a carbonatitic pattern, both have $^{187}Os/^{186}Os$ ratios within the range of estimates of depleted mantle (e.g. Martin et al.,

1992), and distinctly lower than $^{187}Os/^{186}Os$ measurements of basalts from Tubuai (Hauri and Hart, 1992; Chapter 4). Though the Pb isotopic composition of TBA 4-11 is within the range of Tubuai basalts, it is very likely that this is a metasomatic signature, as outlined above. Based on this low $^{187}Os/^{186}Os$ relative to the Tubuai basalts, it would appear that the carbonatite melt which resulted in the TBA 4-11 trace element signature may have had a low Os concentration or low $^{187}Os/^{186}Os$ (possibly due to percolation); in any case, this melt was ineffective in imprinting the high $^{187}Os/^{186}Os$ Tubuai signature on this xenolith. The $^{187}Os/^{186}Os$ ratios of two xenoliths from Savaii (SAV 1-27, depleted garnet-like pattern; SAV 1-1, carbonatitic pattern) are within the range of $^{187}Os/^{186}Os$ measurements of Savaii basalts (Hauri and Hart, 1992; Chapter 4); however, they are also within the range of depleted mantle estimates, so ruling out a lithospheric origin for these xenoliths remains problematic. It is interesting to note, however, that the depleted xenolith SAV 1-27 has a very low $^{187}Os/^{186}Os$ of 1.018, which is near the lowest $^{187}Os/^{186}Os$ ratio so far measured in a Savaii basalt (1.026, Chapter 4). In any case, the the extremetly high degrees of melting calculated for the Savaii xenoliths suggests a mantle plume origin for these xenoliths.

It appears that fractional melting was an important melting process in the Samoan mantle plume and, by analogy, possibly other hotspots as well. This conclusion is supported by the coupled fractionations of Sm/Nd and Lu/Hf in oceanic basalts (Salters and Hart, 1989). In addition, the xenolith cpx trace element patterns require that melting took place in the presence of garnet. The role of garnet in the generation of hotspot magmas has been simultaneously supported by trace element evidence (ex. Feigenson, 1986; Frey and Roden, 1987), and refuted from experimental petrological studies which have failed to find olivine-opx-cpx-garnet multiple saturation in proposed primary magma compositions (ex. Green and Ringwood, 1967; Eggins, 1992). The process of fractional melting requires that erupted melts be some aggregate of instantaneous melts, probably generated at a range of pressures and temperatures. As pointed out by Eggins (1992), this fact may preclude the existence of equilibrium with a garnet lherzolite mineral assemblage. Fractional melting in mantle plumes is consistent with the constraints available from experimental studies on primary magma compositions, trace element studies of hotspot basalts, and the trace element systematics of oceanic island peridotite xenoliths. If instead some of the LREE-depleted xenoliths are fragments of oceanic lithosphere formed during MORB genesis, then the trace element data presented here provide unequivocal evidence for the role of garnet in MORB genesis, in agreement with Salters and Hart (1989).

The model of melt percolation through harzburgite developed in the previous section was shown to be very efficient at creating depletions in Zr and Ti, relative to Sm

and Dy, as previously demonstrated by Keleman et al. (1990). In addition to interphase partitioning as advocated by McDonough et al. (1991), this percolation phenomena may provide an explanation for the widespread presence of Ti and Zr depletions in peridotite clinopyroxenes (Salters and Shimizu, 1988). This is likely to be an important phenomena in creating Zr and Ti depletions especially in xenolith cpx, since the fragments of peridotite entrained in erupting magmas originate from the wallrocks of magmatic conduits, and are thus very likely to have experienced exchange or reaction with a magma. This may explain the general dominance of LREE enriched over LREE depleted xenolith samples (Nixon, 1987), as well as LREE depleted over LREE enriched peridotites in peridotite massifs (ex. Frey et al., 1985), and strongly suggests that peridotite xenoliths are inherently not representative of typical mantle peridotite. Instead, by their nature xenoliths are much more likely to represent mantle which has experienced some interaction with magma, though some very LREE-depleted patterns obviously survive.

The melt percolation phenomena evident in the trace element characteristics of the Group 2 and Group 3 clinopyroxenes indicates the existence of migrating melts in the hotspot mantle beneath Tubuai and Savaii. The scarcity of these signatures in abyssal peridotites (Johnson et al., 1990) may suggest that melt extraction processes were less efficient in the Tubuai and Samoa mantle plumes, compared with mid-ocean ridge environment. The Group 2 and 3 trace element patterns are unequivocal evidence for melt components which remain in the mantle, ultimately to be recycled into the mantle via subduction. An obvious consequence is that these trace element signatures may evolve isotopically enriched signatures with time under the proper conditions.

The degree of trace element heterogeneity in some of the samples is quite remarkable (e.g. SAV 1-46). Since most of these analyses were performed on crushed and separated clinopyroxene grains, it is possible that this heterogeneity may actually reflect trace element zoning of larger pyroxene grains. Assuming a diffusion coefficient in cpx (10^{-12} cm^2/s) and an average cpx fragment size of 0.1 cm, this suggests a time scale of about 300 years for the time period of metasomatism and subsequent cooling. In addition, the variety of trace element patterns within some single xenoliths, as well as the distribution of clinopyroxene in patches and small veins within the xenoliths, indicates that the migration of melt through the mantle in the vicinity of these xenoliths did not take place entirely by porous flow, but that the melt had begun to segregate into channels. From petrographic observations, the distribution of cpx is heterogeneous on the scale of centimeters in most of the xenoliths. This suggests that the length scale for channel spacing at the initiation of channelized flow, at least in the vicinity of a magma conduit, is equivalent to the centimeter-scale sizes of the individual xenolith hand specimens.
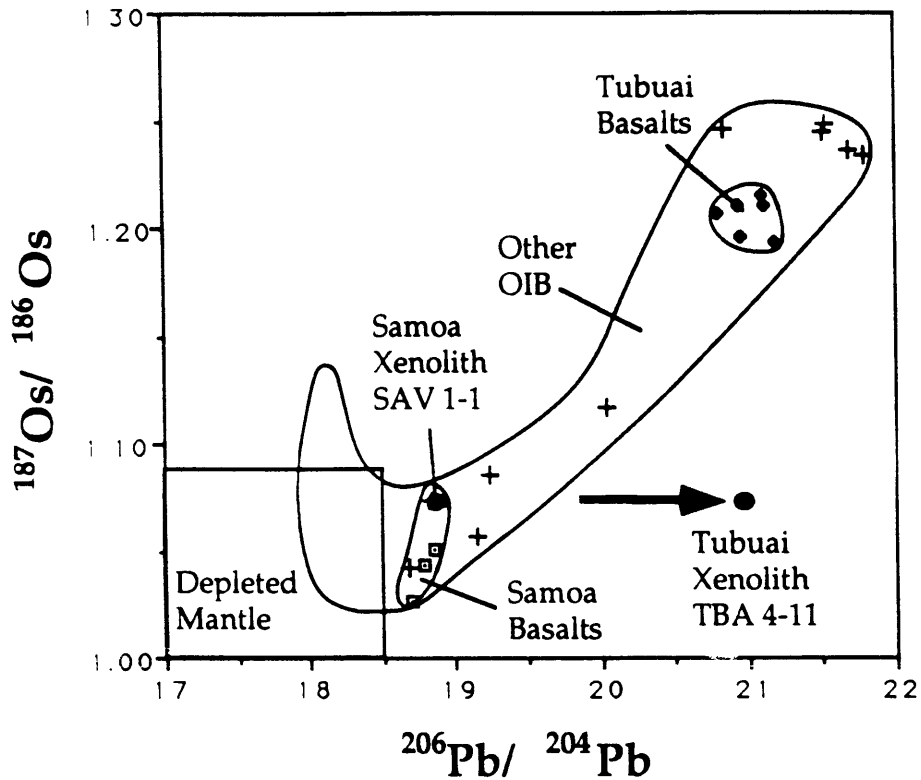
Figure 13. Os and Pb isotope data for xenoliths from Samoa and Tubuai (black dots) relative to basalts from these islands (squares for Samoa, diamonds for Tubuai, crosses for other islands, Chapter 4). Box encloses estimates of the Os-Pb isotopic composition of the depleted mantle (Martin et al., 1990; Chapter 4). Arrow show the direction of change of the isotopic composition of depleted mantle metasomatized by percolating Tubuai basalts.
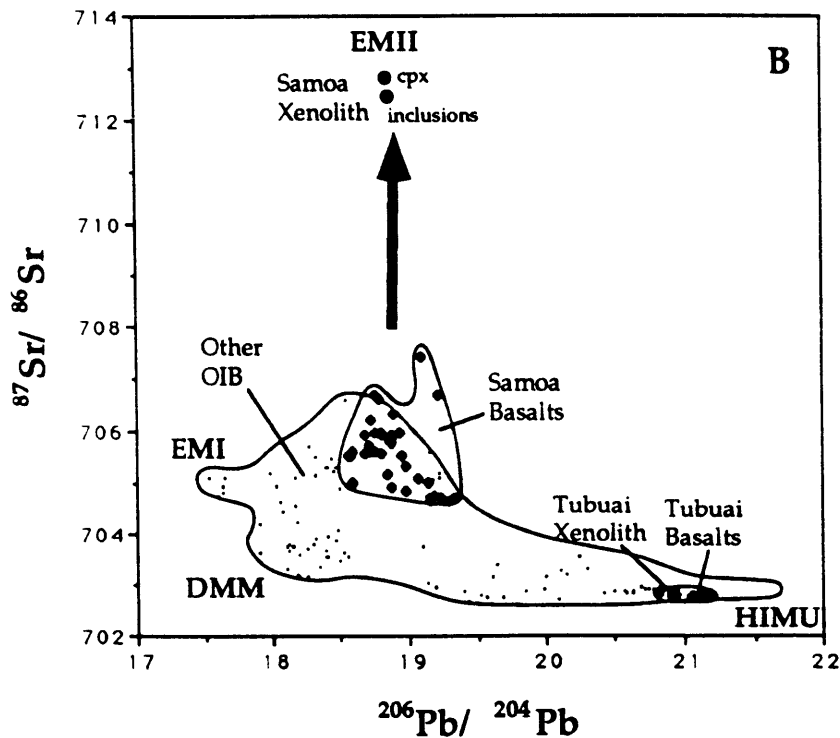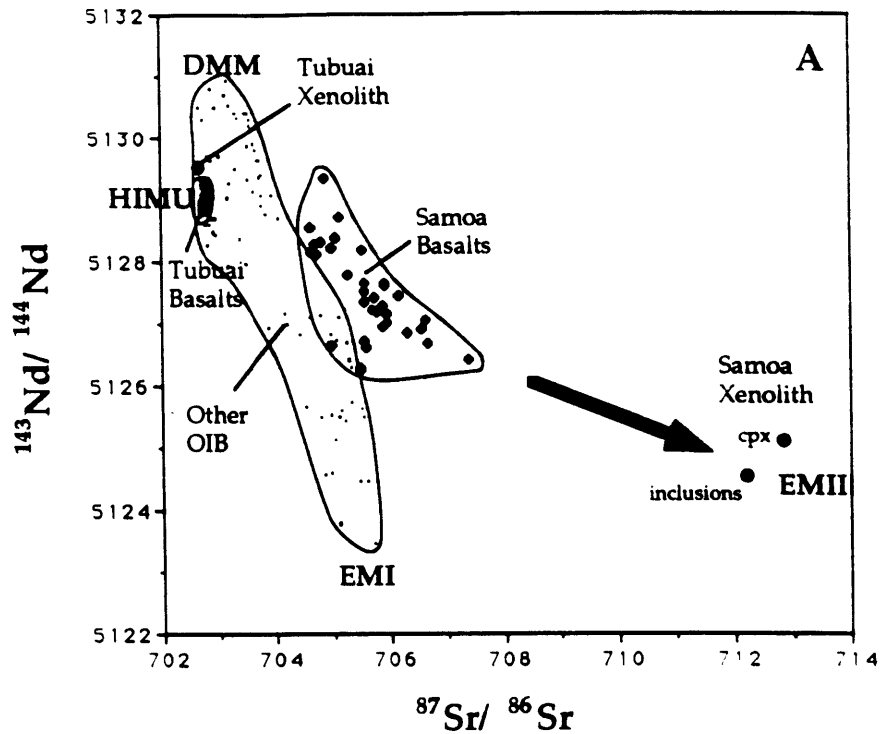
Figure 14. A) Sr-Nd and B) Sr-Pb isotope plots of cpx separates from Samoa and Tubuai xenoliths, relative to fields for Samoa and Tubuai basalts, and other OIBs. The data for TBA 4-11 lies within the field of Tubuai basalts, whereas the data for SAV 1-1 lie on an extension of the Samoa basalt array to much higher $^{87}Sr/^{86}Sr$ and lower $^{143}Nd/^{144}Nd$. The high $^{87}Sr/^{86}Sr$, low $^{143}Nd/^{144}Nd$, and high $^{207}Pb/^{206}Pb$ are broadly similar to modern oceanic sediments (Wright and White, 1987).

The trace element characteristics of the Group 3b samples SAV 1-12, SAV 3-3 #1, and SAV 1-36 #4 demonstrates the suitability of Tubuai and Samoa alkali basalts as the percolating melts which generated many of the Group 2 trace element patterns. However, the clinopyroxenes listed in Fig. 9b indicate the presence of a melt with a trace element composition very similar to carbonatite melt (Nelson et al., 1988). There are basically two origins for carbonatite magma: 1) immiscible exsolution of carbonatite magma from CO_2 rich nephelinite at pressures of 2-25 kilobars (Baker and Wyllie, 1990); and 2) small degree partial melt of carbonated peridotite (Wallace and Green, 1988). In addition, a small degree partial melt of carbonated peridotite will evolve toward nephelenitic composition with increasing degree of melting, resulting in a compositional continuum, probably in terms of trace as well as major elements, between carbonatite melt and nephelinite. Such a carbonate rich melt could also create the trace element patterns of the Group 3b clinopyroxenes. The isotopic compositions of two Group 3b clinopyroxenes (TBA 4-11, SAV 1-1, Table 3) indicate that the enriched endmember isotopic compositions evident at Tubuuai and Savaii are related to these carbonatitic compositions. In particular, the extreme $^{87}Sr/^{86}Sr$ and $^{143}Nd/^{143}Nd$ isotopic compositions of the cpx and inclusions from SAV 1-1 indicates that an isotopically enriched, volatile-rich component was involved in producing melts with very high concentrations of LREE (and Sr, U, Th, and Pb). In addition, since carbonatites are only rarely observed on oceanic islands, carbonatitic melts apparently are not generally erupted in their pure form, but are mixed with other, less isotopically extreme melt fractions, ultimately to be erupted as a basaltic lava at the surface. This interpretation is consistent with the identification of fractional melting as the process responsible for creating the LREE depleted Group 1 signatures.

Irrespective of the mechanism of origin of the carbonatitic melts, it is clear that the isotopically enriched endmember components beneath both Tubuai and Samoa are volatile (CO_2) rich. It is important to ascertain the provenance of this volatile-rich mantle, whether it is a widespread component in the upper mantle, or whether it is restricted to the Tubuai and Samoa mantle plumes. The low concentrations of CO_2, H_2O, and CH_4 in mid-ocean ridge basalts (Moore, 1970; Byers et al., 1986; Michael, 1988) suggests a depletion of volatiles in the upper mantle sources of MORB relative to the higher volatile concentrations in plume-related basalts (Moore and Schilling, 1973; Byers et al., 1985). The presence of a carbonatitic component in the mantle sources of both Tubuai and Savaii argues against a direct relationship between this component and the trace element characteristics which have resulted in the different endmember isotopic compositions of these islands, since these endmember isotope signatures require very different parent/daughter ratios. This indicates

that, although the Tubuai and Samoa plume mantles are volatile rich, the carbonatitic signatures are the result of magma generation processes operative in these hotspots.

The presence of volatiles in these hotspots has important implications for melting in mantle plumes, as discussed for Hawaii by Wyllie (1988). The mantle at the plume axis (about 1500°C) will cross the solidus of peridotite+CO_2+H_2O at a depth of approximately 350 km (Boettcher et al., 1980; Olafsson and Eggler, 1983; Falloon and Green, 1989), generating a small degree partial melt which is rich in CO_2, and may approach a carbonatitic composition (Wallace and Green, 1988). With increasing degrees of fractional melting, as the volatile component is segregated from the melting zone, the solidus of peridotite will shift toward the anhydrous peridotite solidus, requiring further decompression before larger melt fractions are generated. The result is a large region of the mantle plume which is generating small melt fractions, and a much smaller region of the plume which is above the anhydrous peridotite solidus, generating larger melt fractions, with the compositions of the erupted melt products strongly dependent on how the melts are aggregated. The ultimate origins for the volatiles in the Tubuai and Samoa mantle plumes may be in subducted materials recycled into the asthenosphere, and incorporated in upwelling mantle plumes.

8. Conclusions

Clinopyroxenes in peridotite xenoliths from the islands of Savaii and Tubuai display a large degree of trace element heterogeneity, both between and within single xenolith hand specimens. Trace element modelling of the subset of clinopyroxenes with depleted signatures indicates that these samples have experienced large degrees of polybaric fractional melting (18%-42%) within the stability fields of garnet lherzolite and spinel lherzolite. In particular, the extremely fractionated trace element patterns of the Savaii depleted clinopyroxenes requires that these peridotites melted to the point of clinopyroxene exhaustion while in the garnet stability field, leaving a residue of olivine+opx+garnet, which then experienced further melting in the spinel lherzolite field after breakdown of garnet to pyroxene and spinel. These characteristics have thus far not been found in abyssal peridotites, and thus a mantle plume origin may be indicated for these xenolith samples, as well as other LREE enriched xenoliths with clinopyroxene HREE and Ti concentrations similar to the depleted (Group 1) signatures. The high degrees of melting calculated for these samples is in apparent conflict with the low degrees of melting suggested by the trace element modelling of oceanic basalts (ex. Feigenson, 1986; Frey and Roden, 1987). In addition, the requirement of melting in the garnet stability field conflicts with the lack of experimental evidence for equilibrium of primary magma compositions

135

with garnet lherzolite (Green and Ringwood, 1967; Eggins, 1992). However, both of these apparent conflicts can be reconciled with the xenolith data, because fractional melting requires that the erupted basaltic melts are aggregates (mixtures) of many small melt fractions.

The variable degrees of LREE enrichment in most of the Savaii and Tubuai xenoliths is consistent with the migration of basaltic melts through harzburgite. The abundance of LREE enriched xenoliths, and their relative scarcity in abyssal peridotites (REF) indicates that melt extraction is less efficient from mantle plumes than from the mid-ocean ridge mantle. As a result, melt components with fractionated trace element signatures remain in the mantle after the creation of a hotspot volcano, and this material is available for recycling back into the mantle, potentially to create enriched isotopic signatures under the proper conditions of preservation.

Based on the heterogeneous distribution of clinopyroxene in the xenoliths, the mechanism of melt migration was probably channelized flow near the magma conduits from which the xenoliths were derived. The percolation of basalt through harzburgite can explain the widespread occurrence of clinopyroxenes from mantle xenoliths with Zr and Ti depletions relative to the REE. However, several of the clinopyroxene trace element patterns, with very high LREE concentrations and extremely low Zr/Sm and Ti/Dy ratios, require that the percolating melt have the trace element signature of carbonatite melt. This is supported by high concentrations of Sr in these clinopyroxenes, as well as the presence of large amounts of Ba along grain boundaries, and olivine rich in fluid inclusions (probably CO_2). In addition, the association of near-endmember isotopic signatures in these "carbonatitic" clinopyroxenes (EMII and HIMU) demonstrates the volatile rich nature of the mantle plume sources of the Samoa and Tubaui endmember basalts. These volatiles may have their origins in subducted components recycled into the source regions of the Samoa and Tubuai mantle plumes.

References

Baker, M. and P. J. Wyllie (1990) Liquid immiscibility in a nephelenite-carbonate system at 25 kbar and implications for carbonatite origin. Nature, **346**, 168-170.

Bodinier, J. L., G. Vasseur, J. Vernieres, C. Dupuy and J. Fabries (1990) Mechanisms of mantle metasomatism: Geochemical evidence from the Lherz orogenic peridotite. J. Petrol., **31**, 597-628.

Boettcher, A. L., J. K. Robertson and P. J. Wyllie (1980) Studies in synthetic carbonatite systems: solidus relationships for $CaO-MgO-CO_2-H_2O$ to 40 kbar and $CaO-MgO-SiO_2-CO_2-H_2O$ to 10 kbar. J. Geophys. Res., **85**, 6937-6943.

Brousse, R., J. P. Chevalier, M. Denizot, B. Richer de Forges and B. Salvat (1980) Etude geomorphologique de l'ile de Tubuai (Australes). Cah. Pacifique, **2**, 1-54.

Byers, C.D., M.O. Garcia, and D.W. Muenow (1985) Volatiles in pillow rim glasses from Loihi and Kilauea volcanoes, Hawaii. Geochim. Cosmochim. Acta, **49**, 1887-1896.

Byers, C.D., M.O. Garcia, and D.W. Muenow (1986) Volatiles in basaltic glasses from the East Pacific Rise at 21°N: implications for MORB sources and submarine lava flow morphology. Earth Planet. Sci. Lett., **79**, 9-20.

Canil, D. (1991) Experimental evidence for the exsolution of cratonic peridotite from high-temperature harzburgite. Earth Planet. Sci. Lett., **106**, 64-72.

Chase, C. G. (1981) Oceanic island lead: two-stage histories and mantle evolution. Earth Planet. Sci. Lett., **52**, 277-284.

Cox, K. G., M. R. Smith and S. Beswetherick (1987). Textural studies of garnet lherzolites: evidence from high-temperature harzburgites. in *Mantle Xenoliths*. New York, John Wiley & Sons. 537-550.

Diraison, C. (1991) Le volcanisme aerien des Archipels Polynesiens de la Societe, des Marquises et des Australes-Cook. Ph.D. Thesis, Universite de Bretagne Occidentale.

Duncan, R. A. (1985). Radiometric ages from volcanic rocks along the New Hebrides-Samoa lineament. in *Geological Investigations of the Northern Melanesian Borderland*. Houston, Texas, Circum-Pacific Council for Energy and Resources. 67-76.

Duncan, R. A. and I. McDougall (1976) Linear Volcanism in French Polynesia. J. Volcan. Geotherm. Res., **1**, 197-227.

Dunn, T. (1987) Partioning of Hf, Lu, Ti and Mn between olivine, clinopyroxene and basaltic liquid. Contrib. Mineral. Petrol., **96**, 476-484.

Dupuy, C., H. G. Barsczus, J. Dostal, P. Vidal and J.-M. Liotard (1989) Subducted and recycled lithosphere as the mantle source of ocean island basalts from southern Polynesia, central Pacific. Chem. Geol., **77**, 1-18.

Eggins, S. M. (1992) Petrogenesis of Hawaiian tholeiites: 1, phase equilibria constraints. Contrib. Mineral. Petrol., **110**, 387-397.

137

Falloon, T. J. and D. H. Green (1989) The solidus of carbonated, fertile peridotite. Earth Planet. Sci. Lett., **94**, 364-370.

Farley, K. A., J. Natland and H. Craig (1992) Binary mixing of enriched and undegassed (primitive?) mantle components (He, Sr, Nd, Pb) in Samoan lavas. Earth Planet. Sci. Lett., **111**, 183-199.

Feigenson, M. D. (1986) Constraints on the origin of Hawaiian lavas. J. Geophys. Res., **91**, 9383-9393.

Frey, F. A. and M. F. Roden (1987). The mantle source for the Hawaiian islands: Constraints from the lavas and ultramafic inclusions. in *Mantle Metasomatism*. London, Academic Press. 423-463.

Frey, F. A., J. Suen and H. W. Stockman (1985) The Ronda high temperature peridotite: Geochemistry and petrogenesis. Geochim. Cosmochim. Acta, **49**, 2469-2491.

Fujimaki, H., M. Tatsumoto and K. Aoki (1984) Partition coefficients of Hf, Zr and REE between phenocrysts and groundmasses. J. Geophys. Res., **89**, 662-672.

Green, D. H. and A. E. Ringwood (1967) The genesis of basaltic magmas. Contrib. Mineral. Petrol., **15**, 103-190.

Hart, S. R. and T. Dunn (1992) Experimental clinopyroxene/melt partitioning for 24 trace elements. Contrib. Mineral. Petrol., (in press)

Hauri, E. H. and S. R. Hart (1992) Re-Os isotope systematics of EMII and HIMU oceanic island basalts from the south Pacific Ocean. Earth Planet. Sci. Lett., (in press)

Hofmann, A. W. (1984) Mantle evolution by crustal recycling or by mantle metasomatism? (abstr.). Terra Cognita, **4**, 82.

Hofmann, A. W., K. P. Jochum, M. Seufert and W. M. White (1986) Nb and Pb in oceanic basalts: new constraints on mantle evolution. Earth Planet. Sci. Lett., **79**, 33-45.

Irving, A. J. (1978) A review of experimental studies of crystal/liquid trace element partitioning. Geochim. Cosmochim. Acta, **42**, 743-770.

Johnson, K. T. M., H. J. B. Dick and N. Shimizu (1990) Melting in the oceanic upper mantle: an ion microprobe study of diopsides in abyssal peridotites. J. Geophys. Res., **95**, 2661-2678.

Kelemen, P. B., K. T. M. Johnson, R. J. Kinzler and A. J. Irving (1990) High Field strength element depletions in arc basalts due to mantle-magma interaction. Nature, **345**, 521-524.

Lindsley, D. H. and D. J. Andersen (1983) A two-pyroxene thermometer. J. Geophys. Res. Suppl., **88**, A887-A906.

Liotard, J.-M. and H. G. Barsczus (1989) Genese des foidites phonolitiques de Tubuai (Archipel des Australes, Ocean Pacific Sud): Intervention d'un magma d'affinite carbonatitique. C. R. Acad. Sci. Paris, **308**, 1261-1266.

McDonough, W. F., H.-G. Stosch and N. G. Ware (1992) Distribution of titanium and the rare earth elements between peridotitic minerals. Contrib. Mineral. Petrol., **110**, 321-328.

McKay, G. A. (1986) Crystal/liquid partitioning of REE in basaltic systems: extreme fractionation of REE in olivine. Geochim. Cosmochim. Acta, **50**, 69-79.

Michael, P. J. (1988) The concentration, behavior and storage of H_2O in suboceanic mantle: Implications for mantle metasomatism. Geochim. Cosmochim. Acta, **52**, 555-566.

Moore, J. G. (1970) Water content of basalt erupted on the ocean floor. Contrib. Mineral. Petrol., **28**, 272-279.

Moore, J. G. and J.-G. Schilling (1973) Vesicles, water, and sulfur in Reykjanes Ridge basalts. Contrib. Mineral. Petrol., **41**, 105-118.

Nakamura, Y. and M. Tatsumoto (1988) Pb, Nd, and Sr isotopic evidence for a multicomponent source for rocks of Cook-Austral Islands and heterogeneities of mantle plumes. Geochim. Cosmochim. Acta, **52**, 2909-2924.

Navon, O. and E. Stolper (1987) Geochemical consequences of melt percolation: the upper mantle as a chromatographic column. J. Geol., **95**, 285-307.

Nelson, D. R., A. R. Chivas, B. W. Chappell and M. T. McCulloch (1988) Geochemical and isotopic systematics in carbonatites and implications for the evolution of ocean-island sources. Geochim. Cosmochim. Acta, **52**, 1-17.

Nicholls, I. A. and K. L. Harris (1980) Experimental rare earth element partition coefficients for garnet, clinopyroxene and amphibole coexisting with andesitic and basaltic liquids. Geochim. Cosmochim. Acta, **44**, 287-308.

Nixon, P. H. (ed.) (1987). *Mantle Xenoliths*. New York, John Wiley and Sons.

O'Hara, M. J. (1985) Importance of the 'shape' of the melting regime during partial melting of the mantle. Nature, **314**, 58-62.

Olafsson, M. and D. H. Eggler (1983) Phase relations of amphibole, amphibole-carbonate, and phlogopite-carbonate peridotite: petrologic constraints on the asthenosphere. Earth Planet. Sci. Lett., **64**, 305-315.

Palacz, Z. A. and A. D. Saunders (1986) Coupled trace element and isotope enrichment in the Cook-Austral-Samoa islands, southwest Pacific. Earth Planet. Sci. Lett., **79**, 270-280.

Poreda, R., J. G. Schilling and H. Craig (1986) Helium and hydrogen isotopes in ocean-ridge basalts north and south of Iceland. Earth Planet. Sci. Lett., **78**, 1-17.

Richardson, S. H., A. J. Erlank and S. R. Hart (1985) Kimberlite-borne garnet peridotite xenoliths from old enriched subcontinental lithosphere. Earth Planet. Sci. Lett., **75**, 116-128.

Ringwood, A. E. (1979). *Origin of the Earth and Moon*. New York, Springer-Verlag.

Salters, V. J. M. (1989) The use of Hf-isotopes and High Field Strength Elements to constrain magmatic processes and magma sources. PhD, Massachusetts Institute of Technology.

Salters, V. J. M. and N. Shimizu (1988) World-wide occurrence of HFSE-depleted mantle. Geochim. Cosmochim. Acta, 52, 2177-2182.

Salters, V.J.M. and Hart, S.R. (1989) The hafnium paradox and the role of garnet in the MORB source, Nature, 342, 420-422.

Shaw, D. M. (1970) Trace element fractionation during anatexis. Geochim Cosmochim Acta, 34, 237-243.

Shimizu, N. and S. R. Hart (1982) Applications of the ion micro-probe to geochemistry and cosmochemistry. Ann Rev Earth Plan Sci, 10, 483-526.

Stosch, H.-G. (1982) Rare earth element partitioning between minerals from anhydrous spinel peridotite xenoliths. Geochim. Cosmochim. Acta, 46, 793-811.

Takahashi, E. (1986) Melting of a dry peridotite KLB-1 up to 14 GPa: implications for the origin of peridotite upper mantle. J. Geophys. Res., 91, 9367-9382.

Turner, D. L. and R. D. Jarrard (1982) K-Ar dating of the Cook-Austral chain: a test of the hot-spot hypothesis. J. Volcan. Geotherm. Res., 12, 187-220.

Vidal, P., C. Chauvel and R. Brousse (1984) Large mantle heterogeneity beneath French Polynesia. Nature, 307, 536-538.

Walker, D. and C. Agee (1989) Partitioning "equilibrium", temperature gradients, and constraints on Earth differentiation. Earth Planet. Sci. Lett., 96, 49-60.

Wallace, M. E. and D. H. Green (1988) An experimental determination of primary carbonatite magma composition. Nature, 335, 343-346.

White, W. M. and A. W. Hofmann (1982) Sr and Nd isotope geochemistry of oceanic basalts and mantle evolution. Nature, 296, 821-825.

Wilson, J. T. (1963) A possible origin of the Hawaiian Islands. Can. J. Phys., 41, 863-870.

Wright, E. and W. M. White (1987) The origin of Samoa: new evidence from Sr, Nd and Pb isotopes. Earth Planet. Sci. Lett., 81, 151-162.

Wyllie, P. J. (1988) Solidus curves, mantle plumes, and magma generation beneath Hawaii. J. Geophys. Res., 93, 4171-4181.

Zindler, A. and S. R. Hart (1986) Chemical Geodynamics. Ann. Rev. Earth Planet. Sci., 14, 493-571.

Zindler, A. and E. Jagoutz (1988) Mantle cryptology. Geochim. Cosmochim. Acta, 52, 319-333.

Chapter 4

Re-Os Isotope Systematics of HIMU and EMII Oceanic Island Basalts from the South Pacific Ocean

1. Introduction

The Re-Os isotope system has received considerable attention from the geochemical community over the past 10 years, following the pioneering work of Luck et al., (1980). The β^- decay of ^{187}Re to ^{186}Os produces measurable variations in the abundance of ^{187}Os in samples of natural osmium. The very different behaviors of Re and Os during basaltic melt generation, as well as their siderophile and chalcophile characters, provide information quite different from the other parent-daughter systems (Rb-Sr, Sm-Nd, Lu-Hf, U-Th-Pb). The Re-Os system has been used as a unique tracer in studies of crustal and mantle geochemistry (Palmer et al., 1988; Walker et al., 1988; Walker et al., 1989; Esser, 1990; Martin, 1991; Reisberg et al., 1991; Walker et al., 1991), the geochemistry of ore deposits (Hart et al., 1989; Lambert et al., 1989; Martin, 1989; Hattori et al., 1991), and as a geochronometer for dating ores (Luck et al., 1982; Walker et al., 1991) and terrestrial rocks (Walker et al., 1988; Ravizza et al., 1989; Walker et al., 1989; Walker et al., 1991), as well as providing an estimate for the age of the galaxy (Luck et al., 1983).

Re-Os studies have demonstrated that both oceanic and continental crustal materials have much higher Re/Os ratios than peridotites (Morgan et al., 1981; Esser, 1990; Martin, 1991). Re concentrations in crustal materials are typically 10-100 times higher than peridotites, while Os concentrations are 10-10,000 times lower than peridotites. Thus Re is thought to be moderately incompatible, and Os highly compatible, during melt generation. As a result of such high Re/Os ratios, crustal materials also have much higher ^{187}Os/^{186}Os ratios than peridotites (^{187}Os/^{186}Os = 3 to >100 for crust, ^{187}Os/^{186}Os = <0.90 to 1.10 for peridotites: Walker et al., 1989; Walker et al., 1989; Esser, 1990; Luck et al., 1991; Pearson et al., 1991; Reisberg et al., 1991). The high Re concentrations and high Re/Os ratios of crustal materials, relative to mantle peridotite, make the Re-Os system a potentially powerful tracer for examining crustal recycling in the mantle.

The isotopic signatures of some oceanic islands have been interpreted as being derived from crustal material mixed into the mantle sources of these islands (Hofmann et al., 1980; Chase, 1981; Hofmann et al., 1982). Specifically, the EMII signature of high ^{87}Sr/^{86}Sr and high ^{207}Pb/^{204}Pb ratios (Zindler et al., 1986) has been attributed to the recycling of sediments in the mantle (White et al., 1982; Wright et al., 1987). In addition, the high Pb isotope ratios which characterize the HIMU mantle component (Zindler et al., 1986) have been attributed to subducted oceanic crust (Hofmann et al., 1980; Hofmann et al., 1982). The trace element signatures of HIMU have also been attributed to recycled oceanic lithosphere (Palacz et al., 1986; Dupuy et al., 1989), and a number of other oceanic island isotope signatures have also been attributed to this process (Chase, 1981).

In order to constrain theories of crustal recycling in the mantle, the Re-Os and Sr-Nd-Pb isotope systematics have been investigated in a suite of oceanic island basalts from the south Pacific Ocean. The combined Os, Sr, Nd, and Pb isotope results demonstrate that recycling of oceanic crust is responsible for some of the isotopic heterogeneity observed in the oceanic mantle and place constraints on the composition and age of the recycled crust in the mantle sources of these basalts.

2. Geologic Background

The southern Pacific Ocean is home to many linear island chains of volcanic origin. Previous studies have demonstrated that the age of volcanism decreases monotonically toward the east-southeast end of several of these island chains (Duncan et al., 1974; Duncan et al., 1974; Dalrymple et al., 1975; Duncan et al., 1976; Turner et al., 1982), often with active volcanism at the extreme easterly end (Hekinian et al., 1991), supporting a hotspot origin for these features (Wilson, 1963; Morgan, 1971). At least one exception is the Cook-Austral chain, which contains examples of both young (<1 Ma) and old (20 Ma) islands, and includes islands which display periods of volcanic activity separated by millions of years (e.g. Rurutu, 12.2-8.4 Ma and 1 Ma (Duncan et al., 1976)). However, the islands from Mangaia east to Macdonald display a monotonic age progression consistent with the hotspot theory (Diraison, 1991). Another possible exception is the Samoan chain, in which the lavas of the shield building phase are of progressively younger age to the east-southeast (Duncan, 1985; Natland et al., 1985), yet subsequent volcanism has taken place over a 600 km length of the chain within the last 1 Ma, mostly at the northwest end (Natland, 1980).

In contrast to Hawaii (Macdonald et al., 1964), geochemical studies have demonstrated that volcanism in the south Pacific is dominantly alkalic, with rare examples of tholeiitic volcanism (Duncan et al., 1986). The distinct stages of volcanic activity recognized in the Hawaiian chain are observed at some islands in the south Pacific (Samoa, Marquesas) (Duncan et al., 1986; Wright et al., 1987) but not others (Cook-Australs) (Duncan et al., 1976). Trace element and isotopic studies (Liotard et al., 1986; Palacz et al., 1986; Dupuy et al., 1987; Dupuy et al., 1988; Dupuy et al., 1989) have demonstrated that a large degree of geochemical variability is present in the mantle beneath the south Pacific Ocean, and has been recognized in samples as old as 120 Ma (Staudigel et al., 1991). This variability is manifested in geochemical differences between island chains, as well as extreme variability within single islands (Duncan et al., 1986; Woodhead et al., 1989). In addition, examples of all of the oceanic mantle endmembers as defined by Zindler and Hart (Zindler et al., 1986) are found in the south Pacific (DMM-East Pacific

Rise (White et al., 1987); EMI-Pitcairn (Woodhead et al., 1989); EMII-Samoa, Tahaa (White et al., 1982; Wright et al., 1987); HIMU-Mangaia, Tubuai (Vidal et al., 1984; Nakamura et al., 1988)), as well as islands with elevated $^3He/^4He$ (Samoa, McDonald Seamount, Rapa (Farley et al., 1989; Desonie et al., 1992)). The oceanic mantle in this restricted part of the world is strikingly rich in geochemical diversity.

3. Sample Selection

The basalt samples analyzed in this study were collected in the fall of 1990 specifically for Re-Os analysis. Analyzed samples are from the islands of Savaii (Western Samoa), Rarotonga and Mangaia (Cook Islands), Rurutu and Tubuai (Austral Islands) and Tahaa (Society Islands). The samples were chosen to include islands with known extreme isotopic compositions for $^{87}Sr/^{86}Sr$ (Savaii, Tahaa) and Pb isotopes (Tubuai, Mangaia) in order to search for a crustal signature in these islands.

Due to the high Re/Os ratios measured, the ages of the various islands examined in this study are important, in that samples from the older islands require corrections for radiogenic ingrowth since eruption. Though none of the samples have been directly dated, some constraints on their ages exist from field relations. The samples from Savaii are all young (<1 Ma) shield-capping flows, and two are from historic eruptions. The samples from Rarotonga are from the Te Manga group, dated at 1.2-2.3 Ma (Turner et al., 1982). Reported ages from Tahaa range from 1.1 Ma to 3.4 Ma (Gisbert, 1989). The ages of the samples from Rurutu are not well constrained; the range of possible ages is 0.88-12.8 Ma (Duncan et al., 1976). For Tubuai, reported ages range from 5.7 Ma to 10 Ma (Bellon et al., 1980). The oldest island sampled is Mangaia, with reported ages in the range of 16 to 20 Ma (Dalrymple et al., 1975; Turner et al., 1982). Large amounts of each sample (several kg) were collected, and an emphasis was placed on obtaining fresh samples; in the case of Mangaia, this was possible only by collecting stream cobbles, due to the extent of weathering of the few volcanic outcrops. When possible, several samples rich in olivine and pyroxene phenocrysts were chosen from each island in order to analyze samples with high Os concentrations and low Re/Os ratios, in an attempt to minimize uncertainties in the age corrections. Analytical procedures are given in the appendix.

4. Overview of Re-Os Systematics

Due to the geochemical characteristics of the two elements, the Re-Os isotopic system possesses some unique features which distinguish it from other radiogenic isotopic systems. During partial melting of mantle peridotite, Re behaves as a moderately incompatible element, whereas Os is strongly concentrated in the residue (Morgan, 1986).

As a result, mantle-derived melts are characterized by high Re concentrations and high Re/Os ratios relative to the residues of melting. Segregation of the melt leaves a residue with a lower Re/Os ratio than before melting. The behavior of Os is in contrast to Sr, Nd and Pb, which are partitioned into the magma during melting. The result is a much more extreme parent/daughter fractionation in the Re-Os system than in the other isotopic systems.

Due to its high Re/Os ratio, continental crust develops very high $^{187}Os/^{186}Os$ with time. In a study of continental river sediments and glacial loess deposits, Esser (Esser, 1990) measured $^{187}Os/^{186}Os$ ratios of 5.6 to 13.4 for these sediments, which act as integrators of large areas of continental crust. Though the crust is markedly heterogeneous in Re/Os and $^{187}Os/^{186}Os$ ratios, Esser has suggested a $^{187}Os/^{186}Os$ ratio of 10.5 for average continental crust, as well as average Re (400 ppt) and Os (50 ppt) concentrations (Esser, 1990). This is consistent with the existing measurements of continental crustal material (Morgan et al., 1967; Walker et al., 1989).

In addition to their different behaviors during melting, both Re and Os are chalcophile and strongly siderophile, and thus their geochemical behavior may be dominated by trace metallic or sulfide phases. As a result of this, it is likely that both Re and Os were partitioned strongly into the core early in earth history. The relative abundances of the highly siderophile elements in the mantle are approximately chondritic (Jagoutz et al., 1979; Mitchell et al., 1981; Morgan et al., 1981). Also, the chondrite-normalized abundances of these elements in the mantle (about 10^{-2}) are thought to be too high to reflect equilibrium with either a metallic or sulfur-bearing core. It has been suggested that the mantle budget of these elements was provided by accretion of chondritic material subsequent to core formation (Jagoutz et al., 1979; Morgan, 1985; Morgan, 1986); however, disequilibrium effects, incomplete core segregation, or variable metal/silicate and sulfide/silicate partition coefficients may also account for these abundances (Morgan et al., 1981).

The Os isotopic evolution of the earth through geologic time is currently an issue with considerable uncertainty. Due to the possibility of Re/Os fractionation during accretion and core formation, the Os isotope evolution of the silicate earth may be different from that of the whole earth. Analyses of group IIAB and IIIAB iron meteorites (Horan et al., 1992; Morgan et al., 1992) indicates an initial $^{187}Os/^{186}Os$ of $0.794\pm.010$. The measured present day $^{187}Os/^{186}Os$ ratios of chondritic meteorites range from 1.00 to 1.16 (Luck et al., 1983; Walker et al., 1989), with an average of 1.07. Though an early study of osmiridiums of known age (Allegre et al., 1980) suggested that the upper mantle followed a Re-Os evolution with a present day $^{187}Os/^{186}Os$ of 1.04, subsequent

145

osmiridium studies (Hart et al., 1989; Hattori et al., 1991) have demonstrated significant Os isotopic heterogeneity within and between localities, precluding the identification of a well constrained evolution curve. Luck and Allegre (Luck et al., 1991) have subsequently refined their present-day bulk silicate earth estimate to $^{187}Os/^{186}Os$ = 1.05-1.06 based on analyses of ophiolite peridotites. Martin et al. (Martin et al., 1992) have suggested a present-day value of $^{187}Os/^{186}Os$ = 1.10 for the bulk silicate earth based on analyses of abyssal peridotites and a crust-mantle mass balance. A similar value has been suggested by Martin (1991) for the mantle source of Hawaii based on analyses of basalts with elevated $^3He/^4He$. Present-day measured $^{187}Os/^{186}Os$ ratios for peridotite xenoliths from South Africa and Siberia (Walker et al., 1989; Pearson et al., 1991) lie in the range of <0.90 to 1.07, clearly demonstrating the existence of ancient, low Re/Os mantle in the subcontinental lithosphere. Reisberg et al. (Reisberg et al., 1991) measured $^{187}Os/^{186}Os$ ratios from 0.977 to 1.120 in peridotite samples from the Ronda ultramafic complex. A strong negative correlation of $^{187}Os/^{186}Os$ with Mg# in the peridotites suggests that a $^{187}Os/^{186}Os$ of 1.06-1.08 may be representative of undifferentiated mantle, similar to the ordinary chondrite average of 1.07. In detail, however, the Os isotope evolution of the earth's mantle is only broadly constrained.

5. Results

The Sr, Nd, U, Th and Pb concentrations, and Sr, Nd and Pb isotope results are given in Table 1. The concentrations of these elements are similar to those typically reported for alkali basalts (ex. (Palacz et al., 1986)). $^{238}U/^{204}Pb$ (m) ratios vary from 18-61 and Th/U ratios range from 3.14-4.98. Both ratios are high relative to mid-ocean ridge basalts (Tatsumoto, 1978; Cohen et al., 1980; Condomines et al., 1981; Cohen et al., 1982; Jochum et al., 1983; Newman et al., 1983; Goldstein et al., 1991); differences in source chemistry and melting processes are both likely to account for this. The Sr-Nd-Pb isotope ratios given in Table 1 agree well with previously reported data for these islands (White et al., 1982; Vidal et al., 1984; Palacz et al., 1986; Wright et al., 1987; Nakamura et al., 1988). The islands of Savaii and Tahaa are characterized by very high $^{87}Sr/^{86}Sr$ and high $^{207}Pb/^{204}Pb$, and approach the EMII enriched mantle endmember (Zindler et al., 1986). The values reported here are slightly lower than the most extreme $^{87}Sr/^{86}Sr$ ratios reported from Tutuila, American Samoa (Wright et al., 1987; Farley et al., 1989). The islands of Rurutu, Tubuai and Mangaia are characterized by very radiogenic Pb isotope signatures, and the isotopic composition of Mangaia defines the HIMU (high $^{238}U/^{204}Pb$) endmember (Zindler et al., 1986). The two samples from Rurutu delineate a large fraction

146

Sample	$^{87}Sr/^{86}Sr$	$^{143}Nd/^{144}Nd$	$^{206}Pb/^{204}Pb$	$^{207}Pb/^{204}Pb$	$^{208}Pb/^{204}Pb$	Sr (ppm)	Nd (ppm)	U (ppm)	Th(ppm)	Pb (ppm)
Savaii										
SAV-B-5	.70556	.512732	18.693	15 598	38 938	392	25.32	.628	2.75	2.10
SAV-B-6	.70578	.512716	18 860	15.672	39 276	468	29.86	.693	3.27	2 48
SAV-B-7	.70653	.512689	18.789	15.650	39 160	551	49.53	1.55	4 81	2.86
SAV-B-8	.70631	.512685	18 889	15.616	39.144	711	49.72	1.54	6.24	4.90
SAV-B-15	.70600	.512890	18.797	15.606	39.038	570	52.53	1.38	5.18	3.86
Tahaa										
TAA-B-7	.70596	.512639	19.158	15 630	38.922	592	43.95	1.71	6 51	4.53
TAA-B-26	.70623	.512623	19 241	15 657	39 010	700	51.98	1.90	7.25	2 02
Rarotonga										
RAR-B-1	.70427	.512729	18 491	15.585	38 990	753	42.41	1.42	5 37	4.12
RAR-B-9	.70416	.512760	18.834	15 601	39.121	456	23.35	.557	2.12	1.62
RAR-B-12	.70428	.512690	18 672	15 656	39.217	644	47.63	1.37	5.51	4.31
RAR-B-16	.70434	.512683	18 842	15.543	38 804	580	79.69	2.81	14.0	8.53
Rurutu										
RRT-B-21	.70281	.512903	20 847	15.744	40 161	818	22.65	2.21	8.12	2.25
RRT-B-30	.70332	.512925	20.050	15.656	38.804	820	52.75	1.30	4.88	2.48
Tubuai										
TBA-B-3	.70279	.512914	21.115	15.746	40 343	683	51.60	1.78	7.96	2.87
replicate								1.76	7.89	
TBA-B-15	.70279	.512910	20 818	15.750	40.203	494	32.01	1.23	4.72	2 73
TBA-B-16	.70283	.512894	20.960	15.758	40.396	427	31.04	.894	3 83	2.02
TBA-B-19	.70273	.512893	21.195	15.779	40.498	427	33.69	1.14	4.06	1.56
TBA-B-22	.70279	.512904	20.956	15.756	40.234	434	22.86	.915	3.41	1.54
TBA-B-23	.70280	.512927	21.118	15.758	40.330	1056	68.01	3.15	12.2	6.14
replicate								3.14	12 2	
Mangaia										
MGA-B-21	.70285	.512842	21 529	15 809	40 547	407	32 35	1.02	3 57	1 96
replicate								1.02	3.54	
MGA-B-25	.70291	.512864	21 678	18 807	40.512	347	23.22	.730	2.45	1.40
MGA-B-26	.70280	.512864	21.508	15.804	40.405	244	21.11	.673	2.25	1.33
MGA-B-47	.70274	.512842	21.784	15 813	40 734	287	19.97	.635	2.18	1.54
replicate								.636	2.17	
Blanks (pg)						<150	<30	<5	<1	<50

Table 1. Sr, Nd and Pb isotopic and trace element data for oceanic island basalts from the south Pacific Ocean. $^{87}Sr/^{88}Sr$ analyses are on leached whole rock powders, and all other analyses are on unleached powders. $^{87}Sr/^{88}Sr$ and $^{143}Nd/^{144}Nd$ are corrected for instrumental fractionation relative to $^{86}Sr/^{88}Sr$=0.119400 and $^{146}Nd/^{144}Nd$=0.721900 using a power law. Pb isotope data are fractionation corrected (0.12% per a.m.u.) relative to NBS 981 values given by Todt et al (Todt et al., 1984). $^{87}Sr/^{88}Sr$ and $^{143}Nd/^{144}Nd$ data are normalized to .71022 for NBS 987 and .511860 for LaJolla Nd standard, respectively. Reproducibilities of the standards are 0.0045% for Sr, 0.004% for Nd, and 0.02% per a.m.u. for Pb. Concentration data are accurate to 1%.

Sample	Age	$(^{187}Os/^{186}Os)m$	Re (ppt)	Os (ppt)	$^{187}Re/^{186}Os$	$(^{187}Os/^{186}Os)i$	Phenocyrst %
Savaii							
SAV-B-5	1911	1.0261		132		1.0261 ± 0.0031	trace OL
SAV-B-6	1907	1.0510		170		1.0510 ± 0.0032	5% OL
SAV-B-7	≤1 Ma	1.0444	198	213	37.1	1.0439 ± 0.0031	aphyric
SAV-B-8	≤1 Ma	1.0739		26.2		1.0739 ± 0.0032	trace OL,CPX
SAV-B-15	≤1 Ma	1.0629		219		1.0629 ± 0.0032	5% OL
Tahaa							
TAA-B-7	1.3-3.4 Ma	1.0789	118	64.5	73.3	1.0567 ± 0.0154	5% OL, 5% CPX
TAA-B-26	1.3-3.4 Ma	1.1333	186	48.0	155	1.0861 ± 0.0293	5% OL, 10% CPX
replicate			186				
Rarotonga							
RAR-B-1	1.2-2.3 Ma	1.0609		212			15% OL, 25% CPX
RAR-B-9	1.2-2.3 Ma	1.0910	1569	98.3	650	1.0737 ± 0.0157	5% OL
replicate			1621				
RAR-B-12	1.2-2.3 Ma	1.0424	283	556	20.1	1.0419 ± 0.0065	30% OL, 30% CPX
replicate			276				
RAR-B-16	1.2-2.3 Ma	1.1128		50.5			trace CPX
Rurutu							
RRT-B-21	.88-12.8 Ma	1.2493	309	313	39.5	1.2457 ± 0.0077	10% OL, 15% CPX
RRT-B-30	.88-12.8 Ma	1.1214	388	315	49.3	1.1169 ± 0.0083	5% CPX
Tubuai							5% OL
TBA-B-3	6-10 Ma	1.2179	407	646	24.9	1.2149 ± 0.0075	5% OL, 10% CPX
replicate			397				
TBA-B-15	6-10 Ma	1.2134	359	254	56.6	1.2065 ± 0.0058	trace OL
TBA-B-16	6-10 Ma	1.2039	191	221	35.3	1.1956 ± 0.0051	trace OL
replicate		1.2069		213			
TBA-B-19	6-10 Ma	1.2001	361	256	56.5	1.1932 ± 0.0139	trace OL
TBA-B-22	6-10 Ma	1.2165	586	421	54.9	1.2098 ± 0.0057	20% OL, 20% CPX
replicate			569				
TBA-B-23	6-10 Ma	1.2116	231	589	16.0	1.2099 ± 0.0043	10% OL
replicate		1.2120	226	554			
TBA-B-32	6-10 Ma		120				trace OL
Mangaia							
MGA-B-21	16-20 Ma	1.2605	339	265	51.7	1.2483 ± 0.0063	10% OL, 25% CPX
replicate1		1.2644	347	272			
replicate2			354				
MGA-B-25	16-20 Ma	1.2516	480	348	55.2	1.2365 ± 0.0064	20% OL, 20% cpx
MGA-B-26	16-20 Ma	1.2523	200	273	30.1	1.2450 ± 0.0052	15% OL, 20% CPX
replicate		1.2541		259			
MGA-B-47	16-20 Ma	1.235	100	751	5.34	1.2339 ± 0.0040	60% OL, 10% CPX

Table 2. Re-Os isotope data for oceanic island basalts from the south Pacific Ocean. $(^{187}Os/^{186}Os)m$ is the measured $^{187}Os/^{186}Os$ after correction for analytical blank and spike contributions. Re and Os concentrations are reproducible to 2.6% and 4.6% respectively. Errors on the initial $^{187}Os/^{186}Os$ ratios represent the combined uncertainties on sample ages, $^{187}Re/^{186}Os$ (7%), and analytical reproducibility on $(^{187}Os/^{186}Os)m$ (0.3%). Data averages are taken for samples with replicate analyses. Ages are estimated from sample locations and published ages for these islands (Duncan et al., 1976; Bellon et al., 1980; Turner et al., 1982; Natland et al., 1985; Gisbert, 1989). Phenocryst abundances are estimated from visual inspection of the hand specimens.

of the range of previously reported data from this island (Nakamura et al., 1988; McDonough et al., 1991).

The Re-Os data are given in Table 2 and plotted in Figs. 1 and 2. Also plotted in Figure 1 are Re and Os concentration data for basalts and komatiites from Gorgona Island (Walker et al., 1991), komatiites from Munro township (Walker et al., 1988) and basalts from Hawaii (Martin, 1991). Re concentrations in the south Pacific basalts range from 100 to 1621 ppt (parts per trillion, 10^{-12} g/g), and Os concentrations vary from 26 to 750 ppt. The Os concentrations are systematically lower than Os concentrations in komatiites (Walker et al., 1988; Walker et al., 1991). $^{187}Re/^{186}Os$ varies from 5.34 to 650, and exhibits a clear negative correlation with Os concentration (Fig. 1b). The Re and Os concentration data in Table 2 suggest a clustering of Os concentrations into three groups (≤ 100ppt, 100-400 ppt, ≥ 400 ppt).

$^{187}Os/^{186}Os$ ratios for the various islands are also reported in Table 2. Measured $^{187}Re/^{186}Os$ ratios in some of the samples were high enough to require age corrections on $^{187}Os/^{186}Os$. Initial $^{187}Os/^{186}Os$ ratios were calculated using the middle of the age ranges listed in Table 2, and the age corrected $^{187}Os/^{186}Os$ ratios are plotted with the $^{87}Sr/^{86}Sr$, $^{143}Nd/^{144}Nd$, and $^{206}Pb/^{204}Pb$ data in Fig. 2, along with $^{187}Os/^{186}Os$ data from Hawaii, and Iceland reported by Martin (Martin, 1991). Initial $^{187}Os/^{186}Os$ ratios for Samoa vary from 1.0261-1.0739, while $^{187}Os/^{186}Os$ ranges from 1.0567-1.0861 for Tahaa and 1.0419-1.0737 for Rarotonga. The higher values are between the two $^{187}Os/^{186}Os$ estimates for the bulk silicate earth (Luck et al., 1991; Martin et al., 1992). In order to evaluate the data relative to depleted upper mantle, also displayed in Fig. 2 are whole rock $^{187}Os/^{186}Os$ analyses of peridotites with $^{87}Sr/^{86}Sr$, $^{143}Nd/^{144}Nd$, and $^{206}Pb/^{204}Pb$ similar to MORB, as determined from analyses of clinopyroxene separates (Walker et al., 1989; Reisberg et al., 1991). In this context, it should be noted that the peridotite with $^{187}Os/^{186}Os$ of 1.10 is a garnet-rich sample from Ronda which is likely a disaggregated mafic layer (Reisberg et al., 1991). Excluding this sample, the MORB-like peridotites have $^{187}Os/^{186}Os$ around 1.04-1.05, which is low relative to both bulk silicate earth estimates. Thus the results from Samoa, Tahaa and Rarotonga lie in the range of $^{187}Os/^{186}Os$ values characteristic of depleted and undifferentiated mantle.

The initial $^{187}Os/^{186}Os$ ratios vary from 1.2339-1.2483 at Mangaia, 1.1932-1.2149 at Tubuai, and 1.1169-1.2457 at Rurutu. These results are much higher than both depleted mantle values and bulk silicate earth estimates. The $^{187}Os/^{186}Os$ ratios measured for the Mangaia samples are the highest yet reported for young oceanic island basalts. The homogeneity in $^{187}Os/^{186}Os$ observed for the Tubuai and Mangaia samples is consistent with the relative homogeneity in $^{87}Sr/^{86}Sr$, $^{143}Nd/^{144}Nd$, and Pb isotopes from these

islands (Vidal et al., 1984; Nakamura et al., 1988). The data from Rurutu, Tubaui and Mangaia suggest a correlation between $^{187}Os/^{186}Os$ and $^{206}Pb/^{204}Pb$.

6. Discussion

6.1 Re and Os concentrations

From Table 2, it is clear that samples with high abundances of olivine+clinopyroxene phenocrysts have higher Os concentrations and lower $^{187}Re/^{186}Os$ ratios than aphyric samples. The Re-Os concentration systematics in komatiites (Walker et al., 1988; Walker et al., 1991) also suggest the involvement of a low Re/Os phase in which Os is compatible. Preliminary Re and Os partitioning data reported by Watson et al (Watson et al., 1987) suggest that clinopyroxene should have low Re/Os, however both elements are incompatible in this phase. Fractional crystallization of an early liquidus phase, such as olivine, chromite, or sulfides (often associated with olivine), may be capable of lowering the Os concentration of a crystallizing magma, and raising the Re/Os ratio. Differentiated magmas would be expected to have low Os concentrations and high Re/Os ratios. Cumulative basalts, such as the ankaramite samples TBA-B-22, RAR-B-12, MGA-B-21. MGA-B-25, MGA-B-26 and the picrite MGA-B-47 (Table 2) would be expected to have high Os concentrations and low Re/Os ratios. However, some samples with only moderate amounts of phenocrysts show both high Os concentrations (TBA-B-3, 646 ppt) and low Os concentrations (Tahaa samples, 48-65 ppt). This suggests that olivine may not be directly involved in controlling the Os concentrations in these basalts, although the extent to which individual samples may have dissolved cumulate olivine cannot be evaluated here. In this context, the Os concentrations of 100-200 ppt in the Samoa basalts SAV-B-5, SAV-B-6 and SAV-B-7, which are largely free of phenocrysts, may be representative of the Os concentration of a near-primary melt of mantle peridotite.

With one exception, Re concentrations in these basalts are systematically lower than Re concentrations from Hawaiian tholeiites (Martin, 1991) and tholeiites from Gorgona Island (Walker et al., 1991). Some of the lowest Re concentrations are probably due to dilution of the melt with phenocrysts (ex. MGA-B-47). The systematically lower Re contents in the basalts studied here may reflect either differences in the generation of tholeiites and alkali basalts, or differences in source composition (Walker et al., 1991). However, if Re is incompatible during partial melting of peridotite, Re concentrations in alkali basalts should be higher than in tholeiites. The higher Re concentrations of tholeiites might indicate the involvement of a mantle phase which remains in the residue at small degrees of melting, yet might be exhausted during the relatively higher degrees of melting involved in tholeiite generation. With the exception of sample RAR-B-9 from Rarotonga,
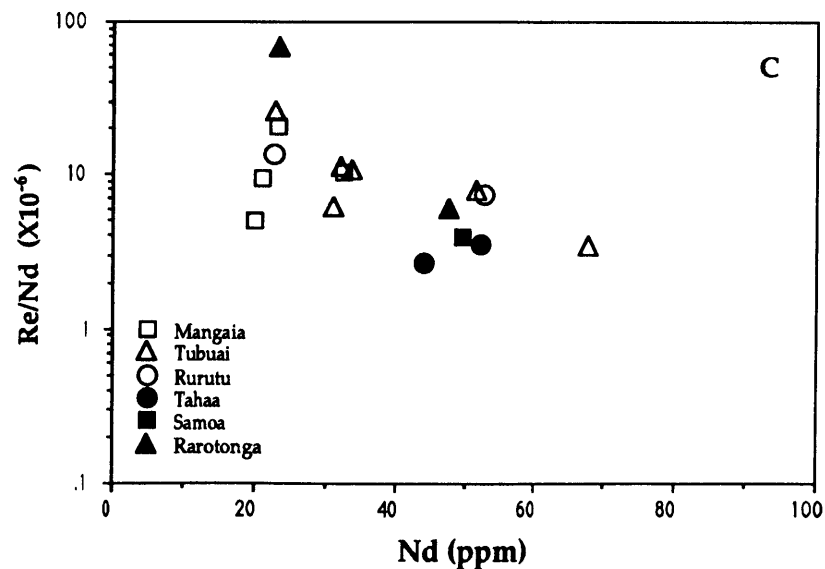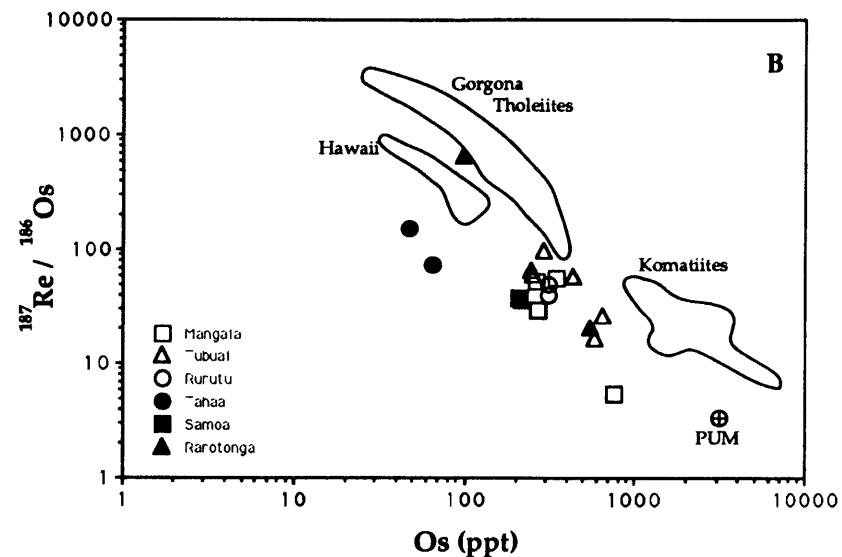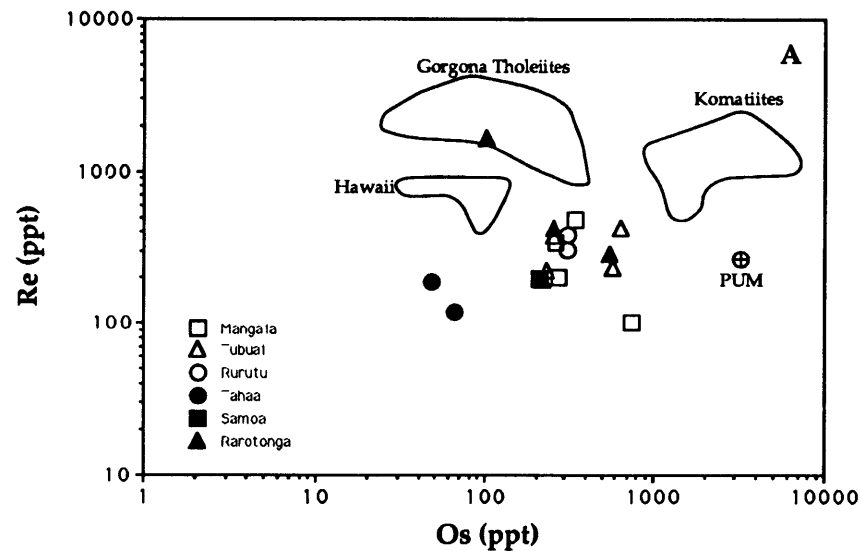
Figure 1. A) Re versus Os concentration for South Pacific oceanic island basalts. Clustering of the Os concentrations into three groups (<100 ppt, 100-400 ppt, >400 ppt) is suggested by the data. B) 187Re/186Os versus Os concentration plot shows a negative correlation. The abundance of phenocrysts in the samples with high Os concentrations suggests the influence of a liquidus phase with low Re/Os in which Os is compatible. PUM is the primitive upper mantle estimate of Morgan (1986). C) Re/Nd versus Nd concentration. The negative trend indicates that Re is more compatible than Nd.

the Re concentrations in Table 2 show little variation (100-586 ppt, average 282 ppt). Compared to Morgan's estimate for the Re concentration of primitive mantle (250 ppt, Morgan, 1986), the average Re concentrations of the basalts in this study suggest an apparent partition coefficient (peridotite/melt) near unity during the generation of alkali basalts. This is consistent with the negative trend in Fig. 1c; if the Re/Nd ratio is pedominantly controlled by partial melting and fractional crystallization, Fig. 1c indicates that Re was more compatible than Nd during these processes.

6.2 $^{187}Os/^{186}Os$ Systematics of EMII Islands

Despite their extreme $^{87}Sr/^{86}Sr$ and elevated $^{207}Pb/^{204}Pb$, the Samoa and Tahaa samples are not distinctive in their $^{187}Os/^{186}Os$ ratios, falling within the range of $^{187}Os/^{186}Os$ for abyssal peridotites (Martin, 1991; Snow, 1991), "normal" ophiolite peridotites (Luck et al., 1991) and MORB-like peridotites (Walker et al., 1989; Reisberg et al., 1991). The high $^{87}Sr/^{86}Sr$ and elevated $^{207}Pb/^{204}Pb$ of the Samoa and Tahaa samples may have their origins in a source containing a component similar to modern sediments, as advocated previously for Samoa (Wright et al., 1987). If sediment is indeed involved in the origin of the Samoan mantle source, the amount of sediment must be small, not more than a few percent, in order to fit the observed Nd and Hf data for Samoa (White et al., 1984). Mixing of such a small amount of sediment into the mantle would have only a small effect on the $^{187}Os/^{186}Os$ ratios, due to the low Os concentration of continental crustal material (Esser, 1990). Mixing of a depleted mantle ($^{87}Sr/^{86}Sr=.703$, $^{143}Nd/^{144}Nd=$ .51290, MORB-like Pb, $^{187}Os/^{186}Os=1.02-1.05$), with 1-2% modern sediment, could reproduce the Samoan data. The relative concentrations of Pb, Sr, Nd and Os in most clastic sediments and peridotite (ratio of ppm sediment/ppm peridotite) decrease in the order Pb-Sr-Nd-Os. Thus, in a sediment/peridotite mixture with a small fraction of sediment, the Pb isotopes would be closest to the sediment component, followed by $^{87}Sr/^{86}Sr$, then $^{143}Nd/^{144}Nd$ and $^{176}Hf/^{177}Hf$, and finally $^{187}Os/^{186}Os$ would be only slightly changed from the peridotite value, if at all. This is essentially the order of deviation of the EMII isotope ratios from depleted mantle values. Some type of metasomatism, which has not strongly effected the Re-Os system, could also be invoked to explain the Samoa and Tahaa data. The present Os isotope data, as well as Nd and Hf isotope data for EMII basalts, indicate that the mantle source of Samoa and Tahaa is nearly chondritic to slightly depleted in Re/Os, Sm/Nd and Lu/Hf. A detailed Re-Os investigation of the EMII islands, with many more samples than reported here, would be needed in order to evaluate the presence of a possible trend consistent with a sedimentary component in these islands.
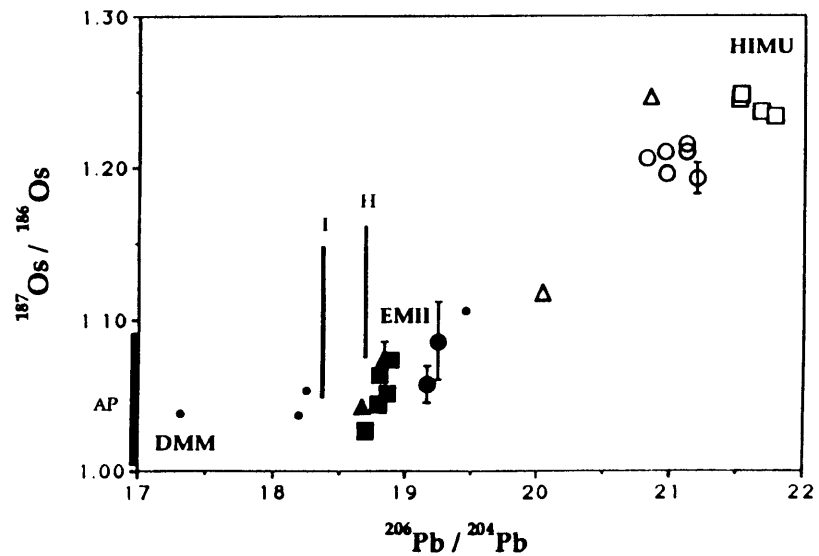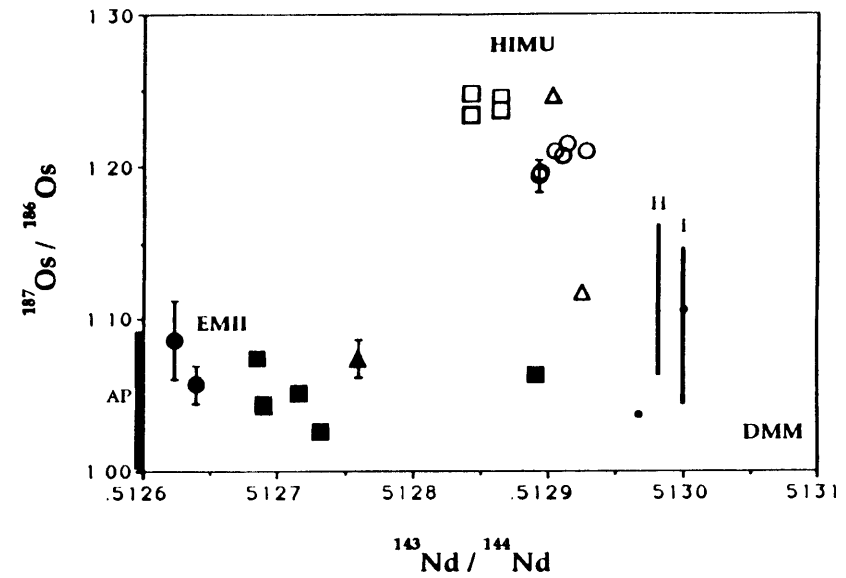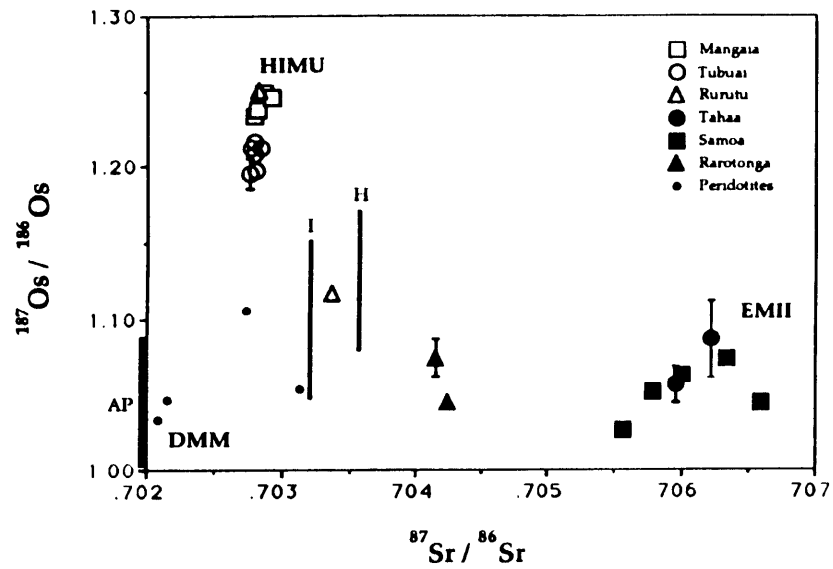
Figure 2. Sr-Nd-Pb-Os isotope ratio diagrams for South Pacific oceanic island basalts. Also shown are data from Hawaii and Iceland (Martin, 1991), the range of data for abyssal peridotites (AP) (Martin, 1991; Snow, 1991), and peridotites with Sr, Nd, and Pb isotope ratios similar to MORB (Walker et al., 1989; Reisberg et al., 1991). Error bars on the $^{187}Os/^{186}Os$ ratios represent the combined uncertainties on sample ages, $^{187}Re/^{186}Os$ (7%), and analytical reproducibility of $^{187}Os/^{186}Os$ (0.3%), and are smaller than the symbols for most samples.

6.3 $^{187}Os/^{186}Os$ Systematics of HIMU Islands

6.3.1 Crustal Contamination

In trying to identify the source of the radiogenic $^{187}Os/^{186}Os$ in the HIMU basalts, we must evaluate crustal contamination of the magmas as a possibility. The islands of Rurutu, Tubuai and Mangaia rest on oceanic lithosphere which is 60-80 Ma old. Given the range of Re/Os ratios measured in oceanic basalts, it is quite possible that the MORB-crustal part of the lithosphere could evolve to $^{187}Os/^{186}Os$ in excess of 1.25 over this time period, and assimilation of large amounts of this material into a magma with low Os concentration could raise the $^{187}Os/^{186}Os$ in the erupted magmas. However, the amount of crust necessary to account for the elevated $^{187}Os/^{186}Os$ ratios would shift the Pb isotopic composition of the magmas toward MORB values, since U/Pb and Th/Pb ratios measured in fresh MORB (Church et al., 1975; Tatsumoto, 1978; Cohen et al., 1980; Cohen et al., 1982) are not high enough to generate the HIMU Pb signature in the required time. Altered MORB crust has higher U/Pb ratios, but assimilation of 60-80 Ma old MORB crust cannot account for the HIMU $^{207}Pb/^{204}Pb$ signature, irrespective of the U/Pb ratio. A strong contamination by altered crust would also result in higher $^{87}Sr/^{86}Sr$ values characteristic of seawater alteration. Variable assimilation of MORB crust into variably Os-depleted basalts would also destroy the relative Os isotopic homogeneity observed at Tubuai and Mangaia. In addition, if this process were important, it would be expected to have an even larger influence on the $^{187}Os/^{186}Os$ ratios of the lavas from Savaii, which rests on seafloor with an age in excess of 100 Ma. This is in conflict with the low $^{187}Os/^{186}Os$ ratios thus far observed in the Samoa data. The peridotitic part of the MORB lithosphere likely has low $^{187}Os/^{186}Os$ ratios, similar to abyssal peridotites (Martin, 1991; Snow, 1991) and "normal" ophiolite peridotites (Luck et al., 1991). While assimilation of this material may be important in some of the variation in the low $^{187}Os/^{186}Os$ samples, it cannot be the source of the high $^{187}Os/^{186}Os$ signatures of the HIMU basalts. Given the above arguments, we can eliminate crustal contamination as a process to generate the observed HIMU Os isotope signatures. Thus the high $^{187}Os/^{186}Os$ ratios are indicative of the Os isotopic composition of the mantle sources of the Rurutu, Tubuai and Mangaia basalts.

6.3.2 Separation of a Metal or Sulfide Phase

Since both Os and Pb are chalcophile elements, it is useful to consider the possibility that the high $^{187}Os/^{186}Os$, high $^{206}Pb/^{204}Pb$ signature is the result of removal of Os and Pb relative to Re and U by the separation of a sulfide phase from some portion of the earth's mantle (Vollmer, 1977; Vidal et al., 1978). This has probably taken place early in the earth's history to form the core. The hypothesis of continuous extraction of siderophile and chalcophile elements from the mantle to the core through geologic time has

been investigated by Newsom et. al. (Newsom et al., 1986), who measured the abundance ratios of siderophile and chalcophile elements to lithophile elements of similar incompatibility (ex. Mo/Pr and W/Ba). If the radiogenic Pb signature is the result of a metal-sulfide segregation process, resulting in a high U/Pb ratio, then this signature should be coupled with a low Mo/Pr or low W/Ba ratio. The near constancy of these ratios (within a factor of 4) in oceanic basalts, irrespective of isotopic composition, indicates that the high $^{206}Pb/^{204}Pb$ signature is not the result of fractionation of a metal-sulfide phase from the mantle (Newsom et al., 1986). Such a process would also be expected to create large variations in the Re/Nd ratio, but the Re/Nd ratios of the HIMU basalts are not systematically unique in Fig. 1c. In addition, without knowledge of the relevant partition coefficients at mantle pressures and temperatures, it is not clear how such a process would affect the Re/Os ratio, since both elements are chalcophile and siderophile elements. While sulfide or metal fractionation of up to 0.1% is possible within the data of Newsom et. al., this small amount is probably not enough to generate the factor of 2-5 increase in the U/Pb ratio, relative to bulk silicate earth, required by the Pb isotope signature of HIMU.

6.3.3 Mantle Metasomatism

The $^{187}Os/^{186}Os$ ratios of the Rurutu, Tubuai, and Mangaia basalts are distinctly higher than measurements for mantle peridotites and other oceanic basalts. In order to evaluate mantle metasomatism as a process for raising the $^{187}Os/^{186}Os$ of the HIMU basalts, it is instructive to compare the HIMU Os data with $^{187}Os/^{186}Os$ measurements of metasomatized peridotites. The measurements of Walker et al (Walker et al., 1989) on xenoliths from the Kaapvaal craton and Pearson et al (Pearson et al., 1991) on South African and Siberian xenoliths from kimberlites all have $^{187}Os/^{186}Os$ less than 1.08. These xenoliths include some extensively metasomatized and LREE-enriched samples, some with incredibly high $^{87}Sr/^{86}Sr$ and low $^{143}Nd/^{144}Nd$, yet the metasomatism apparently did not result in increased Re/Os and $^{187}Os/^{186}Os$ ratios (notwithstanding Re contamination from the kimberlite host (Walker et al., 1989)). The Ronda plagioclase facies peridotites analyzed by Reisberg et al (Reisberg et al., 1991) are also LREE-enriched, with low $^{143}Nd/^{144}Nd$ and very radiogenic $^{206}Pb/^{204}Pb$ (Bourdon et al., 1990). These peridotites had the lowest Re/Os and $^{187}Os/^{186}Os$ of all the Ronda samples, again suggesting that the Re/Os system was resistant to the metasomatism which resulted in enriched signatures in other isotope systems (Reisberg et al., 1991). Though a Re-Os characterization of mantle metasomatism is far from complete, it appears that the metasomatic enrichment processes reflected in these peridotite samples are incapable of generating high $^{187}Os/^{186}Os$ signatures. Given that the measured $^{187}Os/^{186}Os$ ratios of the HIMU basalts are higher

than any peridotite values, we can tentatively rule out metasomatism as a mechanism for producing the high $^{187}Os/^{186}Os$ in these basalts.

6.3.4 Crustal Recycling

It is clear that the Rurutu, Tubuai and Mangaia $^{187}Os/^{186}Os$ systematics require a source with a high time-integrated Re/Os ratio. The only geologic materials thus far recognized to have high Re/Os are magmas, insofar as oceanic and continental crust are the products of melting. Layers of mafic bulk compositions found in the Ronda ultramafic complex, with $^{187}Os/^{186}Os$ ratios of 1.71 to 47.9 (Reisberg et al., 1991), are probably also the products of melting, either as trapped melts (Dickey et al., 1977), cumulates from mafic magmas (Obata et al., 1976; Suen et al., 1987), or ancient, subducted oceanic crust (Allegre et al., 1986). While there is no Pb isotope data for the Ronda mafic samples, Hamelin and Allegre (Hamelin et al., 1988) have measured the Pb isotopic composition of peridotites and mafic layers from several orogenic peridotite massifs. Though substantial heterogeneity exists in the mafic layer data, the Pb isotopic compositions of a few pyroxenites from the Beni Bousera massif approach HIMU values, as do some mafic layers from Ronda (Hart unpublished data). However, it is not known if these mafic rocks have elevated $^{187}Os/^{186}Os$, or if there is a positive correlation between $^{187}Os/^{186}Os$ and Pb isotopic composition. In addition, the elevated $^{187}Os/^{186}Os$ of the Ronda mafic layers were created while the massif was isolated in the subcontinental lithosphere over the last 1.3 Ga (Reisberg et al., 1986; Reisberg et al., 1989; Reisberg et al., 1991). These layers, ranging in thickness from several cm to several meters, likely would not survive the diffusion and mixing processes operating in the convecting mantle (Hofmann et al., 1978), where the HIMU source must reside.

Ancient, subducted oceanic crust may provide a suitable high Re/Os, high $^{187}Os/^{186}Os$ reservoir in the convecting mantle. The oceanic crust, with its several kilometers of thickness, would be more resistant to diffusive and convective mixing than meter scale veins or layers. Due to the high Re concentration and low Os concentration of tholeiitic basaltic crust relative to mantle peridotite, the main effect of recycling oceanic crust is to create areas of locally higher Re concentrations. It is unlikely that the Os in the HIMU magmas was derived entirely from ancient oceanic crust, as this material would probably have much higher $^{187}Os/^{186}Os$ ratios than observed. Only a moderately high mantle Re/Os ratio (about 10-20) is needed to raise the $^{187}Os/^{186}Os$ from depleted mantle values (about 1.05) to the HIMU $^{187}Os/^{186}Os$ values (about 1.25) in a few billion years. This suggests that the time integrated Re/Os ratio of the HIMU source is the result of mixing high Re/Os crust with low Re/Os peridotite.

We can quantitatively model this mixing if we have constraints on the timing of the recycling process. If the HIMU source is a mixture of recycled oceanic crust and mantle peridotite, then the U-Th-Pb evolution of the mixture is totally dominated by the recycled crust, even at low fractions of crust, due to the very low concentrations of these elements in peridotites (Hamelin et al., 1988; Galer et al., 1989, Hauri unpublished data). As a result of this, the Pb isotopic composition of the HIMU source is essentially that of the crustal component, and constraints on the age, U/Pb and Th/U ratios emerge from inversion of the Pb-Pb systematics. The working assumptions are;

1) the depleted MORB mantle (DMM) is assumed to be a second stage reservoir, with a maximum age of 3.0 Ga, derived from the bulk silicate earth (present-day bulk silicate earth values of $^{87}Sr/^{86}Sr=.7047$ (Allegre et al., 1983), $^{143}Nd/^{144}Nd=.512638$ (DePaolo et al., 1976), $^{176}Hf/^{177}Hf=.282880$ (Salters et al., 1990), $^{187}Os/^{186}Os=1.07$, chondrite average, (Walker et al., 1989));(present day DMM taken from most depleted MORB points for $^{87}Sr/^{86}Sr$ (.70220), $^{143}Nd/^{144}Nd$ (.51330) and $^{176}Hf/^{177}Hf$ (.28355), and $^{187}Os/^{186}Os=1.00$);

2) the MORB crust is assumed to be derived from the depleted MORB mantle (DMM) at any time <3.0 Ga ago with initial isotope ratios equivalent to either DMM, or BSE (i.e. a very young DMM);

3) the evolution of the MORB crust from the time of its generation to the present day isotopic composition of HIMU ($^{87}Sr/^{86}Sr=.7028$, $^{143}Nd/^{144}Nd=.512850$, $^{176}Hf/^{177}Hf=.282900$, $^{187}Os/^{186}Os=1.25$) is approximated by a single evolution curve.

For the ^{207}Pb-^{206}Pb system, these assumptions imply that the intersection of any third stage isochron (representing HIMU) with any second-stage isochron (representing DMM) must lie within the present-day MORB field. These assumptions result in the boundary conditions displayed in Fig. 3. N-MORB data are MORB analyses with $^{87}Sr/^{86}Sr<.703$ ((Mahoney et al., 1989; Dosso et al., 1991) and data sources summarized in (Hart, 1988)) and Mangaia data are from Palacz and Saunders, (1986), Nakamura and Tatsumoto, (1988) and this study. Given the above assumptions, the bounding isochrons shown in Fig. 3a are absolute limits on the age of the crustal component in the HIMU source, and indicate an age of 770-2100 Ma. Calculated third stage $^{238}U/^{204}Pb$ ratios range from 19.7-40. Using these ages, the Th/U ratios calculated from the bounds in Fig. 3b range from 1.42-3.56.

Working from the above assumptions and age constraints of 770-2100 Ma, calculated limits on the $^{187}Re/^{186}Os$ of the HIMU source are 8.90-22.80 (Fig. 4a). These ratios are low compared with measured basalt $^{187}Re/^{186}Os$ ratios (Table 2 and Martin, (1991); Walker et al., (1991)). Assuming a peridotite Os concentration of 4000 ppt and
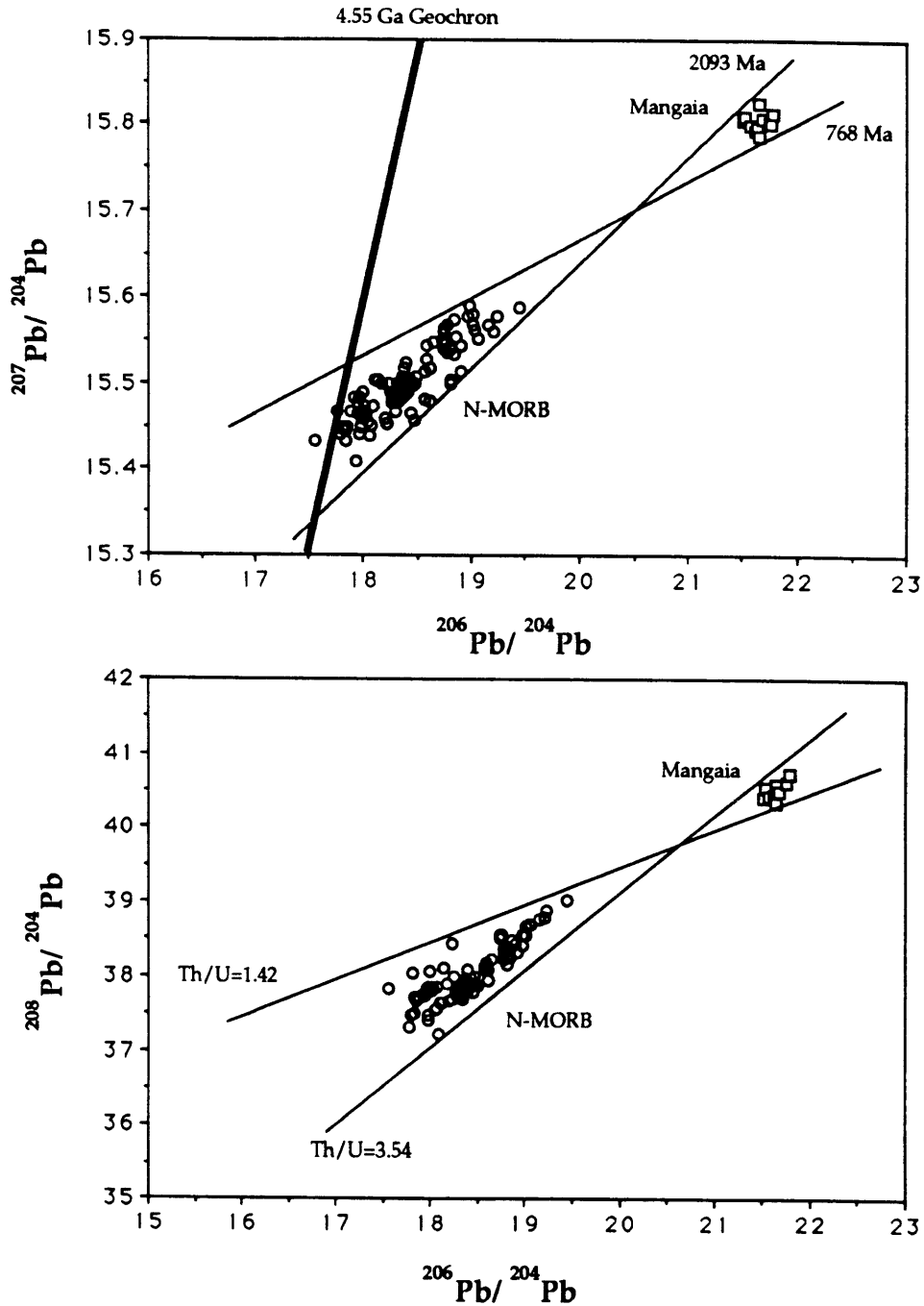
Figure 3. Pb isotope ratio plots with data for N-MORB (defined as MORB with 87Sr/86Sr<.7030, from Mahoney et al., 1989; Dosso et al., 1991; and data sources summarized in Hart, 1988) and Mangaia (Palacz and Saunders, 1986; Nakamura and Tatsumoto, 1988; this study). A) The bounding isochrons delineate the upper and lower limits on the age of the recycled oceanic crust in teh HIMU source (see text). B) Bounding lines showing the limiting Th/U ratios of the recycled oceanic crust in the HIMU source.
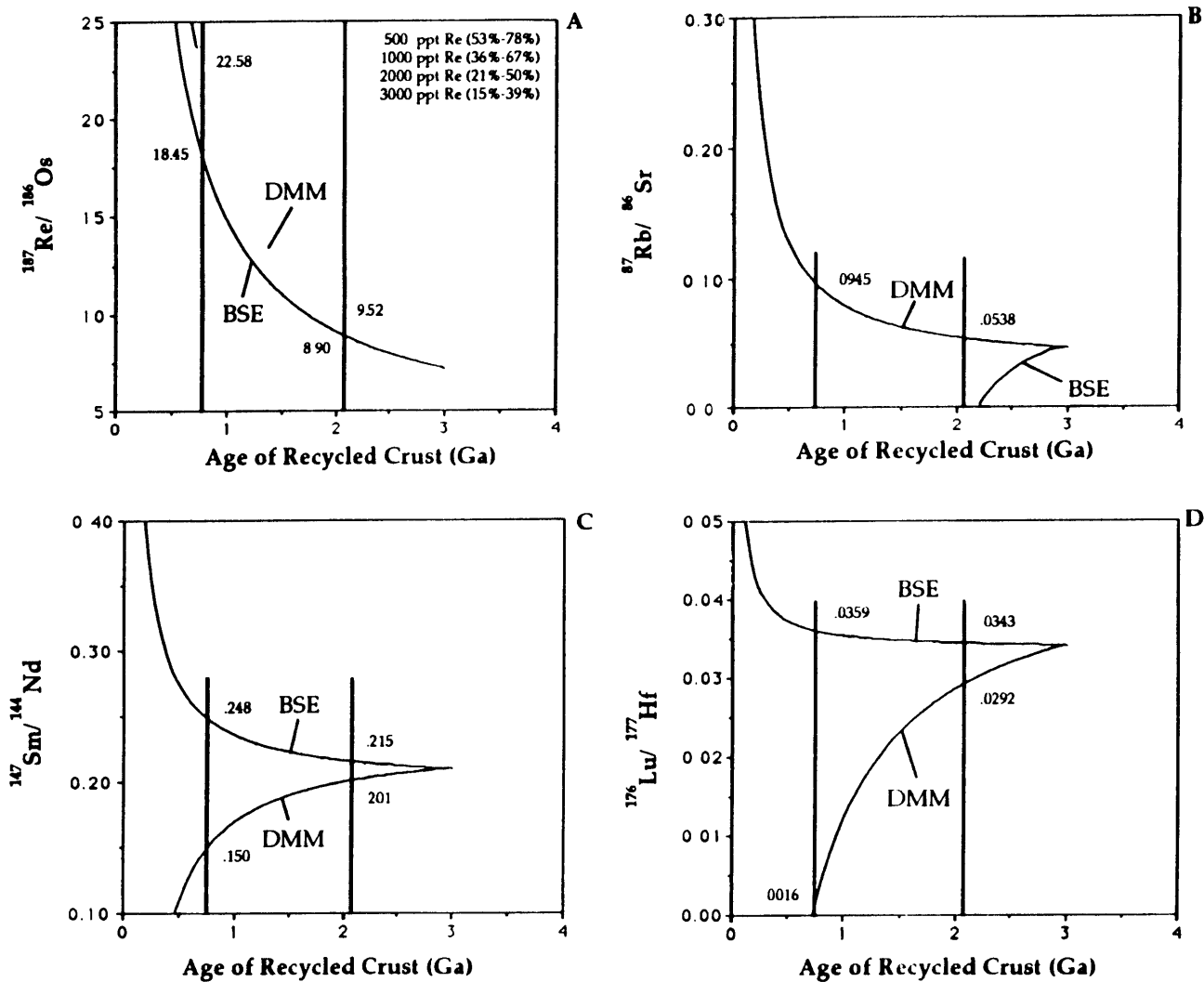
Figure 4. Results of the inversion of the Mangaia isotope data for parent/daughter ratios in the recycled crustal component. The curves represent the parent/daughter ratios calculated for recycled crust of various ages, assuming initial isotopic compositions corresponding to either depleted MORB mantle (DMM) or bulk silicate earth (BSE). The vertical lines are limits on the age of the recycled crust from the Pb isotope inversion (see text, Table 3 and Fig. 3).

	Calculated Subducted Crust	Measured Fresh MORB (data averages)	Avg. N-MORB Hofmann (1988)	Altered MORB Hart&Staudigel (1989)
$^{87}Rb/^{86}Sr$	0 - .095	.006 - .26 (.03)	.032	.223
$^{147}Sm/^{144}Nd$	.150 - .248	.15 - .23 (.20)	.203	.200
$^{176}Lu/^{177}Hf$	.002 - .036	.023 -.040 (.027)	.0281	---
$^{238}U/^{204}Pb$	19.7 - 40	4.8 - 38 (12.3)	9.07	30
$^{232}Th/^{204}Pb$	25 - 142	7.7 - 85 (38.7)	23.9	7.0
Th/U	1.42 - 3.54	1.8 - 4.2 (2.80)	2.63	.23

Table 3. Calculated parent/daughter ratio results in subducted oceanic crust compared with isotope dilution measurements in fresh MORBs, an altered MORB composite (Hart et al., 1989), and average N-MORB of Hofmann (Hofmann, 1988). Averages of the MORB data are given in parentheses. The model parent/daughter ratios are those needed in order for subducted oceanic crust to evolve from either depleted MORB mantle or bulk silicate earth to the composition of the HIMU endmember in 770-2100 Ma (see text). MORB data sources: Rb/Sr and Sm/Nd (White et al., 1978; Mahoney et al., 1989; Dosso et al., 1991), Lu/Hf (Patchett et al., 1980; Patchett, 1983; Salters et al., 1989), U-Pb (Tatsumoto, 1978; Cohen et al., 1980; Cohen et al., 1982), Th/U (Tatsumoto, 1978; Cohen et al., 1980; Condomines et al., 1981; Cohen et al., 1982; Jochum et al., 1983; Newman et al., 1983; Goldstein et al., 1991), Th/Pb (Church et al., 1975).
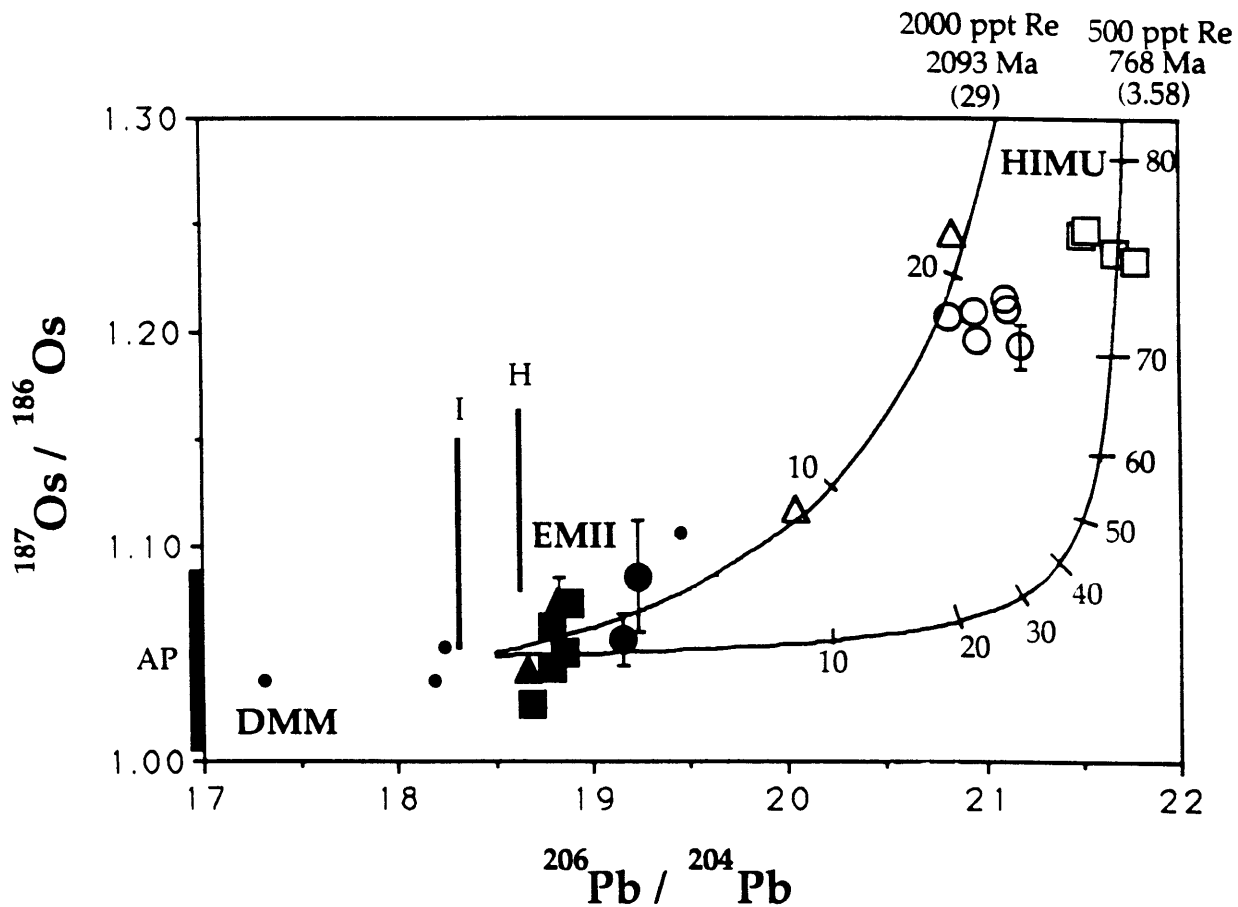
Figure 5. ^{187}Os/^{186}Os versus ^{206}Pb/^{204}Pb for results from this study. The two mixing curves delineate the locus of mixtures of peridotite (Os=4000 ppt, ^{187}Os/^{186}Os=1.05, Pb=10 ppb, ^{206}Pb/^{204}Pb=18.5) with two possible oceanic crustal compositions (2000 ppt Re and 500 ppt Re), both with common Os= 100 ppt, ^{206}Pb/^{204}Pb=21.80, Pb=100 ppb). The ages represent the time at which the crust was formed, and the numbers in parentheses are the putative present-day ^{187}Os/^{186}Os ratios of the crust as if it evolved as a closed system.

161

crustal Re concentrations of 500-3000 ppt, the calculated $^{187}Re/^{186}Os$ ratios constrain the amount of crust in the HIMU source to be 15%-78%. These calculated percentages of crust are quite sensitive to the crustal Re concentration and peridotite Os concentration, and are only illustrative. The lower age limit (770 Ma) requires the highest $^{187}Re/^{186}Os$ and largest amount of crust, whereas the upper age limit (2100 Ma) requires the lower $^{187}Re/^{186}Os$ and a smaller amount of crust in the HIMU source. Even at 15% crust, the Sr, Nd and Hf evolution of the HIMU source is determined largely by the crustal component, and in a similar fashion, we can place limits on the range of possible Rb/Sr, Sm/Nd and Lu/Hf ratios in the crustal component (Figs. 4b-d).

Table 3 summarizes the results of the inversion along with the ranges for these trace element ratios measured by isotope dilution for fresh MORB glasses (Church et al., 1975; Tatsumoto, 1978; White et al., 1978; Cohen et al., 1980; Patchett et al., 1980; Condomines et al., 1981; Cohen et al., 1982; Jochum et al., 1983; Newman et al., 1983; Patchett, 1983; Mahoney et al., 1989; Salters et al., 1989; Dosso et al., 1991; Goldstein et al., 1991), and compared with estimates of average N-MORB (Hofmann, 1988) and altered MORB (Hart et al., 1989). The limits on these ratios calculated from the inversion are remarkable for their similarity to the range of values measured in fresh mid-ocean ridge basalts. This result was also found by Chauvel et al., (1992) from modelling of the trace element and isotopic characteristics of HIMU basalts. If the mantle sources of Rurutu, Tubuai and Mangaia contain subducted oceanic crust, this is a surprising result, considering the large additions of U, Rb and seawater Sr to the upper crust during alteration (Hart et al., 1982). In detail, the Rb/Sr, U/Pb and Th/Pb ratios are slightly higher than the averages of the MORB results. The deviations of the Rb/Sr and U/Pb ratios are in the direction of those for altered MORB crust (Hart et al., 1989) (Table 3), but Th/Pb and Th/U are higher than expected for altered crust. Given that the MORB crust is obviously affected by low temperature alteration, the similarity of the model parent/daughter ratios to fresh MORB may be used to suggest that; 1) the low temperature alteration signature may be largely removed during passage through the subduction zone, and/or; 2) the altered portion of the MORB crust makes up only a small part of the total crustal budget for the elements in Table 3. These calculations serve to demonstrate the suitability of subducted oceanic crust as a component in the generation of the HIMU reservoir.

The inversion results imply that the role of mass transfer during subduction zone processing was largely to remove the alteration signature from the subducting slab, at least for the elements examined here. In detail, however, the inversion results for U/Pb and Th/Pb are high relative to the N-MORB average of Hofmann (Hofmann, 1988), though the Th/U constraints are consistent. If the N-MORB averages are representative of the

composition of the basalt which is being subducted (i.e. small contributions from more enriched MORB and OIB), then the inversion results suggest a depletion of Pb relative to U and Th in the recycled oceanic crust. Chauvel et al., (1992) have proposed that Pb is leached from basaltic crust during hydrothermal alteration and deposited at the ridge in metalliferous sediments. This Pb is probably transfered to the continental crust during subduction and arc magmatism (O'Nions et al., 1979), and may be concentrated in a low U/Pb lower crust (Doe et al., 1979), possibly during plagioclase and amphibole fractionation from arc magmas.

6.4 Constraints on Melt Percolation

The high $^{187}Os/^{186}Os$ of the Tubuai and Mangaia basalts also serves as a tracer for evaluating the interaction of these magmas with the depleted upper mantle, which probably has $^{187}Os/^{186}Os$ in the range of 1.00-1.08. Due to the high Os concentration of mantle peridotite relative to basalts, the $^{187}Os/^{186}Os$ ratio of a given magma is quite sensitive to assimilation of peridotite with a different $^{187}Os/^{186}Os$ ratio. For example, assimilation of 10% of a peridotite (3000 ppt Os) with $^{187}Os/^{186}Os$ of 1.05 into a magma (300 ppt Os) with $^{187}Os/^{186}Os$ of 1.25 will lower the $^{187}Os/^{186}Os$ of the magma to 1.15. Magma-wallrock reaction (Kelemen et al., 1990) or melt percolation (McKenzie, 1984; Navon et al., 1987) through peridotite with low $^{187}Os/^{186}Os$ should also have a significant effect on the $^{187}Os/^{186}Os$ of the magma. In the case of percolation of melt through peridotite, it is well known that each element moves at some fraction of the melt velocity which is proportional to the element's bulk solid/melt partition coefficient (McKenzie, 1984; Navon et al., 1987). Because Os is a compatible element, the bulk peridotite/melt partition coefficient for Os is much higher than for Sr, Nd, Hf and Pb. As a result, for any reasonable melt velocity, the incompatible elements Sr, Nd, Hf and Pb will move much faster than Os, and the fronts of these elements will be almost entirely separated from that of Os after only a few hundred meters of percolation.

The effect on the isotopic composition of the melt is such that the Sr, Nd, Hf and Pb isotopic compositions will reflect the source material, whereas the Os isotopic composition will reflect that of the matrix through which the melt is moving. The only way to prevent this fractionation of the compatible elements from the incompatible elements is to move the magma through the matrix fast enough to prevent significant exchange of compatible elements with the matrix peridotite. This essentially implies the existence of a channel or fracture network which can transport the magma from the source region within the plume to the surface, ultimately to be erupted. The high $^{187}Os/^{186}Os$ ratios for the HIMU basalts, and the consistent covariation of the isotope ratios of the two elements with the largest difference in peridotite/melt partition coefficients (Os and Pb), requires that

interaction with low $^{187}Os/^{186}Os$ mantle had a negligible effect on the isotopic composition of the basalts erupted on Rurutu, Tubuai and Mangaia.

6.5 Global Isotope Systematics

With the presently available Re-Os data, it is now possible to delineate much of the global Sr-Nd-Pb-Os isotopic variability in the oceanic mantle (Fig. 2). The position of the depleted mantle is estimated from $^{187}Os/^{186}Os$ measurements of abyssal peridotites (Martin, 1991; Snow, 1991) and other peridotites with MORB-like Sr, Nd and Pb isotopes (Walker et al., 1989; Reisberg et al., 1991). Estimates of the positions of the various endmembers defined by Zindler and Hart (Zindler et al., 1986) are shown in Figs. 2a-c. Notwithstanding the lack of MORB $^{187}Os/^{186}Os$ data, it is likely that the MORB source is characterized by $^{187}Os/^{186}Os$ ≤1.08, and DMM may have $^{187}Os/^{186}Os$ as low as the lowest measured $^{187}Os/^{186}Os$ for abyssal peridotites of 1.0032 (Martin, 1991). The position of EMI is unknown due to the lack of Re-Os data for this endmember, though Sr, Nd and Pb isotope affinities with the subcontinental mantle may suggest a low $^{187}Os/^{186}Os$ signature for EMI (<1.00?). The $^{187}Os/^{186}Os$ data for Samoa and Tahaa suggests that the EMII endmember is characterized by $^{187}Os/^{186}Os$ ratios which lie between estimates of depleted mantle (about 1.00) and bulk silicate earth (about 1.08), consistent with the EMII $^{143}Nd/^{144}Nd$ and $^{176}Hf/^{177}Hf$ signatures (Patchett et al., 1980; White et al., 1982; Wright et al., 1987). The homogeneity of the Tubuai and Mangaia $^{187}Os/^{186}Os$ data suggests that a value of about 1.25 is representative of the Os isotopic composition of HIMU. Martin (Martin, 1991) has proposed that a mantle source exists with high $^{3}He/^{4}He$ and $^{187}Os/^{186}Os$ of around 1.10, based on Re-Os analyses of basalts from Hawaii and Iceland. The only island in the present study with documented high $^{3}He/^{4}He$ is Savaii, Western Samoa (Farley et al., 1989), with $^{187}Os/^{186}Os$ of 1.0261 to 1.0739. These results suggest that the proposed high $^{3}He/^{4}He$ endmember (Kurz et al., 1983; Kurz et al., 1985; Kurz et al., 1987), recently recognized in the Sr-Nd-Pb isotope data and termed FOZO by Hart et al (Hart et al., 1992) may be characterized by a range of $^{187}Os/^{186}Os$ within the range of estimates of depleted mantle.

The identification of the HIMU isotopic signature (high $^{187}Os/^{186}Os$, high $^{206}Pb/^{204}Pb$, low $^{87}Sr/^{86}Sr$) with recycled oceanic crust has important implications for mixing relationships in the earth's mantle. The earth presently has 37,000 km of subduction zones, and if we extrapolate the present subduction velocity of 80 km/Ma (Reymer et al., 1984) back through time, this suggests that the total volume of oceanic crust subducted in 3 Ga is roughly 7% of the total volume of the mantle (or 10% since 4.55 Ga). This contrasts with the relative rarity of the extreme HIMU signature, which has only been observed in the Cook-Austral Islands, St. Helena (Chaffey et al., 1988) and two

seamounts in the western Pacific Ocean (Staudigel et al., 1991). This suggests that the extremely high Pb isotopic compositions represent only the most well preserved (i.e. least well mixed), and possibly the oldest, subducted crust. The slightly higher $^{207}Pb/^{204}Pb$ signature of St. Helena, relative to the Cook-Austral Islands trend, also suggests that St. Helena represents a separate source than that for Tubuai and Mangaia, with a slightly different history. Realistically, there is likely to be a continuum of Pb isotopic compositions between DMM and HIMU which would correspond to either younger, or more well mixed, recycled oceanic crust. Depending on the individual histories, there could also be a variety of $^{187}Os/^{186}Os$ isotopic compositions in these parts of the mantle.

There may also be a recycled oceanic crustal signature in the data for N-MORB. From Fig. 3, it is obvious that there are many MORBs with $^{87}Sr/^{86}Sr$ less than .70300 that also have radiogenic Pb isotopic compositions (Ito et al., 1987; Dosso et al., 1991). If the MORB mantle is the depleted mantle complement of the continental crust, then it should be very depleted in highly incompatible elements such as U, Th, and Pb. As a result, it will be more susceptible to having its Pb isotopic signature dominated by a recycled component. In this context, "less depleted" MORB mantle might lie closer to the geochron, whereas "more depleted" MORB mantle, prone to contamination by a recycled oceanic crustal component, would tend to lie farther to the right of the geochron. If in fact a large fraction of the mantle exists with Pb isotopic compositions near the geochron, but susceptible to contamination with recycled oceanic crust due to very low Pb concentrations, then this may provide an explanation for the enigmatic "Pb paradox", especially in MORBs. More $^{187}Os/^{186}Os$ data is needed to test these ideas, on both MORBs and OIBs with a variety of Pb isotopic compositions.

7. Conclusions

The Re-Os isotope systematics in a group of oceanic island basalts from the south Pacific Ocean have been examined in order to constrain theories of crustal recycling in the mantle. The highly variable Os concentrations in the lavas are controlled by a low Re/Os phase (or phases) in which Os is compatible, possibly olivine, chromite, and/or sulfides. These Os concentration variations determine the Re/Os ratios of the erupted basalts.

The $^{187}Os/^{186}Os$ ratios of EMII basalts from Samoa and Tahaa range from 1.0261 to 1.0861, while $^{187}Os/^{186}Os$ in HIMU basalts from Rurutu, Tubuai and Mangaia varies from 1.1169 to 1.2483. Sediment involvement in the origin of the EMII mantle component is not ruled out by the $^{187}Os/^{186}Os$ data for the Samoa and Tahaa lavas. However, the Os isotope systematics of peridotite-crust mixtures indicate that the $^{187}Os/^{186}Os$ ratio of these mixtures are only very weakly influenced by the small amounts of sediment proposed in the

EMII endmember (1-3%). The high $^{187}Os/^{186}Os$ ratios in basalts from Rurutu, Tubuai and Mangaia provide strong evidence for the role of ancient subducted oceanic crust in the HIMU mantle endmember. The HIMU Pb isotope systematics constrain the age of the recycled crust to be 770-2100 Ma, with a $^{238}U/^{204}Pb$ of 19.7-40 and a Th/U ratio of 1.42-3.65. Other calculated parent daughter ratios in the subducted crust are similar to fresh MORB, suggesting that the parent/daughter fractionations which occur during MORB genesis are sufficient to generate the most extreme HIMU compositions in recycled oceanic crust. The identification of the HIMU isotopic signature (high $^{187}Os/^{186}Os$, high $^{206}Pb/^{204}Pb$, low $^{87}Sr/^{86}Sr$) with recycled oceanic crust suggests that other oceanic mantle sources, including that of some mid-ocean ridge basalts, may contain a component of subducted basaltic crust.

Appendix: Analytical Procedures

Hand samples were split into large pieces using a hydraulic carbon-steel splitter, and these pieces were broken down using a tungsten carbide jaw crusher. The crushed fragments were rinsed with distilled water, dried, and reduced to powder in an agate shatterbox. For the analysis of Pb, Sr, and Nd isotopes and trace element concentrations, 50 mg of powder was spiked with ^{84}Sr, ^{150}Nd, ^{235}U, ^{230}Th, and ^{205}Pb, and dissolved in a mixture of HNO_3, HCl and HF on a hotplate at a surface temperature of 125 °C for several days in a closed 7 ml Savillex screw cap beaker. Pb was separated first in 0.5 N HBr on a column of 20μl of AG1x8 (200-400 mesh) and purified by repeating the column step. The eluants from the Pb chemistry were evaporated to dryness and redissolved in 8 N HNO_3. U and Th were separated together in 8 N HNO_3 on column of 100 μl of AG1x8 (200-400 mesh) and eluted with 6.2 N HCl and 0.5 N HBr. The liquid from the U-Th step was taken to dryness and dissolved in 2.5 N HCl. Subsequent procedures for the separation of alkalies, Sr and REE are given by Hart and Brooks (Hart et al., 1977), and separation of Sm and Nd follows the procedure of Richard et al (Richard et al., 1976), modified by Zindler et. al. (Zindler et al., 1979). Mass spectrometry of Pb, Sr and Nd was performed on the Woods Hole VG354 5-collector mass spectrometer. Pb was run using the silica gel-phosphoric acid technique on single Re filaments in the static mode using 5 Faraday cups, and the data is corrected for fractionation relative to the NBS 981 values given by Todt et al (Todt et al., 1984). Reproducibility of the Pb runs is 0.02% per amu based on repeat runs of NBS 981. Sr was run on single W filaments with a Ta oxide activator (Birck, 1986) in a 3-step dynamic mode with 5 Faraday cups. The ^{87}Sr/^{86}Sr data are normalized to a value of .71022 for NBS 987, and repeat analyses of this standard indicate a reproducibility of 0.0045%. Nd was loaded on the Ta side filament of a Ta-Re double filament assembly, and was run in a 3-step dynamic mode with 5 Faraday cups. ^{143}Nd/^{144}Nd was normalized to a value of .511860 for the LaJolla Nd standard, and repeat analysis of this standard indicate a reproducibility of 0.0040%. U and Th were analyzed on the NIMA-B mass spectrometer at Woods Hole. U and Th were loaded together on a single Re filament with colloidal graphite and analyzed using the electron multiplier, and were corrected for fractionation based on repeat analyses of SRM 500 U. Trace element concentrations (except Re and Os) are accurate to better than 1%. Analytical blanks are given in Table 1 and are insignificant for all analyses reported here.

Analysis of Re and Os Isotopes by Oxygen-Enhanced N-TIMS

Re and Os Separation. All the acids and H_2O used in the separation of Re and Os were purified by subboiling distillation in Vycor glass, quartz or Teflon. For analysis of Re, 1-5 grams of rock powder was weighed out, spiked with ^{185}Re, and dissolved in a 10:1 mixture of HF and HNO_3 in a 60 ml closed Savillex PFA Teflon screw cap vessel. The sample was agitated in an

167

ultrasonic bath for 15 minutes, then set on a hot plate at a surface temperature of 100 °C for several days. The sample was opened, evaporated to dryness, and dissolved in several milliliters of 0.2 N HNO_3. The liquid was centrifuged and loaded onto a column of 1 ml of AG1X8 anion exchange resin (200-400 mesh). The sample was washed with 0.2 N HNO_3, 0.2 N HCl, and 0.2 N HNO_3, and Re eluted with 8 N HNO_3. The sample Re was taken to dryness at a surface temperature of 75 °C. This procedure was then repeated with a smaller column (20 µl resin).

For Os analysis, Os was preconcentrated from the rock matrix by nickel sulfide fire assay (Hoffman et al., 1978). Prior to the fire assay, 30-100 grams of rock powder were weighed into a Coors glazed ceramic crucible, spiked with ^{190}Os , and then, after the spike had dried, mixed with a glass rod in order to distribute the spike evenly through the powder. The flux consisted of a mixture of 20 g borax, 10 g Na_2CO_3, 4 g Ni powder, and 2 g sulfur. The flux was added to the sample powder and homogenized with a glass rod. The sample was fused at 1000 °C for 1.5 to 3 hours (blanks were fused for 1 hour). During the fusion, the platinum-group elements are concentrated in the immiscible NiS bead which segregates at the bottom of the crucible (Hoffman et al., 1978). For fusions with high sample/flux ratios, typically the NiS formed several small beads. After cooling, the NiS beads were extracted by crushing the crucible and its contents and picking out the beads.

The NiS bead was dissolved in 6.2 N HCl on a hotplate at a surface temperature of 150-200 °C under a nitrogen flow. After cooling, the solution was filtered through a 0.45 µm Millipore cellulose filter. The Os was concentrated in the residue left on the filter paper. The distillation and collection of Os as the volatile OsO_4 (b.p. 100 °C) is similar to the procedure described by Luck (Luck et al., 1982). The sample Os is distilled from a solution of CrO_3 (VI) in 4 N H_2SO_4 and collected in concentrated HBr chilled in an ice water bath. The HBr solution was then transferred to a 15 ml Savillex PFA Teflon screw cap beaker, capped tightly, and heated in an oven at 100 °C overnight to allow the reduction of OsO_4 by HBr to go to completion. The beaker was then opened and evaporated on a hotplate at 75°C to a volume of less than 1 µl for the purification step. **Purification.** The sample Os was purified by ion exchange using single resin beads (Luck et al., 1982; Reisberg et al., 1991). The Os sample in HBr was taken to a <1 µl volume, and 8 µl of water containing a single bead of Chelex 20 resin (20 mesh) was added, resulting in a solution of <1 N HBr. The beaker was mounted on the edge of a disc rotating at 30 r.p.m., rotated for 1 hour, allowed to sit for 1 hour, and the bead transferred to a clean 3 ml beaker. The bead was rinsed with 100 µl of 0.5 N HBr and the sample Os was eluted by adding 30 µl of concentrated HBr and agitating in an ultrasonic bath for 30 minutes. The resin bead was discarded and the solution evaporated at 75 °C to <1 µl for loading.

For the overall separation and purification, the Re yield is about 80-90%, while the Os yield varied from 50-90%. Measured blanks averaged 35 pg for Re (including filament blank) and 40

pg Os for the full procedures. The analytical blank had a measured $^{187}Os/^{186}Os$ of 6.60. The Re and Os data in Table 3 are corrected for these analytical blanks.

Mass Spectrometry. The negatively charged oxides of Re (ReO_4^-) and Os (OsO_3^-) are produced by the oxidation of the sample Re and Os by barium oxide on the surface of a Pt filament (Creaser et al., 1991; Volkening et al., 1991). Barium nitrate was prepared by dissolving $BaCO_3$ in dilute nitric acid and repeated dissolution and precipitation from concentrated HNO_3. This serves to convert all the Ba to $Ba(NO_3)_2$ and also to oxidize and eliminate organics. The final precipitate is dissolved in water to yield a solution with a concentration of 5000 mg/g of $Ba(NO_3)_2$. Filaments for mass spectrometry consist of 1x20 mil zone refined 99.95% Pt ribbon (H. Cross). This ribbon contains small amounts of Re, presumably as contamination from the manufacturing of Re products. This is a potential problem due to the possible isobaric interference of $^{187}Re^{16}O_3^-$ on $^{187}Os^{16}O_3^-$ during mass spectrometry. Several different techniques to clean Re from the Pt ribbon were tried, including cleaning in concentrated HNO_3, cleaning in H_2O_2, fluxing with sodium carbonate, and heating in air, none of which were successful. However, based on standard runs, the isobaric interference of $^{187}Re^{16}O_3^-$ on $^{187}Os^{16}O_3^-$ was not observed during our measurements of Os, even for filaments which were not cleaned using the above methods.

Pt filaments are outgassed at 1000 °C for 20 minutes under a vacuum of $<10^{-7}$ torr. The sample Re is dissolved in 1 µl of 0.1 N HNO_3 and is mixed with 1-3 µg of $Ba(NO_3)_2$ which is then loaded onto the filament and dried at 0.5 amps. It is important to minimize the area of the loads of Re, Os and $Ba(NO_3)_2$, so as to minimize the Re oxide signal from the filament and thus the potential for isobaric interference. Repeated analyses of Re spike indicate an average filament Re blank of 0.38 pg for two different batches of Pt filament, with a range from 0.2-0.52 pg. However, occasionally high Re levels were observed during some Os runs, which may be related to local concentrations of Re contamination on the Pt ribbon.

For Os samples, the Os in <1 ml HBr is loaded onto the center of the filament and dried down gently at 0.5 amps. The Os is then reduced to the metal on the filament by heating to 600 °C under a vacuum of $<10^{-6}$ torr for 3-12 hours. In addition to reducing the sample Os, this serves to burn off any volatile contaminants which may be carried over from the sample distillation. Then 1-3 mg of $Ba(NO_3)_2$ is loaded directly on top of the Os and dried at 0.5 amps. At this stage, the Os sample is ready for mass spectrometry.

Re and Os isotope ratio measurements were made on the NIMA-B 9-inch, 60° sector thermal ionization mass spectrometer at the Woods Hole Oceanographic Institution. Ions are accelerated through a potential of 4800 V and collected by a Johnston 15 stage discreet dynode electron multiplier operated in the analog mode at a gain of 24000.

For Re analysis the filament was immediately raised to about 700 °C, which is just below running temperature. As soon as ReO_4^- peaks were observed, the filament temperature was raised

rapidly so as to result in the maximum signal intensity in the shortest possible time. This was typically at a temperature of 750-800 °C as measured by optical pyrometry. Ion currents for several hundred picograms of Re were on the order of 10^{-13} to 10^{-12} amps. Intensities were measured at masses 249 ($^{185}Re^{16}O_4^-$), 251 ($^{187}Re^{16}O_4^-$) and 252.5 (zero), and 251/249 was usually measured to better than 0.1%. The sample Re, loaded from nitric acid, is already in its most oxidized form (Re_2O_7), and it is likely that the formation of ReO_4^- occurs at different temperatures and with different efficiencies for the sample Re (Re_2O_7) and the filament Re (Re metal). This procedure for measuring Re is that which minimizes the contribution of Re from the filament, as determined by repeated measurements of Re spike.

For Os analysis, an oxygen pressure of $6-8\times10^{-7}$ torr is established in the source by leaking filtered oxygen through an inlet valve. The filament is gradually brought to a running temperature of 600-800 °C over 30 minutes. Peak intensities were measured at masses 240 ($^{192}Os^{16}O_3^-$), 238 ($^{190}Os^{16}O_3^-$), 237 ($^{189}Os^{16}O_3^-$) and 236 ($^{188}Os^{16}O_3^-$) for three seconds and mass 235 ($^{187}Os^{16}O_3^-$) for six seconds. Interferences from Pt dioxide, W trioxide, and unidentified peaks on masses 234 ($^{186}Os^{16}O_3^-$) and 232 ($^{184}Os^{16}O_3^-$) make measurements of these isotopes very difficult on small amounts of Os, and no data was collected for these masses. The background is measured at mass 232.5 for six seconds. Ion currents were typically $2-10\times10^{-13}$ amps at mass 240 for nanogram-sized basalt Os loads. The data were corrected for mass dependent isotope fractionation using an exponential law, and are normalized to 240/236 =3.09219 calculated from $^{192}Os/^{188}Os$ = 3.08271 (Luck et al., 1983) and $^{17}O/^{16}O$ = 0.0003708 and $^{18}O/^{16}O$ = 0.002045 (Nier, 1950). Our data reduction accounts for the contribution of the spike to $^{192}Os/^{188}Os$, $^{190}Os/^{188}Os$ and $^{187}Os/^{188}Os$, and the variable oxide contributions on 240/236 resulting from variable amounts of ^{190}Os (spike) and radiogenic ^{187}Os. The data is reported as $^{187}Os/^{186}Os$ which is calculated from the measured $^{187}Os/^{188}Os$ and $^{186}Os/^{188}Os$ = 0.12035 (Luck et al., 1983). In-run precisions were always better than 0.1% on $^{187}Os/^{188}Os$ and $^{190}Os/^{188}Os$. No corrections for $^{187}Re^{16}O_3^-$ on $^{187}Os^{16}O_3^-$ were necessary for these measurements.

Os runs without oxygen suffered from poor ion yields, typically less than 1%, and isobaric interference from $^{187}Re^{16}O_3^-$ was severe. Without oxygen, OsO_2^- and OsO_4^- species were also observed, though at low intensity. The presence of oxygen gas has two effects. The first effect is to enhance the oxide speciation of Re and Os to ReO_4^- and OsO_3^- by reducing the level of the subordinate oxides to background levels. The second effect is to improve the overall ionization efficiency for ReO_4^- and OsO_3^-, resulting in higher signal intensities and higher ion yields. Under optimum conditions of temperature and oxygen pressure, the potentially serious interference of $^{187}Re^{16}O_3^-$ on $^{187}Os^{16}O_3^-$ is eliminated within the resolution of our measurements. However, this interference can become substantial at higher temperatures and/or non-optimal oxygen pressures.

Table A1 shows the results of a number of runs of Os standard solution of varying sizes. Ionization efficiencies for Os range from >4% to 14%, with no apparent systematic variations with sample size. The average ionization efficiency of about 10% is more than a factor of two higher than reported by Creaser et al (Creaser et al., 1991) and far in excess of Os ionization yields reported for other methods (Luck, 1982; Fehn et al., 1986; Russ et al., 1987), allowing the measurement of very small amounts of pure Os. Considering the overall transmission of the mass spectrometer (30-50%), this suggests that at much as 40% of the Os may be forming negatively charged oxide ions. The measured $^{187}Os/^{186}Os$ ratios for the standard runs are reproducible to better than 0.15% over five orders of magnitude in sample size (excluding the 800 fg run).

Table A1 also shows several measurements of 250 pg of Re spike and 250 pg of Re standard solution, as a check on the reproducibility of the Re measurements. The Re isotopic compositions are reproducible to 0.1% for standard Re and 1% for spike Re. These results demonstrate that the interference from the filament Re blank is dependent on the isotopic composition of the Re loaded on the filament, and is also likely a function of the amount of sample Re loaded. As a result of this, no attempt was made to explicitly correct for the filament Re blank.

Table A2 shows the results of a more stringent test on the reproducibility of the isotope ratio measurements. Re and Os were separated from the Samoa basalt sample SAV-B-8, split into aliquots of various sizes, and run as a check on the reproducibility for actual samples. The reproducbility of the sample Re and Os is essentially the same as that for the standards, which reinforces the quality of the separation and mass spectrometry procedures. This is important given the fact that sample Re and Os invariably contain traces of impurities which may degrade the measurement.

The reproducibilities of the Re and Os basalt analyses in Table 3 are calculated from replicate analyses of separate powder aliquots subject to separate dissolutions or fusions. The average reproducibilities of Re and Os concentrations are 2.6% and 4.6% respectively. The $^{187}Os/^{188}Os$ ratios are reproducible to 0.3% after correction for the analytical blank and spike contributions. This measure of the reproducibility incorporates all aspects of the analytical technique.

Sample Size (Os)	Ion Yield	$^{187}Os/^{186}Os$	$^{189}Os/^{188}Os$	$^{190}Os/^{188}Os$	$^{187}Re/^{185}Re$ 200 pg (standard)	$^{187}Re/^{185}Re$ 250 pg (spike)
100 ng	----	1.4476 ± 0.0006	1.2198 ± 0.0002	1.9824 ± 0.0004	1.6742 ± 0.0009	.06015 ± 0.00007
1 ng	> 4%	1.4452 ± 0.0008	1.2198 ± 0.0002	1.9822 ± 0.0003	1.6741 ± 0.0007	.05954 ± 0.0004
1 ng	----	1.4470 ± 0.0005	1.2196 ± 0.0002	1.9848 ± 0.0002	1.6730 ± 0.0009	.06019 ± 0.00006
100 pg	>10.4%	1.4476 ± 0.0011	1.2200 ± 0.0005	1.9838 ± 0.0006	1.6748 ± 0.0003	.05995 ± 0.00002
100 pg	>11.1%	1.4467 ± 0.0017	1.2194 ± 0.0007	1.9837 ± 0.0016	1.6753 ± 0.0002	.06006 ± 0.00003
100 pg	14%	1.4444 ± 0.0011	1.2195 ± 0.0014	1.9841 ± 0.0013	1.6735 ± 0.0003	.05964 ± 0.00008
10 pg	12%	1.4456 ± 0.0089	1.2194 ± 0.0040	1.9847 ± 0.0036	1.6725 ± 0.0002	.05922 ± 0.00003
1 pg	9.4%	1.4448 ± 0.0062	1.2190 ± 0.0033	1.9838 ± 0.0037	1.6753 ± 0.0003	.05964 ± 0.00002
1 pg	11.3%	1.4448 ± 0.0099	1.2206 ± 0.0026	1.9866 ± 0.0031	1.6744 ± 0.0002	.05987 ± 0.00003
800 fg	10.1%	1.450 ± 0.015	1.223 ± 0.013	1.9890 ± 0.0170	1.6737 ± 0.0011	.05955 ± 0.00003
Average		1.4460 ±0.0025	1.2197 ±0.0009	1.9840 ±0.0026	1.6741 ± 0.0019	.05978 ± 0.00063

Table A1. Isotope data for osmium standard solution, Re standard solution, and ^{187}Re spike measured by oxygen-enhanced N-TIMS. Errors on the average values are 2σ, and within-run errors are reported as 2σ of the mean. Isotopic ratio data are corrected for instrumental mass fractionation and oxide contribution.

Sample Size	$^{187}Os/^{186}Os$	$^{190}Os/^{188}Os$
1 ng	1.0749 ± 0.0010	4.1581 ± 0.0008
600 pg	1.0750 ± 0.0011	4.1565 ± 0.0013
300 pg	1.0732 ± 0.0011	4.1624 ± 0.0018
100 pg	1.0733 ± 0.0012	4.1593 ± 0.0015
30 pg	1.0732 ± 0.0017	4.1570 ± 0.0024
Average	1.0739 ± 0.0019	4.1587 ± 0.0047

Table A2. Os isotopic data for aliquots of Os separated from Samoa basalt sample SAV-B-8. Errors on the average values are 2σ, and within-run errors are reported as 2σ of the mean. Data are corrected for mass fractionation and oxide contribution. Elevated $^{190}Os/^{188}Os$ ratios relative to the natural ratio are due to the addition of ^{190}Os spike for isotope dilution measurement.

References

Allegre, C. J., S. R. Hart and J. F. Minster (1983) Chemical structure and evolution of the mantle and the continents determined by inversion of Nd and Sr isotopic data, II. Numerical experiments and discussion. Earth Planet. Sci. Lett., **66**, 191-213.

Allegre, C. J. and J. M. Luck (1980) Osmium isotopes as petrogenetic and geological tracers. Earth Planet. Sci. Lett., **48**, 148-154.

Allegre, C. J. and D. L. Turcotte (1986) Implications of a two component marble-cake mantle. Nature, **323**, 123-127.

Bellon, H., R. Brousse and A. Pantaloni (1980) Ages de l'ile de Tubuai: l'alignement des Australes et des Cook. Cah. Pacific, **2**,

Birck, J. L. (1986) Precision K-Rb-Sr isotopic analysis: application to Rb-Sr chronology. Chem. Geol., **56**, 73-83.

Bourdon, B., A. Zindler and L. Reisberg (1990) Pb isotopic results for the Ronda ultramafic complex (abst.). Geol. Soc. Aus. Abs., **27**,12.

Chaffey, D. J., R. A. Cliff and B. M. Wilson (1988) Characterization of the St. Helena magma source, in "Magmatism in the Ocean Basins", A.D. Saunders and M.J. Norry, eds., Geol. Soc. London. Special Publication, **42**, Blackwell Scientific, London, pp. 257-276.

Chase, C. G. (1981) Oceanic island lead: two-stage histories and mantle evolution. Earth Planet. Sci. Lett., **52**, 277-284.

Chauvel, C., A. W. Hofmann and P. Vidal (1992) HIMU-EM: the French Polynesian connection. Earth Planet. Sci. Lett., **110**, 99-119.

Church, S. E. and M. Tatsumoto (1975) Lead isotope variations in oceanic ridge basalts from the Juan de Fuca-Gorda Ridge area, N.E. Pacific Ocean. Contrib. Mineral. Petrol., **53**, 253-279.

Cohen, R. S., N. M. Evensen, P. J. Hamilton and R. K. O'Nions (1980) U-Pb, Sm-Nd and Rb-Sr systematics of mid-ocean ridge basalt glasses. Nature, **283**, 149-153.

Cohen, R. S. and R. K. O'Nions (1982) The lead, neodymium and strontium isotopic structure of ocean ridge basalts. J. Petrol., **23**, 299-324.

Condomines, M., P. Morand and C. J. Allegre (1981) ^{230}Th-^{238}U radioactive disequilibria in tholeiites from the FAMOUS zone (Mid-Atlantic Ridge, $36°50'$N): Th and Sr isotopic geochemistry. Earth Planet. Sci. Lett., **55**, 247-256.

Creaser, R. A., D. A. Papanastassiou and G. J. Wasserburg (1991) Negative thermal ion mass spectrometry of osmium, rhenium, and iridium. Geochim. Cosmochin. Acta, **55**, 397-401.

Dalrymple, G. B., R. D. Jarrard and D. A. Clague (1975) K-Ar ages of some volcanic rocks from the Cook and Austral Islands. Geol. Soc. Am. Bull., **86**, 1463-1467.

DePaolo, D. J. and G. J. Wasserburg (1976) Nd isotopic variations and petrogenetic models. Geophys. Res. Lett., **3**, 249-252.

Desonie, D. L., R. A. Duncan and M. D. Kurz (1992) Helium isotopic composition of isotopically diverse basalts from hotspot volcanic lineaments in French Polynesia (abst). EOS, 72, 536.

Dickey, J. S., M. Obata and C. J. Suen (1977). Partial fusion *versus* fractional crystallization: hypotheses for the differentiation of the Ronda ultramafic massif of southern Spain. Magma Genesis. Bull. Oregon Dept. Geol. Min. Indust.

Diraison, C. (1991) Le volcanisme aerien des Archipels Polynesiens de la Societe, des Marquises et des Australes-Cook. Ph.D. Thesis, Universite de Bretagne Occidentale.

Doe, B. R. and R. E. Zartman (1979). Plumbotectonics: the Phanerozoic. Geochemistry of hydrothermal ore deposits. New York, John Wiley and Sons. 22-70.

Dosso, L., B. B. Hanan, H. Bougault, J.-G. Schilling and J.-L. Joron (1991) Sr-Nd-Pb geochemical morphology between 10° and 17° N on the Mid-Atlantic Ridge: a new MORB isotope signature. Earth Planet. Sci. Lett., 106, 29-43.

Duncan, R. A. (1985). Radiometric ages from volcanic rocks along the New Hebrides-Samoa lineament., in "Geological Investigations of the Northern Melanesian Borderland", Houston, Texas, Circum-Pacific Council for Energy and Resources, pp. 67-76.

Duncan, R. A., M. T. McCulloch, H. G. Barsczus and D. R. Nelson (1986) Plume versus lithosphere sources for melts at Ua Pou, Marquesas Islands. Nature, 322, 534-538.

Duncan, R. A. and I. McDougall (1974) Migration of volcanism with time in the Marquesas Islands, French Polynesia. Earth Planet. Sci. Lett., 21, 414-420.

Duncan, R. A. and I. McDougall (1976) Linear Volcanism in French Polynesia. J. Volcan. Geotherm. Res., 1, 197-227.

Duncan, R. A., I. McDougall, R. M. Carter and D. S. Coombs (1974) Pitcairn Island - another Pacific hotspot? Nature, 251, 679-682.

Dupuy, C., H. G. Barsczus, J. Dostal, P. Vidal and J.-M. Liotard (1989) Subducted and recycled lithosphere as the mantle source of ocean island basalts from southern Polynesia, central Pacific. Chem. Geol., 77, 1-18.

Dupuy, C., H. G. Barsczus, J. M. Liotard and J. Dostal (1988) Trace element evidence for the origin of ocean island basalts: an example from the Austral Islands (French Polynesia). Contrib. Mineral. Petrol., 98, 293-302.

Dupuy, C., P. Vidal, H. G. Barsczus and C. Chauvel (1987) Origin of basalts from the Marquesas Archipelago (south central Pacific Ocean); isotope and trace element constraints. Earth Planet. Sci. Lett., 82, 145-152.

Esser, B. K. (1990) Osmium isotope geochemistry of terrigenous and marine sediments. Ph.D., Yale University.

Farley, K. A., J. Natland, J. D. MacDougall and H. Craig (1989) He, Sr and Nd isotopes in Samoan basalts: evidence for enriched and undepleted mantle components (abst). EOS, 71, 1669.

Fehn, U., R. Teng, D. Elmore and P. W. Kubic (1986) Isotopic composition of osmium in terrestrial samples determined by accelerator mass spectrometry. Nature, 323, 707-710.

Galer, S. J. G. and R. K. O'Nions (1989) Chemical and isotopic studies of ultramafic inclusions from the San Carlos volcanic field, Arizona: a bearing on their petrogenesis. J. Petrol., **30**, 1033-1064.

Gisbert, T. (1989) Volcanologie de l'ile de Tahaa, Archipel de la Societe. Docteur en Sciences, Universite de Paris-Sud, Orsay.

Goldstein, S. J., M. T. Murrell, D. R. Janecky, J. R. Delaney and D. A. Clague (1991) Geochronology and petrogenesis of MORB from the Juan de Fuca and Gorda ridges by $^{238}U/^{230}Th$ disequilibrium. Earth Planet. Sci. Lett., **107**, 24-41.

Hamelin, B. and C. J. Allegre (1988) Lead isotope study of orogenic lherzolite massifs. Earth Planet. Sci. Lett., **91**, 117-131.

Hart, S. R. (1988) Heterogeneous mantle domains: signatures, genesis and mixing chronologies. Earth Planet. Sci. Lett., **90**, 273-296.

Hart, S. R. and C. Brooks (1977) The geochemistry and evolution of the early precambrian mantle. Contrib. Mineral. Petrol., **61**, 109-128.

Hart, S. R., E. H. Hauri, L. Oschman and J. A. Whitehead (1992) Mantle plumes and entrainment: the isotopic evidence. Science, **256**, 517-520.

Hart, S. R. and E. D. Kinloch (1989) Osmium isotope systematics in Witwatersrand and Bushveld ore deposits. Econ. Geol., **84**, 1651-1655.

Hart, S. R. and H. Staudigel (1982) The control of alkalies and uranium in sea water by ocean crust alteration. Earth Planet. Sci. Lett., **58**, 202-212.

Hart, S. R. and H. Staudigel (1989). Isotopic characterization and identification of recycled components. in "Crust/mantle recycling at convergence zones", S.R. Hart and L. Gulen, eds., NATO ASI Series, Vol. 258, Kluwer Academic Publishers, Boston, pp. 15-28.

Hattori, K. and S. R. Hart (1991) Osmium isotope ratios of platinum-group minerals associated with ultramafic intrusions: Os isotopic evolution of the mantle. Earth Planet. Sci. Lett., **107**, 499-514.

Hauri, E. H., S. R. Hart and G. E. Ravizza (1990) High Precision Measurements of Re and Os isotopes by oxygen-enhanced negative thermal ionization mass spectrometry (abst.). Abstracts of the A.O. Nier Symposium on Inorganic Mass Spectrometry

Hekinian, R., D. Bideau, P. Stoffers, J. L. Cheminee, R. Muhe, et al. (1991) Submarine intraplate volcanism in the south Pacific: geologic setting and petrology of the Society and Austral regions. J. Geophys. Res., **96**, 2109-2138.

Hoffman, E. L., A. J. Naldrett, J. C. V. Loon, R. G. V. Hancock and A. Mason (1978) The determination of all the platinum group elements and gold in rocks and ore by neutron activation analysis after preconcentration by a nickel sulfide fire-assay technique of large samples. Anal. Chim. Acta, **102**, 157-166.

Hofmann, A. W. (1988) Chemical differentiation of the Earth: the relationship between mantle, continental crust, and oceanic crust. Earth Planet. Sci. Lett., **90**, 297-314.

Hofmann, A. W. and S. R. Hart (1978) An assessment of local and regional isotopic equilibrium in the mantle. Earth Planet. Sci. Lett., **38**, 44-62.

Hofmann, A. W. and W. M. White (1980) The role of subducted oceanic crust in mantle evolution. Carnegie Inst. Wash. Yearb., **79**, 477-483.

Hofmann, A. W. and W. M. White (1982) Mantle plumes from ancient oceanic crust. Earth Planet. Sci. Lett., **57**, 421-436.

Horan, M. F., J. W. Morgan, R. J. Walker and J. N. Grossman (1992) Rhenium-osmium isotope constraints on the age of iron meteorites. Science, **255**, 1118-1121.

Ito, E., W. M. White and C. Goepel (1987) The O, Sr, Nd and Pb isotope geochemistry of MORB. Chem. Geol., **62**, 157-176.

Jagoutz, E., H. Palme, H. Baddenhausen, K. Blum, M. Cendales, et al. (1979) The abundance of major, minor and trace elements in the Earth's mantle as derived from primitive ultramafic nodules. Proc. Lunar. Sci. Conf., **10th**, 2031-2050.

Jochum, K. P., A. W. I. Hofmann E, H. M. Seufert and W. M. White (1983) K, U and Th in mid-ocean ridge basalt glasses and heat production, K/U and K/Rb in the mantle. Nature, **306**, 431-436.

Kelemen, P. B., K. T. M. Johnson, R. J. Kinzler and A. J. Irving (1990) High Field strength element depletions in arc basalts due to mantle-magma interaction. Nature, **345**, 521-524.

Kurz, M. D., M. O. Garcia, F. A. Frey and P. A. O'Brien (1987) Temporal helium isotopic variations within Hawaiian volcanoes: basalts from Mauna Loa and Haleakala. Geochim. Cosmochim. Acta, **51**, 2905-2914.

Kurz, M. D., W. J. Jenkins, S. R. Hart and D. Clague (1983) Helium isotopic variations in volcanic rocks from Loihi seamount and the island of Hawaii. Earth Planet. Sci. Lett., **66**, 388-406.

Kurz, M. D., P. S. Meyer and H. Sigurdsson (1985) Helium isotopic systematics within the neovolcanic zones of Iceland.

Lambert, D. D., J. W. Morgan, R. J. Walker, S. B. Shirey, R. W. Carlson, et al. (1989) Rhenium-osmium and samarium-neodymium isotopic systematics of the Stillwater Complex. Science, **244**, 1169-1174.

Liotard, J. M., H. G. Barsczus, C. Dupuy and J. Dostal (1986) Geochemistry and origin of basaltic lavas from Marquesas Archipelago, French Polynesia. Contrib. Mineral. Petrol., **92**, 260-268.

Luck, J.-M. and C. J. Allegre (1991) Osmium isotopes in ophiolites. Earth Planet. Sci. Lett., **107**, 406-415.

Luck, J. M. (1982) Geochimie du Rhenium-Osmium: Methode et Applications. University of Paris VII.

Luck, J. M. and C. J. Allegre (1982) The study of molybdenites through the 187Re-186Os chronometer. Earth Planet. Sci. Lett., **61**, 291-296.

Luck, J. M. and C. J. Allegre (1983) 187Re-186Os systematics in meteorites and cosmochemical consequences. Nature, **302**, 130-132.

Luck, J. M., J. L. Birck and C. J. Allegre (1980) 187Re-187Os systematics in meteorites: early chronology of the solar system and the age of the galaxy. Nature, **283**, 256-259.

Macdonald, G. A. and T. Katsura (1964) Chemical composition of Hawaiian lavas. J. Petrol., **5**, 82-133.

Mahoney, J. J., J. H. Natland, W. M. White, R. Poreda, S. H. Bloomer, et al. (1989) Isotopic and geochemical provinces of the western Indian Ocean spreading centers. J. Geophys. Res., **94**, 4033-4052.

Martin, C. E. (1989) Re-Os isotopic investigation of the Stillwater Complex, Montana. Earth Planet. Sci. Lett, **93**, 336-344.

Martin, C. E. (1991) Os isotopic characteristics of mantle derived rocks. Geochim. Cosmochim. Acta., **55**, 1421-1434.

Martin, C. E., B. K. Esser and K. K. Turekian (1992) Re-Os isotopic constraints on the formation of mantle and crustal reservoirs. Austral. J. Earth Sci., **38**.

McDonough, W. F. and C. Chauvel (1991) Sample contamination explains the Pb isotopic composition of some Rurutu Island and Sasha seamount basalts. Earth Planet. Sci. Lett., **106**, 397-404.

McKenzie, D. P. (1984) The generation and compaction of partially molten rock. J. Petrol., **25**, 713-765.

Mitchell, R. H. and R. R. Keays (1981) Abundance and distribution of gold, palladium, and iridium in some spinel and garnet lherzolites: implications for the nature and origin of precious metal-rich intergranular components in the upper mantle. Geochim. Cosmochim. Acta, **45**, 2425-2442.

Morgan, J. W. (1985) Osmium isotope constraints on earth's late accretionary history. Nature, **317**, 703-705.

Morgan, J. W. (1986) Ultramafic xenoliths: clues to Earth's late accretionary history. J. Geophys. Res., **91**, 12,375-12,387.

Morgan, J. W. and J. F. Lovering (1967) Rhenium and osmium abundances in some igneous and metamorphic rocks. Earth Planet. Sci. Lett., **3**, 219-224.

Morgan, J. W., R. J. Walker and J. N. Grossman (1992) Rhenium-osmium isotope systematics in meteorites I: magmatic iron meteorite groups IIAB and IIIAB. Earth Planet. Sci. Lett., **108**, 191-202.

Morgan, J. W., G. A. Wandless, R. K. Petrie and A. J. Irving (1981) Composition of the Earth's upper mantle, 1; Siderophile trace elements in ultramafic nodules. Tectonophysics, **75**, 47-67.

Morgan, W. J. (1971) Convection plumes in the lower mantle. Nature, **230**, 42-43.

Nakamura, Y. and M. Tatsumoto (1988) Pb, Nd, and Sr isotopic evidence for a multicomponent source for rocks of Cook-Austral Islands and heterogeneities of mantle plumes. Geochim. Cosmochim. Acta, **52**, 2909-2924.

Natland, J. H. (1980) The progression of volcanism in the Samoan linear chain. Am. J. Sci., **280**, 709-735.

Natland, J. H. and D. L. Turner (1985). Age progression and petrological development of Samoan shield volcanoes: evidence from K-Ar ages, lava compositions and mineral studies., in "Geological Investigations of the Northern Melanesian Borderland", Houston, Texas, Circum-Pacific Council for Energy and Resources, pp. 139-171.

Navon, O. and E. Stolper (1987) Geochemical consequences of melt percolation: the upper mantle as a chromatographic column. J. Geol., **95**, 285-307.

Newman, S., R. C. Finkel and J. D. Macdougall (1983) 230Th-238U disequilibrium systematics in oceanic tholeiites from 21°N on the East Pacific Rise. Earth Planet. Sci. Lett., **65**, 17-33.

Newsom, H. E., W. M. White, K. P. Jochum and A. W. Hofmann (1986) Siderophile and chalcophile element abundances in oceanic basalts, Pb isotope evolution and growth of the Earth's core. Earth Planet. Sci. Lett., **80**, 299-313.

Nier, A. O. (1950) A redetermination of the relative abundances of the isotopes of carbon, nitrogen, oxygen, argon and potassium. Phys. Rev., **77**, 789-793.

O'Nions, R. K., N. M. Evensen and P. J. Hamilton (1979) Geochemical modeling of mantle differentiation and crustal growth. J. Geophys. Res., **84**, 6091-6101.

Obata, M. and J. S. Dickey (1976) Phase relations of mafic layers in the Ronda peridotite. Carnegie Inst. Wash. Yearb., **75**, 562-566.

Palacz, Z. A. and A. D. Saunders (1986) Coupled trace element and isotope enrichment in the Cook-Austral-Samoa islands, southwest Pacific. Earth Planet. Sci. Lett., **79**, 270-280.

Palmer, M., K. K. Falkner, K. K. Turekian and S. E. Calvert (1988) Sources of osmium isotopes in manganese nodules. Geochim. Cosmochim. Acta, **52**, 1197-1202.

Patchett, P. J. (1983) Hafnium isotope results from Mid-ocean ridges and Kerguelen. Lithos, **16**, 47-51.

Patchett, P. J. and M. Tatsumoto (1980) Hafnium isotope variations in oceanic basalts. Geophys. Res. Lett., **7**, 1077-1080.

Pearson, D. G., S. B. Shirey, R. W. Carlson, F. R. Boyd, P. H. Nixon, et al. (1991) Re-Os and Sm-Nd isotopic constraints on the chronology of lithospheric mantle formation and enrichment events (abst.). EOS, **72**, 527.

Ravizza, G. and K. K. Turekian (1989) Application of the 187Re-187Os system to black shale chronology. Geochim. Cosmochim. Acta., **53**, 3257-3262.

Reisberg, L. and A. Zindler (1986) Extreme isotopic variations in the upper mantle: evidence from Ronda. Earth Planet. Sci. Lett., **81**, 29-45.

Reisberg, L., A. Zindler and E. Jagoutz (1989) Further Sr and Nd isotopic results from peridotites of the Ronda Ultramafic Complex. Earth Planet. Sci. Lett., **96**, 161-180.

Reisberg, L. C., C. J. Allegre and J. M. Luck (1991) The Re-Os systematics of the Ronda Ultramafic Complex of southern Spain. Earth Planet. Sci. Lett., **105**, 196-213.

Reymer, A. and G. Schubert (1984) Phanerozoic addition rates to the continental crust and crustal growth. Tectonics, **3**, 63-77.

Richard, P. N., N. Shimizu and C. J. Allegre (1976) $^{143}Nd/^{146}Nd$, a natural tracer: An application to oceanic basalts. Earth Planet. Sci. Lett., **31**, 269-278.

Russ, G. P., J. M. Bazan and A. R. Date (1987) Osmium isotopic ratio measurements by inductively coupled plasma source mass spectrometry. Anal. Chem., **59**, 984-989.

Salters, V. J. M. and S. R. Hart (1989) The Hf-paradox, and the role of garnet in the MORB source. Nature, **342**, 420-422.

Salters, V. J. M. and S. R. Hart (1990) The mantle sources of ocean islands and arc basalts: the Hf isotope connection. Earth Planet. Sci. Lett., **104**, 364-380.

Snow, J. E. (1991) Os isotopic composition of the oceanic upper mantle. EOS, **72**, 527.

Staudigel, H., K.-H. Park, M. Pringle, J. L. Rubenstone, W. H. F. Smith, et al. (1991) The longevity of the South Pacific isotopic and thermal anomaly. Earth Planet. Sci. Lett., **102**, 24-44.

Suen, C. J. and F. A. Frey (1987) Origins of the mafic and ultramafic rocks in the Ronda peridotite. Earth Planet. Sci. Lett., **85**, 183-202.

Tatsumoto, M. (1978) Isotopic composition of lead in oceanic basalts and its implication to mantle evolution. Earth Planet. Sci. Lett., **38**, 63-87.

Todt, W., R. A. Cliff, A. Hanser and A. W. Hofmann (1984) $^{202}Pb + ^{205}Pb$ double spike for lead isotopic analyses. Terra Cognita, **4**, 209.

Turner, D. L. and R. D. Jarrard (1982) K-Ar dating of the Cook-Austral chain: a test of the hot-spot hypothesis. J. Volcan. Geotherm. Res., **12**, 187-220.

Vidal, P., C. Chauvel and R. Brousse (1984) Large mantle heterogeneity beneath French Polynesia. Nature, **307**, 536-538.

Vidal, P. and L. Dosso (1978) Core formation: catastrophic or continuous? Sr and Pb isotope geochemistry constraints. Geophys. Res. Lett., **5**, 169-171.

Volkening, J., T. Walczyk and K. G. Heumann (1991) Osmium isotope ratio determinations by negative thermal ionization mass spectrometry. Int. J. Mass Spec. Ion Phys., **105**, 147-159.

Vollmer, R. (1977) Terrestrial lead isotopic evolution and formation of the earth's core. Nature, **270**, 144-147.

Walker, R. J., R. W. Carlson, S. B. Shirey and F. R. Boyd (1989) Os, Sr, Nd, and Pb isotope systematics of southern African peridotite xenoliths: Implications for the chemical evolution of subcontinental mantle. Geochim. Cosmochim. Acta., **53**, 1583-1595.

Walker, R. J., L. M. Echeverria, S. B. Shirey and M. F. Horan (1991) Re-Os isotopic constraints on the origin of volcanic rocks, Gorgona Island, Columbia: Os isotopic evidence for ancient heterogeneities in the mantle. Contrib. Mineral. Petrol., **107**, 150-162.

Walker, R. J. and J. W. Morgan (1989) Rhenium-osmium isotope systematics of carbonaceous chondrites. Science, **243**, 519-522.

Walker, R. J., J. W. Morgan, A. J. Naldrett, C. Li and J. D. Fassett (1991) Re-Os isotope systematics of Ni-Cu sulfide ores, Sudbury Igneous Complex, Ontario: evidence for a major crustal component. Earth Planet. Sci. Lett., **105**, 416-429.

Walker, R. J., S. B. Shirey, G. N. Hanson, V. Rajamani and M. F. Horan (1989) Re-Os, Rb-Sr, and O isotope systematics of the Archean Kolar schist belt, Karnataka, India. Geochim. Cosmochim. Acta, **53**, 3005-3013.

Walker, R. J., S. B. Shirey and O. Stecher (1988) Comparative Re-Os, Sm-Nd and Rb-Sr isotope and trace element systematics for Archean komatiite flows from Munro Township, Abitibi Belt, Ontario. Earth. Planet. Sci. Lett., **87**, 1-12.

Watson, E. B., D. Ben Othman, J. M. Luck and A. W. Hofmann (1987) Partitioning of U, Pb, Hf, Yb, Cs, Re, Os between chromian diopsidic pyroxene and haplobasaltic liquid. Chem. Geol., **62**, 191-208.

White, W. M. and A. W. Hofmann (1982) Sr and Nd isotope geochemistry of oceanic basalts and mantle evolution. Nature, **296**, 821-825.

White, W. M., A. W. Hofmann and H. Puchelt (1987) Isotope geochemistry of Pacific mid-ocean ridge basalts. J. Geophys. Res., **92**, 4881-4893.

White, W. M. and P. J. Patchett (1984) Hf-Nd-Sr isotopes and incompatible element abundances in island arcs: Implications for magma origins and crust-mantle evolution. Earth Planet. Sci. Lett., **67**, 167-185.

White, W. M. and J. G. Schilling (1978) The nature and origin of geochemical variation in Mid-Atlantic Ridge basalts from central North Atlantic. Geochim. Cosmochim. Acta, **42**, 1501-1516.

Wilson, J. T. (1963) A possible origin of the Hawaiian Islands. Can. J. Phys., **41**, 863-870.

Woodhead, J. D. and M. T. McCulloch (1989) Ancient seafloor signals in Pitcairn Island lavas and evidence for large amplitude, small length-scale mantle heterogeneities. Earth Planet. Sci. Lett., **94**, 257-273.

Wright, E. and W. M. White (1987) The origin of Samoa: new evidence from Sr, Nd and Pb isotopes. Earth Planet. Sci. Lett., **81**, 151-162.

Zindler, A. and S. R. Hart (1986) Chemical Geodynamics. Ann. Rev. Earth Planet. Sci., **14**, 493-571.

Zindler, A., S. R. Hart, F. A. Frey and S. P. Jakobsson (1979) Nd and Sr isotope ratios and rare earth element abundances in Reykjanes peninsula basalts: evidence for mantle heterogeneity beneath Iceland. Earth Planet. Sci. Lett., **45**, 249-262.

Chapter 5

The Nature of Entrainment in Mantle Plumes: A Boundary Layer Model with a Temperature-Dependent Power Law Rheology and Depth-Dependent Physical Properties

1. Introduction

Since the earliest recognition that the earth's mantle was isotopically heterogeneous (Faure and Hurley, 1963; Gast et al., 1964), studies have attempted to elucidate the origins of these variations in the context of physical models of the earth (Armstrong, 1968; Tatsumoto, 1978; Allegre et al., 1980; Anderson, 1982). With the advent of plate tectonic models (e.g. Vine, 1972) and theories of buoyancy driven fluid flow applied to the earth (Wilson, 1963; Oxburgh and Turcotte, 1968), it was recognized that the mantle could behave as a convecting, viscous fluid over geologic time scales. Numerous subsequent studies in various disciplines have attempted to clarify the complexities of mantle convection, using methods of observation (Anderson, 1967; Jordan, 1977; Dziewonski and Anderson, 1981), experiment (Goetze and Kohlstedt, 1973; Whitehead and Parsons, 1978; Lees et al., 1983), and theory (Parmentier et al., 1976; Yuen and Peltier, 1980; Richter and McKenzie, 1981).

Recent years have seen increased efforts at integrating the information available from the geophysical, geochemical, and fluid dynamic approaches (Allegre, 1982; Richter et al., 1982; Davies, 1984; Hart and Zindler, 1989). Studies which have combined geochemical observations with geophysical data (Hart, 1984) and fluid dynamic models (Davies, 1984) have resulted in a better understanding of the processes by which chemical heterogeneities may be created, maintained, and modified in a dynamic earth. However, a great deal remains to be discovered about about the ultimate origins of the geochemical signatures observed in studies of mantle derived rocks.

This study attempts to relate aspects of viscous flow in thermally buoyant mantle plumes with geochemical observations of volcanic rocks from oceanic islands. The existence of buoyant plumes in the mantle are robust features of any fluid mechanical description of the interior of the earth, and provide a compelling mechanism for the creation of age-progressive volcanic island chains (Wilson, 1963; Morgan, 1971). Since geochemical investigations of oceanic basalts have provided most of the data describing the chemical heterogeneity of the convecting mantle, constraints on the origins of these chemical signatures and their expression at the surface of the earth should be obtainable from fluid dynamic studies of the flow in buoyant plumes. In this chapter, a generalized fluid flow model for thermally buoyant mantle plumes is developed, in which experimentally constrained physical properties of the mantle are incorporated. This model does not pretend to exactly describe the sizes, temperatures, and flow velocities of actual mantle plumes. Such information can only come from detailed knowledge of the physical properties of the mantle at relevant temperatures, pressures, and strain rates, some of which are impossible to measure experimentally. Instead, the emphasis is on describing very

general aspects of the fluid flow which are likely to be robust features over a wide range of parameter space, and to see if these features provide some constraints on the nature of the geochemical heterogeneities observed in oceanic volcanics.

2. Boundary Layer Plume Model

This study examines the vertical, steady-state boundary layer flow around a point source of heat in axisymmetric coordinates (Fig. 1). In this analyses, only the plume conduit is examined; the plume source, and the ultimate fate of the plume material at the top of the conduit, are not specified, nor are they required for the examination of the conduit. Due to the relative magnitudes of temperature and velocity gradients in the vertical direction compared to the radial direction, boundary layer theory (Schlichting, 1968) provides a good framework in which to describe flow in thermal plumes. The fluid is assumed to be incompressible, with the exception of thermal buoyancy (Boussinesq approximation), and viscous dissipation is ignored. In addition, the vertical momentum equation is assumed to represent a balance between buoyancy and the radial component of the shear stress in the vertical direction (Yuen and Schubert, 1976). The equations governing the conservation of mass, energy, and momentum are:

$$\frac{\partial}{\partial Z}(UR) + \frac{\partial}{\partial R}(VR) = 0 \tag{1}$$

$$U\frac{\partial T}{\partial Z} + V\frac{\partial T}{\partial R} - \frac{K}{R}\left[\frac{\partial}{\partial R}(R\frac{\partial T}{\partial R}) + \frac{\partial}{\partial Z}(R\frac{\partial T}{\partial Z})\right] = 0 \tag{2}$$

$$-\frac{\partial P}{\partial Z} + \frac{1}{R}\left[\frac{\partial}{\partial R}(\tau_{zr}R) + \frac{\partial}{\partial Z}(\tau_{zr}R)\right] + \rho g\alpha\Delta T = 0 \tag{3}$$

where P is the non-hydrostatic pressure, (U,V) are the horizontal and vertical velocities, (R,Z) are the radial and axial coordinates, T is temperature, t is the shear stress tensor, r is density, k is thermal diffusivity, a is the coefficient of thermal expansion, and ΔT is the excess plume temperature. For the boundary layer approximation, it is assumed that the flow is slow, so that the non-hydrostatic pressure term in (2) can be ignored, and that vertical gradients in temperature and velocity are small compared with the radial gradients. With these approximations, the conservation equations reduce to:
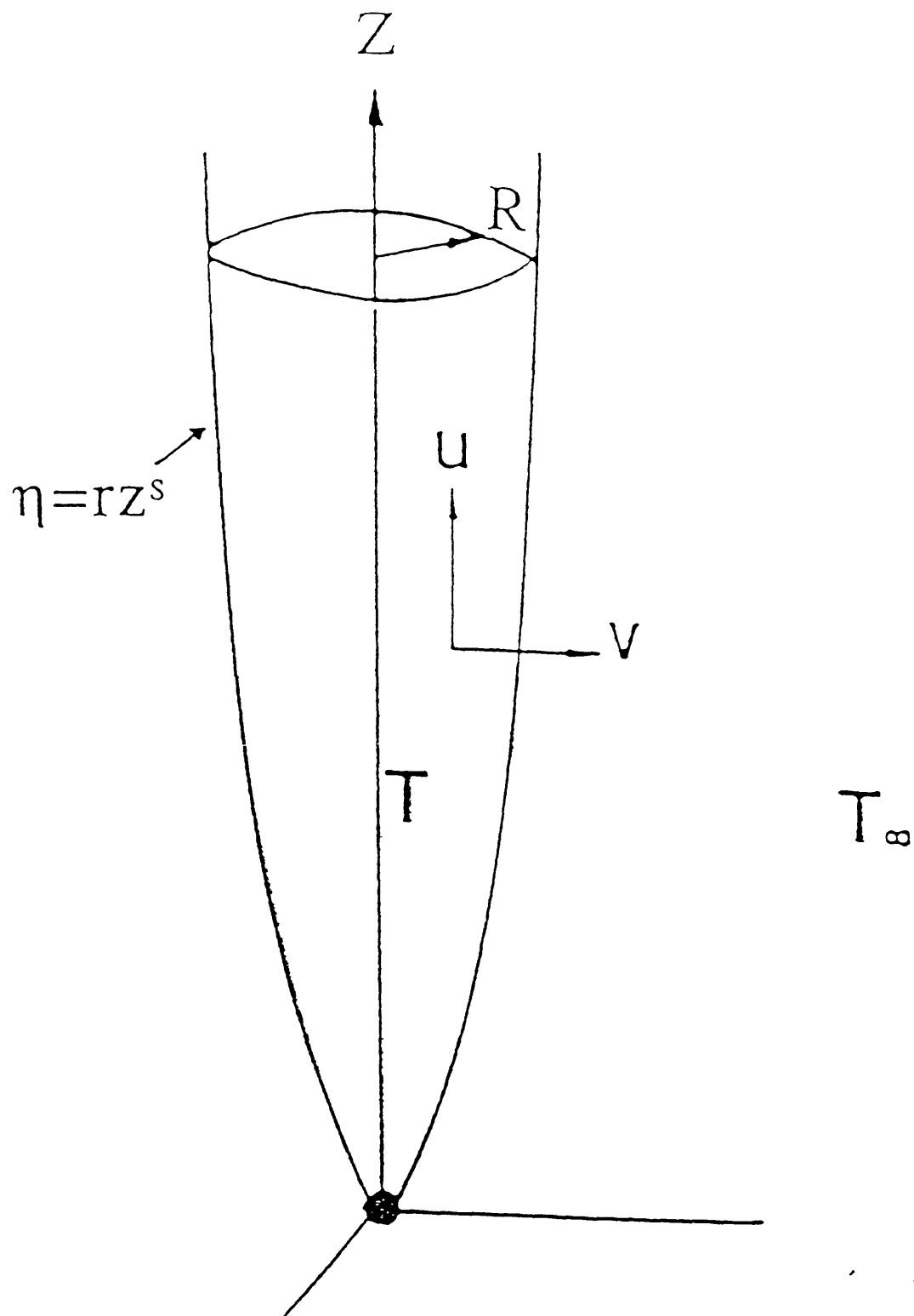
Figure 1. Coordinate system for the axisymmetric boundary layer model. The edge of the plume is described by the curve $\eta=rz^s$ in R-Z space.

$$\frac{\partial}{\partial Z}(UR) + \frac{\partial}{\partial R}(VR) = 0 \tag{4}$$

$$U\frac{\partial T}{\partial Z} + V\frac{\partial T}{\partial R} - \frac{K}{R}\frac{\partial}{\partial R}(R\frac{\partial T}{\partial R}) = 0 \tag{5}$$

$$\frac{1}{R}\frac{\partial}{\partial R}(\tau_{zr}R) + \rho g\alpha\Delta T = 0 \tag{6}$$

$$\tau_{zr} = \left(\mu_o\, F_{\Delta T}\, \frac{\partial U}{\partial R}\right)^{\frac{1}{n}} \tag{7}$$

where n is the power law creep exponent, μ_o is a pre-exponential factor (viscosity), $F_{\Delta T}$ describes the temperature dependence of the rheology, and the strain rate is approximated by the vertical velocity gradient in the radial direction (Yuen and Schubert, 1976). The linear, Newtonian power law (n=1) is valid in the limit of low deviatoric stress, where diffusion creep is the relevant deformation mechanism (Weertman and Weertman, 1975). Deformation by the mechanism of dislocation creep is described by a non-Newtonian power law (n>1). Experimental deformation studies, though conducted at strain rates several orders of magnitude above typical tectonic values, have measured non-Newtonian rheologies for olivine, indicating a value for n of 2-5 (Goetze and Kohlstedt, 1973).

The standard Arrhenius relationship for the temperature dependence of viscosity has a functional form which is incompatible with the form of the conservation equations, and thus cannot be used. Instead, the temperature dependence of the rheology is given by an empirical relationship:

$$F_{\Delta T}=\exp(\exp(\exp(\exp[A - \frac{Z}{h}C\Delta T]))) \tag{8a}$$

which will be abbreviated by:

$$F_{\Delta T} = \exp^4\!\left(A - \frac{Z}{h}C\Delta T\right) \tag{8b}$$

In this parameterized temperature dependence term, the number of successive exponentials, as well as the constants A and C, can be fit to an Arrhenius function for viscosity for any activation energy (Goetze and Kohlstedt, 1973; Stocker and Ashby, 1973), and is a

186

function of ΔT relative to the ambient temperature of the fluid (1300 °C in this case). In this relationship, the dependence of viscosity on pressure is ignored.

The boundary layer equations are non-dimensionalized according to:

$$(r,z) = \frac{(R,Z)}{h} \qquad (9)$$

$$(u,v) = (U,V)\frac{h}{\kappa} \qquad (10)$$

$$\theta = \frac{\Delta T}{\Delta T_{BL}} \qquad (11)$$

where ΔT_{BL} is the difference between the ambient fluid temperature (1300°C) and the axial temperature of the plume at its base ($z=1$). The length scale h is a free parameter which is undetermined. The equations are solved by substitution of a stream function ψ based on a similarity variable, such that:

$$u = \frac{1}{r}\frac{\partial \psi}{\partial r}$$

$$v = -\frac{1}{r}\frac{\partial \psi}{\partial z} \qquad (12)$$

The similarity transformation is:

$$\eta = rz^s$$
$$\theta = \theta(\eta)$$
$$\psi = zf(\eta) \qquad (13)$$

where η is the similarity variable, s is the similarity exponent, and ψ is the stream function. After substitution of the similarity variables, the momentum equation becomes:

$$f''' + (n-2)\frac{f''}{\eta} + (2-n)\frac{f'}{\eta^2} + (C\Delta T_{BL})(F)'(f''\theta' - \frac{f}{\eta}\theta') +$$

$$(F)^{-\frac{1}{n}}(f'' - \frac{f'}{\eta})^{\frac{n-1}{n}}[r^4z^{-2}][r^3z]^{\frac{n-1}{n}} Ra\ \theta = 0$$

$$(14)$$

187

where

$$\langle F \rangle' = \exp^3(A-C\Delta T_{BL}\theta) \ \exp^2(A-C\Delta T_{BL}\theta) \ \exp(A-C\Delta T_{BL}\theta)$$

$$\langle F \rangle = \exp^4(A-C\Delta T_{BL}\theta) \qquad (15)$$

In order for the similarity solution to be valid, η must be the only independent variable, and thus the term

$$\left[r^4z^{-2}\right]\left[r^{-3}z\right]^{\frac{n-1}{n}} \qquad (16)$$

must be some power of η. This condition is met when

$$s = -\frac{n+1}{n+3} \qquad (17)$$

and thus

$$\left[r^4z^{-1}\right]\left[r^{-3}z\right]^{\frac{n-1}{n}} = \eta^{\frac{1}{n}} \qquad (18)$$

The boundary of the plume is defined as the value of η at which the excess temperature drops to 1% of the excess temperature at the plume axis; thus, the plume conserves buoyancy. The transformed momentum and energy equations are:

$$f'''+(n-2)\frac{f''}{\eta} +(2-n)\frac{f'}{\eta^2} +(C\Delta T_{BL})\langle F \rangle'(f''\theta'- \frac{f'}{\eta}\theta')+$$

$$\langle F \rangle^{-\frac{1}{n}} (f''- \frac{f'}{\eta})^{\frac{n-1}{n}} \eta^{\frac{1}{n}} \ Ra \ \theta = 0$$

$$(19)$$

$$\eta\theta' + f\theta = 0 \qquad (20)$$

The dimensionless parameter Ra is a power-law Rayleigh number:

188

$$Ra = \frac{n\rho g\alpha\Delta T_{BL}h^{\frac{n+2}{n}}}{[\mu_0\kappa]^{\frac{1}{n}}}$$

(21)

This Rayleigh number should not be confused, or compared, with the equivalent parameter used in studies of fluid layer convection, due to the different length scales used (see below). For the constant viscosity case (C=0) with a linear rheology (n=1), these equations reduce to the point source equations of (Brand and Lahey, 1967; Liu and Chase, 1991).

The transformed momentum and energy equations are coupled ordinary differential equations in one variable, and are integrated with a fourth order Runge-Kutta-Fehlberg algorithm using the shooting method. In this method of integration, the nonlinear properties of the governing equations are fully preserved, which is important for describing the flow in a fluid with a variable viscosity. The equations were solved subject to the boundary conditions:

$$\theta(0)=1$$ (22)

$$\theta'(0)=0$$ (23)

$$f(0)=0$$ (24)

$$f'(0)=0$$ (25)

$$f'(\infty)=0$$ (26)

$$\theta(\infty)=0$$ (27)

Equation (25) indicates a stress free condition at the plume axis. Equation (23) specifies zero temperature gradient at the plume axis; eqs. (26) and (27) indicate that the excess temperature and vertical velocity vanish far from the plume. The boundary conditions far from the plume were satisfied at $\eta=5$, which in the dimensional results discussed below, corresponds to a distance of roughly 10,000-30,000 km from the plume centerline; carrying the integration out to larger values of η results in only minor changes in the dimensional results (i.e. about <1% increase in centerline vertical velocity for $\eta=10$). The results are dimensionalized by assuming the base of the plume starts at z=1. Thus, height above the base of the plume (z*) is related to the coordinate system through a virtual origin, where the virtual origin (z=0) is located a distance h below the base of the plume:

$$z=(z*+h)/h$$ (28)

E	creep activation energy	523	kJ mol^{-1}
A	rheological parameter	.30428	
C	rheological parameter	1.37×10^{-4}	°C^{-1}
$\mu_{0,1}$	pre-exponential factor (n=1)	1	kg m^{-1} s^{-1}
$\mu_{0,3}$	pre-exponential factor (n=3)	3.25×10^{-10}	kg^3 m^{-3} s^{-5}
ρ	fluid density	3300	kg m^{-3}
g	gravitational acceleration	9.81	m s^{-2}
α	coefficient of thermal expansion	1.45×10^{-5}	°C^{-1}
κ	thermal diffusivity	2.5×10^{-6}	m^2 s^{-1}

Table 1. Physical properties of the fluid used during the numerical modelling.

Dimensional quantities can be calculated from the non-dimensional results by the following expressions:

$$\tau = \left[\frac{\mu_o \kappa}{h^2}\right]^{\frac{1}{n}} \left[\exp^4(A-C\Delta T_{BL}\theta)\right]^{\frac{1}{n}} \left[\left(\frac{z^*+h}{h}\right)^{3s+1}\left(\frac{f''}{\eta} - \frac{f'}{\eta^2}\right)\right]^{\frac{1}{n}} \tag{29}$$

$$\mu = \tau \left[\left(\frac{\kappa}{h^2}\right)\left(\frac{z^*+h}{h}\right)^{3s+1}\left(\frac{f''}{\eta} - \frac{f'}{\eta^2}\right)\right]^{-1} \tag{30}$$

$$U = \left(\frac{\kappa}{h}\right)\left(\frac{z^*+h}{h}\right)^{2s+1}\left(\frac{f'}{\eta}\right) \tag{31}$$

$$V = -\left(\frac{\kappa}{h}\right)\left(\frac{z^*+h}{h}\right)^{s}\left(\frac{f}{\eta} + sf'\right) \tag{32}$$

$$\Delta T = \left(\frac{z^*+h}{h}\right)^{-1}\Delta T_{BL}\,\theta \tag{33}$$

$$R = \left(\frac{z^*+h}{h}\right)^{-s} h\,\eta \tag{34}$$

The length scale h is a critical parameter in converting the results of the numerical integration into dimensional information. Yuen and Schubert (1976) set Ra=1 and solved for h in order to dimensionalize their results. However, this is clearly assuming the scale length of the problem. This problem does not have a unique length scale which could be used for every plume. For example, in the problem of convection of a fluid layer, the depth of the layer is used to scale the results through the Rayleigh number. But in the case of an isolated plume of infinite vertical extent, the choice of a value for h is not at all clear. In principle, from equation (33), a value of h could be constrained experimentally through the drop in the axial temperature with height; however, it is not clear if such a value could be extrapolated to different fluids under different conditions.

An important result which depends directly on h is the percent entrainment, defined as the percentage of the mass flux at the top of the system (z=2700 km) in excess of the mass flux at the base of the system:

191

$$\% E = 100 \{ \text{mass flux (2700 km)} / \text{mass flux (0 km)} \} -1 \qquad (35)$$

The percent entrainment goes as R^2, and thus the actual value of %E depends only on the relative values of z* (depth of the fluid layer) and h. For a fixed layer depth z*, the value of h determines the distance of that layer from the point source, and determines the curvature of the plume boundary with height (Fig. 1). If h is large, then the plume radius and the axial temperature change little with height, and thus entrainment is small. For small h, the plume radius and axial temperature vary more with height, and entrainment is larger. In the present study, the emphasis is not on absolute amounts of entrainment, but on describing the processes which enhance or diminish entrainment.

For the results presented below, the value of h was varied from 1000-5000 km, and ΔT_{BL} varied from 250-1000°C. The results of the numerical experiments described below show, however, that the processes which govern the entrainment of ambient fluid are largely independent of the actual value of h. Thus the results are of general interest in describing the entrainment process in viscous fluids. The differences in the flow regime for linear (Newtonian) and non-linear (non-Newtonian) rheologies will be examined, assuming that thermal expansion, thermal diffusivity, and viscosity (at constant temperature) do not vary with depth. In this case, the plume conserves buoyancy along its length. The values of the various physical constants used are given in Table 1. In a later section, the effect of the variation of μ_0, α, and κ with depth on the growth of the plume boundary will be discussed.

3. Flow Characteristics of Thermal Plumes

3.1 Linear and Non-Newtonian Rheologies

Figures 2 and 3 show quantitative results for two integrations of the model, with linear (n=1) and non-Newtonian (n=3) rheologies, both with a creep activation energy of 523 kJ/mol, which is appropriate for olivine (Goetze and Kohlstedt, 1973). The value of h used is 2700 km, which is essentially the assumed depth of the fluid layer (allowing 100 km each for upper (lithosphere) and lower (CMB) boundary layers). These results were calculated at a height of 2700 km above the base of the plume.

Figure 2 shows that the effect of the non-Newtonian rheology is to narrow the radial velocity and temperature profiles. In both cases, the vertical velocity profile extends to much larger radii than the temperature profile. This is due to viscous coupling of the ambient fluid to the flow in the plume conduit. This effect is easily recognizable by considering the fluid's Prandtl number, which is the ratio of the kinematic viscosity to the thermal diffusivity:

$$Pr = \nu / \kappa \qquad (35)$$

For the earth's mantle, this number is on the order of 10^{24}. The kinematic viscosity can be thought of as a momentum diffusivity, and for the mantle we can see that the diffusion of momentum, or force, is much faster than the diffusion of heat, and thus the different scale lengths of the velocity and temperature boundary layers. This feature is characteristic of high Prandtl number fluids.

In addition, the vertical velocity profile for the non-Newtonian plume displays a region around the plume axis, out to about 10 km, with a very low velocity gradient. This part of the plume is surrounded by a region in which the velocity drops off very rapidly, and finally the velocity decays exponentially to zero. This "plug flow" is a robust characteristic of nonlinear rheologies (Parmentier et al., 1976). In the Newtonian plume, the velocity gradients are not as localized, and instead the profile displays a more gradual decay as a function of radius.

The reason for this difference in velocity field can be seen from Figure 2c. In the linear case, the viscosity depends only on temperature, and so the radial viscosity profile mirrors the temperature (Fig. 2b). In the non-Newtonian case, the viscosity at the plume center increases to infinity toward the plume axis (Fig. 2c). This is due to the inverse dependence of viscosity on strain rate, which drops to zero at the plume axis. This high viscosity at the plume axis makes this material very rigid and difficult to deform, resulting in the low axial velocity gradient shown in Fig. 2a. Farther from the axis, the effects of decreasing temperature (Fig. 2b) and increasing shear stress (Fig. 2d) on viscosity work against each other, and so the viscosity reaches a minimum value. Far from the plume center, the viscosity in the non-Newtonian case remains low due to the finite shear stress in the ambient fluid. This lower viscosity in the ambient fluid for the non-Newtonian case allows the shear stress to be relieved closer to the plume center, thus narrowing the velocity field relative to the linear case. The higher vertical velocities in the non-Newtonian plume also result in a lower radial pressure in the conduit, further narrowing the velocity profile.

It is important to note that these characteristics of the non-Newtonian plume do not depend on the activation energy of the dislocation creep process. In the regions of the plume where the non-Newtonian viscosity deviates most from the linear case, the strain rate dependence dominates over the temperature dependence. At the plume center, the strain rate drops to zero, and thus the viscosity must tend toward infinity, no matter the temperature dependence. Far from the plume, the temperature has decayed to zero, yet the strain rate is still finite, resulting in a lower viscosity compared with the linear case. By
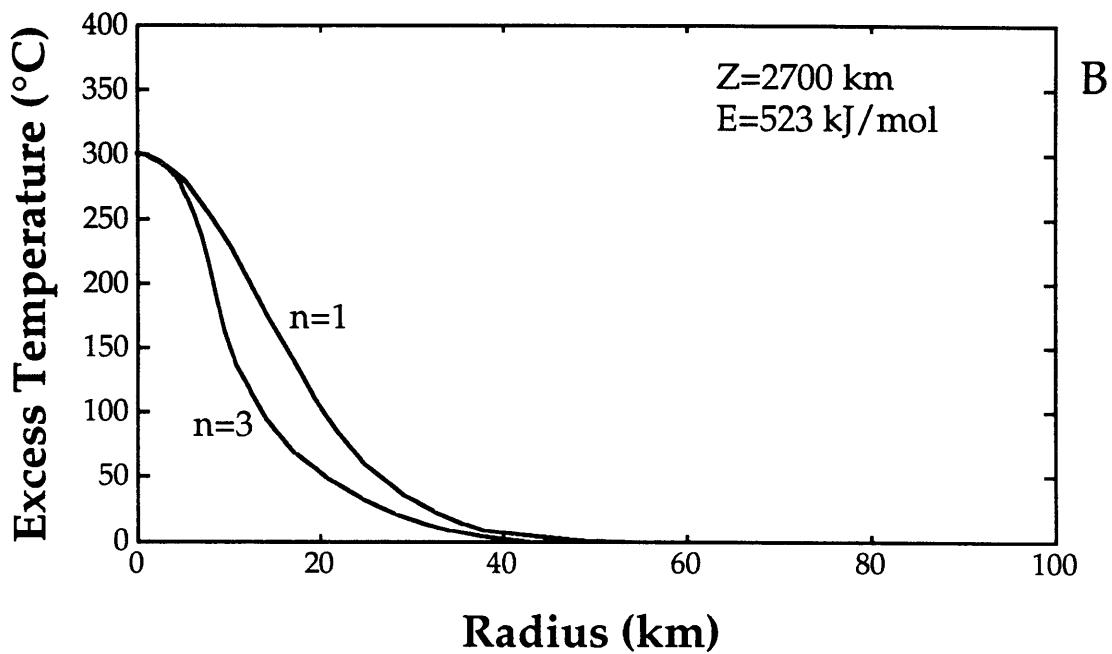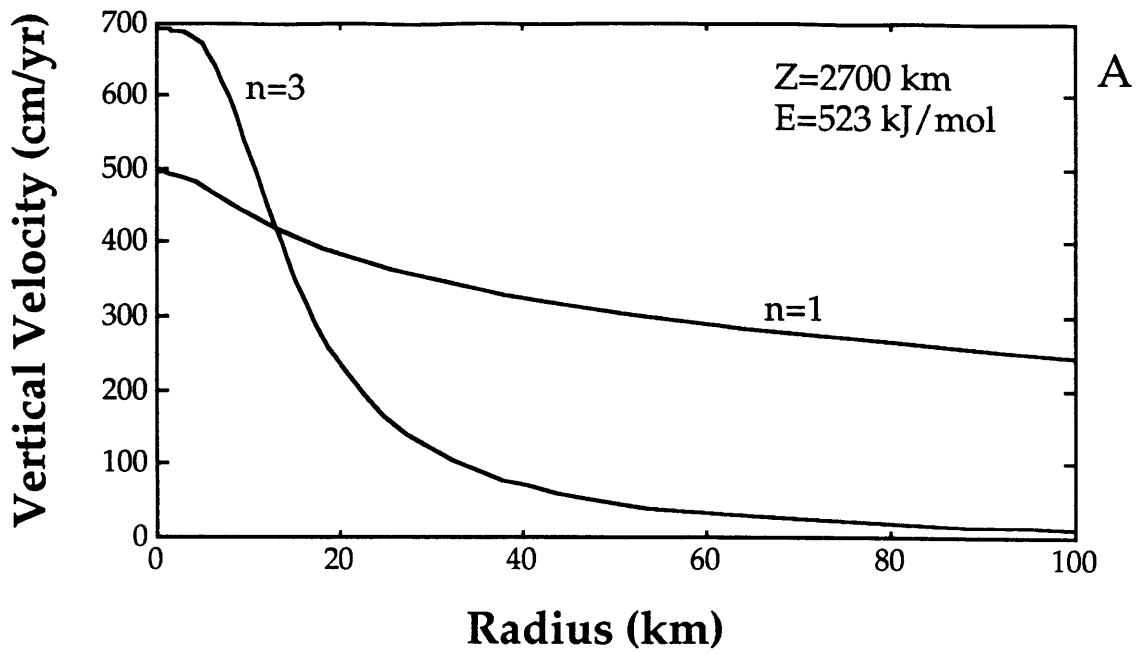
193

Figure 2. A) Vertical velocity profiles, and B) Excess temperature profiles for Newtonian (n=1) and non-Newtonian (n=3) plumes, both with creep activation energies of 523 kJ/mol. Profiles were calculated at a height of 2700 km above the base of the plume, and for an excess temperature at the base of the plume of 600 °C.

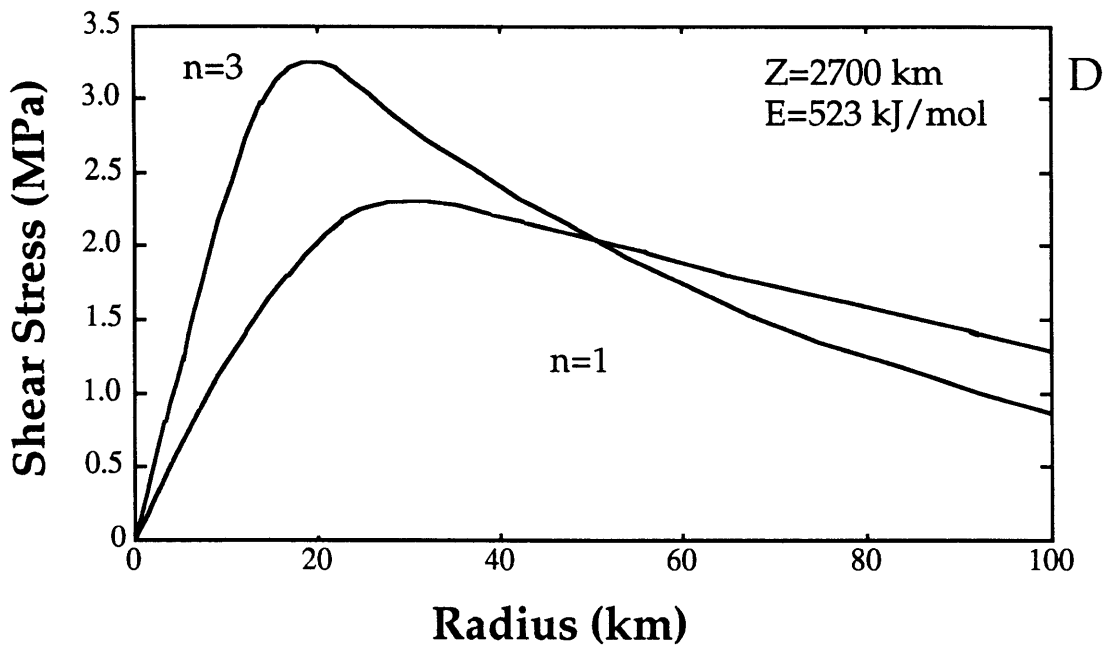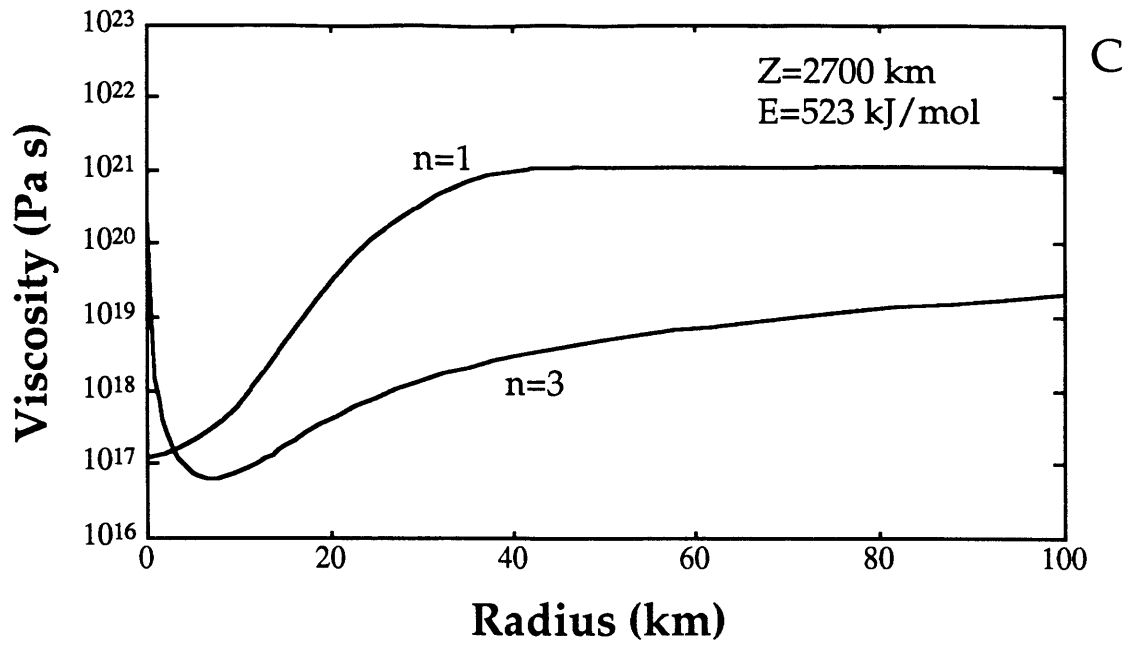Figure 2. C) Viscosity profiles, and D) shear stress profiles for Newtonian (n=1) and non-Newtonian (n=3) plumes, both with creep activation energies of 523 kJ/mol. Profiles were calculated at a height of 2700 km above the base of the plume, and for an excess temperature at the base of the plume of 600 °C.

increasing the activation energy, and thus the temperature dependence of the viscosity, the main effect would be to shift the location of the viscosity minimum toward the plume axis. This would narrow the region of "plug flow" at the center of the plume, but would not eliminate it entirely.

In reality, the viscosity exactly at the plume axis in the non-Newtonian case will not be infinitely high. At the axis, shear stress and strain rates are low, and so the deformation mechanism will be diffusion creep, which is linear (n=1). However, the transition to dislocation creep (non-Newtonian) takes place at shear stresses of 10^{-2} to 10^{-1} MPa (Turcotte and Schubert, 1982), which would be established only a few meters from the plume axis (Fig. 3b). At this distance from the axis, strain rates are still negligible in the linear case (Fig. 2a). This analysis indicates that the "plug flow" exhibited by the non-Newtonian rheology is a persistent feature which is independent of the temperature dependence of viscosity.

3.2 Mechanism of Thermal Entrainment

Equation (34) shows that the radius of the plume conduit, defined as the point at which the axial excess temperature decays to 1%, increases as a function of height above the plume source. The increase in radius goes as the 1/2 power in the linear case, and as the 2/3 power for n=3. The growth of this boundary layer is due to the entrainment of ambient fluid into the plume flow. Heat diffuses outward into the ambient fluid, and this heat increases the buoyancy of the fluid near the plume, and also lowers its viscosity. As a result, this material gains additional vertical velocity, and becomes part of the plume flow. The process is aided by a slow flow of ambient material toward the plume conduit, which balances the mass of entrained fluid flowing up the conduit.

In order to illustrate the fluid flow during this process, streamlines were calculated for the above non-Newtonian plume, and are plotted in Figure 3. These streamlines are the paths of fluid flow for the calculated model, and it can be seen that ambient fluid crosses the plume boundary, which increases with height. In this case, the plume boundary was defined as the point at which the excess temperature dropped to 1% of the axial value, and so defines the horizontal limit of the excess temperature of the plume. In this particular case, the plume radius increases by about 40% through the depth of the fluid layer (Fig. 3).

In addition to this entrainment process, a significant redistribution of fluid occurs within the plume conduit. For example, in Fig. 3a, fluid which starts out at the plume boundary (R=50 km) near the base of the system flows toward the center of the conduit, and is located 20 km from the axis near the top of the system. This indicates that fluid which is entrained at the plume boundary continues to move toward the center of the plume due to a small, but finite horizontal velocity component, which vanishes at the plume axis.
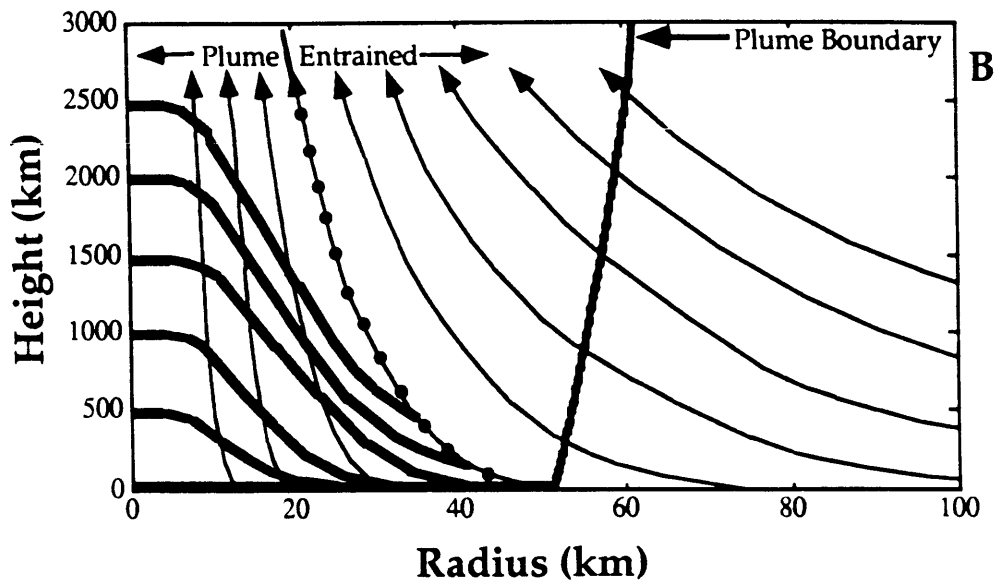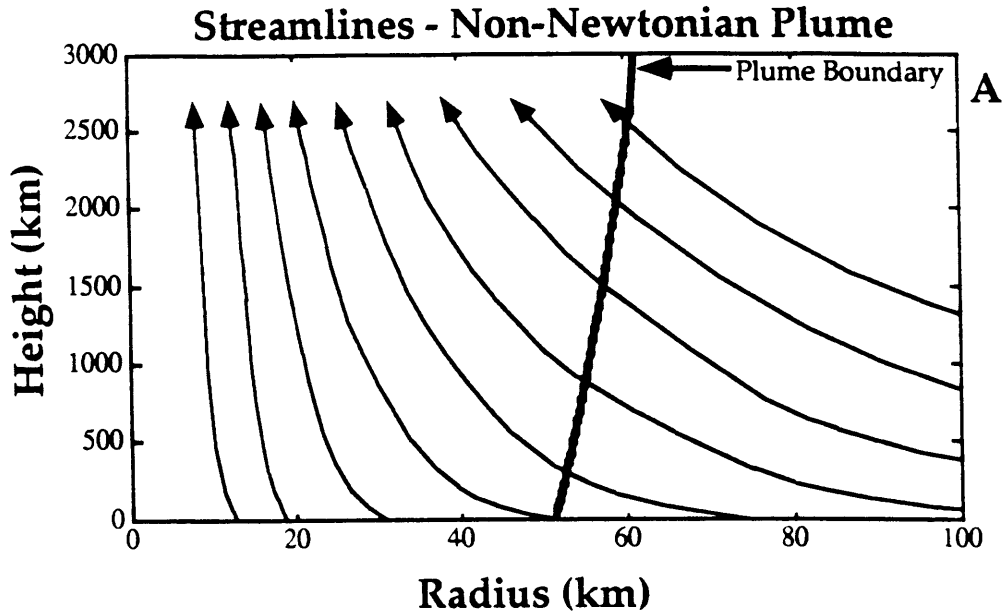
196

Figure 3. A) Streamlines calculated for the non-Newtonian (n-3) plume shown
in Fig. 2. Heavy line marks the plume boundary, defined as the point at which
the excess temperature has dropped to 1% of the axial value. Arrows indicate the
direction of flow. B) Streamlines as in A, but showing the deformational evolution
of a layer 75 km thick (heavy horizontal line at the base of the plume). The original
volume of plume source fluid is deformed toward the axis by a slow radial inflow
of entrained fluid. The streamline marked with dots indicates the boundary between
the original source fluid and the entrained fluid.

Although this laminar entrainment process does not result in intimate mixing of the plume and ambient fluids on a small scale, significant juxtaposition and translation of different parcels of fluid, due to shear within the conduit, does occur during this process.

Figure 3b shows the evolution with time of a layer of 75 km thickness (heavy horizontal line) which is located at the base of the plume. The fluid at the plume axis rises much faster than fluid at the periphery, and so this layer is deformed due to the differential velocities along different streamlines. In addition, as noted above, the fluid at the edge of the plume near its base moves slowly toward the plume axis. The directions of motion indicated by the streamlines show that the original plume source material is effectively compressed toward the plume center with increasing height. The streamline indicated by the black dots (Fig. 3b) delineates the boundary between the original source fluid (inside) and the entrained fluid (outside).

The streamlines in Fig. 3 demonstrate that the fluid which is ultimately entrained into the conduit originates at the lowest levels of the system. Because the conduit radius increases as z^{-s}, and the velocity goes as z^{2s+1}, the plume mass flux (UR^2) increases linearly with height (z). However, due to the shape of the streamlines, this increase in mass flux does not representatively sample the full depth of the fluid, but instead pulls fluid up from the base of the system. In the present example, even the fluid which is finally entrained at a height of 2700 km, at the very top of the fluid layer, originated from a depth of greater than 1500 km. This the why the radius of the plume increases as $z^{-1/2}$ (n=1) and $z^{-2/3}$ (n=3); this curvature reflects the increase in the mass flux due to entrainment at the lowest levels.

3.3 Parameterization of the Laminar Entrainment Process

The plume Rayleigh number defined in equation (21) is a measure of the strength of the plume, which increases with increasing DT and increasing h. Another measure of the plume strength is the buoyancy flux (Sleep, 1990), which is defined as:

$$B = 2\pi\rho\alpha \int_0^R U \, \Delta T \, R \, dR \tag{36}$$

Figure 4a is a plot of the plume strengths, calculated in terms of Ra and B from the numerical results for the non-Newtonian case (n=3). Lines connect the results obtained using the same value for h (1000-5000 km), and at four different values of ΔT_{BL} (250°C, 500°C, 750 °C, 1000°C). For a given value of h, buoyancy flux is positively correlated

with ΔT_{BL}. This figure shows that Ra and B are well correlated, and that the variation of B with h for a constant ΔT_{BL} essentially mirrors the effect of increasing ΔT_{BL}.

The mechanism of thermal laminar entrainment is essentially determined by the balance between the outward conduction of heat and the horizontal convergence of fluid toward the conduit. This balance can be conveniently expressed through the Nusselt number, which describes the relative magnitudes of heat transport by advection and conduction (Turcotte and Schubert, 1982). For the case of the plume conduit, this parameter is defined as:

$$Nu = VR/\kappa \qquad (37)$$

where R is the radius of the plume boundary (as defined above), V is the horizontal velocity at the plume boundary, and κ is the thermal diffusivity. A smaller relative value for Nu indicates that diffusion of heat is strong compared with the advective flux of heat. Since it is the lateral diffusion of heat which drives the entrainment of ambient fluid into the plume, a lower value of Nu should imply more entrainment. A larger value of Nu indicates that the horizontal convergence of fluid toward the conduit limits the outward diffusive flux of heat, reducing the entrainment of ambient fluid. Nusselt numbers were calculated for the non-Newtonian results; however, the Newtonian integrations were of insufficient accuracy to calculate a precise value for Nu (due to the inaccuracy of the horizontal velocity), and these results are not shown.

The plume Nusselt numbers are plotted against Ra in Fig. 4b. For the non-Newtonian rheology, the variation of Nu with h again essentially mirrors the effect of temperature; in fact, a single curve could be fit to these data. A similar result is indicated by Fig. 4c, where Nu is plotted against buoyancy flux. The numerical results indicate that the effect of increasing Ra is to decrease the plume radius by increasing the horizontal velocity of fluid which is converging toward the conduit. Balanced against this increased convergence of fluid is the higher vertical velocity of the fluid, which effectively decreases the amount of time for heat to conduct away from a given volume of fluid. The net result of these competing effects is that entrainment decreases with increasing Nu, as shown in Fig. 4d. This is the expected result; at higher Nu, the greater horizontal advection of fluid toward the conduit decreases the lateral extent to which heat can diffuse, and so entrainment is less. Qualitatively, these results demonstrate that stronger, more intense plumes will suffer less fractional entrainment than smaller, weaker plumes.
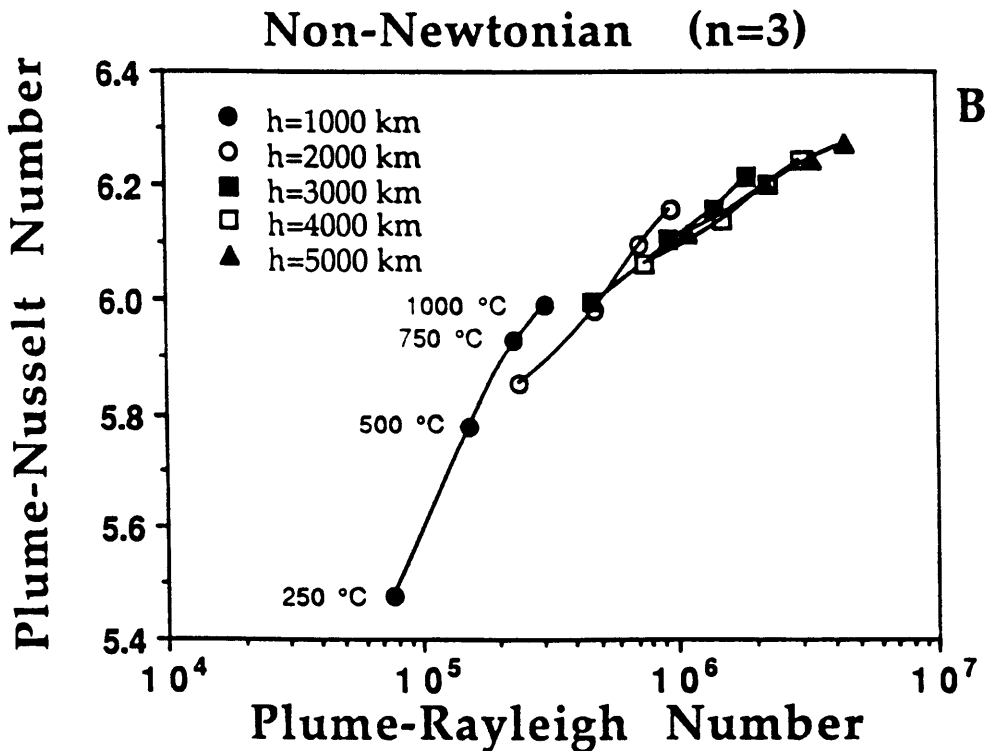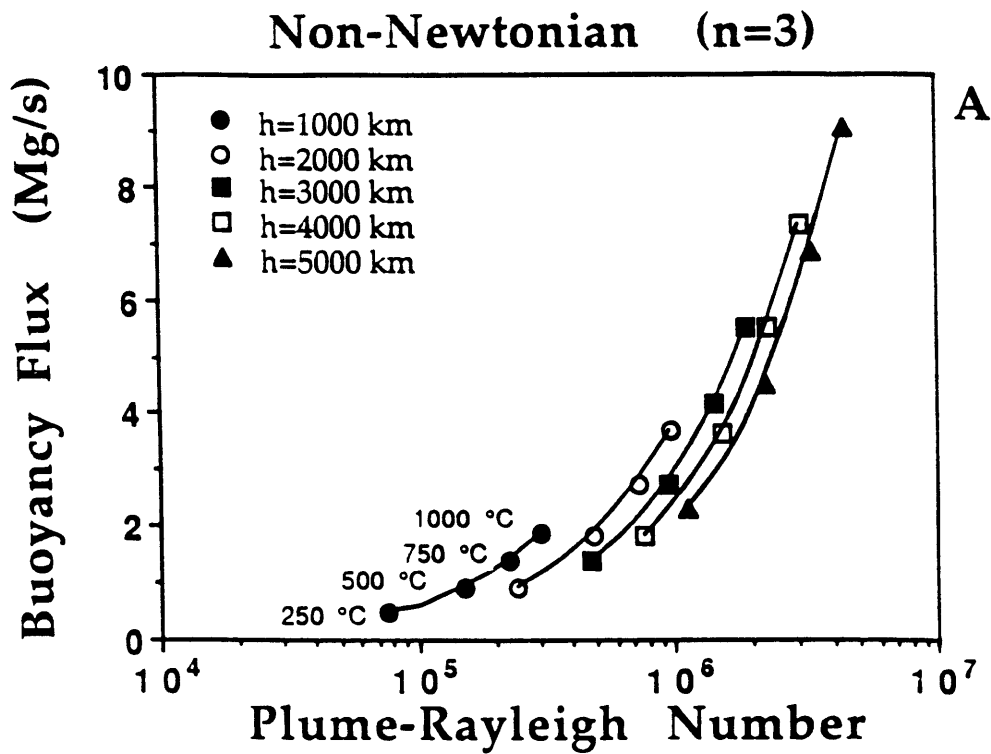
199

Figure 4. Plot of bouyancy flux versus plume Rayleigh number for non-Newtonian plumes. The positive vorreltaion show the consistency of thest two measures of plume strength. B) Plot of plume Nusselt number versus plume Rayleigh number shows that advective heat transport is increasingly large compared with diffusive heat transport with increasing Rayleigh number. Results were calculated with vaues of ΔT_{BL} of 250°C, 500°C, 750°C, and 1000 °C, and values of h of 1000-5000 km.

200

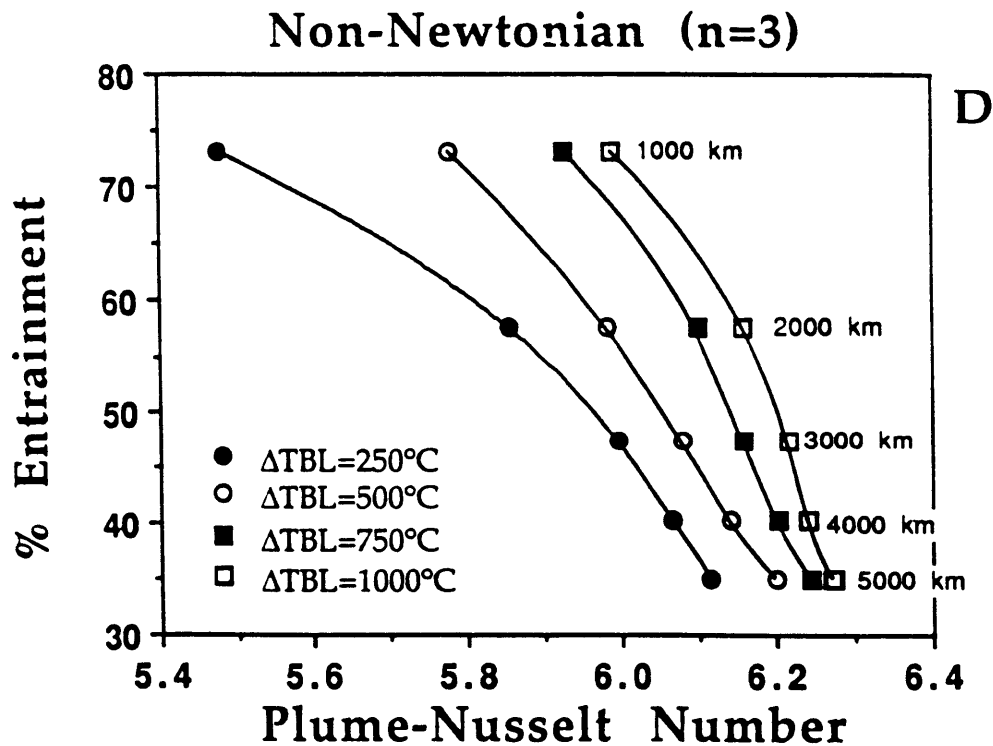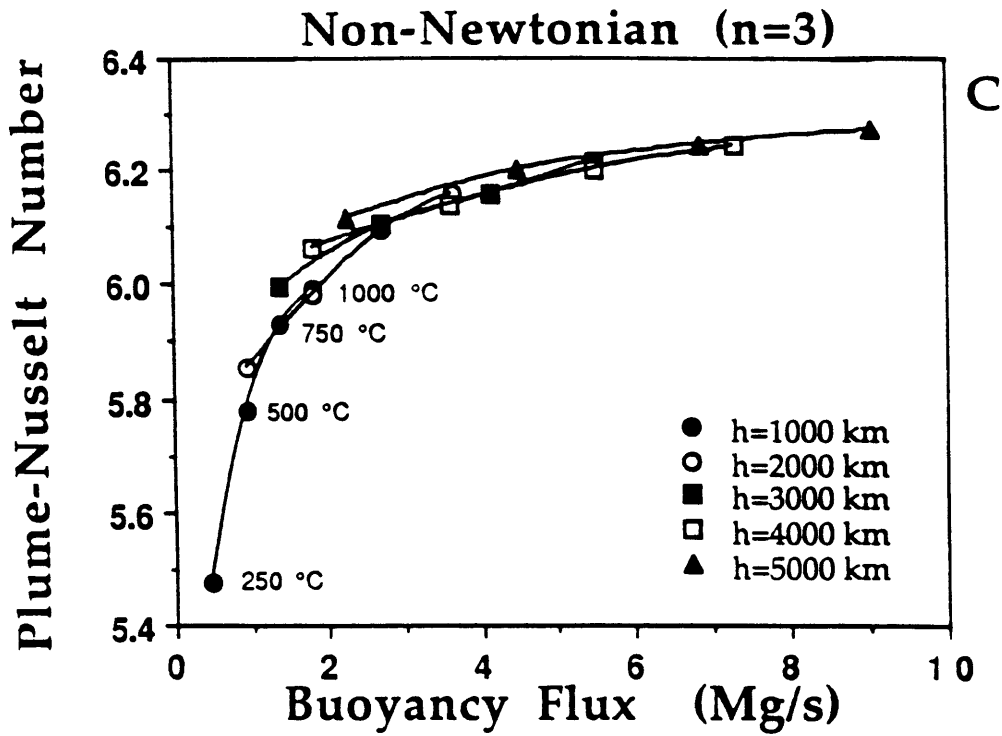## Non-Newtonian (n=3)

C

Non-Newtonian (n=3)

D

Figure 4. C) Plot of plume Nusselt number versus buoyancy flux for the non-Newtonian plumes. D) %Entrainment versus plume Nusselt number shows that, with a decreasing contribution from diffusie heat transport, entrainment is less. Entrainment is defined as the fraction of excess mass flux at the top of the plume conduit relative to the mass flux at the base.

201

3.4 Variable α, μ_o, and κ

Recent studies of the seismic equation of state (Anderson, 1987) and laboratory experiments on mantle compositions (Chopelas and Boehler, 1989) have demonstrated that the physical properties μ_o, α, and κ vary significantly with density, and thus with depth in the earth. Chopelas and Boehler (1989) discovered experimentally that the coefficient of thermal expansion of olivine decreases with increasing density according to:

$$\alpha = \alpha_0 \left(\frac{\rho}{\rho_o}\right)^{-6}$$

(38)

where α_0 and ρ_0 are the values for the uppermost mantle. This results in a decrease of the coefficient of thermal expansion by a factor of about 20 down to the base of the mantle. In addition, based on the theoretical dynamics of crystal lattice structure with increasing pressure, Anderson (1987) has proposed that thermal conductivity decreases with density according to:

$$k = k_0 \left(\frac{\rho}{\rho_o}\right)^{-3}$$

(39a)

Alternatively, Osako and Ito (1991) have measured the thermal conductivity of $MgSiO_3$ perovskite at high pressures, and propose that thermal conductivity *increases* with depth by at least a factor of four through the depth of the mantle, which can be expressed as:

$$k = k_0 \left(\frac{\rho}{\rho_o}\right)^{3}$$

(39b)

Laboratory studies of the rheology of olivine have also shown that the viscosity of the mantle should increase with depth (Stocker and Ashby, 1973). In the present model, the fluid is incompressible, and so fluid density does not vary with depth. However, we can qualitatively study the effect of these density-variable parameters by making them functions of depth (z). For a value of h=4030 km, the dimensionless height z across the full depth of the mantle varies by the same amount as the normalized density ρ_o/ρ, such that:

$$\left(\frac{\rho}{\rho_o}\right)^{-1} = (0.6\, z)^{1}$$

(40)

202

For different values of h, the exponent on the quantity (0.6 z) can be changed to match the density increase through the depth of the mantle. Since thermal diffusivity has been assumed to be constant in eq. (10), its depth dependence cannot be modelled here. However, esing eq. (40) as a proxy for density allows thermal expansion and viscosity to be expressed as functions of depth:

$$\alpha = \alpha_{ref} \, z^a \tag{41}$$

$$\mu_o = \mu_{ref} \, z^b \tag{42}$$

where the exponents a and b describe the dependence of the coefficient of thermal expansion and viscosity with depth relative to reference values specified at the top of the system. By substituting (41-42) into equation (21), the Rayleigh number becomes:

$$Ra = \frac{n\rho g \alpha_{ref} \Delta T_{BL} h^{\frac{n+2}{n}}}{\left[\mu_{ref} K\right]^{\frac{1}{n}}} \; z^{\frac{an-b}{n}} \tag{43}$$

Because thermal expansion and viscosity are not functions of R, we can carry this term through the derivation in Section 2. Equation (16) now becomes:

$$\left[r^4 z^{-2}\right]\left[r^{-3} z\right]^{\frac{n-1}{n}} z^{\frac{an-b}{n}} \tag{44}$$

To obtain a solution, the similarity exponent (eq. 17) becomes:

$$s = \frac{(a-1)n-b-1}{n+3} \tag{45}$$

This different expression for the similarity exponent (s) has a profound effect on the nature of the plume flow and the shape of the plume conduit as a function of height, and thus for the nature of entrainment. The effects of these depth dependent properties will be illustrated for the Newtonian case; the effects would be similar for the nonlinear rheology. Substituting eq. (45) into the equations (31), (32), (34), (21), and (37), we see that:

$$U \propto z^{\frac{2(a+b)-3}{4}}$$ (46)

$$V \propto z^{\frac{a-b-2}{4}}$$ (47)

$$R \propto z^{-\frac{a-b-2}{4}}$$ (48)

$$Ra \propto z^{a-b}$$ (49)

Thus the fluid velocities and the shape of the plume boundary will be quite different from the constant property case, depending on the values of a and b. In addition, Ra will be a function of z (relative to Ra_{ref}), and so the plume strength will vary with height. The effects of depth dependent α and μ_0 will be discussed separately for a Newtonian rheology. The effects of the depth-dependent variables would be similar in the non-Newtonian case.

3.4.1 Variable thermal expansion

The effect of increasing thermal expansion with height should be to increase the buoyancy, at constant temperature, of a given parcel of fluid, resulting in an increase in the vertical velocity with height. Figure 5 shows that this is indeed the effect. At higher values of a, the plume boundary is seen to make a transition from growth with height to a radius which decreases with height. Figure 5 shows that the vertical velocity increases with height due to the increasing buoyancy, and that Ra also increases with height. The narrowing of the plume boundary with height indicates that entrainment is minimal in the upper levels of the fluid layer, and that most of the fluid is entrained from the base of the system.

3.4.2 Depth-dependent viscosity

Figure 6 shows the effect of a viscosity increase with depth (decrease with height, Eq. 43) on the shape of the plume boundary. In these diagrams, the exponents -6, -10, -14, and -22 result in an increase in viscosity with depth by factors of 21, 165, 1276, and 9846 respectively across the depth of the fluid layer (2700 km). The effect of increasing viscosity with depth is to change the flow such that the plume radius decreases with height. From Figure 6, the effect of decreasing viscosity with height (increasing viscosity with depth) is to cause the vertical velocity to increase with height in the plume. This is the expected result; since viscosity provides the resistance to the buoyancy force, the vertical
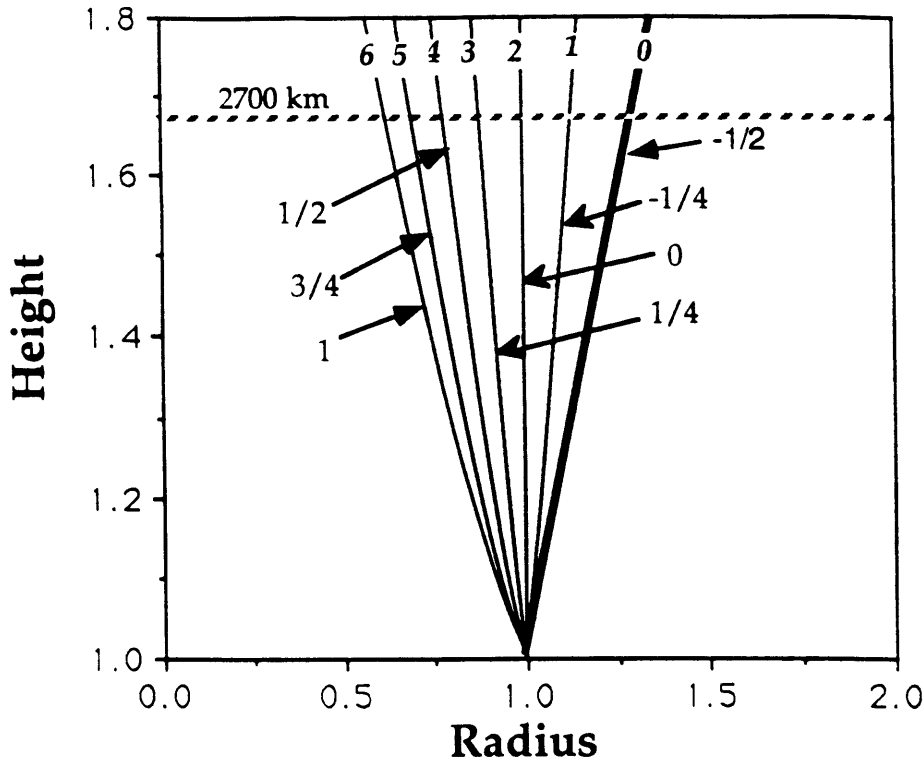
	a=1	a=2	a=3	a=4	a=5	a=6
s	-1/4	0	1/4	1/2	3/4	1
U	1/2	1	3/2	2	5/2	3
V	-1/4	0	1/4	1/2	3/4	1
R	1/4	0	-1/4	-1/2	-3/4	-1
Ra	1	2	3	4	5	6

Figure 5. Curves describing the shape of the plume boundary, in non-dimensional coordinates, for different values of a, the power of the depth dependence of thermal expansion (eq. 41). The dark curve shows the shape of the plume boundary for constant thermal expansion and ambient viscosity. Numbers by arrows indicate the value of s, the similarity exponent; numbers in italics indicate the value of a. The table shows the values of the similarity exponent (s), and the power of the depth dependences of vertical velocity (U), horizontal velocity (V), radius (R), and plume Rayleigh number (Ra) from eqs. (46-49), for different values of a. The decrease of the radius with height is due to the increase in buoyancy with height, resulting in higher vertical velocities in the conduit with height. Results are for a Newtonian rheology.

Height

Radius

2700 km
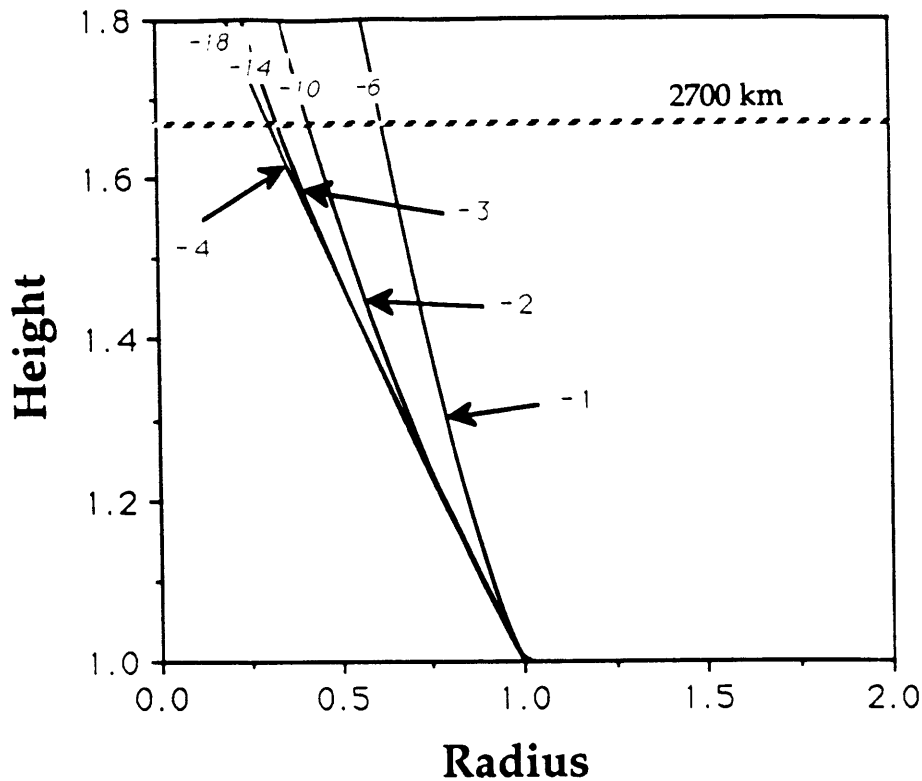
	$c=-6$	$c=-10$	$c=-14$	$c=-18$
s	1	2	3	4
U	9/4	17/4	25/4	33/4
V	1	2	3	4
R	-1	-2	-3	-4
Ra	6	10	14	18

Figure 6. Curves describing the shape of the plume boundary, in non-dimensional coordinates, for different values of b, the power of the depth dependence of viscosity (eq. 41). Numbers by arrows indicate the value of s, the similarity exponent; numbers in italics indicate the value of b. The table shows the values of the similarity exponent (s), and the power of the depth dependences of vertical velocity (U), horizontal velocity (V), radius (R), and plume Rayleigh number (Ra) from eqs. (46-49), for different values of b. The decrease of the radius with height is due to the decrease in ambient viscosity with height, resulting in higher vertical velocities in the conduit with height. Results are for a Newtonian rheology.

velocity increases as the viscous resistance decreases with height. From Figure 6, Ra is shown to increase with height, reflecting the increasing strength of the plume in the upper levels of the fluid layer. The largest changes in radius still occur at the base of the fluid layer, indicating that this is the location of most of the entrainment. Since the vertical velocity is slowest at the base of the plume, lateral diffusion of heat is also greatest there, again resulting in entrainment of fluid near the base of the plume.

3.4.3 Variable thermal diffusivity

Although a depth-dependent thermal diffusivity cannot be quantitatively modelled here, we can qualitatively estimate its effect on plume flow and entrainment. Since the lateral conduction of heat is the main driving force for entrainment, the effect of thermal diffusivity which decreases with depth (increases with height above the base of the mantle) should be to promote more entrainment in the upper levels of the system. This suggests that thermal diffusivity which increases with height (analogous to the suggestion of Anderson, 1987; Eq. 39a) causes the plume boundary to expand outward in the upper part of the fluid. However, a thermal diffusivity which decreases with height (analogous to the measurements of Osako and Ito, 1991; Eq. 39b), has the effect of enhancing the entrainment of lower mantle material relative to upper mantle material, since that is the regios where thermal conductivity would be highest

4. Implications for Entrainment in Mantle Plumes

4.1 Constraints from Boundary Layer Theory

In attempting to extrapolate the results of experiment or theory to the earth's mantle, one must always be aware of the various assumptions upon which the models rest. While recent experimental studies have presented a qualitative picture of mantle plumes, an increased understanding of the nature of fluid flow in these features requires better knowledge of the physical properties of the earth at depth, and more detailed modelling of the various features associated with mantle plumes which may be unique to the earth. The assumption of incompressibility in the present model requires that the effects of adiabatic cooling be ignored. In addition, viscous heating has been neglected, an effect which would produce heat in the regions of highest shear. However, the effects of adiabatic cooling and viscous heating tend to counteract each other (Zhao and Yuen, 1987), and so these approximations are not likely to significantly change the results presented here. In addition, though this model has incorporated experimentally constrained physical properties of olivine, extrapolation of these quantities to higher pressure phases may not be warranted. However, the physical phenomena which have been shown to drive entrainment in this study will probably also be the same processes which govern

entrainment in mantle plumes, irrespective of the precise deformation processes operative in higher pressure phases.

The most important question to be addressed is whether entrainment actually occurs in mantle plumes. As previously stated, the accuracy of the dimensional results of this model are only as good as the accuracy of the assumptions and physical parameters. However, we may make some broad inferences from Fig. 2. Both of the plumes depicted in Figure 2 are characterized by high vertical velocities, compared with plate velocities and velocities calculated for plumes in a constant-viscosity mantle (Parmentier et al., 1975). For the non-Newtonian axial velocity of 7 meters/year, this indicates that plume material from the base of the mantle would reach the surface in roughly 400,000 years. While this modelled velocity may seem excessive, it should be noted that, even with this high velocity, the plume radius has increased by 40% through the full depth of the mantle, and the calculated entrainment is 47%. If actual mantle plume velocities are lower, then this implies a lower Rayleigh number for the plume, and consequently more entrainment. This indicates that entrainment should be a process of some significance in mantle plumes.

The primary constraint derived from the present analysis is the location of origin of the fluid which is entrained. For physical properties which are constant with depth, and a viscosity which depends on temperature and shear stress, the fluid which is entrained into a thermally buoyant plume originates from near the base of the plume, and entrainment of fluid from the upper levels of the system is minor. The effect of increasing viscosity with depth results in less entrainment of fluid in the upper levels, due to the increase of the vertical velocity of the plume. This effect is also enhanced by a coefficient of thermal expansion which increases with plume height. The direction of the depth dependence of these two parameters (*decreasing* thermal expansion, *increasing* viscosity) are rather firmly established. Whether thermal conductivity increases or decreases with depth in the earth is more controversial (Anderson, 1987; Osako and Ito, 1991). However, from Figs. 5 and 6, it is clear that the two strongest effects are increasing viscosity and decreasing thermal expansion with depth. Together, these effects indicate that the ambient mantle which is entrained into mantle plumes should originate dominantly from the lower mantle, and that entrainment of upper mantle material into thermal plumes should be minimal.

An interesting characteristic of the non-Newtonian rheology is the existence of "plug flow" in the thermal plume conduit (Fig. 2), due to the high viscosity of the fluid at the plume axis. If such a rheology is applicable to the whole of the mantle, then this rheology provides a mechanism for transporting fluid through the full depth of the fluid layer without significant shear mixing and dilution, as suggested by Fig. 3b and the results of Yuen and Hansen, (1991). The high-viscosity fluid at the plume axis will be resistant to

208

deformation, and its path through the mantle will be "lubricated", in a sense, by the low viscosity minimum in the fluid surrounding the plume. This mechanism could be important in transporting mantle, in a pure, unmixed state, from the source region of the plume to the upper levels of the earth.

4.2 Constraints from Isotope Geochemistry

Isotopic data from oceanic island basalts (OIB) and mid-ocean ridge basalts (MORB) have provided most of the evidence for a chemically heterogeneous mantle. The isotopic signatures of hotspot volcanics should thus be able to provide some evidence for entrainment in the mantle plume sources of these island chains. Figure 7 shows a two-dimensional plot of the currently available data for $^{87}Sr/^{86}Sr$, $^{143}Nd/^{144}Nd$, and $^{206}Pb/^{204}Pb$ on basalt samples from oceanic islands worldwide (Hart et al., 1992, and references therein). In this diagram, fields enclose data from several islands or island chains which are characterized by linear arrays suggestive of two-component mixing. These arrays display a fan-shaped appearance, converging on a volume in Sr-Nd-Pb isotopic space which is different from the depleted MORB mantle endmember (Zindler and Hart, 1986), and distinct from the source of typical N-type MORB (defined as MORB with $^{87}Sr/^{86}Sr<.703$, Hart et al., 1992). This feature of the data strongly suggests the existence of a mantle component which is common to hotspots worldwide. This component is not very well defined, but its approximate range of isotopic composition is $^{87}Sr/^{86}Sr=.7025$-.7035, $^{143}Nd/^{144}Nd=.51310$-.51290, and $^{206}Pb/^{204}Pb=18.80$-19.50.

In addition to the region of convergence in the heavy isotope data, existing He isotope data for the island chains with elongate arrays show an increase in $^3He/^4He$ as the region of convergence is approached. For the Hawaiian array, $^3He/^4He$ ranges from 10-16 Ra (Ra=atmospheric $^3He/^4He$ ratio) for basalts from Koolau and Lanai (Faggart et al., 1990) near the EMI end of the array, and up to 32 Ra for tholeiites from Loihi (Kurz et al., 1983). In addition, $^3He/^4He$ increases from 3.5-8 Ra along the Azores array (Kurz et al., 1992), from 6.0-10.8 Ra from Mangaia to Rapa along the Macdonald hotspot track (Desonie et al, 1991), from 6.8-11.3 along the Society Islands array (Desonie et al., 1991; Staudacher and Allegre, 1989), and $^3He/^4He$ values from 12-25 Ra are observed for the Samoa array (Farley et al., 1992). Other islands with high $^3He/^4He$, which include Iceland, Galapagos, Reunion, Caroline Islands, Juan Fernandez, Bouvet, and Macdonald Seamount (Condomines et al., 1983; Kurz et al., 1985; Craig, 1990; Trull et al., 1990; Desonie et al., 1992; Kurz et al., 1992) all lie near the convergence region, suggesting that this component is also characterized by high $^3He/^4He$. High $^3He/^4He$ has previously been proposed to be associated with "primitive", or undifferentiated mantle (Poreda et al., 1986; Faggart et al., 1990). The Sr-Nd-Pb isotopic composition of this region, however, has
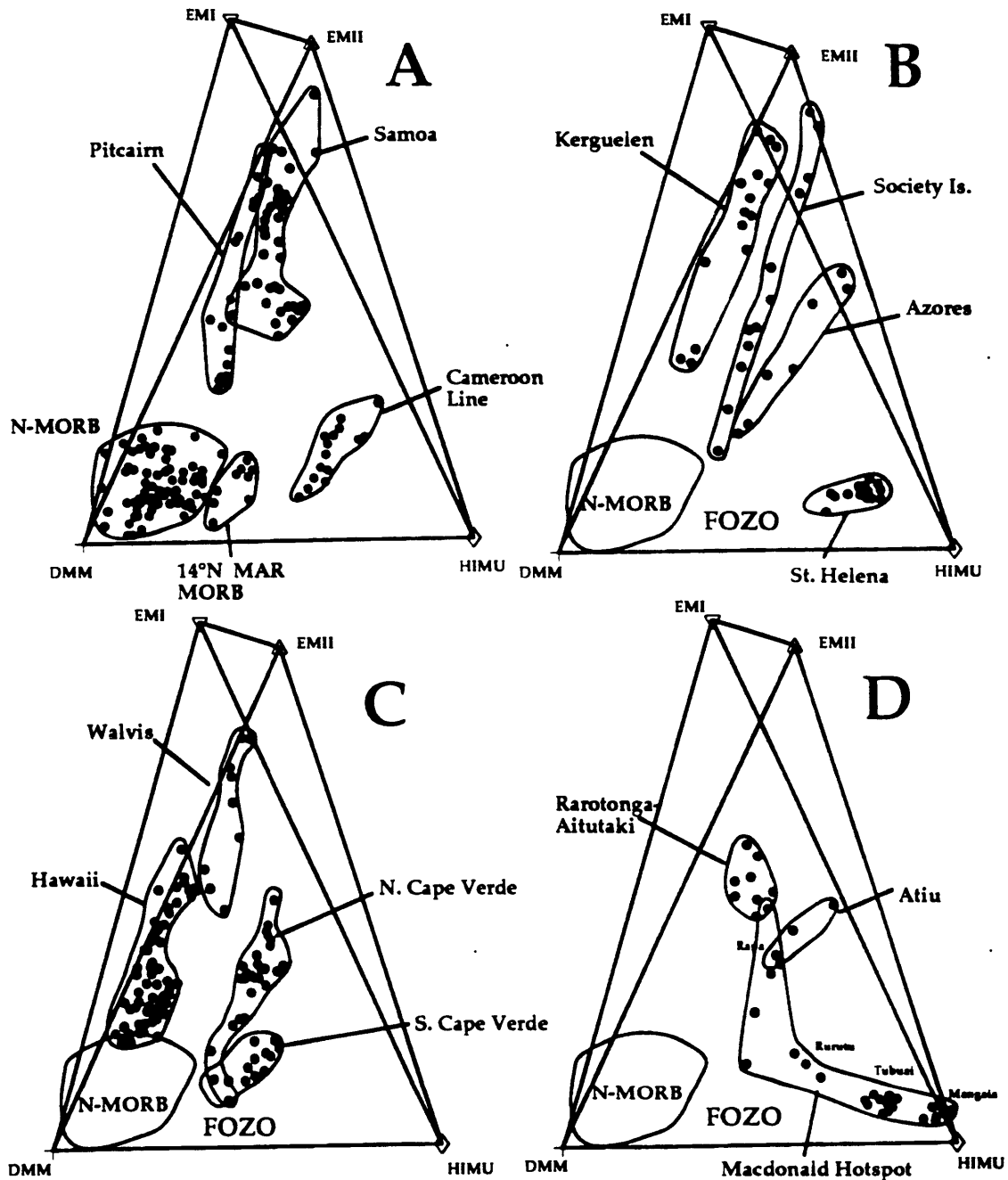
Figure 7. Two dimensional projections of the Sr-Nd-206Pb/204Pb isotope data for oceanic island basalts, from Hart et al. (1992). The data are fully enclosed by a tetrahedron, with the corners corresponding to the DMM-HIMU-EMI-EMII endmembers described by Zindler and Hart (1986). The arrangement of the data arrays shows a fan-shaped pattern converging toward the middle of the tetrahedron (FOZO), indicating a common component to hotspots from around the world which is distinct from N-type MORB. MORB data from 14°N on the mid-Atlantic ridge plot near FOZO (Dosso et al, 1990).

210

slightly depleted $^{87}Sr/^{86}Sr$ and $^{143}Nd/^{144}Nd$, and radiogenic $^{206}Pb/^{204}Pb$, all of which preclude it being primitive, undifferentiated mantle. This high $^{3}He/^{4}He$ component has previously not been recognized in the heavy isotope data, leading some to suggest that $^{3}He/^{4}He$ has been decoupled from the heavy isotope systems (Poreda et al., 1986; Zindler and Hart, 1986). However, stratigraphically controlled studies incorporating $^{3}He/^{4}He$ and heavy isotope systems systems (Kurz et al., 1987; Kurz and Kammer, 1991), as well as the evidence presented here, demonstrate consistent covariation between He isotopes and those of Sr, Nd, and Pb, and show that this component is a common to a number of hotspots from around the world. This high $^{3}He/^{4}He$ endmember has been termed FOZO by Hart et al. (1992).

Using this data to constrain entrainment processes in mantle plumes is a complex issue. This requires knowledge about the interaction of the plume flow with the moving lithosphere (Yuen and Fleitout, 1985), as well as detailed information on the pathways of magma segregation and mixing processes. However, one constraint that is immediately clear from Fig. 7 is that, with the exception of ridge centered hotspots, neither DMM nor typical N-MORB sources are components in any of the mixing arrays shown in Fig. 7; this point is emphasized by the increasing $^{3}He/^{4}He$ ratios of some of these arrays approaching FOZO. This lack of mixing with MORB mantle is consistent with the prediction from entrainment theory that entrainment of the uppermost mantle should be insignificant in mantle plumes. This absence of upper mantle entrainment would seem to be inconsistent with the model for entrainment in an inclined plume conduit (Richards and Griffiths, 1989; Griffiths and Campbell, 1991); the sharpness of the bend in the Hawaii-Emperor Seamount chain essentially requires that the inclination of the plume conduit take place in the uppermost mantle (Griffiths and Richards, 1989). However, with the possible exception of lithospheric components in some post-shield volcanics (Chen and Frey, 1985), no evidence for MORB source components exists in the isotope data for the Hawaiian Islands.

An exception to the absence of MORB source in the OIB ararys is that ridge-centered hotspots often show evidence of mixing with the uppermost mantle; Iceland and the Galapagos Islands are classic examples (Schilling, 1973; Hart et al., 1973; Sun et al., 1975; Zindler et al., 1979; White et al., 1992). It is likely that these plumes have incorporated ambient MORB mantle due to the superposition of the sub-ridge mantle flow on the upwelling plume flow. In addition to these islands, the MORB data of Dosso et al. (1990) from 14°N on the Mid-Atlantic Ridge have exceptionally high $^{206}Pb/^{204}Pb$, but have $^{87}Sr/^{86}Sr<.7030$. This region of the MAR also exhibits other geochemical anomalies such as LREE enrichment (Dosso et al., 1990), but it is not anomalously shallow, and no obvious expression of a hotspot exists. Whether this and other mid-ocean ridge anomalies

represent nascent plumes, or an expression of a heterogeneous MORB source, is a classic problem (e.g. see Allegre et al., 1984). However, the general absence of typical N-MORB mantle as a component in these arrays remains valid.

In the context of the present results, if FOZO does in fact have high $^3He/^4He$, then it may be suggested that an origin for plumes from a thermal boundary layer at 670 km depth can be discounted. If such plumes existed, they would be expected to entrain upper mantle, and so show some mixing toward MORB, which is clearly not observed in Fig. 7 (with the exception of ridge-centered hotspots). If FOZO is associated with a boundary layer at 670 km (instead of core-mantle boundary), then plumes with FOZO as a component should still show mixing toward MORB, since it is the downward motion of the upper mantle which would replenish material in a 670 km thermal boundary layer. Even if the boundary layer were made up entirely of subducted oceanic crust, such sinking cold plumes should still entrain upper mantle material due to the lateral conduction of "coldness", in much the same manner as hot plumes entrain ambient mantle. In addition, experimental studies of layered convection (Richter and McKenzie, 1981; Olson, 1984) have shown significant disruption of a density-stratified boundary due to viscous coupling between the layers. Thus the location of FOZO in the mantle above 670 km is deemed unlikely due to the absence of a high $^3He/^4He$ signature in N-type MORB. Since it is unlikely that an origin for mantle plumes in a 670 km boundary layer can be reconciled with the presence of a high $^3He/^4He$ FOZO, this provides support for convection across the 670 km discontinuity, and probably throughout the entire mantle.

The arrays shown in Fig. 7 essentially connect the isotopic composition of FOZO with variable isotopic compositions characterized by more enriched signatures in $^{87}Sr/^{86}Sr$, $^{143}Nd/^{144}Nd$, and $^{206}Pb/^{204}Pb$. In addition, the enriched mantle compositions are often not pure EMI (Walvis, Pitcairn), EMII (Societies, Samoa), or HIMU (Macdonald), but often seem to be compositions along the binary joins of the EMI-EMII-HIMU triangle (Kerguelen EMI-EMII; Azores EMII-HIMU; Cameroon Line EMI-HIMU). As noted by Hart et al. (1986), this may be evidence for mixing events which have taken place previous to the mixing toward FOZO. Alternatively, the most isotopically enriched ends of these arrays may have developed through time in reservoirs with the specific Rb/Sr, Sm/Nd, and U/Pb ratios needed to generate these various isotopic signatures, instead of being specific mixtures of isotopically homogeneous endmembers. For example, the Azores may not be a mixture of EMII and HIMU, but instead might be a distict reservoir characterized by relatively high Rb/Sr, Sm/Nd, and U/Pb. This view is supported by the absence of linear arrays which trend parallel to the joins of the EMI-EMII-HIMU triangle (Fig. 7). In this scenario, it is still possible that intermediate enriched compositions are due to mixing

between components prior to long-term isolation and isotopic evolution, such as a high Rb/Sr component and a high U/Pb component (both with high Sm/Nd) for the Azores. Alternatively, since the parent-daughter characteristics of EMI, EMII, and HIMU are likely associated with specific processes which fractionate Rb/Sr, Sm/Nd, and U/Pb in the required directions, the enriched ends of the arrays in Fig. 7 which are intermediate between EMI-EMII-HIMU may result from the superposition to varying degrees of these processes. These issues remain unanswered, and the analysis presented here is consistent with all of these possibilities.

The binary nature of these arrays begs the question as to which components are present in the plume source, and which components are entrained. In this respect, $^3He/^4He$ is an excellent tracer. Due to the lack of high $^3He/^4He$ signatures in MORB, high $^3He/^4He$ indicates a source which is distinct from the uppermost mantle. Based on the evidence from entrainment theory, this would seem to implicate a lower mantle origin for the high $^3He/^4He$ component. However, the location of FOZO in the lower mantle does not provide an answer to whether FOZO is plume source, or entrained mantle. For example, plumes are often proposed to originate from a thermal boundary layer at the core-mantle boundary (Stacey and Loper, 1983). This requires that the thermal boundary layer be replenished to replace the mantle which was lost to mantle plumes. The core-mantle boundary layer (CMBL) is essentially replenished by the downward motion of the lowermost mantle toward the core. Thus, if FOZO is present in the lower mantle, then it must also be present in the CMBL.

Two endmember scenarios are possible which would be consistent with the isotope data and the results from entrainment theory:

1) *The enriched components (EMI, EMII, HIMU, and intermediate compositions) are located in the CMBL, and FOZO represents entrained lower mantle.*

Evidence for the presence of both FOZO and pure endmember components exists in the isotope data for Samoa (EMII), Pitcairn (EMI)(Woodhead and McCulloch, 1989), and the Macdonald hotspot chain (HIMU), indicating that all three enriched endmember components must be available for mixing with FOZO in the lower mantle. To make the CMBL and the lower mantle isotopically distinct would require some process which transports material in a relatively pure state through the mantle to the CMBL, whereupon it is incorporated into mantle plumes. The model presented here, and the numerical mantle convection modelling of (Malevsky et al., 1991) indicate that subduction in a fluid with a non-Newtonian rheology may be just such a mechanism. The behavior of plumes with both positive and negative buoyancy is similar to the flow depicted in Fig. 2a, though with

213

an inverted temperature profile. In a fluid with a stress dependent rheology, subducted slabs could sink through the mantle with minimal, though possibly still significant, mixing with ambient mantle; because the pressure at the head of the descending plume induces shear in the fluid ahead of it, this allows the slab to sink through the mantle surrounded by a sheath of low viscosity mantle. The identification of the HIMU signature at Tubuai and Mangaia with recycled oceanic crust (described in Chapter 4), coupled with evidence for a high $^3He/^4He$ signature at Macdonald seamount, provides support for this scenario.

2) FOZO represents the source mantle for plumes in the CMBL, and enriched components are entrained from the lower mantle.

This would suggest that recycled crustal materials may not be able to sink all the way to the CMBL. If the lower mantle rheology were Newtonian, and exhibited a significant increase in viscosity with depth, this would provide increasing resistance to subduction with depth. Instead, the recycled crust may not sink through the mantle fast enough to accumulate in large amounts at the CMB, and would instead be swept up in the background convective flow within most of the mantle, to be available for entrainment into mantle plumes.

The entrainment theory presented above indicates that the strongest plumes will be least entrained (Fig. 4), and thus the strongest plumes would contain the lowest fraction of entrained (EMI-EMII-HIMU) components. Basalts from Koolau (Roden et al., 1984) have enriched isotopic compositions which approach the EMI endmember, which contradicts the prediction that Hawaii should be the least entrained plume. However, the expression of plume isotopic signatures in erupted lavas is critically dependent on the melting and melt segregation process, and so this is not a fatal blow to this scenario.

Evidence in favor of this model comes from the high $^3He/^4He$ values measured at Hawaii and Iceland, two plumes with high buoyancy fluxes (Sleep, 1990). The $^3He/^4He$ measurements on basalts from Loihi and the neovolcanic zones of Iceland (Kurz et al., 1983; Kurz et al., 1985) are the highest values yet reported for oceanic islands, and provide support for the idea that the strongest (i.e. least diluted) plume signature should be observed at the strongest plumes. In addition, the streamlines in Fig. 3 indicate that the entrained mantle should occupy a region at the periphery of the plume. The well documented geochemical gradients along the Reykjanes Ridge leading up to Iceland (Hart et al., 1973; Schilling, 1973; Sun et al., 1975; Zindler et al., 1979; Poreda et al., 1986) demonstrate mixing between the Iceland plume and upper mantle MORB source. The region of highest melt production, highest $^3He/^4He$ values, and location of the maxima of the Icelandic thermal anomaly indicate that the Iceland plume is centered beneath the island
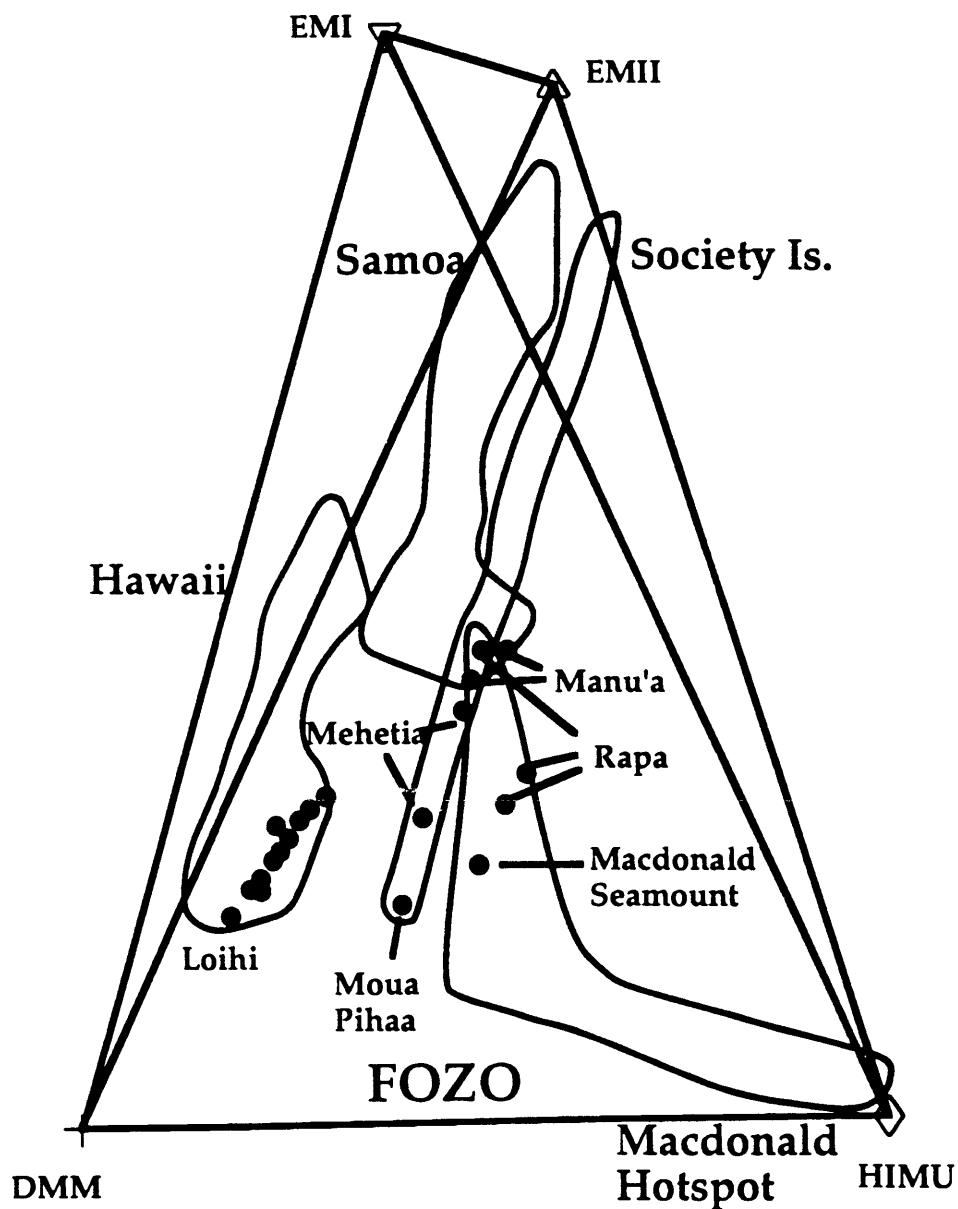
214

Figure 8. Two-dimensional projection of Sr-Nd-206Pb/204Pb
isotope data for OIB, as in Fig. 8. Diagram show the fields for
several island chains in the Pacific Ocean. Data for the youngest
volcanoes in each chain lie toward the middle of the tetrahedron
in the region of convergence. Of these islands, Loihi (20-33 Ra),
Mehetia (11.8 Ra), Rapa (11 Ra), and Macdonald Seamount (9 Ra)
have documented high 3He/4He ratios. He data from Kurz et al.
(1983), Staudacher and Allegre (1989), and Desonie et al. (1991).

215

proper (Sleep, 1990). The location of the Reykjanes Ridge at the edge of the Iceland swell provides support for the location of entrained (MORB source) material at the periphery of the plume. The scale of the "anomalous" geochemical signature along the Reykjanes Ridge (>400 km) indicates that this feature is not simply a result of melt generation/segregation processes acting on a smaller feature.

In addition to the evidence described above, the presence of a strong FOZO signature in some island chains (all from the Pacific) seems to be connected with the most recent shield building volcanism within the chain. Loihi Seamount (Hawaii), Macdonald Seamount (Macdonald), Manu'a Islands (Samoa), and Mehetia Seamount (Society) all lie at the FOZO end of the data arrays (Fig. 8). Most of these young volcanos (Loihi, Mehetia, Macdonald) are characterized by $^3He/^4He > 9$ Ra (Staudacher and Allergre, 1989; Desonie et al., 1991). In addition, the highest $^3He/^4He$ data from Iceland comes from the southeastern neovolcanic zone, which became active only 1.5 Ma ago (Kurz et al., 1985) and is the youngest of the three rift zones on Iceland. If the mantle at the plume axis is at the highest temperature, and is rising at the highest velocity, then melt production will be greatest at the axis of the plume, and these melts may be the dominant melt products at nascent volcanic features. This idea may be supported by the $^3He/^4He$ data from Loihi, in which the highest $^3He/^4He$ ratios come from tholeiitic basalts (26-35 Ra), and a basanite records the lowest Loihi value (20 Ra) (Kurz et al., 1983). At Samoa, however, Farley et al. (1992) have measured $^3He/^4He$ values of 8-25 Ra within a single exposure of shield flows from the island of Tutuila, which indicates the complexity of this problem.

In actuality, the two scenarios presented above, both of which place FOZO and the enriched components in the lower mantle, are not mutually exclusive. It is likely that the truth lies somewhere in between. For example, the isotopic composition of the basalts along the Macdonald hotspot chain change abruptly from endmember HIMU compositions (Mangaia, Rurutu, Tubuai, 20-6 Ma) to compositions near the center of the tetrahedron (Rapa, Macdonald Seamount, 6 Ma-present) (Fig. 7). The ages of volcanics from the islands of Tubuai and Rapa overlap between 6-7 Ma, indicating that these two islands, in the same island chain, were simultaneously erupting basalts with very different isotopic compositions. This seems to require an abrupt change in the isotopic composition of the mantle being supplied by the plume.

In reality, it is likely that the mantle in the boundary layer source of most mantle plumes is probably already heterogeneous, and whether a plume carries endmember components or FOZO mantle may instead depend on the local concentrations of these materials in the lower mantle. The necessity of maintaining isotopically distinct upper and lower mantles does not require layered convection, but may the the result of different time

scales of mixing for the upper and lower mantles. In this case, it is possible that this difference in isotopic composition may be the time integrated signature of a lower mantle with a distinct major element composition. Mineral/melt partitioning data for the various parent/daughter systems in ultra-high pressure phases would be enormously important for testing this issue.

5. Conclusions

The nature of viscous fluid flow in mantle plumes is modelled as an axisymmetric thermal boundary layer originating from a point source of heat. The model incorporates experimentally constrained rheological and physical properties for upper mantle compositions. Newtonian plumes are characterized by a broad velocity profile. Non-Newtonian plumes have much narrower radii, and exhibit "plug flow" at the axis of the conduit in which a rheologically rigid core of fluid rises through a sheath of low viscosity fluid. The model indicates that significant amounts of ambient fluid are entrained in the plume flow due to the horizontal diffusion of heat. This heat increases the buoyancy and lowers the viscosity of fluid at the plume boundary, incorporating this fluid in the conduit flow. Streamlines calculated from the model indicate that extensive deformation of the fluid in the conduit takes place, and that the original source material is focussed toward the center of the conduit by the convergence of entrained ambient fluid. The modelled flow regime indicates significant shearing and juxtaposition of source and ambient fluids.

The results of numerical experiments demonstrate that the entrained fluid originates from the lowest levels of the system. The incorporation of a viscosity which increases with depth results in an increasing vertical velocity with height in the plume, resulting in little entrainment in the upper fluid levels. Incorporation of a coefficient of thermal expansion which decreases with depth results in increasing buoyancy, and thus vertical velocity, with height in the plume. The increasing strength of the plume with height indicates minimal entrainment of fluid from the upper levels of the system, and demonstrates that the entrained fluid must originate from near the base of the plume.

Quantitative results from the model suggest that the entrainment of ambient mantle into mantle plumes should be an important process. The combined Sr-Nd-Pb isotope data show a convergence of linear arrays for individual islands and island chains upon an isotopic composition of $^{87}Sr/^{86}Sr$=.7025-.7035, $^{143}Nd/^{144}Nd$=.51310-.51290, and $^{206}Pb/^{204}Pb$=18.80-19.50. This focus zone (FOZO) may also be characterized by high $^{3}He/^{4}He$, indicating an origin for this component in the lower mantle. The isotopic data alone place few strong constraints on the isotopic composition of plume source versus entrained compositions; however, the results from entrainment theory require that

217

isotopically enriched compositions, as well as FOZO, must at some point reside in the lower mantle. This does not require a layered mantle per se, but may suggest that the residence time of mantle below 670 km may be longer than that of the upper mantle source of MORB.

References

Allegre, C. J. (1982) Chemical Geodynamics. Tectonophysics, **81**, 109-132.

Allegre, C. J., O. .Brévart, B. Dupré and J. F. Minster (1980) Isotopic and chemical effects produced in a continuously differentiating convecting earth mantle. Phil. Trans. R. Soc. London, **A297**, 447-477.

Anderson, D. L. (1967) Phase changes in the upper mantle. Geophys. J. R. Astron. Soc., **14**, 135-164.

Anderson, D. L. (1982) Isotopic evolution of the mantle: a model. Earth Planet. Sci. Lett., **57**, 13-24.

Anderson, D. L. (1987) A seismic equation of state II. Shear properties and thermodynamics of the lower mantle. Phys. Earth Planet. Int., **45**, 307-323.

Armstrong, R. L. (1968) A model for the evolution of strontium and lead isotopes in a dynamic. Earth Rev. Geophys., **6**, 175-199.

Brand, R. S. and F. J. Lahey (1967) The heated laminar vertical jet. J. Fluid Mech., **29**, 305-315.

Chen, C. Y. and F. A. Frey (1985) Trace element and isotopic geochemistry of lavas from Haleakala Volcano, east Maui, Hawaii: implications for the origin of Hawaiian basalts. J. Geophys. Res., **90**, 8743-8768.

Chopelas, A. and R. Boehler (1989) Thermal expansion measurements at very high pressure, systematics, and a case for a chemically homogeneous mantle. Geophys. Res. Lett., **16**, 1347-1350.

Condomines, M., K. Gronvold, P. J. Hooker, K. Muehlenbachs, R. K. O'Nions, et al. (1983) Helium, oxygen, strontium and neodymium isotopic relationships in Icelandic volcanics. Earth Planet. Sci. Lett., **66**, 125-136.

Craig, H. (1990) Helium isotope distribution in mantle hotspots. EOS, **71**, 1669.

Davies, G. F. (1984) Geophysical and isotopic constraints on mantle convection: an interim hypothesis. J. Geophys. Res., **89**, 6017-6040.

Desonie, D. L., R. A. Duncan and M. D. Kurz (1992) Helium isotopic composition of isotopically diverse basalts from hotspot volcanic lineaments in French Polynesia (abst). EOS, **72**, 536.

Dziewonski, A. and D. L. Anderson (1981) Preliminary reference earth models. Phys. Earth Planet. Inter., **25**, 297-356.

Faggart, B. E., A. R. Basu, M. Tatsumoto and H. Craig (1990) Temporal and spatial Sr, Nd, Pb, and He isotopic compositional variations in Hawaiian volcanism. EOS, **71**, 1669.

Farley, K. A., J. Natland and H. Craig (1992) Binary mixing of enriched and undegassed mantle components in Samoan lavas. Earth Planet. Sci. Lett., (in press).

Faure, G. and P. M. Hurley (1963) The isotopic composition of strontium in oceanic and continental basalt: application to the origin of igneous rocks. J. Petrol., 4, 31-50.

Gast, P. W., G. R. Tilton and C. Hedge (1964) Isotopic composition of lead and strontium from Ascension and Gough Islands. Science, 145, 1181-1185.

Goetze, C. and D. L. Kohlstedt (1973) Laboratory study of dislocation climb and diffusion in olivine. J. Geophys. Res., 78, 5961-5971.

Griffiths, R. W. and I. H. Campbell (1991) On the dynamics of long-lived plume conduits in the convecting mantle. Earth Planet. Sci. Lett., 103, 214-227.

Griffiths, R. W. and M. A. Richards (1989) The adjustment of mantle plumes to changes in plate motion. Geophys. Res. Lett., 16, 437-440.

Hart, S. R. (1984) A large scale isotopic mantle anomaly in the Southern Hemisphere. Nature, 309, 753-757.

Hart, S. R., D. C. Gerlach and W. M. White (1986) A possible new Sr-Nd-Pb mantle array and consequences for mantle mixing. Geochim. Cosmochim. Acta, 50, 1551-1557.

Hart, S. R., E. H. Hauri, L. Oschman and J. A. Whitehead (1992) Mantle plumes and entrainment: the isotopic evidence. Science, 256, 517-520.

Hart, S. R., J. G. Schilling and J. L. Powell (1973) Basalts from Iceland and along the Reykjanes Ridge: Sr isotope geochemistry. Nature, 246, 104-107.

Hart, S. R. and A. Zindler (1989). Constraints on the nature and development of chemical heteroeneities in the mantle. in *Mantle Convection*. New York, Gordon and Breach Science Publishers. 261-387.

Jordan, T. H. (1977) Lithospheric slab penetration into the lower mantle beneath the Sea of Okhotsk. J. Geophys., 43, 473-496.

Kurz, M. D., M. O. Garcia, F. A. Frey and P. A. O'Brien (1987) Temporal helium isotopic variations within Hawaiian volcanoes: basalts from Mauna Loa and Haleakala. Geochim. Cosmochim. Acta, 51, 2905-2914.

Kurz, M. D., W. J. Jenkins, S. R. Hart and D. Clague (1983) Helium isotopic variations in volcanic rocks from Loihi seamount and the island of Hawaii. Earth Planet. Sci. Lett., 66, 388-406.

Kurz, M. D. and D. P. Kammer (1991) Isotopic evolution of Mauna Loa volcano. Earth Planet. Sci. Lett., 103, 257-269.

Kurz, M. D., A. P. LeRoex and H. J. B. Dick (1992) Earth Planet. Sci. Lett., (in press).

Kurz, M. D., P. S. Meyer and H. Sigurdsson (1985) Helium isotopic systematics within the neovolcanic zones of Iceland. Earth Planet. Sci. Lett., 74, 291-305.

Kurz, M. D., R. B. Moore, D. P. Kammer and A. Gulessarian (1992) Earth Planet. Sci. Lett., (in press).

Lees, A. C., M. S. T. Bukowinski and R. Jeanloz (1983) Reflection properties of phase transition and compositional change models of the 67- km discontinuity. J. Geophys. Res., **88**, 8145-8159.

Liu, M. and C. G. Chase (1991) Boundary-layer model of mantle plumes with thermal and chemical diffusion and buoyancy. Geophys. J. Int., **104**, 433-440.

Malevsky, A. V., D. A. Yuen and L. M. Weyer (1991) Viscosity fields associated with chaotic non-Newtonian mantel convection. EOS, **72**, 479.

Morgan, W. J. (1971) Convection plumes in the lower mantle. Nature, **230**, 42-43.

Olson, P. (1984) An experimental approach to thermal convection in a two-layered mantle. J. Geophys. Res., **89**, 11,293-11,301.

Osako, M. and E. Ito (1991) Thermal diffusivity of $MgSiO_3$ perovskite. Geophys. Res. Lett., **18**, 239-243.

Oxburgh, E. R. and D. L. Turcotte (1968) Mid-ocean ridges and geotherm distribution during mantle convection. J. Geophys. Res., **73**, 2643-2661.

Parmentier, E. M., D. L. Turcotte and D. L. Torrance (1976) Studies of finite amplitude non-Newtonian thermal convection with application to convection in the earth's mantle. J. Geophys. Res., **81**, 1839-1846.

Parmentier, E. M., D. L. Turcotte and K. E. Torrance (1975) Numerical experiments on the structure of mantle plumes. J. Geophys. Res., **80**, 4417-4425.

Poreda, R., J. G. Schilling and H. Craig (1986) Helium and hydrogen isotopes in ocean-ridge basalts north and south of Iceland. Earth Planet. Sci. Lett., **78**, 1-17.

Richards, M. A. and R. W. Griffiths (1989) Thermal entrainment by deflected mantle plumes. Nature, **342**, 900-902.

Richter, F. M., S. F. Daly and H. C. Nataf (1982) A parameterized model for the evolution of isotopic heterogeneities in a convecting system. Earth Planet. Sci. Lett., **60**, 178-194.

Richter, F. M. and D. P. McKenzie (1981) On some consequences and possible causes of layered mantle convection. J. Geophys. Res., **86**, 6133-.

Roden, M. F., Frey, F. A., and Clague, D. A. (1984) Geochemistry of tholeiitic and alkalic lavas from the Koolau Range, Oahu, Hawaii: implications for Hawaiian volcanism. Earth Planet. Sci. Lett., **69**, 141-158.

Schilling, J. G. (1973) Icelandic mantle plume: geochemical evidence along the Reykjanes Ridge. Nature, **242**, 565-571.

Schlichting, H. (1968). *Boundary Layer Theory*. McGraw-Hill.

Sleep, N. (1990) Hotspots and mantle plumes: some phenomenology. J. Geophys. Res., **95**, 6715-6736.

221

Stacey, F. D. and D. E. Loper (1983) The thermal boundary-layer interpretation of D" and its role as a plume source. Phys. Earth Planet. Int., 33, 45-55.

Staudecher, T. and Allegre, C.J. (1989) Noble gases in glass samples from Tahiti: Teahitia, Rocard and Mehetia. Earth Planet. Sci. Lett., 93, 210-222.

Stocker, R. L. and M. E. Ashby (1973) On the rheology of the upper mantle. Rev. Geophys. Space Phys., 11, 391-426.

Sun, S. S., M. Tatsumoto and J. G. Schilling (1975) Mantle plume mixing along the Reykjanes Ridge axis: lead isotopic evidence. Science, 190, 143-147.

Tatsumoto, M. (1978) Isotopic composition of lead in oceanic basalts and its implication to mantle evolution. Earth Planet. Sci. Lett., 38, 63-87.

Trull, T. W., M. Roden, S. hart, F. Frey, M. Garcia, et al. (1990) He-Sr-Nd-Pb isotopic compositions of Koolau basalts. EOS, 71, 657.

Turcotte, D. L. and G. Schubert (1982). *Geodynamics: Applications to Continuum Physics to Geological Problems*. John Wiley & Sons.

Vine, F. J. (1972) The continental drift debate. Nature, 266, 19-22.

Weertman, J. and J. Weertman (1975) High temperature creep of rock and mantle viscosity. Ann. Rev. Earth Planet. Sci., 3, 293-317.

Whitehead, J. A. and B. Parsons (1978) Observations of convection at Rayleigh numbers up to 760,000 in a fluid with large Prandtl number. Geophys. Astrophys. Fluid Dyn., 9, 201-217.

Wilson, J. T. (1963) A possible origin of the Hawaiian Islands. Can. J. Phys., 41, 863-870.

Woodhead, J. D. and M. T. McCulloch (1989) Ancient seafloor signals in Pitcairn Island lavas and evidence for large amplitude, small length-scale mantle heterogeneities. Earth Planet. Sci. Lett., 94, 257-273.

Yuen, D. A. and L. Fleitout (1985) Thinning of the lithosphere by small-scale convective destabilization. Nature, 313, 125-128.

Yuen, D. A. and U. Hansen (1991) The dynamics of thermochemical boundary layers at the CMB and the 670 km discontinuity. EOS, 72, 450-451.

Yuen, D. A. and W. R. Peltier (1980) Mantle plumes and the thermal stability of the D" layer. Geophys. Res. Lett., 7, 625-628.

Yuen, D. A. and G. Schubert (1976) Mantle plumes: a boundary layer approach for Newtonian and non-Newtonian temperature-dependent rheologies. J. Geophys. Res., 81, 2499-2510.

Zhao, W. and D. A. Yuen (1987) The effects of adiabatic and viscous heatings on plumes. Geophys. Res. Lett., 14, 1223-1226.

Zindler, A. and S. R. Hart (1986) Chemical Geodynamics. Ann. Rev. Earth Planet. Sci., **14**, 493-571.

Zindler, A. and S. R. Hart (1986) Helium: problematic primordial signals. Earth Planet. Sci. Lett., **79**, 1-8.

Zindler, A., S. R. Hart, F. A. Frey and S. P. Jakobsson (1979) Nd and Sr isotope ratios and rare earth element abundances in Reykjanes peninsula basalts: evidence for mantle heterogeneity beneath Iceland. Earth Planet. Sci. Lett., **45**, 249-262.

CHAPTER 6

Conclusions

The primary goal of this dissertation has been to provide new constraints on the origins and development of chemical heterogeneities in the mantle, ultimately to aid in the study of mantle convection through geochemistry. The strategy has been to examine a broad range of topics which are relevant to this end, including the geochemical behavior of elements which are used as isotopic tracers, examining the scale of geochemical variability in the mantle, the geochemical signatures of isotopically extreme mantle compositions, the fluid dynamic characterization of mixing processes in mantle plumes, and an examination of the mechanisms of melt generation and segregation beneath oceanic islands. All of these issues are important geological problems in their own right, and represent fertile ground for more detailed, interdisciplinary studies which will ultimately provide further insight into the nature of chemical change in a dynamic earth.

The trace element and isotopic systematics of peridotites and mafic layers from the Ronda Ultramafic Complex, southern Spain (Chapter 2), provides information bearing on the geochemical behavior of the highly incompatible elements U, Th, and Pb in the mantle, and on the scale of geochemical variability in a large, exposed peridotite massif. Garnet is demonstrated to be a significant host for U in the mantle, and together with clinopyroxene, these two minerals control the abundances and partitioning relationships of U and Th during the melting of anhydrous peridotite. Clinopyroxene, plagioclase, and to a lesser extent garnet are hosts for Pb in mantle peridotite; however, the role of trace sulfide in these rocks is inferred to exert some control over the abundance and partitioning of Pb. Considering only the silicate phases, the uncertainty in mineral/melt partition coefficients for U, Th, and Pb are such that it is possible that a garnet-bearing peridotite which is a residue of melting can have high Sm/Nd and high U,Th/Pb ratios; with time, such a peridotite would develop high $^{143}Nd/^{144}Nd$ and $^{206}Pb/^{204}Pb$ and low $^{87}Sr/^{86}Sr$, which is in the direction of the HIMU component. However, the negative correlation between $^{143}Nd/^{144}Nd$ and $^{206}Pb/^{204}Pb$ for MORB indicates that Nd/Sm and U/Pb should be coupled in the depleted mantle. In addition, the high time-integrated Re/Os ratio of the HIMU mantle source (Chapter 4) indicates that a high-U/Pb depleted mantle cannot be the source of HIMU volcanics; since Os is a compatible element (D peridotite/melt about 10), the mineral.melt partition coefficient for Re between garnet and melt would have to be extraordinarily high (i.e. >100 for 10% garnet in the mode). This is inconsistent with the
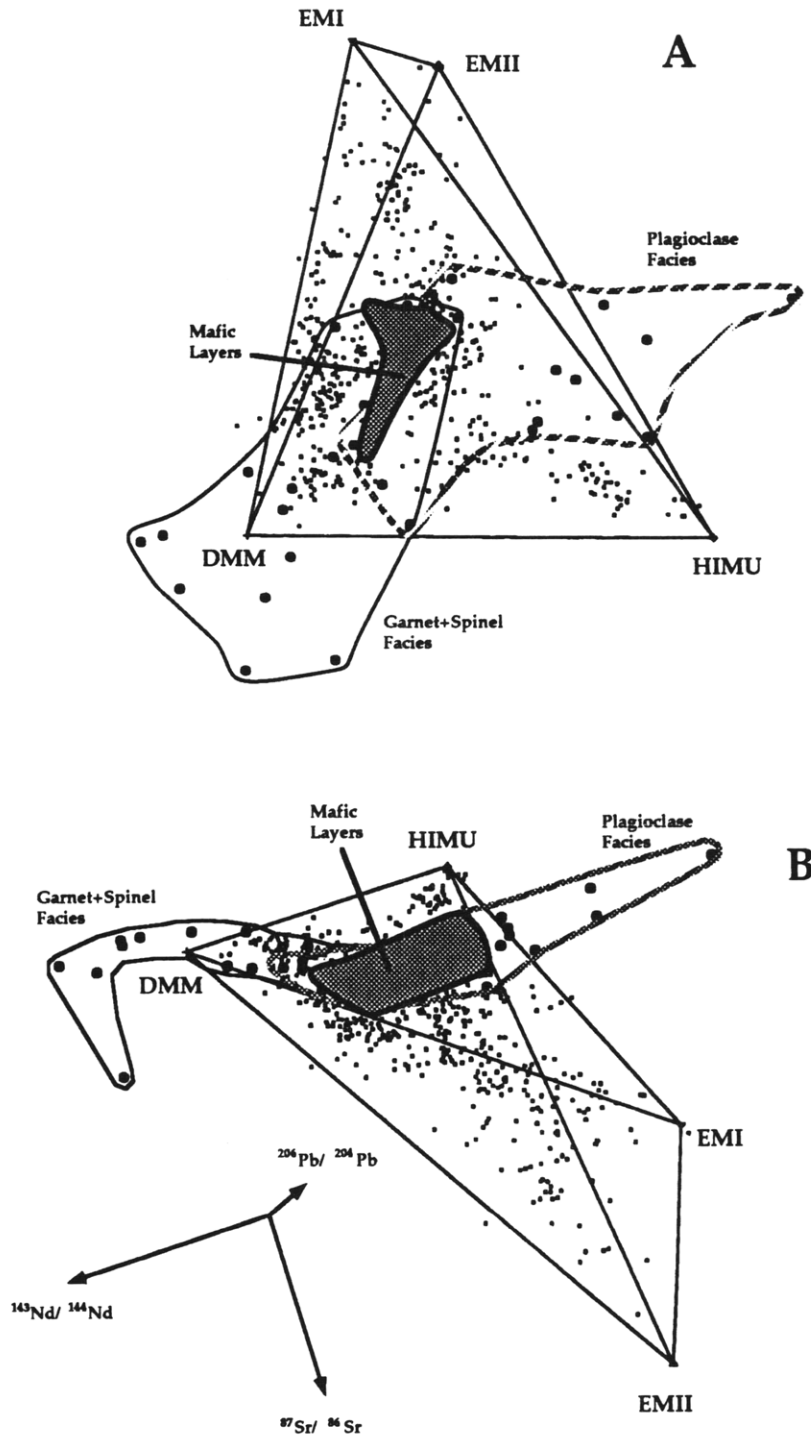
224

Figure 1. Projections of the Sr-Nd-Pb isotope data for the Ronda peridotites and mafic layers from Chapter 2. A) Projection onto the DMM-HIMU-EMI base triangle, as in Chapter 5, Fig. 7. Fields enclose data from peridotites from the garnet+spinel facies and placioclase facies, and mafic layer data (shaded field). B) Oblique projection of same data as in A, but rotated forward about 120°. The data are seen to form two distinct, quasi-planar fields which overlap in the region occupied by the mafic layers.

Re concentrations of the OIB in Chapter 4. In addition, the high $^{206}Pb/^{204}Pb$ Ronda peridotites are characterized by low $^{187}Os/^{186}Os$ (Reisberg et al., 1991).

The Pb-Pb systematics of garnet- and spinel-facies peridotites and mafic layers indicate a heterogeneity on the order of 3 Ga old. This Pb isotope signature may have been created within the massif 3 Ga ago, or may have been metasomatically imprinted on the massif 1.3 Ga ago. Figs. 1 and 2 show the Sr-Nd-Pb isotopic compositions of Ronda peridotites plotted with respect to the OIB tetrahedron from Chapter 5. It is obvious that Ronda covers a large fraction of the range of OIB data, and that the isotopic composition of MORB and that of many different oceanic islands could be generated by selectively melting certain parts of the Ronda massif. In this respect, it is important to assess whether Ronda may be representative of the convecting mantle, from which the full variety of OIB may be derived simply by selective melting, or if this heterogeneity is due to a residence in the subcontinental lithosphere. The lower mantle is unlikely to be as heterogeneous as Ronda, since at lower mantle temperatures diffusion alone would be effective at homogenizing the centimeter-scale variability observed in the garnet-facies (Chapter 2, Fig. 2). In addition, it is probable that the heterogeneity at Ronda is not representative of the upper mantle. The isotopic variability at Ronda is quite large compared with the heterogeneity at St. Paul's Rocks, which is a tectonic exposure of the uppermost oceanic mantle (Roden et al., 1984). This interpretation favors a history for Ronda in the subcontinental lithospheric mantle, where temperatures would be cool enough to develop cm-scale heterogeneities. In regards to this, the average isotopic composition of the garnet and spinel facies Ronda peridotites is similar to MORB, whereas the average isotopic composition of the plagioclase facies would lie within the field of the basalts from the Cameroon Line (Halliday et al., 1988) (compare Fig. 1 with Chapter 5, Fig. 7). Additionally, the average of the entire massif may be similar to the isotopic composition of the Ronda mafic layers, since they lie in the region of overlap of the garnet-spinel and plagioclase facies. This would be consistent with an origin as products of partial melting of the Ronda peridotite. In short, it is likely that the mantle which forms the sources of OIBs must be heterogeneous on the order of 25 km (i.e. the distance between adjacent Hawaiian volcanos), but the very fine-scale heterogeneity at Ronda is due to a subcontinental residence on the order of 1.3 Ga.

An investigation of the trace element and isotopic compositions of clinopyroxenes in peridotite xenoliths from Savaii, Western Samoa and Tubuai, Austral Islands (Chapter 3) reveals geochemical signatures which are not present in basalts from these islands, due to the inherent averaging of melting processes. The data indicate similarities in the melting and melt segregation processes beneath these isotopically extreme islands. Samples with

LREE depleted clinopyroxenes, with positive Zr and negative Ti anomalies, are the result of polybaric fractional melting of peridotite in the garnet- and spinel lherzolite stability fields, with the Savaii samples having experienced a larger mean degree of melting than the Tubuai samples. The extreme fractionation of adjacent HREE in the Savaii samples requires that they have melted to the clinopyroxene-out point (about 20%) while retaining residual garnet; the low concentrations of HREE in these same samples requires a further 10-20% melting in the spinel lherzolite stability field. Due to the extremely high total degrees of melting experienced by these samples (33-42%) compared with abyssal peridotites (10-20%), as well as the high degree of melting in the garnet lherzolite stability field, suggests a mantle plume origin for at least the Savaii xenoliths. Though peridotite xenoliths are usually considered to be fragments of the lithosphere, a plume origin is entirely consistent with fluid dynamic modelling which predicts advective thinning of the lithosphere by upwelling plume mantle (Yuen and Fleitout, 1985). If, however, these xenoliths are fragments of the lithosphere which is residual after MORB melting, then the Group 1 trace element patterns provide unequivocal evidence for the participation of garnet during MORB genesis.

A large majority of the xenolith clinopyroxenes from both Savaii and Tubuai are LREE enriched to varying degrees, and many samples display significant intergrain trace element heterogeneity. This highly variable yet systematic heterogeneity was the result of metasomatism by percolating melts undergoing chromatographic trace element fractionation. The unsupported $^{143}Nd/^{144}Nd$ of the TBA 4-11 xenolith (i.e. high $^{143}Nd/^{144}Nd$ coupled with low Sm/Nd) indicates that this metasomatism was recent, and most likely associated with the melting events which formed the respective islands. The trace element compositions of some LREE enriched clinopyroxenes are consistent with the percolating melt being typical oceanic island basalt. The clinopyroxenes with the highest LREE concentrations from both islands, which also have very low Ti and Zr concentrations and large amounts of grain-boundary hosted Ba, require that the percolating melt in these cases had the trace element signature of carbonatite melt. The extreme isotopic compositions of SAV 1-1 relative to Samoan basalts (Chapter 3, Fig. 14) indicates that these melts were not erupted in their pure form, but were mixed with melts of less enriched isotopic compositions; this is consistent with the fractional melting hypothesis for mantle plumes advanced in Chapter 3. The LREE-enriched xenoliths examined here have essentially served at "traps" for collecting small melt fractions which would not otherwise reach the surface. These "carbonatitic" signatures indicate the presence of volatile-rich, isotopically extreme components in the mantle beneath Tubuai and Savaii, possibly due to crustal recycling; the Sr-Nd-Pb isotopic composition of SAV 1-1 bears a notable

resemblance to modern oceanic sediments (Wright and White, 1987). These data indicate that the melt generation/segregation process in hotspots takes some average of the composition of the plume mantle; exactly how this averaging taps different parts of the plume requires detailed knowledge of the physics of magma extraction. In regard to this, the dominance of LREE-enriched over LREE-depleted xenoliths, and the scarcity of LREE-enriched signatures in abyssal peridotites, indicates that melt extraction is less efficient from hotspots than from the sub-ridge mantle.

The Re-Os isotope systematics of oceanic island basalts from Rarotonga, Savaii, Tahaa, Rurutu, Tubuai, and Mangaia were examined (Chapter 4) in order to place further constraints on the composition of isotopically extreme mantle, using the information available from the study of a parent-daughter system whose elements have unique geochemical behaviors compared with other isotope tracers. The Savaii and Tahaa samples, with high $^{87}Sr/^{86}Sr$ and $^{207}Pb/^{204}Pb$ ratios (EMII), as well as basalts from Rarotonga, have $^{187}Os/^{186}Os$ ratios of 1.026-1.086, within the range of estimates of bulk silicate earth and depleted upper mantle. Though recycled sediment may be required to generate the most extreme Sr-Nd-Pb isotopic compositions observed at Samoa, is process will have a fairly minor effect on the Re/Os systematics of the sediment-peridotite mixture, due to the low Re and Os concentrations of oceanic sediments (Ravizza, pers. comm.). The basalts from Rurutu, Tubuai, and Mangaia (Macdonald hotspot), characterized by high Pb isotope ratios (HIMU), have $^{187}Os/^{186}Os$ ratios of 1.117-1.248, higher than any estimates for bulk silicate earth, and higher than Os isotope ratios of metasomatized peridotites. Though the Ronda mafic layers are characterized by high $^{187}Os/^{186}Os$ ratios (Reisberg et al., 1991), their possible analogs in the convecting mantle cannot function as the HIMU source. Mafic layers will contribute almost all of the Pb to a melt of a peridotite-mafic layer mixture, and so they must have high $^{206}Pb/^{204}Pb$. But almost all of the Os in the melt will be contributed by the peridotite, not by the mafic layers (which have low Os concentrations). The result of mixing melts of mafic layers and melts of peridotite would define a strongly curved hyperbola, with most melts having low $^{187}Os/^{186}Os$ and high $^{206}Pb/^{204}Pb$. The high $^{187}Os/^{186}Os$ ratios indicate the presence of recycled oceanic crust in the mantle sources of Rurutu, Tubuai, and Mangaia, which would be more resistant to convective dispersion than the meter-scale Ronda mafic layers. The Re/Os ratios calculated for the HIMU mantle source require substantial amounts of crustal material to be recycled into the mantle; since the subduction of MORB is by far the largest return of crust to the mantle, this is the most likely source for the HIMU signature. Furthermore, the mixing of the Macdonald hotspot array toward FOZO (Chapter 5, Fig. 7), and the carbonatitic
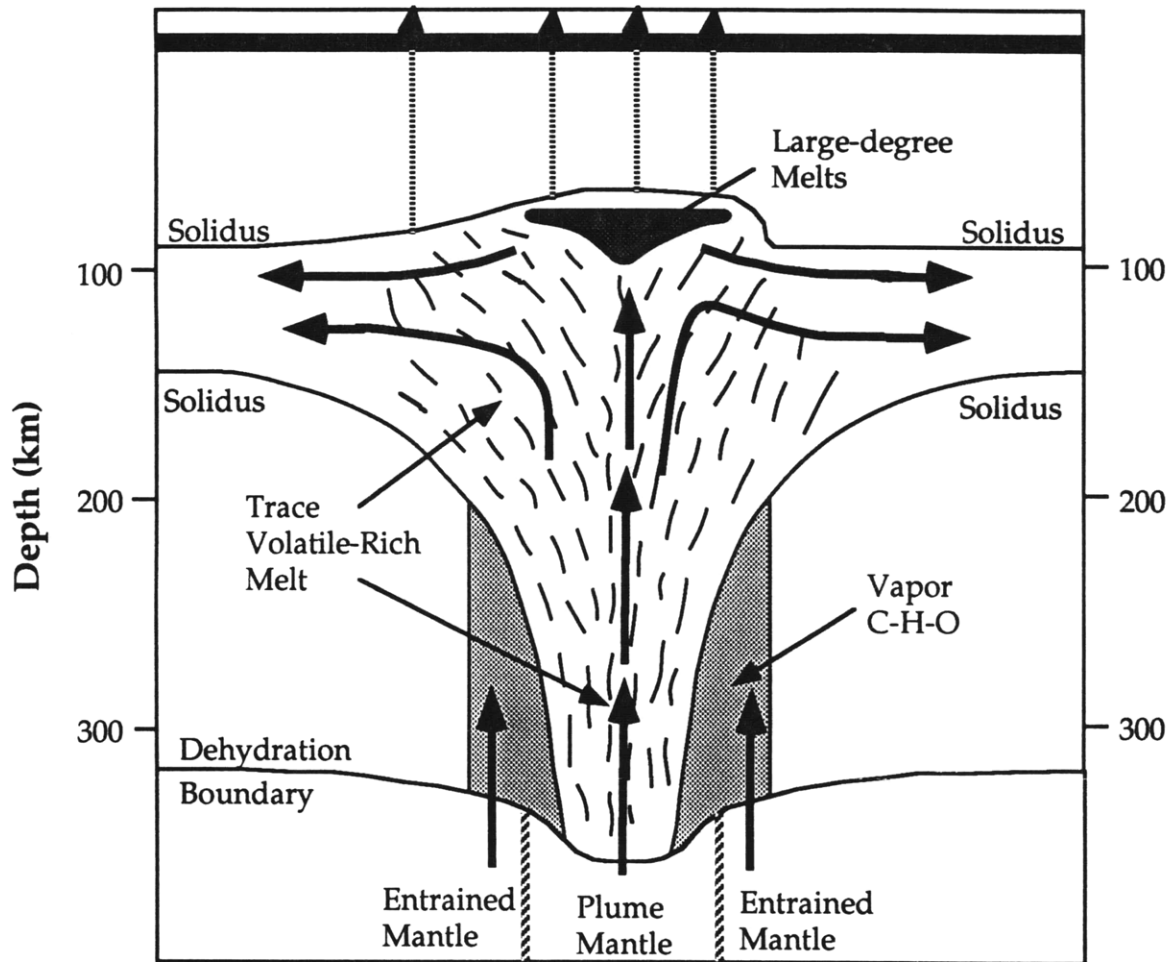
Figure 2. Schematic cross section through a concentrically zoned, volatile-bearing mantle plume undergoing fractional melting, adapted after Wyllie (1988). The plume is isotopically zoned, with "plume mantle" at the center and "entrained mantle" at the periphery. The plume crosses the volatile-bearing peridotite solidus at 350-400 km depth and begins to generate volatile-rich, small degree partial melts, some of which may have compositions similar to carbonatite. The melting plume is characterized by a large volume of mantle which is generating small degree, incompatible element-rich melts and a smaller volume of mantle above the anhydrous peridotite solidus generating higher degree melts. The compositions of erupted basalts depends strongly on how these various melts are mixed and segregated. Significant uncertainty remains in the distribution of plume mantle, entrained mantle, and lithosphere beneath hotspot volcanos; such information can come only from detailed fluid dynamic modelling of plume-lithosphere interaction employing an experimentally constrained peridotite rheology.

signatures present in the Tubuai xenoliths (Chapter 3, Fig. 4), indicates that oceanic crust and volatiles are recycled into the lower mantle.

The homogeneity of the Sr-Nd-Pb-Os isotopic data for Tubuai and Mangaia indicate that melt percolation through low-$^{187}Os/^{186}Os$ mantle, observed to occur in xenoliths from Tubuai (Chapter 3, Fig. 13), had little effect on the composition of the erupted magmas. The combined Os-Pb isotope systematics are a very sensitive indicator of melt percolation by porous flow; since Os is a compatible element and Pb is highly incompatible, porous flow through depleted mantle will be most obvious, and most hyperbolic, in the $^{187}Os/^{186}Os$ -$^{206}Pb/^{204}Pb$ signature. The evidence of melt percolation in the Tubuai xenoliths is clear, but the fact that low $^{187}Os/^{186}Os$ ratios are not observed in the Tubuai volcanics emphasizes the minor influence that melt percolation must have on the composition of erupted basalts at Tubuai and Mangaia, and probably other hotspot volcanos as well.

A fluid dynamic model for mantle plumes was developed in Chapter 5 by examining a vertical, axisymmetric boundary layer originating from a point source of heat, and incorporating experimentally constrained rheological and physical properties of the mantle. This model was constructed in order to examine the possible mixing processes at work in mantle plumes. Non-Newtonian plumes exhibit "plug flow" at the conduit axis, providing a mechanism for the transport of deep mantle material, through the full depth of the mantle, in an unmixed state. Plumes are demonstrated to entrain ambient mantle via the horizontal conduction of heat, which increases the buoyancy and lowers the viscosity of mantle at the plume boundary. Streamlines calculated from the fluid dynamic model demonstrate that most of the entrained mantle originates from below 1500 km depth; this effect is likely to be enhanced by lower thermal expansivity and higher viscosity in the lower mantle.

Examination of the global isotopic database for oceanic island basalts reveals the presence of a mantle component (FOZO), common to many hotspots worldwide, characterized by depleted $^{87}Sr/^{86}Sr$ and $^{143}Nd/^{144}Nd$, radiogenic $^{206,207,208}Pb/^{204}Pb$, and high $^{3}He/^{4}He$. This component is isotopically distinct from the source of MORB; thus, with the exception of ridge centered hotspots such as Iceland and the Galapagos, upper mantle does not appear to be a component in most hotspots, in agreement with entrainment theory. The modelled entrainment process does not result in intimate, fine scale mixing between "source" and "entrained" mantle, but instead results in a concentric zoning about the plume axis, with source mantle at the center and entrained mantle at the periphery. In this scenario, the binary mixing arrays in Fig. 7 of Chapter 5 are not due to the mixing of distinct volumes of mantle, but are the expression of magma mixing during fractional

230

melting and melt extraction in the individual plumes. The similarity of Sr/Pb, Sr/Nd, and Nd/Pb ratios in OIBs may then provide an alternative explanation for the quasi-linearity of the binary arrays. Such a scenario is depicted in Fig. 2, which is adapted from (Wyllie, 1988). A concentrically zoned, volatile-bearing plume will be characterized by a large volume which is between the volatile-bearing and anhydrous peridotite solidi, and which is generating incompatible and volatile element rich, small degree partial melts. At the axis of the plume is a smaller region above the anhydrous peridotite solidus which is generating higher degree melts. The way in which these melt fractions of diverse compositions are mixed together depends strongly on the physics of fracture formation in a two-phase, viscous, non-Newtonian medium. One observation which may be pertinent to this case is the common association of replacive dunites with shear zones in the Josephine peridotite (Keleman, pers. comm.). If in fact melts are localized along shear zones, then this may provide a mechanism for mixing of melts from the concentric zones of the plume; in Figs. 2 and 3 from Chapter 5, it is apparent that the region of greatest shear in a plume is located near the boundary between "source" and "entrained" mantle.

The combined fluid dynamic and isotopic results indicate that both FOZO and enriched mantle components (EMI, EMII, HIMU, and intermediate compositions) must be available for transport into the lower mantle; thus the origin of the HIMU signature in recycled oceanic crust requires mass exchange between the upper and lower mantle. In addition, the absence of a MORB source (=upper mantle) signature in off-ridge hotspots, coupled with high $^3He/^4He$ in FOZO and the low $^3He/^4He$ of MORB, suggests that mantle plumes do not originate from a thermal boundary layer at 670 km, and thus that convection must penetrate the full depth of the mantle. However, the MORB source and FOZO, associated with the upper and lower mantle, respectively, are still isotopically distinct, though there may be some overlap in Sr, Nd, Pb, and Os isotopic compositions. The preservation of isotopically different upper and lower mantles does not require layered convection, but may be the result of a longer residence time for the mantle below 670 km than the upper mantle, possibly the result of an increasing mean viscosity with depth.

References

Halliday, A. N., A. P. Dickin, A. E. Fallick and F. J.G. (1988) Mantle dynamics: A Nd, Sr, Pb and O isotopic study of the Cameroon Line volcanic chain. J. Petrol., **29**, 181-211.

Reisberg, L. C., C. J. Allegre and J. M. Luck (1991) The Re-Os systematics of the Ronda Ultramafic Complex of southern Spain. Earth Planet. Sci. Lett., **105**, 196-213.

Roden, M. K., S. R. Hart, F. A. Frey and W. G. Melson (1984) Sr, Nd and Pb isotopic and REE geochemistry of St. Paul's rocks: The metamorphic and metasomatic development of an alkali basalt magma source. Contrib Mineral Petrol, **85**, 376-390.

Wright, E. and W. M. White (1987) The origin of Samoa: new evidence from Sr, Nd and Pb isotopes. Earth Planet. Sci. Lett., **81**, 151-162.

Wyllie, P. J. (1988) Solidus curves, mantle plumes, and magma generation beneath Hawaii. J. Geophys. Res., **93**, 4171-4181.

Yuen, D. A. and L. Fleitout (1985) Thinning of the lithosphere by small-scale convective destabilization. Nature, **313**, 125-128.